3D Geomechanical Model for Gas Storage Bergermeer

Report for TAQA Energy BV

Prepared by

Fenix Consulting Delft BV

Date
March 2018

3D Geomechanical Model for Gas Storage Bergermeer

Report for TAQA Energy BV

Date
March 2018

DISCLAIMER

Fenix Consulting Delft nor any person acting on behalf of Fenix:

- **Makes any warranty or representation, express or implied, with respect to the accuracy, completeness, or usefulness of the information contained in this report, or that the use of any apparatus, method, or process disclosed in this report may not infringe privately owned rights; or**

- **Assumes any liability with respect to the use of, or for damages resulting from the use of, any information, apparatus, method, or process disclosed in this report.**

*****

Nederlandse Samenvatting

Dit rapport bevat een geomechanische evaluatie van gasopslag-operaties in het Bergermeer reservoir, met het doel om het seismische risico in kaart te brengen. Het toegepaste model gaat uit van opslagcycli waarbij de maximale injectie en productie snelheden worden toegepast in het huidig vergunde drukbereik van 77 tot 133 bar.
Bij het oorspronkelijke ontwerp van het opslagproject is een voorspelling gemaakt van de reactie van het reservoir op drukwisselingen en het potentiële seismische risico. Een elastisch model voorspelde geen enkele seismiciteit tijdens opvullen en opslag-cycli. Deze voorspelling stemt overeen met de waarneming van louter zeer zwakke micro-seismiciteit. Het elastische model biedt echter geen verklaring voor de waargenomen micro-seismiciteit. Bovendien kan het de geringe bodemstijging gedurende de opvulfase en opslag-cycli niet verklaren. Zorg voor de omgeving vereist dat die micro-seismiciteit verklaard wordt met een aangepast model dat gekalibreerd is op de bodembeweging, waarmee mogelijke toekomstige veranderingen in de micro-seismische activiteit voorspeld kunnen worden.
In de huidige studie is een nieuw geomechanisch model dat corrigeert voor seismische geïnduceerde slip op de breuken, gekalibreerd met gegevens van de injectie- en productieperiodes, zodat een veilig gebruik van de opslag beoordeeld kan worden. De beoordeling is gebaseerd op gesteente-spanning, bodemdaling, reservoirdruk-geschiedenis en micro-seismische gegevens.
De interpretatie van de gesteente-spanning voor het Bergermeer reservoir levert een lagere waarde op vergeleken met eerdere modellen. Tevens wordt het geomechanische model vergeleken met de waargenomen bodembeweging gemeten met 4 GPS stations tijdens het opvullen van de opslag tussen Januari 2014 en December 2016. De gefilterde GPS curves laten slechts een kleine opheffing zien gedurende de refill en opslag fase wat aangeeft dat het reservoir stijver is vergeleken met de depletie fase. Verder tonen de stations een vertraagde uitzetting van het reservoir ten opzichte van de drukverhoging, met een gemiddelde relaxatietijd van een paar maanden. De beste verklaring van de vertraagde opheffing is een reservoirstijfheid die afhangt van de snelheid van veranderingen in de reservoirdruk.
Micro-seismische gegevens tot juni 2017 zijn gecontroleerd en herplaatst door Q-con (zoals beschreven in aparte rapporten). De seismische trillingen konden gerelateerd worden aan de belangrijkste breuken. De meeste activiteit was langs de centrale breuk en de sterkste bevingen kwamen uit de nabijheid van het punt van de breuk, waar het breukvlak de twee reservoirblokken scheidt. Dit punt was kritisch gespannen zoals bleek uit de bevingen tijdens productie en het model. Slip op het breukvlak zorgde niet alleen voor een verlaging van de schuifspanning in het gebied dat slipt, maar tevens voor een verhoging van de schuifspaning op de randen van het slipgebied, vooral aan de boven en onderkant van het reservoir.
De intensiteit van de micro-seismische activiteit was het sterkst tijdens opvullen van de opslag met kussengas tot 77 bar, wat suggereert dat de eerder gespannen breuk lokaal werd gereactiveerd tijdens refill. De sterkste micro-seismische activiteit was begin 2013, waarna de activiteit afnam. In 2013 was het drukverschil tussen beide zijden van de centrale breuk het grootst, maar op zichzelf kan dit de seismiciteit niet verklaren, omdat op dat moment de stabilisatie van de breuk bij hogere druk reeds de overhand had. De plekken op de breuk waar de schuifspanning was toegenomen kunnen de meeste seismiciteit tijdens kussengasinjectie verklaren, die ophield toen de druk verder opliep, waardoor de breuk stabiliseerde. Met het oog op de wijd verspreide seismiciteit op de breuk ligt het voor de hand dat heterogeniteiten de micro-seismische trillingen met lage magnitude verklaren, omdat die veroorzaakt zijn door afschuivingen die maar enkele vierkante meters beslaan.
Tijdens de opslagcycli is er voortdurend zwakke microseismische activiteit waargenomen op de Oostelijke randbreuk. Het is opmerkelijk dat deze activiteit optreedt wanneer de injectie opgestart wordt, terwijl de verwachting is dat elastisch gedrag een verdere stabilisering zou geven bij drukverhoging. De micro-seismiciteit is heel zwak, met magnitude onder -1, dus alleen kleine scheuren of breukcontacten kunnen daar verantwoordelijk voor zijn. Aangenomen dat micro-seismiciteit evenredig is met afschuivingssnelheid, kan de waargenomen activiteit verklaard worden. De lagere micro-seismische activiteit tijdens productie komt overeen met het Kaiser effect, dat bij herbelasten onder de maximale belasting minder seismische activiteit voorspelt.
De westelijke randbreuk is meer kritisch gespannen dan de oostbreuk, zodat de afwezigheid van enige seismische activiteit op deze breuk waarschijnlijk verklaard wordt door een lagere neiging tot seismische slip door andere eigenschappen van het gesteente bij deze breuk.

Mede omdat de micro-seismische activiteit duidelijk is afgenomen na meerdere snelle drukverhogingen in het reservoir in de afgelopen jaren, is het hoogstwaarschijnlijk dat toekomstige gas opslag cycli in de range 77-133 bar gedaan kunnen worden zonder het veroorzaken van sterke bevingen. Dit wordt ondersteund door de simulaties.

Conclusies

- De waargenomen seismische activiteit is sterk geconcentreerd in tijd en ruimte. De kritische spanning op de centrale breuk heeft een tijdelijk karakter, zoals de seismische waarnemingen laten zien. Gedeelten van de breuk die seismisch actief waren tijdens opvullen worden na verloop van tijd weer inactief. Dit toont aan dat er geen grote oppervlakken zijn op de breuk die kritisch gespannen raken, zodat er alleen kleine bevingen kunnen optreden.
    - Op de centrale breuk, waar de meeste activiteit optrad was er een Noord-Zuid trend van de activiteit over de tijd. Deze trend wordt verklaard door het verschil in herstel van de schuifspanning tussen het noordelijke en zuidelijke deel van de breuk.
- De geomechanische reactie van het Bergermeer gasreservoir is geanalyseerd op basis van spanning, bodembeweging en seismiciteit:
    - De opheffing aan het maaiveld is minder dan voorspeld met elastisch gedrag, dat gekalibreerd was op bodemdaling tijdens productie. De beste verklaring voor de kleine opheffing en tijdsvertragingvan de bodembeweging is snelheids- en spanningsafhankelijke reservoirstijfheid.
    - Calibratie van de frictie coëfficiënt levert een waarde op van 0.65 voor de Centrale breuk. Het model voorspelt dan een cumulatief seismisch moment dat overeenkomt met het waargenomen moment. Een lagere frictie coëfficiënt is ook mogelijk, maar dan geeft het model een slechtere overeenkomst met de waargenomen seismiciteit tijdens opvullen van het reservoir.
    - Calibratie van de frictie coëfficiënt voor de oost-breuk geeft een frictie coëfficiënt van 0.6, wat overeenkomt met enkele niet voelbare bevingen die tezamen een equivalente cumulatieve magnitude hebben van 2.5. Dit komt overeen met de waarneming dat geen voelbare aardbevingen (magnitude van ongeveer 1.5 voor het Bergermeer reservoir) zijn geïnduceerd op de oostbreuk. Een paar aardbevingen met die magnitude zouden geïnduceerd kunnen zijn tijdens depletie, zonder waargenomen te worden aangezien er nog geen microseismisch monitor systeem in plaats was.
    - De meeste seismische activiteit sinds 2007 trad op tijden kussengas injectie. De activiteit was veel zwakker tijdens de snelle drukwisselingen van de opslag cycli en de activiteit op de Centrale breuk is helemaal opgehouden. Daarom zijn de breuksystemen gestabiliseerd, wat verklaard wordt door herstel van de gemiddelde spanning op de breuk en continue slip.
    - Seismisch activiteit op de Centrale breuk tijdens refill kan verklaard worden met de toegevoegde schuifspanning als gevolg van de afschuiving tijdens de aardbevingen in de depletie fase.
        - Verdwijnen van de activiteit op de Centrale breuk kan verklaard worden met voortgaande slip op de breuk als die kritisch wordt. De meeste slip zou niet-seismisch zijn omdat de micro-seismiciteit maar een paar procent van het seismische moment kan verklaren dat het model geeft.
        - Het drukverschil over de breuk had slechts een klein effect op de seismiciteit.
        - De beste overeenkomst van het model met de seismische waarnemingen voorspelt dat er geen seismiciteit zal optreden op de centrale breuk tijdens toekomstige opslag cycli.
- Het seismisch risico is klein voor toekomstige opslag-cycli. Deze conclusie wordt gedragen door waarnemingen en het gecalibreerde model.
    - In het ergste geval dat er geen slip plaats heeft gevonden op de Centrale breuk tijdens de refill en de opslag cycli, is de maximum mogelijk aardbevingsmagnitude voor toekomstige opslag cycli 2.2.
    - De Oost-breuk wordt niet meer kritisch tijdens kussengas injectie en toekomstige cycli. De waargenomen seismiciteit wordt veroorzaakt door heterogeniteit van de breuk, zoals

scheuren en contactpunten op de breuk die maar een oppervlak hebben van enkele vierkante meter.

- De micro-seismiciteit treedt voornamelijk op tijdens injectie periodes. Dit kan verklaard worden omdat het Kaiser effect voornamelijk van toepassing is op herbelasting terwijl zwakke micro-seismiciteit verwacht wordt bij ontlasting van de breuk.

- Als de Oostbreuk nooit afschuiving gehad heeft, zou er nog overmatige schuifspanning op de breuk kunnen zitten die, als de breuk toch zou gaan schuiven, een aardbeving met magnitude 1.7 kan induceren.

Executive Summary

This report contains a geomechanical evaluation of the Bergermeer storage reservoir response to gas operations with the aim to determine seismic risk. The applied model used storage cycles with maximum injection and production capacity between the current permit range of 77 and 133 bar.
In the original design of the gas storage project, a forecast was made of the reservoir response and potential seismicity. An elastic model predicted no seismicity at all during refill of the reservoir and storage cycles. This prediction agrees with the observation of only weak micro-seismicity during refill. However, the elastic model does not provide an explanation for the micro-seismicity and it does not account for the much stiffer surface displacement observed during refill and storage. Hence, it is prudent to explain the micro-seismicity with a modified model that is calibrated on the surface movement, so that future evolution of seismicity can be predicted.
In this study, a new geomechanical model that incorporates seismic fault slip is calibrated with the acquired data of the injection and production periods, to assess the safe operation of the project.
The evaluation is based on stress, subsidence, reservoir pressure history and micro-seismic data. The stress measurement interpretation yields a lower stress than used in previous modelling work. Further, the geomechanical model response is compared to the observed surface heave in 4 GPS stations during the injection stages between January 2014 and December 2016. Filtered GPS surface displacement curves show only a small uplift during refill and storage, indicating a much stiffer reservoir response compared with depletion. Also, the stations show a delayed reservoir expansion with respect to the pressure, with an average relaxation time of a few months. The most plausible cause of the time delay in the surface displacement is rate dependent stiffness in the reservoir.
Micro-seismic data up to June 2017 were quality checked and relocated by Q-con (as described in separate reports). The micro-seismic events could be migrated to the main reservoir faults. Most activity occurred along the midfield fault and the stronger events were located near the point where the fault separates the reservoir blocks. This point was critically stressed as inferred from depletion seismicity and modelling. Slip on the fault not only decreased shear stress in the slip area but also increased shear stress at the edges of the slip area, mostly at the top and bottom of the reservoir.
The intensity of micro-seismic activity during refill was strongest during cushion gas injection (up to 77 bar) which suggests that previously critically stressed patches of the fault were re-activated by refill. The strongest event occurred in early 2013, while activity later declined. In 2013 the pressure differential was peaking, but the pressure differential between the two reservoir compartments alone cannot explain fault re-activation, because of the dominance of the elastic stress recovery. The regions with increased shear stress can explain much of the refill seismicity, which ceased when the pressure was increased, giving a more stable fault. In view of the distributed micro-seismic activity on the fault, it is plausible that heterogeneity explains the events with very small magnitude, having very small slippage areas in the order of a few square metres.
During the storage cycles, continued weak micro-seismic activity was observed on the Eastern bounding fault. It is remarkable that this seismic activity occurs mostly at the beginning of the injection season, while the model predicts that rising pressure stabilizes the fault. The micro-seismicity is very weak, below magnitude -1, so only small fractures or fault asperities are involved in the slippages. Assuming that micro-seismic rate is proportional to shear stress rate can explain the activity at the start of injection. Lower micro-seismic activity during production can be explained by the Kaiser effect that predicts low activity during re-loading.
The West bounding fault is more critically stressed than the East fault, so that the absence of seismic activity is most likely explained by a smaller tendency to create seismic slip, caused by different fault zone properties and saturation.
Since micro-seismic activity was already declining during several rapid pressure increases in recent years, it is likely that future gas storage operations that make use of the full swing capacity of 77-133bar can be performed, without inducing strong seismic events. This is supported by the simulations.

Conclusions

- Observed seismic activity is strongly clustered in space and time. Stress criticality on the Midfield fault has a transient signature as evidenced by seismic monitoring data. Fault patches that were seismically active during refill can become inactive after a certain amount of time has passed. This

shows that there are no large areas of the fault that become critical, so only weak seismic events can be induced.
    - On the midfield fault, where most seismicity occurred a North-South migration of the seismicity was observed with time. This shift is probably related to a difference in shear stress recovery between Northern and Southern parts of the fault.
- The geomechanical response of the reservoir has been analyzed based on the relation between stress, surface displacement and seismicity:
    - Surface heave is smaller than predicted by elastic behaviour calibrated to depletion subsidence. The most plausible cause of the small heave and time delay of the surface displacement is rate and stress dependent stiffness in the reservoir.
    - Calibration of the friction coefficient yields a value of 0.65 for the midfield fault. The model then gives a cumulative seismic moment equivalent to the observed seismic moment. A smaller friction coefficient is also possible, but in that case the match with refill seismicity becomes poorer.
    - Calibration of the friction coefficient for the East fault gives a friction coefficient of 0.6, which corresponds to multiple non-felt events with an equivalent cumulative magnitude of 2.5. This agrees with the observation that no felt earthquakes were observed at the East fault during depletion, which would have magnitude of about 1.5 for the Bergermeer reservoir. A few earthquakes of this magnitude could have happened during depletion without being detected as no micro-seismic monitoring was in place yet.
    - Most seismic activity since 2007 occurred during cushion gas injection. The activity was much weaker during the fast pressure increases during storage cycles and the activity on the Midfield fault has ceased. Therefore, the fault systems are stabilizing, which is explained by average stress recovery on the fault and continuous slippage.
    - Refill seismicity on the Midfield fault can be explained with the additional shear stress induced by slip from the depletion earthquakes.
        - Disappearance of seismicity on the Midfield fault can be matched by assuming continuous slip on the fault when it becomes critical. Much of this slip should be non-seismic since the micro-seismicity accounts only for a few percent of the potential slip.
        - The pressure differential between the two compartments had a minor effect on seismicity.
        - For the best match no seismicity is expected for the Midfield fault during future storage cycles.
- Seismic risk is deemed small for future gas storage cycles. This conclusion is supported both by observation and the calibrated model.
    - Assuming a worst case that no slip has occurred on the Midfield fault during refill and storage cycles, the maximum possible magnitude for an earthquake during future storage cycles is 2.2.
    - The East fault does not become critically stressed again during refill and storage cycles. The observed weak micro-seismicity is caused by critically stressed heterogeneities such as fractures and fault asperities that are only a few metres in diameter.
        - The micro-seismicity occurs mostly during injection periods. This can be explained since the Kaiser effect applies to re-loading, but weak micro-seismicity is still expected during unloading.
    - If the East fault never slipped, there could still be excess stress on the fault, assuming a default friction coefficient of 0.6. If the fault would still slip, it could induce a small earthquake with magnitude 1.7.

Contents

List of Figures

List of Tables

Nomenclature

Units: SI (m= metre, s= second, kPa =10^3Pa, MPa =10^6Pa, GPa =10^9Pa)

Dimensions: m= mass, L= length, t= time

Variable		Description	Units	Dimensions
a_i, a_∞	:	shear modulus fraction	[-]	(-)
A_p	:	Poroelastic coefficient	[-]	(-)
A	:	Area	[m^2]	(L^2)
$A_{k,i}$	:	Amplitude of noise period i of station k	[m]	(L)
c	:	cohesion	[MPa]	(m/Lt^2)
c_g	:	grain compressibility	[1/MPa]	(Lt^2/m)
c_r	:	rock compressibility	[1/MPa]	(Lt^2/m)
c_m	:	compaction coefficient	[1/MPa]	(Lt^2/m)
E	:	Young's modulus	[GPa]	(m/Lt^2)
E_{eff}	:	Effective Young's modulus	[GPa]	(m/Lt^2)
$\tilde{E}$	:	elastic coefficient	[Pa/m]	(m/L^2t^2)
G, G_{EL}	:	Shear modulus	[GPa]	(m/Lt^2)
G_∞	:	Relaxed shear modulus at infinite time	[GPa]	(m/Lt^2)
g	:	Stress gradient	[kPa/m]	(m/L^2t^2)
H	:	Height	[m]	(L)
L_z	:	Chacaractersitic height	[m]	(L)
K_h	:	horizontal stress ratio	[-]	(-)
M_0	:	seismic moment	[N m]	(mL^2/t^2)
M_c	:	compaction moment	[N m]	(mL^2/t^2)
M_w	:	moment magnitude	[-]	(-)
p	:	pressure	[MPa]	(m/Lt^2)
$p(N,t)$	:	poisson distribution	[-]	(-)
$R_{c,N}$	:	average critical stress ratio	[-]	(-)
t	:	time	[s]	(t)
$t_{0,k,i}$	:	time shift for noise period i of station k	[s]	(t)
$T_{k,i}$	:	period of noise cycle i	[s]	(t)
u, v, w	:	displacement	[m]	(L)
$\boldsymbol{u}$	:	displacement vector	[m]	(L)
u_{dip}	:	displacement in dip direction	[m]	(L)
u_{strike}	:	displacement in strike direction	[m]	(L)
V_{res}	:	reservoir volume	[m^3]	(L^3)
α_B	:	Biot coefficient	[-]	(-)
ε	:	strain	[-]	(-)

ε_T	:	volumetric strain	[-]	(-)
$\in_k$	:	average deviation in surface heave of station k	[m]	(L)
$\in$	:	average deviation in surface heave	[m]	(L)
ε	:	strain	[-]	(-)
ν	:	Poisson's ratio	[-]	(-)
η	:	viscosity	[Pa s]	(m/L t)
μ	:	friction coefficient	[-]	(-)
Γ	:	viscoelastic shear relaxation function	[MPa]	(m/Lt^2)
σ_d	:	deviatoric stress	[MPa]	(m/Lt^2)
$\sigma_{H,max}$	:	maximum horizontal stress	[MPa]	(m/Lt^2)
$\sigma_{H,min}$	:	minimum horizontal stress	[MPa]	(m/Lt^2)
σ_{vert}	:	vertical stress	[MPa]	(m/Lt^2)
σ_n	:	normal stress on fault plane	[MPa]	(m/Lt^2)
τ	:	shear stress	[MPa]	(m/Lt^2)
τ_i	:	relaxation time	[s]	(t)

1 Introduction

In this report, first the issues of seismicity related with pressure cycling between 77 and 133 bar average reservoir pressure will be evaluated using a calibrated geomechanical model.
Concern about seismic risk in Bergermeer arose since the reservoir induced significant earthquakes of magnitude up to 3.5, causing some minor damage to houses. These earthquakes occurred during the depletion phase that lasted till 2007 when the gas field had been depleted down to 35 bar. Figure 1 shows the pressure history and earthquakes. The earthquakes originated from the midfield fault shown in Figure 2; the location of the cross-section in the horizontal plane is near the separation of the two compartments by the fault (KNMI, 2008; Dahm, 2010).

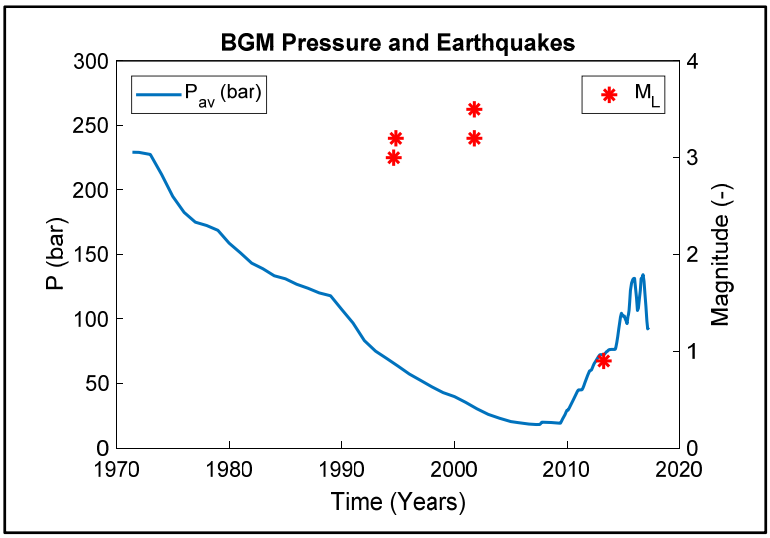

Figure 1: Bergermeer pressure history and earthquakes. The strongest events occurred after depletion, but some four hundred micro-seismic events (below magnitude 0) were also observed during refill.

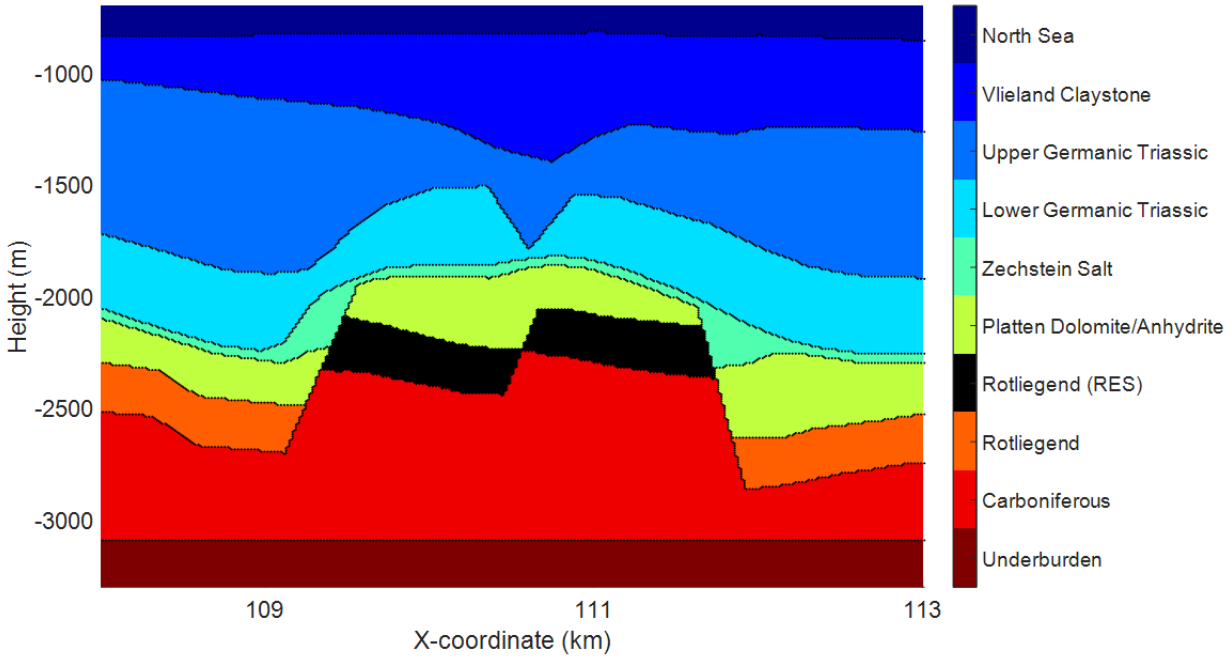

Figure 2: Cross-Section of Bergermeer reservoir, through the midfield fault south of the point where the blocks are juxtaposed.

When the reservoir was considered for gas storage, it was decided to first investigate the mechanism of seismicity and determine the seismic risk during refill of the gas reservoir and subsequent production-injection cycles. As a result, the Bergermeer reservoir is probably the most studied and modelled reservoir of the small gas reservoirs in the Netherlands. Although additional seismic risk was deemed small, it was not realistic to rule out any seismicity, so it was decided to operate the gas storage with a seismic risk management system. The central component is a so-called Traffic Light System (TLS) based on permanent monitoring of seismicity. Figure 3 shows an empirical relation between magnitudes and rupture area size with observed Bergermeer earthquakes (Dowrick *et al.*, 2004). The sizes of the slippage area in the Bergermeer earthquakes are also shown as well as a few Groningen earthquakes. These inferred slip areas are larger than the empirical correlation, but there is quite some uncertainty in these data as well as a large scatter between results. The reason is that moment magnitude is proportional to slip area and stress drop. When the inferred stress drop is small (as is obvious from the Bergermeer analysis which yielded 0.3MPa for the stress drop) then the slip area will be large. In the calibrated model, the slip is estimated on the fault and this will be used to compute magnitude. Since the model is calibrated on observed moment magnitude, the prediction is based on the observations, so becomes insensitive to assumptions about the relation between magnitude and stress drop.
The Traffic Lights for Bergermeer were defined by: Green: Magnitude lower than 1.5 (events not felt at surface), Yellow: magnitude range from 1.5 to 2.5, Orange: magnitude range from 2.5 to 3.5 and Red: Magnitude above 3.5. The seismic activity caused by depletion (between 1972 and 2007) in 1994 and 2001 was close to the upper limit of the TLS, while the seismic activity during the refilling of the storage with cushion gas and storage cycles (2010-2017) is far below the lower limit of 1.5 with a maximum magnitude of 0.9 at the end of the cushion gas injection. Since the monitoring yielded a large data set over the last years, a next step can now be made in calibrating the geomechanical model with the additional observations. By using more measurements, especially micro-seismicity, the model delivers a more reliable prediction of potential seismic risk associated with future storage cycles.

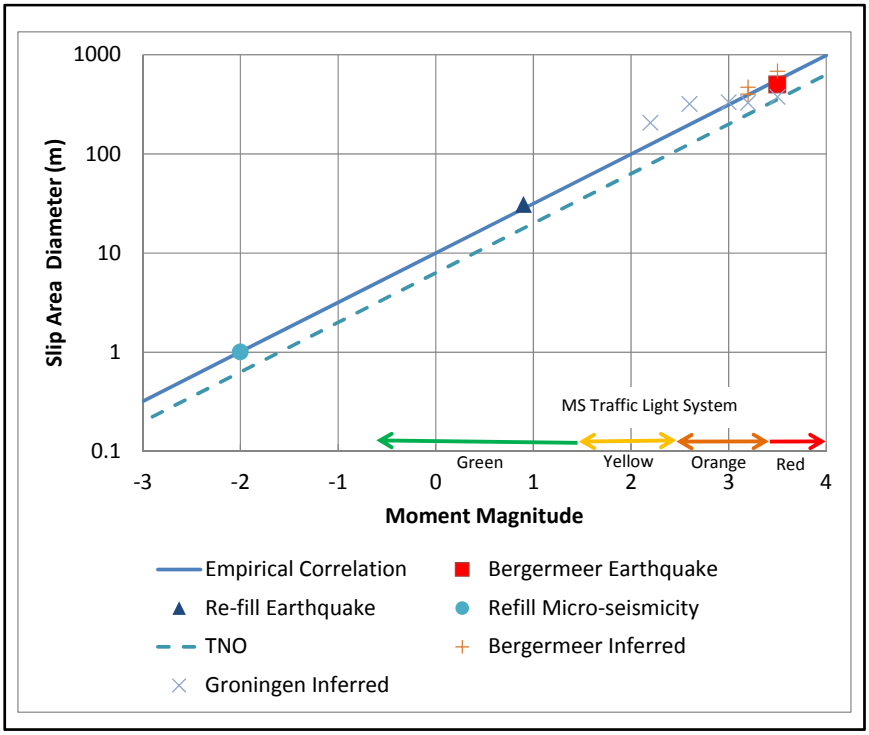

Figure 3: Correlation between size of rupture area (for a square area) and earthquake magnitude. For reference the observed maximum magnitude earthquake is plotted in Bergermeer and the micro-seismicity during re-fill of the reservoir. Using seismic traces the size of the slip area and the stress drop can be inferred. These slip area dimensions are plotted for Bergermeer and Groningen. For a computed maximum slip area, the empirical relation gives a conservative estimate of magnitude. The TNO correlation is based on a theoretical relation and is even more conservative.

Past modelling work predicted increased stability of the faults for increasing gas pressure (Baker, 2013). However, some of the modelling indicated the possibility of slip for critically stressed faults during cushion gas injection, when the slip of the earthquakes was included in the model (TNO, 2009; TNO, 2011; Orlic, 2013). After several years of operation of the gas storage it can be concluded that the original, elastic models were quite accurate. Compared with the depletion earthquakes, the micro-seismic activity observed during refill and storage cycles was very weak. Still, it is of interest to investigate the mechanism of micro-seismic activity so that a prediction can be made of seismic activity during future storage cycles.

The conventional theory is that in Dutch gas fields, depletion causes shear stress increase on the faults, which may then induce earthquakes. This implies that during re-fill, there will be unloading of the faults and the stability of the faults should be recovered by increasing pressure. This will be also valid for faults that have slipped, since increase of pressure and the resulting reservoir expansion will reduce the shear stress and move the fault's stress state away from the failure envelope. This is called the Kaiser effect based on the research on acoustic emission by Joseph Kaiser (1950) which was on metals, but the effect has also been found in other materials like cement and rock.

However, the conventional theory has to be re-examined in the context of observations that gas storage reservoirs often induce seismicity (although with small magnitude) during re-fill, as observed not only in Bergermeer, but also in other fields. Since elastic behaviour is expected to show no seismicity during re-pressurization, there must be an inelastic effect that causes seismicity, like fault slippage. Fault slippage will not only induce shear stress decrease but also enhance shear stress at the edge of the slippage area, which may later cause seismicity. Also, inelastic rock behaviour introduces hysteresis in the reservoir and fault stresses during re-pressurization. This causes seismicity if the stress state exceeds the failure envelope.

In previous reports (Q-con, 2015, 2016, 2017), an extensive description was given of the data used to calibrate the model. Only a summary will be given of the observed data that shed light on the reservoir response during refill. The most important data for seismic risk assessment using a geomechanical model are the stress, surface displacement and seismic activity itself. In a normal faulting regime, the vertical and minimum horizontal stresses determine fault stability. The vertical stress can be reliably determined from logs and the horizontal stress has been measured in LOT's and a minifrac after depletion. Although the stress data is limited, it can be used for estimating the virgin stress and the stress path during depletion which yields a new interpretation of the measured stress. The previous geomechanical model used higher minimum horizontal stress than measured which possibly yields an underestimation of seismic risk. Furthermore, it is known from other fields that during repressurization hysteresis in stress and stiffness may occur (Santarelli, 1994). Stiffness hysteresis can be determined from surface movement.

Obviously, for seismic risk evaluation, it is of utmost importance to calibrate the model on observed seismicity. The micro-seismic data has been re-analyzed by Q-con because previous work contained errors in the location of the micro-seismic events. Furthermore, using realistic location uncertainty, the micro-seismic events could be migrated to the faults, which is a necessary condition for relating them to the geomechanical model. The evolution of the seismicity with rising pressure and pressure differential has also been investigated (Q-con, 2016).

At the time of creating the new geomechanical model, three full storage cycles could be used for model calibration. For assessing potential risks it is preferable to match the available measurements with a simple constitutive model. This can then be used for predicting the seismic response. Of most interest for evaluating gas storage operations are time dependent effects. The outcome of elastic models is trivial, once they are calibrated on depletion. Any seismicity could only be caused by inelastic effects, so we will consider those in the model calibration and forecast. Of most interest in this respect are:

- Slippage based on Mohr-Coulomb failure
- Pressure diffusion, especially pressure differentials and the lag of aquifer pressure.
- Time and stress path dependent behaviour of reservoir rock and the fault zone as well as salt creep.

Preferably, the reservoir response would be explained by pressure diffusion and salt creep, since these are established, well understood mechanisms for time dependence. However, it will be shown that other inelastic effects are required. That introduces non-uniqueness, since many inelastic phenomena may occur in rock deformation. We will use the simplest possible mechanisms that can explain the observations with the least number of additional parameters. That approach is necessary to avoid introduction of too many new parameters that could never be properly calibrated.

The monitoring data are first discussed in Chapters 2 and 3. In Chapter 2 the subsidence data will be reviewed that were obtained from continuous GPS records and intermittent geodetic measurements. Chapter 3 introduces the micro-seismic monitoring data as described in detail by Q-con (2016).
Chapter 4 describes the geomechanical model set-up, the initialization and calibration procedure, the philosophy of seismic risk prediction for a TLS and the work flow for matching the observations with the model. In addition, it introduces the theory for fault slip required to match depletion seismicity. Chapter 5 presents the results of the calibration procedure. It shows the calibrated stress path and presents the match of subsidence during depletion and the match of the stiffer response and time delay during refill and storage. After describing the initial calibrated stress behaviour, the section analyses the elastic simulation of the depletion period and investigates the impact of salt creep on depletion. Chapter 6 starts with the description of fault slip model required to account for the cumulative moment by the depletion seismicity and the resulting shear stress changes. Fault slip is first simulated in a 2D cross-section, to investigate fault criticality during refill. Next, the fault slip is estimated for the 3D model, based on the depletion simulation. Different assumptions will be made for the application of fault slip, so that the model is matched to observations and the model sensitivity to different assumption can be assessed. Finally, this chapter presents the application of the calibrated model to the forecast of stress and seismicity during future storage cycles. Chapter 7 describes the subsidence behaviour for future storage cycles with a swing in the range 77-133bar and Chapter 8 concludes by discussing the results and presents the conclusions.

2 Surface Displacement Monitoring

Surface Displacement from Geodetic Surveys

There are several nearby fields next to the Bergermeer reservoir which contributed to the subsidence during depletion, see Figure 4. The normalized subsidence, shown in Figure 5 is rather linear with time.
The combined effect has been modelled by TAQA (2017), which yielded a good fit to observed data with very reasonable values for the reservoir compaction coefficients. The contribution from Bergermeer was about 12 cm subsidence at the centre of the subsidence bowl.

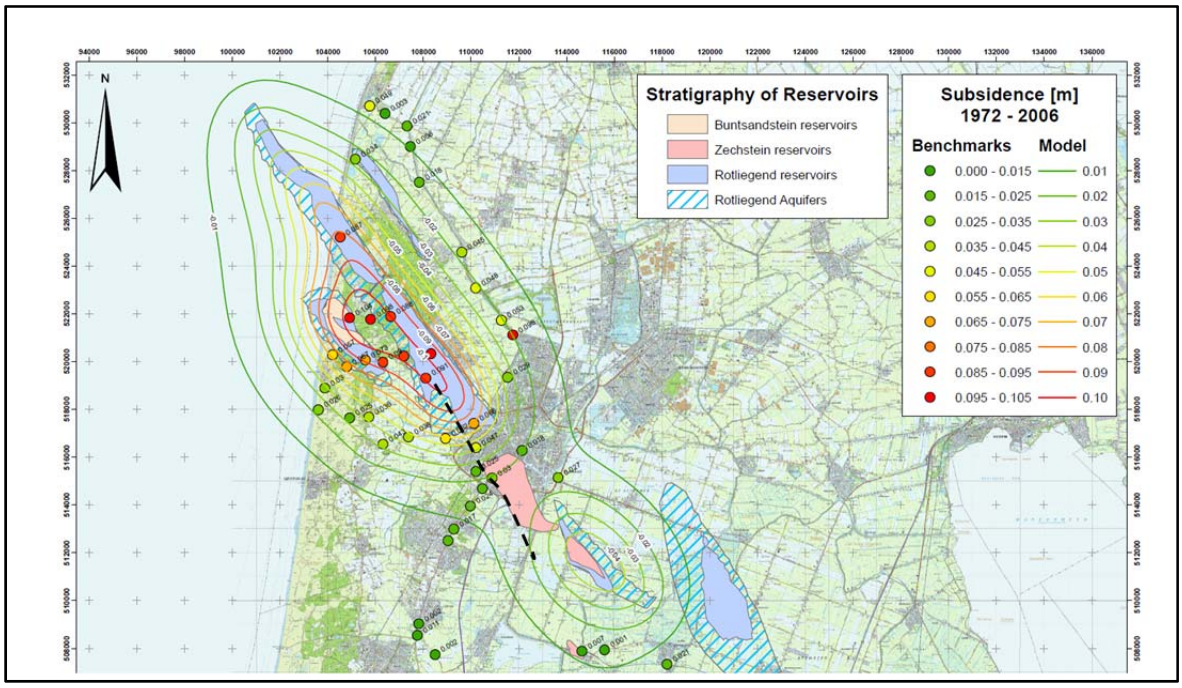

Figure 4: Gas fields near Bergermeer that contributed to total subsidence over the field.

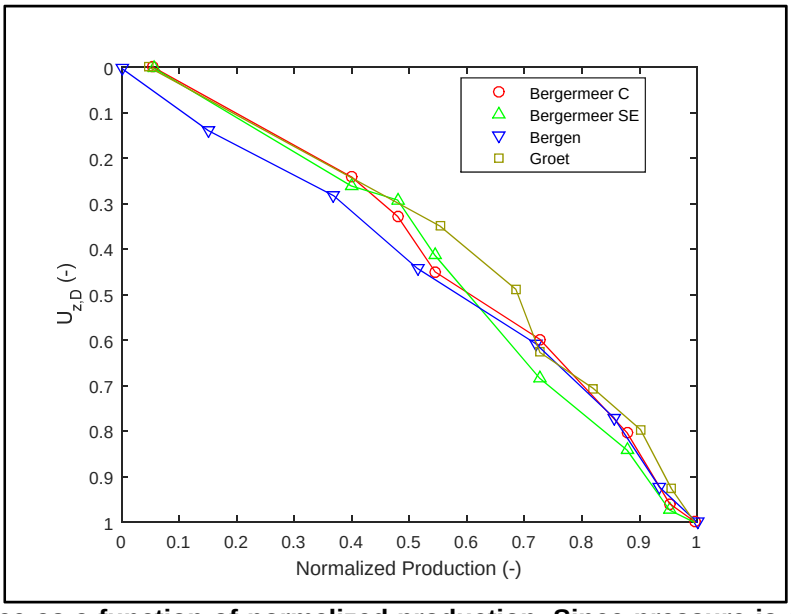

Figure 5: Subsidence as a function of normalized production. Since pressure is almost proportional to production this shows that initially the subsidence is almost linearly dependent on pressure, hence no subsidence delay is seen.

GPS subsidence data

The surface heave in the Bergermeer is measured by 4 GPS stations, TAQA2 -TAQA5, shown in Figure 6 on a map of the Bergermeer field. A 5th station (TAQA-6) serves as reference background signal and is subtracted from the observed surface displacement. A detailed analysis of the GPS subsidence is given in Appendix I.

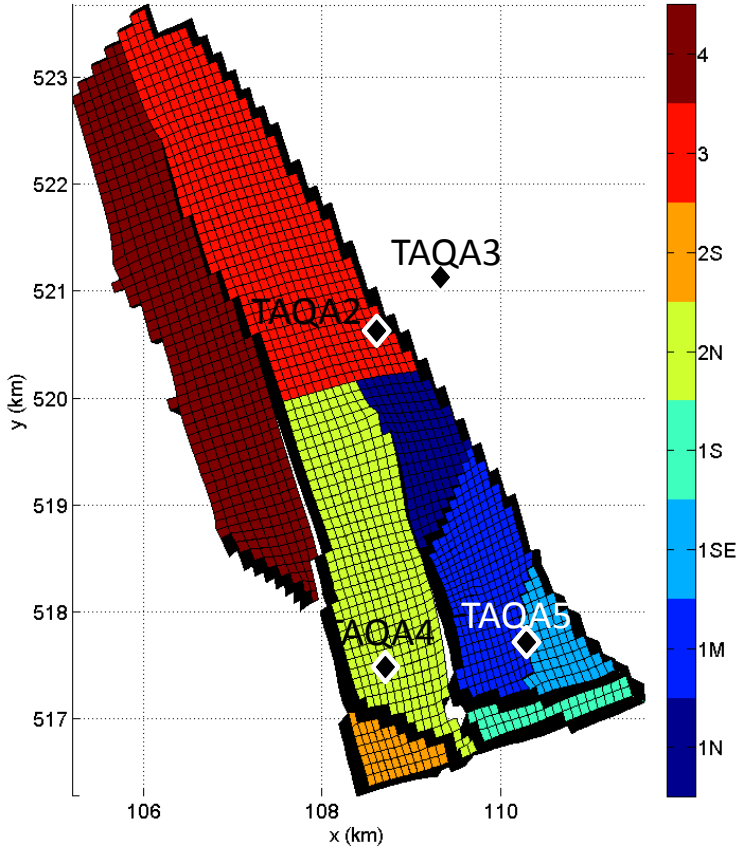

Figure 6: Reservoir domains and the location of the 4 GPS stations

Figure 7 shows the surface heave data versus the average gas pressure from the Eclipse reservoir model. The data shown is obtained after high frequency noise filtering and after subtracting the periodic signals present in the data (Marel, 2015). The noise filtering revealed a periodic signal of about 0.4 year of unknown origin. No clear correlation was found with environmental parameters such as annual temperature evolution, precipitation, air pressure and the 175 days period related to the position of the GPS satellites.
The filtered data shows:

- A clear correlation with the reservoir pressure.
- Much stiffer response in surface movement than during depletion.
- A delayed response with respect to pressure changes especially for TAQA-2 and TAQA-3, which are located far from the main wells. The strongest heave in TAQA2 followed by TAQA4 and TAQA5 that are near each other. Station TAQA3 shows the smallest increment in displacement per bar pressure increment.

The data of each station shows a clear time delay with respect to change in the average pressure. This indicates a viscoelastic response rather than an elastic response. The viscoelastic response is approximated with the Kelvin-Voigt (KV) model. The KV model can be described with a damper-spring system in parallel, where the response of the spring is delayed by a damper (see Figure 8). Over time, the influence of the damper diminishes and the response of the spring remains.

Figure 7 shows a fit of the KV model to the data. The Kelvin-Voigt part of the data fit is for all stations in good agreement. These will be used for the comparison to the response of the geomechanical model.

Conclusion

The GPS data support the following conclusions:

- Surface heave is smaller than predicted by an elastic response calibrated to depletion subsidence.
- The surface displacement lags the change in average reservoir pressure by a few months. This indicates time dependent behaviour of the reservoir.
- Geodetic measurements agree with the trends seen in the GPS data.
- The filtered GPS data can be fitted satisfactorily with a viscoelastic Kelvin-Voigt model.

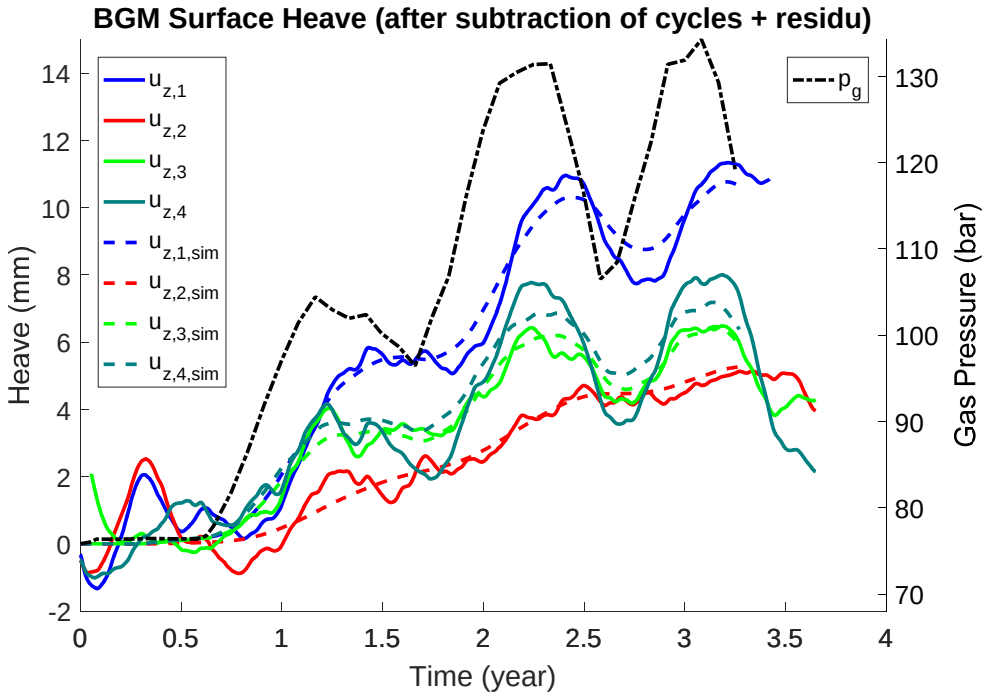

Figure 7: (Left axis) Filtered surface heave data from GPS stations (solid lines) and the Kelvin-Voigt model (dashed lines). (Right axis) gas pressure.

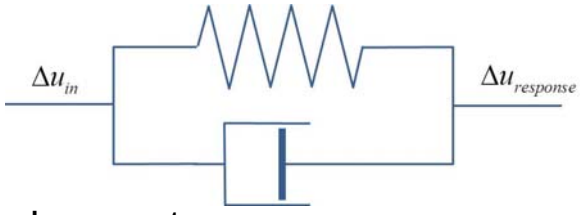

Figure 8: Kelvin-Voigt spring damper system.

3 Micro-seismic Observations

Review of data and the re-analysis by Q-con

Figure 9 is a plot of micro-seismic activity on a fault map of the field. The Midfield fault ends in the reservoir and is connected to small oblique faults BGM11 and Block1A-1B (designated Midfield fault system). The long East bounding fault is connected to the small Block1-2 fault and the West fault is visible in the lower left corner; the two bounding faults at the southern are visible at the bottom.
Q-con performed a thorough quality check and subsequent re-analysis of the micro-seismic event locations, since previous work used incorrect acquisition parameters (Q-con, 2016). Although some significant changes in the event locations were observed, the overall picture remained the same: most activity, especially stronger events occurred on the Midfield fault system. All micro-seismic events could be migrated to the faults by intersecting the uncertainty ellipsoid with the fault plane. A complication was that for some events there were two possible solutions for the location (on both sides of the monitoring array); in most cases the location could be resolved but uncertainty remained for a few events.

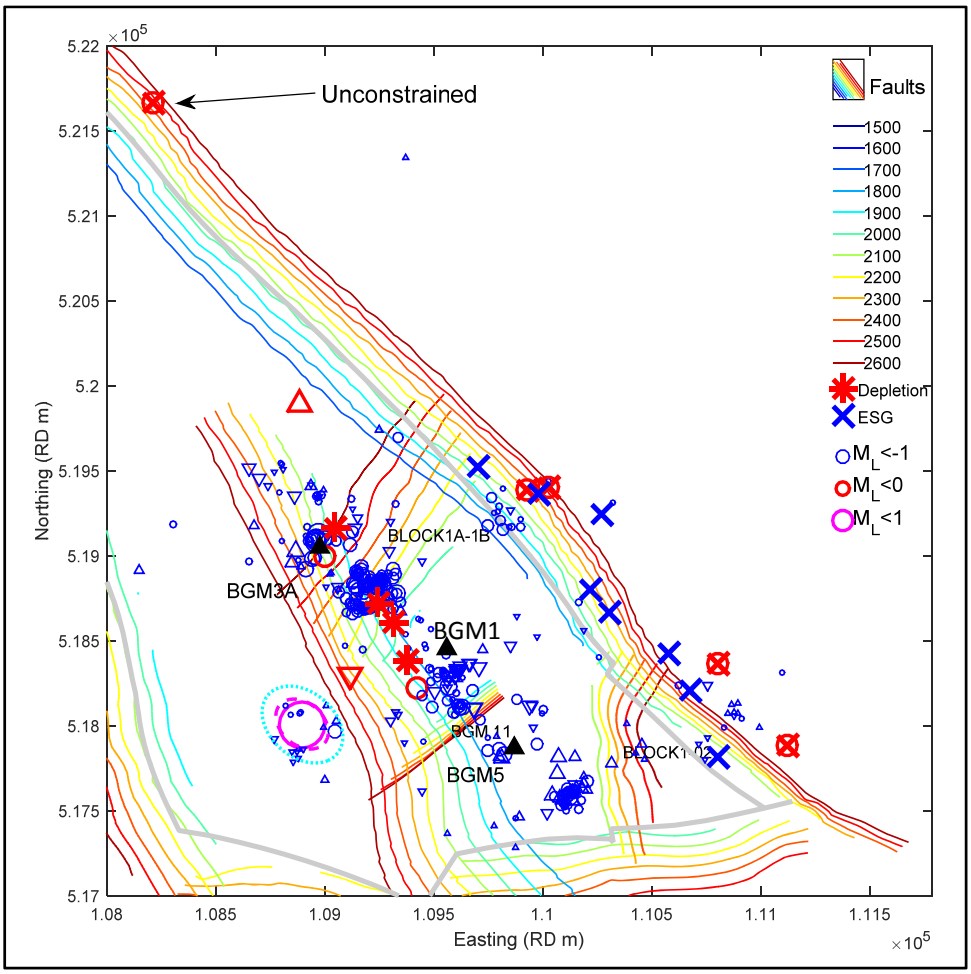

Figure 9: Relocated events in the horizontal plane, before migrating to the faults. Also, the assumed location of the four depletion induced earthquakes is shown. Black triangles indicate the observation wells. Events have been colour coded to show the magnitude. Different symbols indicate whether the symmetric solutions could be resolved (Yes: up triangles, No: down triangles, Resolved since one solution is near fault: circles). The event that was located far to the north (see Figure 10), turned out to be coming from outside the reservoir. The size of the symbols indicates event magnitude.

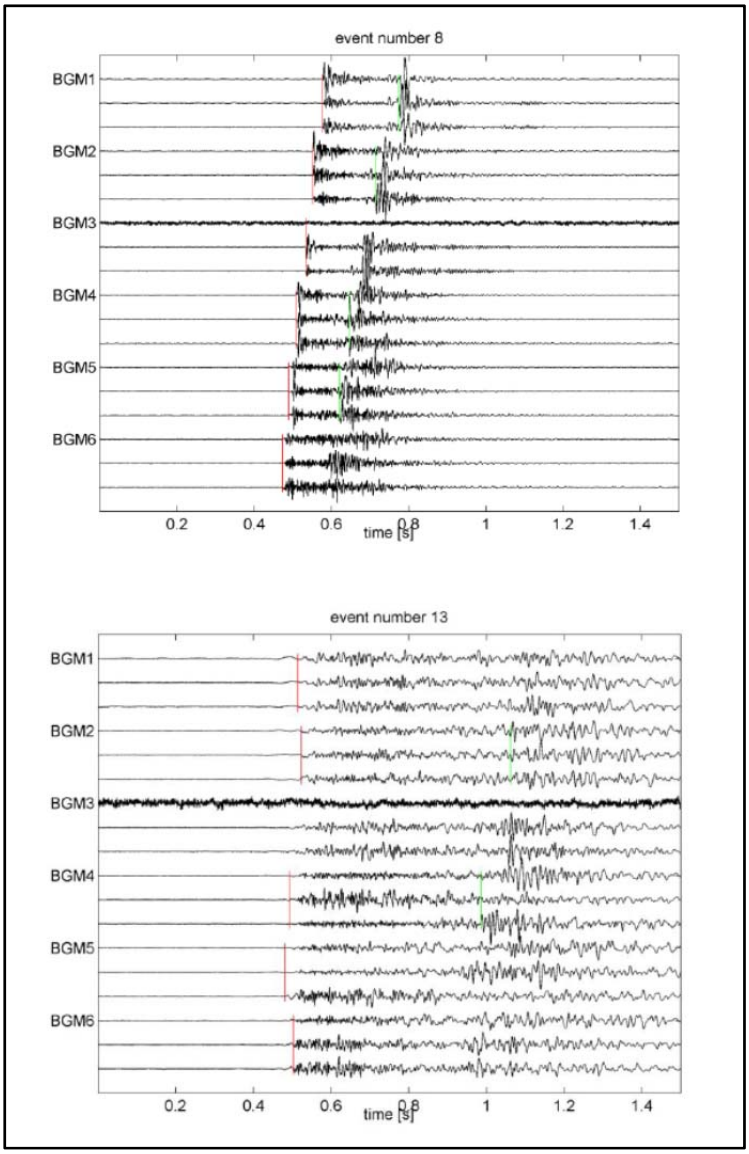

Figure 10: (Top) Unfiltered seismogram section of a reservoir event occurring on 24-Jan-2016 18:10:17. P- (red) and S-phase (green) onsets are indicated. (Bottom) Unfiltered seismogram section of an event occurring on 17-Oct-2016 20:57:53. P-phase onsets are indicated in red. Onsets of a secondary phase with different polarization are indicated in green. Note the lower signal frequencies and the longer seismogram duration compared to the reservoir event shown in the top panel.

The uncertainty ellipsoid and the resulting intersection of the ellipsoid with the fault plane for the strongest event are shown in Figure 11. There is considerable uncertainty for this strongest event (magnitude 0.9), especially in the vertical direction. The recent events that were recorded by the ESG system (in well BGM-01) are also plotted. The latest event that was recorded appeared to originate from the East fault, but far to the north from the reservoir (TAQA, 2017).

Careful analysis of the seismograms by Q-con showed that this event (Figure 10) has a different signature compared with all other events, so it is deemed not a reservoir event. It turns out that the location and magnitude is unconstrained, because the S-wave data were inconsistent with the P-wave. It is therefore left out of the calibration of the model; most likely it came from one of the nearby fields to the north of Bergermeer.

It is remarkable that all seismic activity is induced by the Midfield and Eastern faults, while the Western fault is quiet. One explanation might be that weak activity is not recorded since the Western fault is much farther from the observation wells. However, if we take the longest distance from the observation well to events on the East fault, it is possible to detect events on the West fault that are closest to the observation well. It is therefore concluded that the West fault is non-seismic.

The depletion induced earthquakes in 1994 and 2001 were recorded with the regional geophones. Although their relative location could be determined accurately, the absolute location is uncertain (KNMI, 1994; KNMI, 2001; Dahm, 2010). However, it was deemed reasonable that they should have occurred near the juxtaposition point on the midfield fault. The strongest seismicity during cushion gas injection occurred also along this section of the fault.

Relation with Faults

Most events could be migrated to the main faults, which is important for establishing the link between seismicity and geomechanical simulations, since the stress analysis in the geomechanical model is focused on the faults. Since it is reasonable to consider the Midfield fault and BGM-11 and Block1A-1B faults in combination it does not matter very much for the analysis to which of these three faults the location was assigned. Moreover, from the micro-seismic analysis (Q-con, 2016) it appears that events coming from these faults are strongly linked with one event triggering another on the crossing fault.

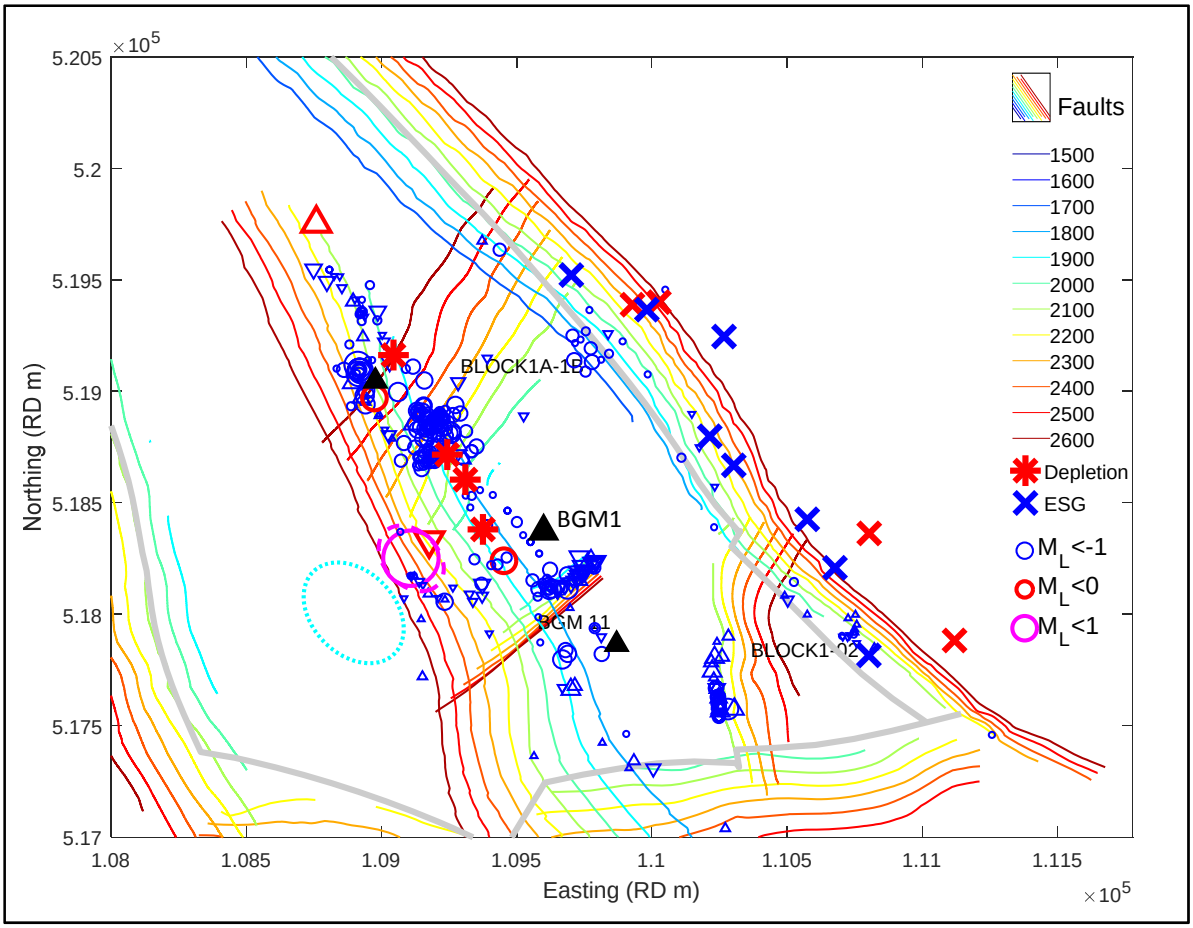

Figure 11: Relocated events after migration to the faults. Mirror events that could not be resolved are indicated with up or down pointing triangles. Also, the assumed location of the depletion induced earthquakes is shown. The dashed magenta ellipse indicates the intersection of the uncertainty ellipsoid of the strongest event during cushion gas injection with a plane parallel to the fault plane through the original location.

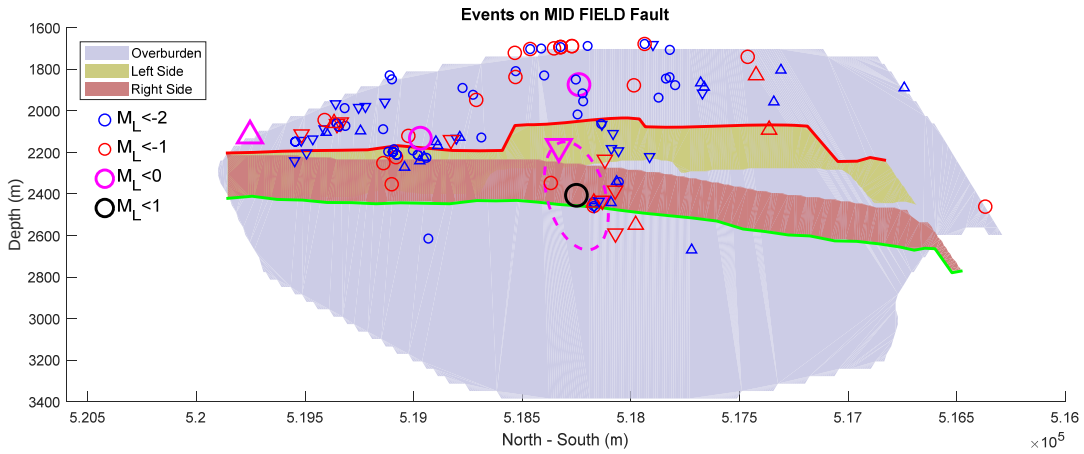

Figure 12: Projection of the Midfield fault on the North-South vertical plane with migrated seismic events. Mirror events that could not be resolved are indicated with up or down pointing triangles. The strongest events occurred on the Northern part of the fault where the reservoir blocks are juxtaposed. The dashed magenta ellipse indicates the intersection of the uncertainty ellipsoid of the strongest event during cushion gas injection with a plane parallel to the fault plane through the original location.

Figure 12 shows the event locations on the midfield fault. Activity occurs along the entire fault but the strongest event was near the most critical point where the fault separates the reservoir blocks (the juxtaposition point or so called “scissor point”).
An important conclusion made by Q-con in the seismic data analysis was the clustering of the events. It turned out that some events showed a very similar waveform indicating close spatial proximity of the events. There was a large cluster of 38 events during the refill phase , but most of them were rather small and occurred within a time interval of hours. After that, activity appeared at a different location far from the previous cluster. This is characteristic for a fault with a few critical patches that may slip but there are no nearby patches that may be triggered which might lead to a large avalanche of slipping patches and a large slip area. As a result, such behaviour will only yield small micro-seismic events.
On the opposite Eastern fault, see Figure 13, there was also activity, but much weaker in magnitude. Also, some events occurred on the Block1A-1B fault and BGM-11 fault. A few events were observed on the other faults. When the reservoir expands some of the stress is transferred to the faults and apparently this is inducing slippage on the faults.

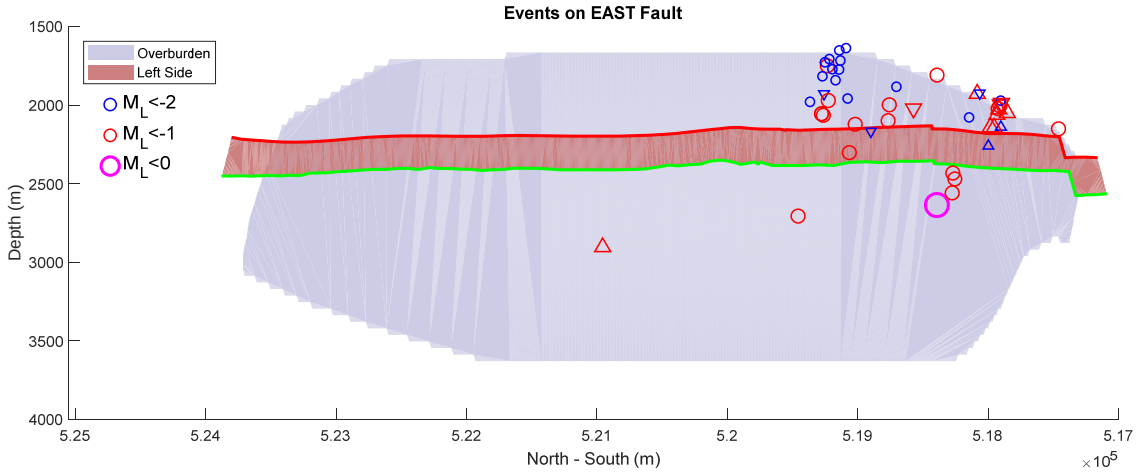

Figure 13: Projection of the East fault on the North-South vertical plane with migrated seismic events. Note that the scale of the axes differs from figure 15, the East fault is approximately two times longer than the Midfield fault.

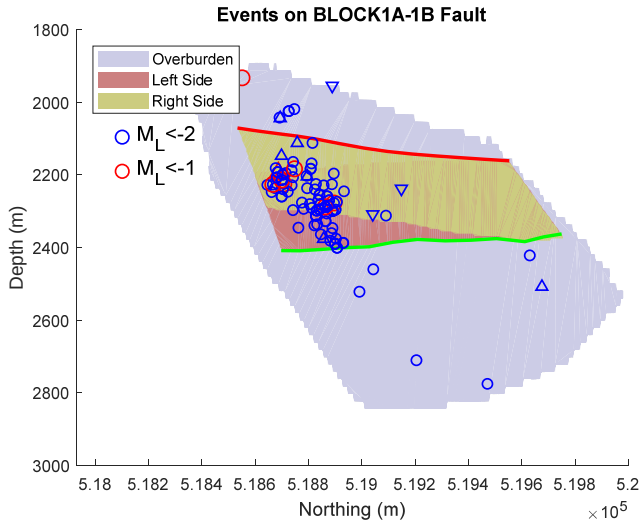

Figure 14: Projection of the Block1A-1B fault on the East-West vertical plane with migrated seismic events.

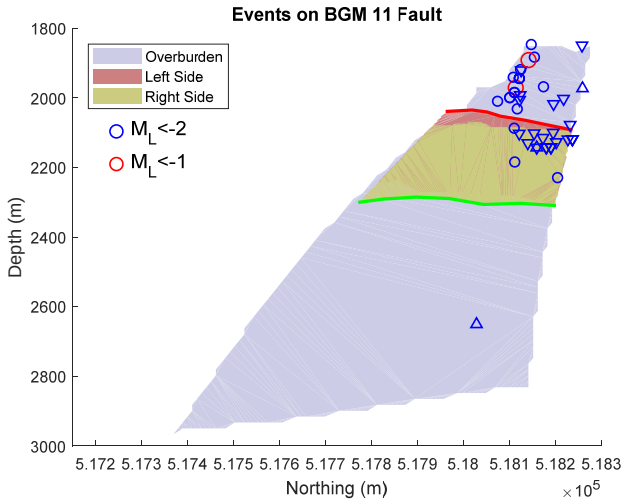

Figure 15: Projection of the BGM11 fault on the East-West vertical plane with migrated seismic events.

Although micro-seismicity is ubiquitous on the fault surfaces, larger events are close to the reservoir, considering the uncertainty in the depth location. The uncertainty ellipse for the strongest event is indicated in Figure 12 and in general the uncertainty is about 400 m. The recent relocation of events by Q-con of the ESG data which occurred on the East fault resulted in a downshift by 300 m, giving also an idea of the uncertainty. Therefore, the micro-seismicity appears to be related to the stress concentration near the reservoir.

So, it is prudent to regard the micro-seismicity as related to the stress development in the reservoir. It will be attempted to explain the seismic activity in terms of the stress evolution of the reservoir and why micro-seismicity occurs while the reservoir pressure increases, which should reduce the stress on the faults.

Time Dependence of Micro-Seismic Activity

We will calibrate the geomechanical reservoir model so that the model can be used to make a forecast of seismicity. To do so, we first need a qualitative interpretation of the seismic data. The model does not predict seismic activity, but the criticality of the fault which could induce earthquakes. A qualitative interpretation of the data is valuable, since the seismic record indicates whether the fault system becomes more critical over time or stabilizes.

Figure 16 shows micro-seismic activity vs. time and the average pressure and pressure difference between the east and west compartments (top graph). The cumulative seismic moment by fault system and injection and production rate are plotted in the lower graph.

The plot of seismic moment (on a logarithmic scale) is quite useful since it will quickly level off with constant activity. If seismic activity becomes stronger such a plot will show a stair step pattern. Such a plot would flag a system that becomes gradually more critical.

In Bergermeer a few relatively strong earthquakes happened during depletion and micro-seismic activity was observed during cushion gas injection, mainly on the Midfield fault. This continued with the first storage cycle but around 100 bar average pressure, the activity on the Midfield fault system ceased and it has been quiet since.

On the East fault, more continuous activity has been observed, concentrated during start-up of injection. The evaluation of the interpretation of ESG by Q-con yielded mostly the same locations, but in a few cases Q-con gave a different interpretation. This yields a more consistent picture of the East fault seismicity showing reduced activity during the last storage cycle compared with previous cycles.

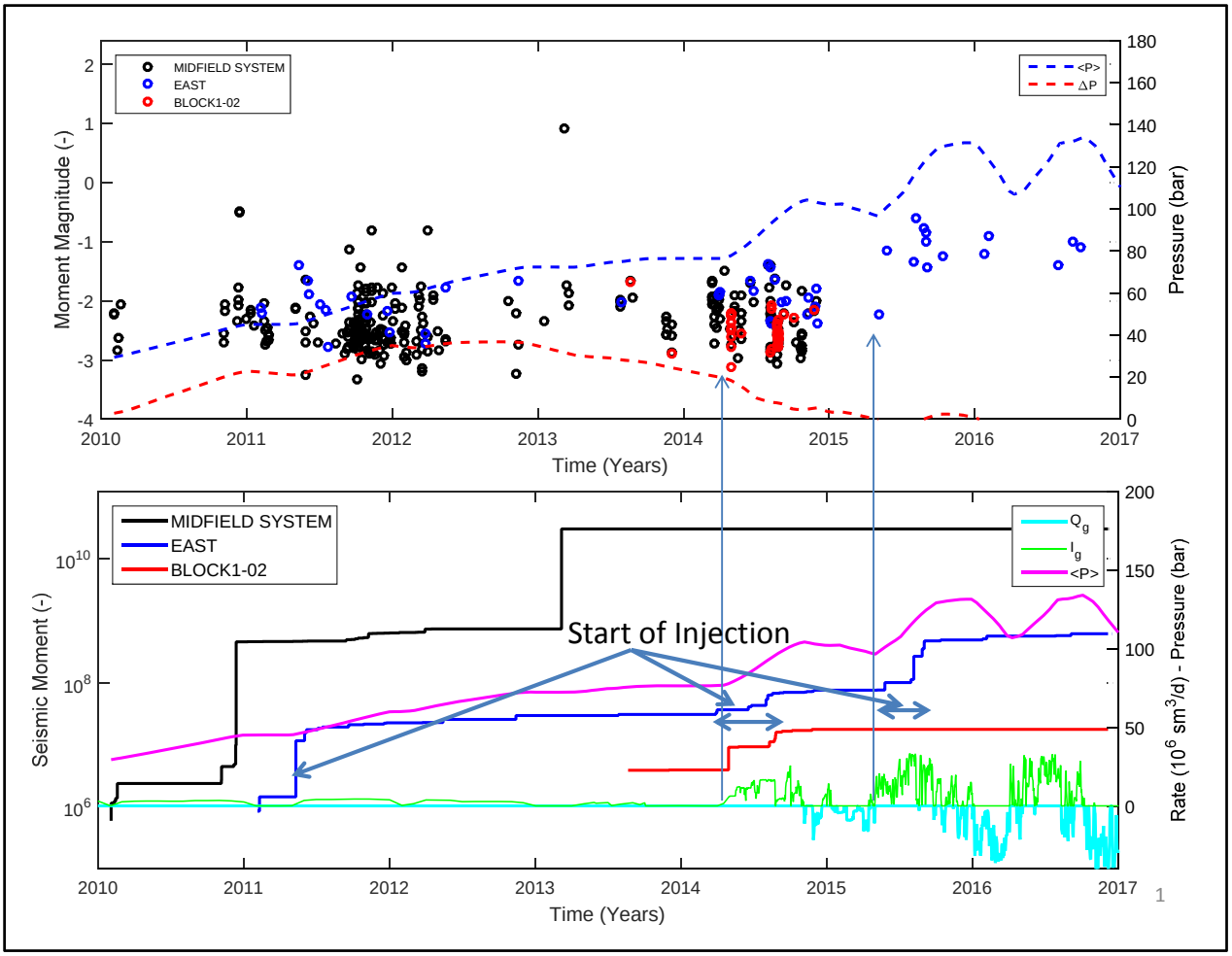

Figure 16: Seismic activity in Bergermeer and pressure vs time (upper). Cumulative seismic moment and injection and production rate is plotted in the lower graph.

Conclusion

The seismic data analysis supports the following conclusions that will be used for calibrating the model:

- The seismicity during refill occurs on the midfield fault at a location which was already seismically active during production.
- Most seismic activity since 2007 occurred during cushion gas injection. The activity was much weaker during the fast pressure increases during storage cycles and the activity on the Midfield fault has completely vanished. This shows that the fault systems are stabilizing.
- The seismicity on the east fault is transient in nature and starts quickly after start of injection.
- Observed seismic activity is strongly clustered in space and time. Stress criticality on faults as evidenced by seismic monitoring data has a transient signature. Fault patches that were seismically active during refill become silent after a certain amount of time. This shows that there are no large areas of the fault that become critical, so only weak earthquakes can be induced.
    - On the midfield fault, where most seismicity occurs, and on the Eastern fault a North-South migration of the seismicity was observed with time.

4 Geomechanical Modelling

Introduction

The geomechanical models developed by TNO (2008, 2011) have been supported by a subsidence model by Panterra (2010) and recently a 3D model was built by Baker-GMI (2013) based on the previous work by TNO. The focus in these studies was on subsidence and seismicity.
TAQA (2017) modelled the subsidence due to Bergermeer and neighbouring fields to match the observed subsidence bowl including recent geodetic measurements. In this way, the contribution from Bergermeer could be discerned and the compaction coefficient could be determined. TNO also modelled subsidence which was an important anchor point for the geomechanical models developed by TNO (TNO, 2008; 2009; 2011). The subsidence caused by Bergermeer was about 12 cm which is quite moderate, but can be measured accurately so that it is useful for calibration of reservoir stiffness.
Both 2D and 3D models were used to interpret the seismic events (1994, 2001) that were induced during depletion. Many studies were conducted to investigate the effect of salt viscoelasticity, cooling due to cold gas injection and load cycles during gas storage. In the TNO models, the faults were modelled including slip if the critical stress was exceeded. The models indicated large slip occurring on the midfield fault during depletion, in agreement with the observed earthquakes. In some models, small slippages also occurred during re-injection but overall the models showed an elastic unloading response with stabilization of the fault during re-pressurization. The GMI model yielded a fully elastic response, as expected, with no instability of the faults during re-pressurization. In that model, some hysteresis was seen due to a different pressure during injection compared with depletion, but this effect was caused by aquifer pressure diffusion and is not related to inelasticity of the formation.
Cooling of the reservoir happened due to the cold gas injection, but the stress changes were rather small and only of significance near the injectors. The thermal stress front propagated slowly through the reservoir and when it reached the fault it gave only a small change in the stability of the fault. It was concluded that cooling of the reservoir would not give a significant contribution to seismic risk. This is important, since the cold front travels slower than the pressure and stress change, so cooling could explain time dependence of seismicity.
The GMI model was also used to quantify the cooling effect of cold water injection. Since the mass of water injection is very small (at 80,000 m^3 maximum or 80,000 ton) compared with gas injection of some 3 million ton, the cooling effect of the water will be much smaller despite its heat capacity being twice as high. Therefore, it comes as no surprise that the thermal stress on the midfield fault caused by water injection was found to be insignificant (see also Appendix IV).

Geomechanical Model Geometry

Appendix V describes the Geomechanical model construction in detail. The Geomechanical model is based on a new geological interpretation (Petrel model) provided by TAQA. In the new interpretation blocks 1N, 1M and 1SE (see Figure 6) are separate blocks separated by Faults, whereas in the old model it was one domain gradually varying in height. This gives a smaller offset for block 1N whereas the offset for block 1M that has fairly constant height is dominated by the gradual change in height of block 2N.
The geomechanical model is constructed by creating Fault blocks from the Fault surfaces and intersecting those with horizons. Figure 17 shows the horizons used in the model in a cross-section through the scissor point of the Midfield fault.
The primary objective of the model is the computation of the fault stresses, which determines the extent of the horizons. The extent of the entire model is determined by the surface movement. This results in an inner domain that is roughly similar in size as the Baker model. Figure 18 shows the Fault structure in between the under burden and top Zechstein. The Faults directly connected to the reservoir end at these two horizons. For computational simplicity Faults were extended to the boundaries of the inner domain, even if there is no offset. This does not affect the stress computation. Compared to the Baker model the offset at the faults west of the west fault are explicitly taken into account. It also shows the additional faults between block 1N and 1M and 1M and 1SE. Figure 19 shows the entire inner block.
The current model also takes the Faults above the midfield fault and the corresponding offset in the overburden into account. These overburden faults were included to investigate potential seismicity in the

overburden due to compaction and expansion of the reservoir. It turns out that this is not happening, but we kept these faults in the model for completeness.
Since the subsidence bowl gets very large it is necessary to extend the model. This can be done simply by embedding the inner block in a layer cake, as shown in Figure 20. Subsidence is hardly influenced by detailed underground structure, although lamination (and contrasts in modulus) has some impact on subsidence. The Baker model showed significant boundary effects in the subsidence bowl, but this is considerably reduced in the extended model used here.

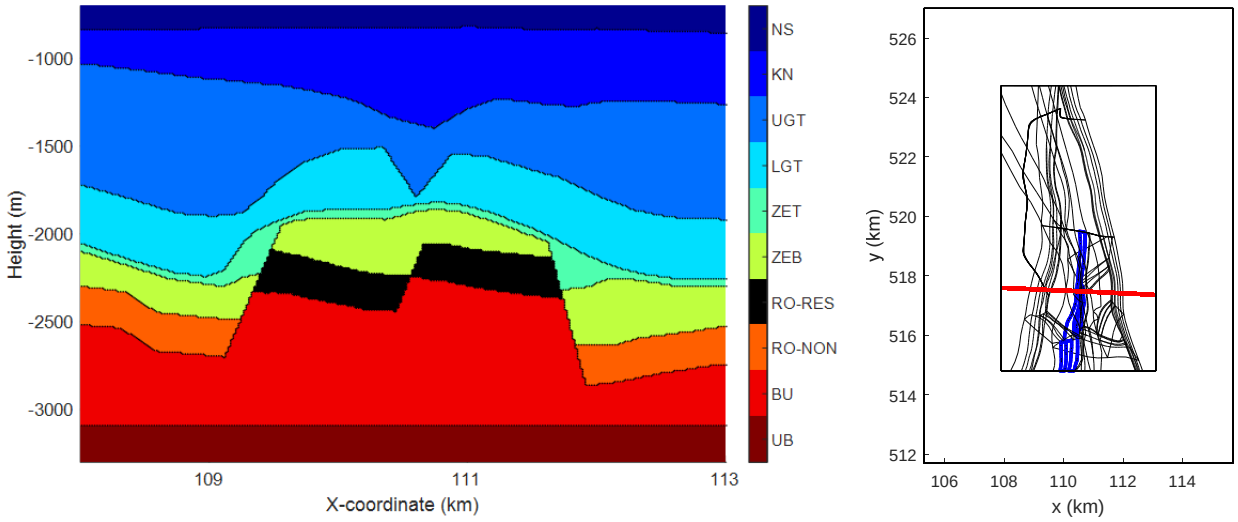

Figure 17: (left) Cross section perpendicular to the Midfield fault near the scissor point, with indication of geological formations. North Sea (NS), top Vlieland Claystone (KN), top Upper Germanic Trias (UGT), top Lower Germanic Trias (LGT), top Zechstein Salt (ZET), Top platen Dolomite and Anhydrite (ZEB), Top Rotliegend (RO), Top Carboniferous (BU) and the under burden (UB). (right) location of the cross section: Horizontal plane through Bergermeer reservoir with cross section through the midfield fault.

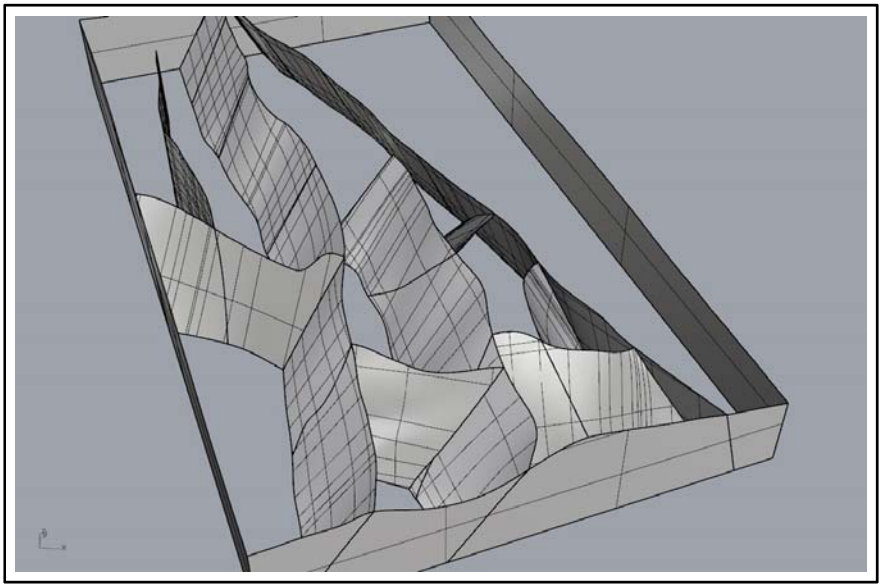

Figure 18: Reservoir fault geometry below top Zechstein, which surface acted as top of the reservoir level faults. Some faults ended in the block that defined the model, so that it was necessary to add auxiliary surface to close the faults tips into solids. This is an aid for gridding, but has no impact on the stresses since there is no offset of the horizons on these auxiliary surfaces.

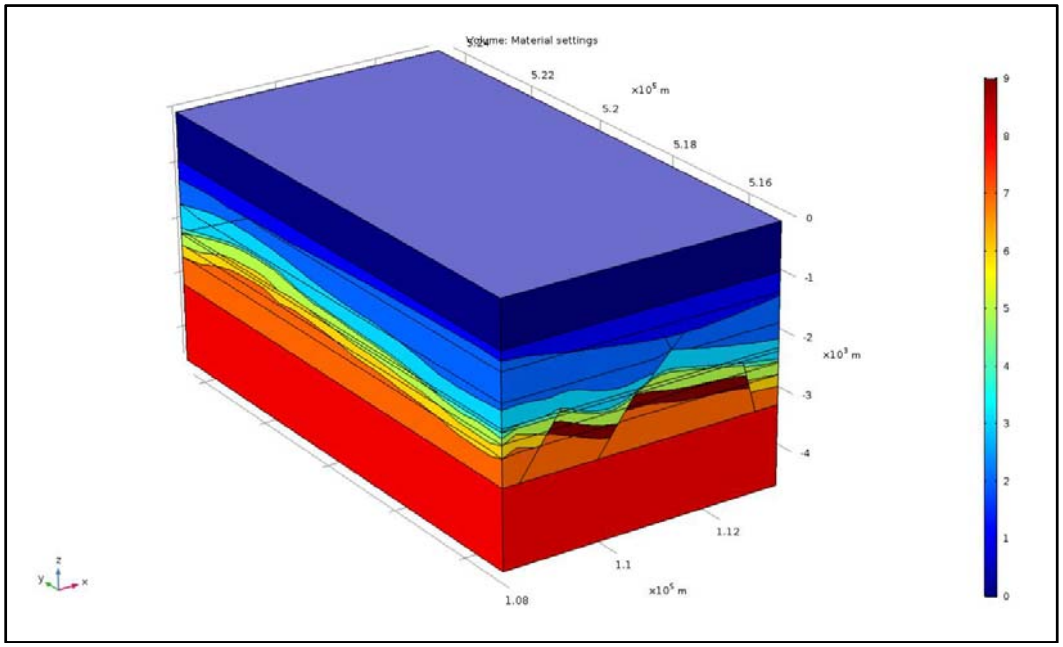

Figure 19: Inner box with domains that were obtained by cutting all fault blocks with the horizons defined for each fault block.

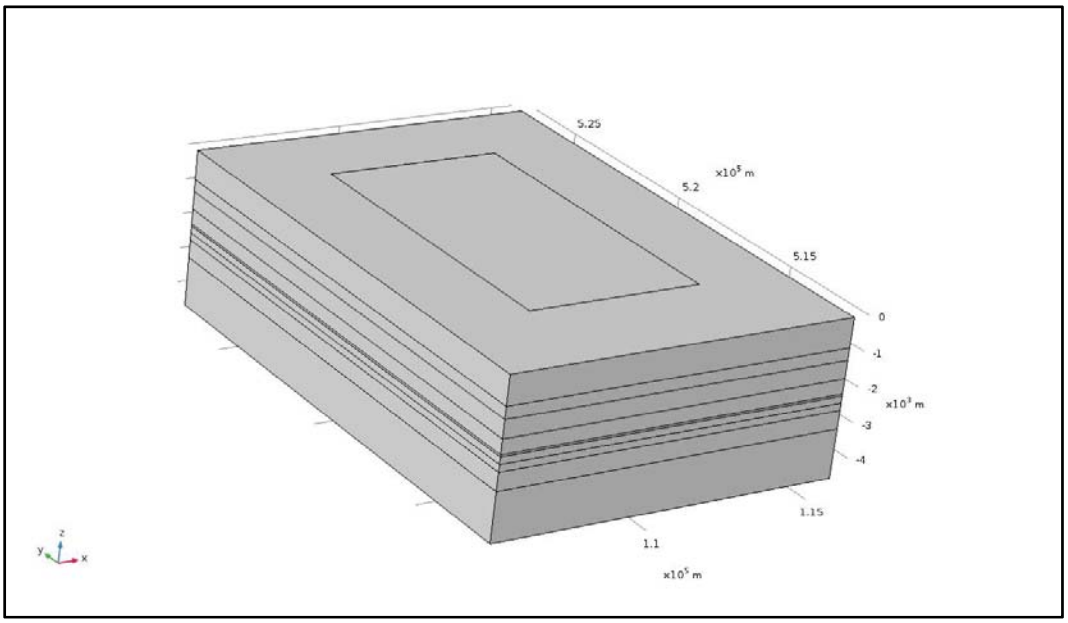

Figure 20: **The model was enlarged with an outer box with layer cake geometry.**

Model Input Parameters

The geomechanical properties were based on data from the previous models. Most properties agree with the TNO model. The biggest difference with the Baker model is in the modulus of the non-reservoir rock that is in contact with the reservoir. In the Baker model, the reservoir modulus was decreased to match the subsidence and the same factor was applied to the non-reservoir rock. This gave very low values for the Zechstein carbonates and anhydrite. Since differential compaction is a function of the contrast in rock stiffness, it is important to assign the right stiffness to the non-reservoir rock, so we kept the high values for the modulus of the Zechstein rocks.

Table 1: Geomechanical Properties for populating the model

Formation		density	Youngs	PR	Biot	grad-P	grad-Smin	grad-Smax	grad-Sv	Smin/Sv	Smax/Sv
		kg/m3	Gpa	(-)	(-)	(kPa/m)	(kPa/m)	(kPa/m)	(kPa/m)	(-)	(-)
North Sea	NS	2200	1	0.25	0.7	10	14.9	19.5	22	0.69	0.90
Vlieland Claystone	KN	2300	10	0.25	0.7	10	15.0	19.7	22	0.69	0.90
Upper Germanic Triassic	UGT	2300	10	0.25	0.7	10	15.2	19.9	22	0.69	0.90
Lower Germanic Triassic	LGT	2400	20	0.25	0.7	10	15.3	20.1	22	0.69	0.90
Zechstein Salt	ZET	2160	35	0.3	0.7	10	22.3	22.3	22	1.00	1.00
Zechstein Platten-Dolomite and Anhydrite	ZEB	2600	43	0.25	0.7	10	20.2	20.2	22	0.90	0.90
Rotliegend	RO	2500	18	0.175	1	10	15.5	20.4	23	0.68	0.90
Carboniferous	BU	2600	30	0.2	0.7	10	15.8	20.7	23	0.69	0.90
Underburden	UB	2600	30	0.2	0.7	10	16.0	21.2	24	0.68	0.90

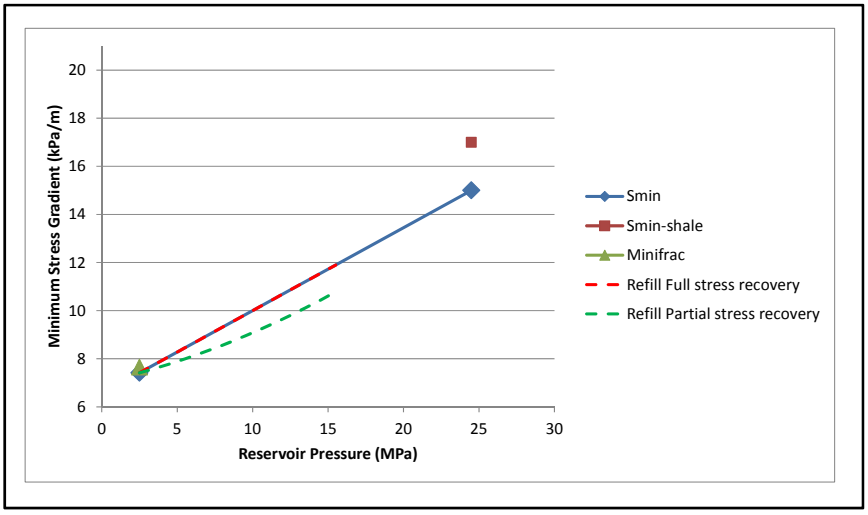

Figure 21: Minimum stress gradient versus reservoir pressure inferred from LOT's and an injection test. Stress recovery is shown for two scenarios: linear stress path with full stress recovery (red dashed) and stress path with partial stress recover (green dashed).

Stress Data

The vertical stress is well constrained by density logs and reservoir pressure. The stress regime is normal with horizontal stresses less than vertical stress. Therefore, vertical and minimum horizontal stresses determine the shear stress and normal stress on the faults for potential fault slippage.

There are only two anchor points for the minimum horizontal stress: LOT's in the overburden and a minifrac in the depleted state. Figure 21 shows these measured data points together with the interpreted stress path. It is known from fracturing experience that reservoir stress is generally lower than shale stress, so the minimum stress is assumed lower than the LOT stress. Also, the minifrac was disregarded in the Baker geomechanical model, but the data seem to represent a clear fracture response, so in the new model, this data point is representative for the depleted reservoir stress.

The stress recovery during refill and storage cycles is unknown and will be used as calibration parameter and calibrated against the observed micro-seismicity and surface displacement. Figure 21 gives an example for full and partial stress recovery.

Eclipse Simulated Reservoir Pressure

The reservoir model was history matched by SGS until 2017. A reference forecast was made with a swing between 77 bar and 133 bar gas pressure. TAQA provided the Eclipse model output which is used in the geomechanical simulation as input for the stress analysis. So, there is no flow simulation in the geomechanical model, but the pressure distribution at selected time steps is applied as external stress on the reservoir domains.

Pressure Adjustment in cells adjacent to fault

Pressures within a block in the Eclipse simulation are very uniform because of high reservoir permeability. The average block or bulk volume average pressure (defined as $p_{BV} = \Sigma_i V_i p_{i,dc} / \Sigma_i V_i$ with $p_{i,dc}$ the cell depth corrected pressure and V_i the cell volume), which is the Geomechanical relevant pressure, follows the gas pressure almost instantaneously (Figure 22). The hysteresis of the block average reservoir pressure versus the gas pressure is simply the result of a different pressure evolution of the various blocks weighted with different water and gas volumes.

However, to match the water table in the wells, the water relative permeability in the cells adjacent to the midfield Fault was reduced by a factor 10000. This gives pressures in those cells that strongly lag the corresponding block pressure, especially during the fast storage and forecast cycles (Figure 23). Figure 24 shows pressures in the cell adjacent to the fault that are much higher than the nearly uniform block pressures at both sides they belong to. Moreover, it gives a pressure difference of up to 80 bars in the cells adjacent to the fault cells, while the pressure drop in the corresponding block (excluding the fault zone) does not exceed 5bar east of the midfield fault and 27bar west of the Fault over time (Figure 25).

Using such a delayed pressure as fault pressure will result in unstable fault behaviour, because the high fault pressure coincides with low normal stresses. Although it is possible that the damaged zone around a fault may have a reduced permeability, it is highly unlikely that such a zone would extent over 200m in width. For a thinner Fault zone, pressure diffusion would act much quicker and give much smaller pressure differentials between the fault zone and the reservoir.

As such the pressures in the cells adjacent to the fault are considered to be an artefact of the history match method and are not considered to be representative for the actual pressure in those cells. To correct for this, the pressure in the cell adjacent to the fault get assigned the pressure of the nearest cell of the adjacent row in the same block corrected for the depth. This gives a much more gradual and realistic pressure distribution over a block (Figure 24). This adjustment gives a change in average block gas pressure smaller than 0.4bar and a change in average block pressure that remains smaller than 4bar (Figure 22, Figure 26), while the average pressure over the cells adjacent to the fault at each side of the fault follows the block pressure free of hysteresis (Figure 23).

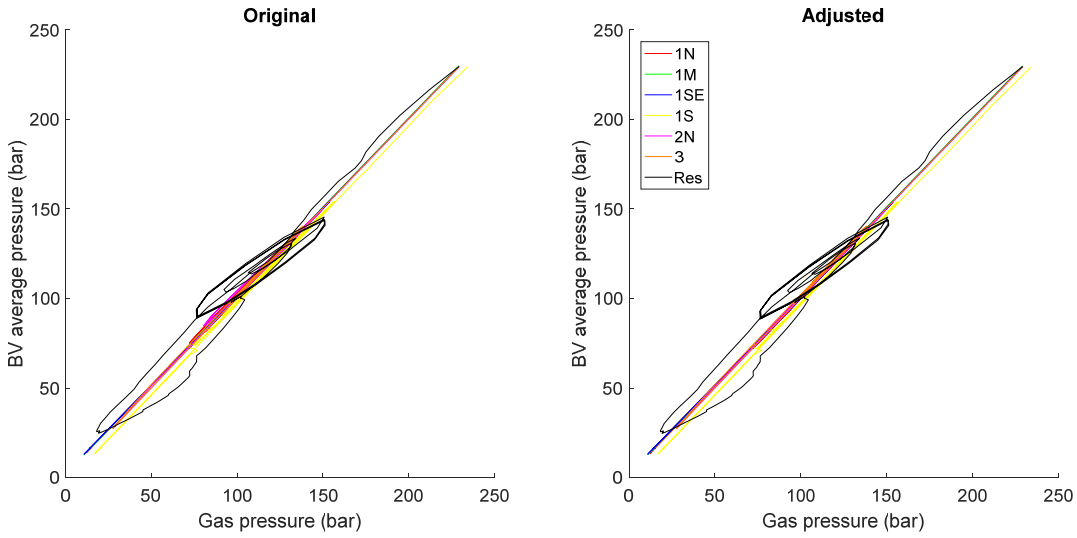

Figure 22: Gas vs Block or bulk volume (BV) average pressures (left) original eclipse pressure (right) adjusted Eclipse pressure. Blocks names refer to Figure 6, Res refers to reservoir average

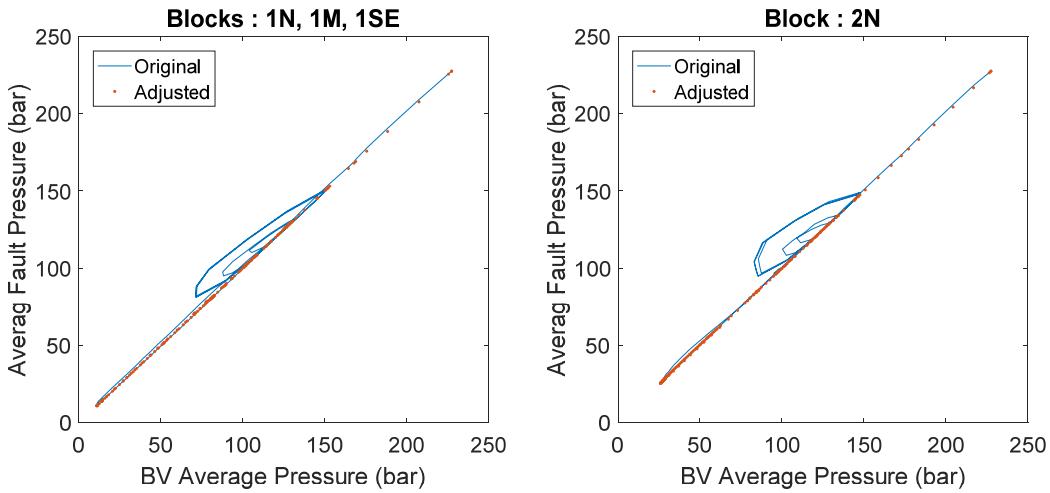

Figure 23: Average Pressure in the cells adjacent to Fault vs average block pressure (left) East of Fault (right) West of Fault

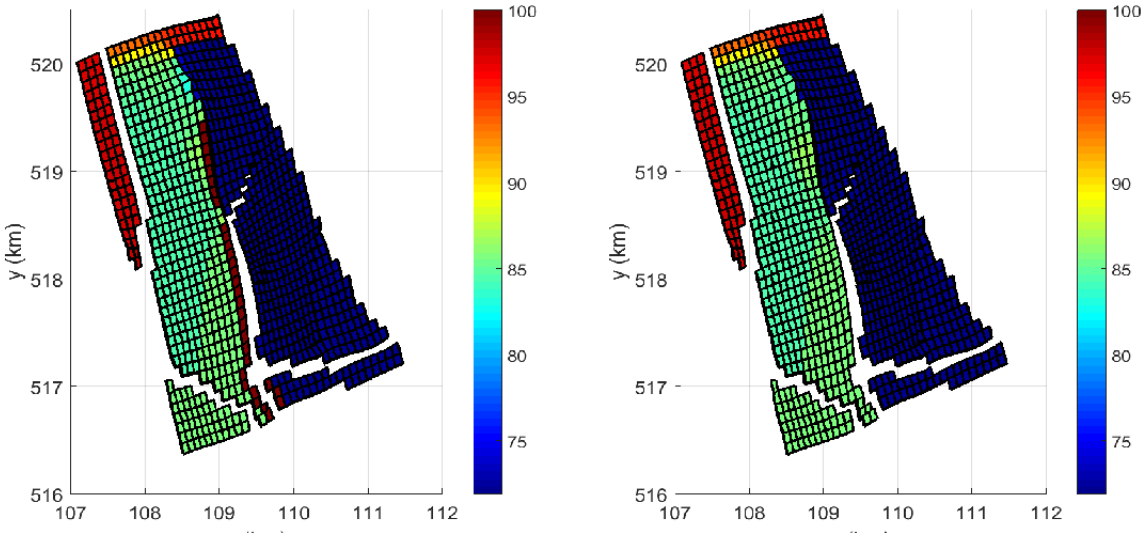

Figure 24: Top view of the reservoir pressure in March 2019. (left) original pressure (truncated at 100bar) show unrealistic high pressure in the cells adjacent to the fault. (right) Adjusted pressures show very gradual transition.

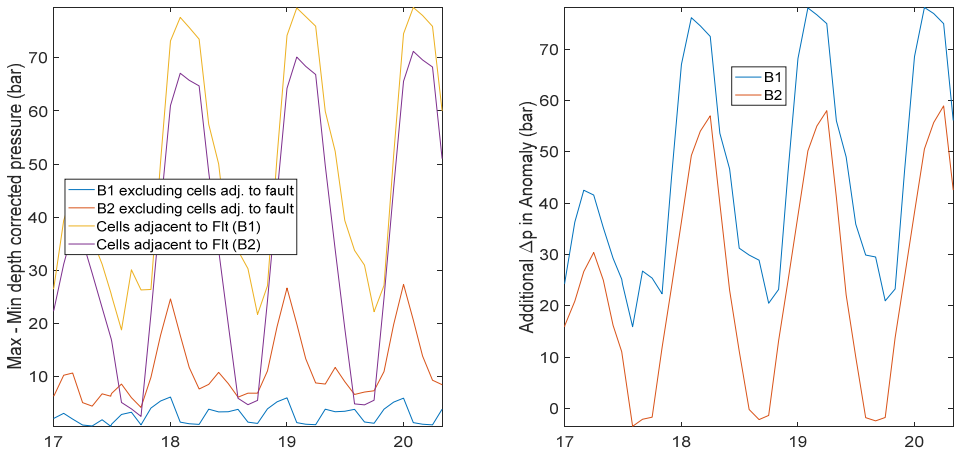

Figure 25: Maximum minus Minimum cell pressure for block (B1) east of the midfield fault excluding the cells adjacent to the fault, block (B2) west of the fault excluding the cells adjacent to the fault and the pressure differences over the cells adjacent to the fault.

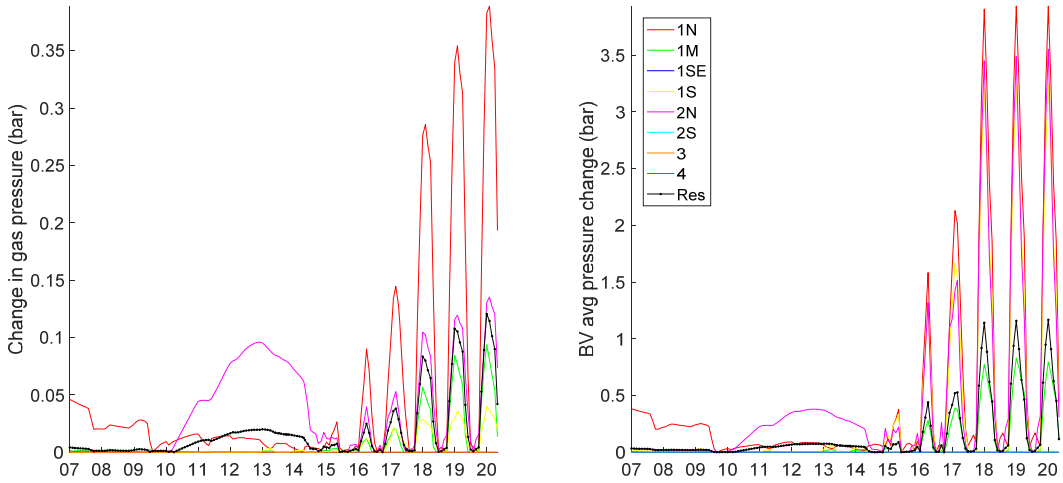

Figure 26: Effect of pressure adjustment on average block and reservoir pressure. (Left) change in average gas pressure and (Right) change in bulk volume average pressure. Block numbers refer to the domains shown in Figure 6.

Aquifer Response

The aquifer connected to the Bergermeer gas field is limited in extent and it has a high permeability so that it will follow the gas pressure. Figure 27 shows the water saturation and the pressure change in the Eclipse model that was used for the pressure input in the geomechanical model, between early 2015 and August 2016. The pressure change is almost uniform in the gas bearing Main block and Western block but also in the connected water bearing blocks in the south and west we see almost uniform pressure. For subsidence, any pressure change is relevant; in view of the small compressibility of water, even a small water flow can result in large pressure changes which will translate into compaction and subsidence.

In the current Eclipse model, the aquifers are quite well connected to the gas reservoir. So, the aquifer response plays a role in the subsidence matching, but it cannot explain for the observed delay relative to the gas pressure as will be shown.

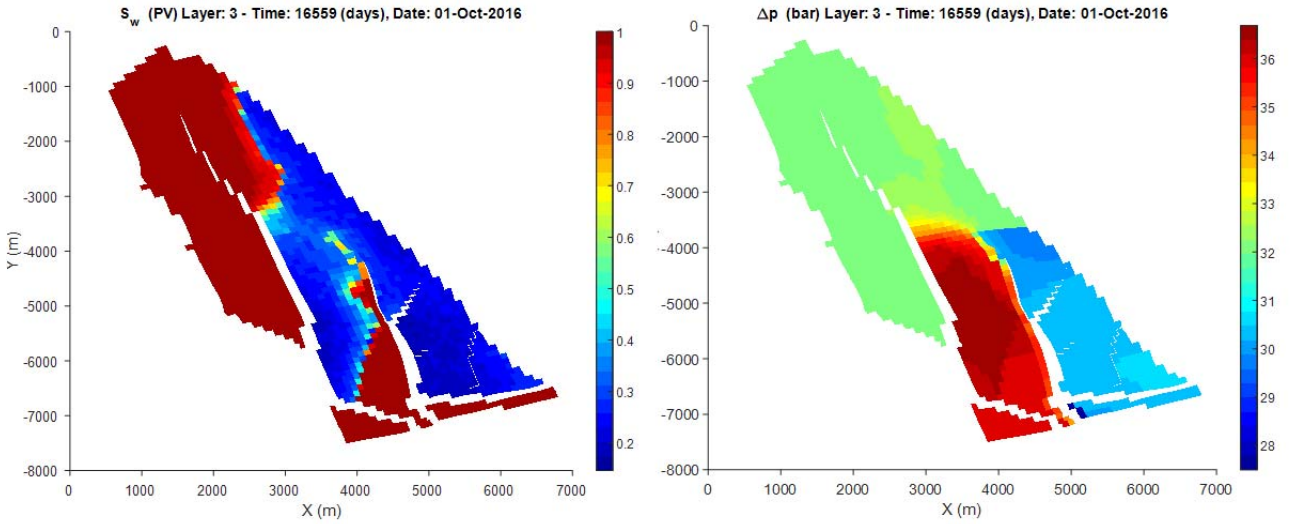

Figure 27: Results from the Eclipse history match. Left: Water saturation distribution in October 2016. Uniform pressure difference during a storage cycle, between early 2015 and Oct 2016. The pressure differential shows good pressure communication with aquifers, both connected to the gas zone in the Main block and Western block, but also in separate blocks to the south and west of the gas reservoir.

Pressure Mapping from Eclipse to COMSOL

The cells of the adjusted Eclipse reservoir model have a brick-shape with vertical cell dimension two orders of magnitude smaller than the horizontal dimensions. In contrast, the cells in the Finite Element Model (FEM) are tetrahedrons with uniform aspect ratios, while the cells are refined near the faults. Therefore, the discretization in the FEM model is much coarser in the vertical direction. An additional difference is that the Faults in the Eclipse model are staircase shaped surfaces, while they are gradually changing in the FEM simulation. Consequently, one must verify that sufficient amount of pressure detail is preserved in the FEM model. The pressure is mapped from Eclipse to COMSOL per Fault block (see Figure 6) in the following way:

1. For each FEM point find the associated Eclipse cell
2. Assign the depth corrected pressure to the FEM point
3. Create a (spatially) linearly interpolated pressure per fault block and per time step using the pressure in the FEM points

Figure 28 shows that the minimum and maximum point pressures as well as the depth corrected Bulk volume average block are in good agreement between COMSOL and Eclipse. The deviation in the Southern aquifers (blocks 1S and 2S) is a consequence of the extension of the FEM model to the South compared to the Eclipse model. This was done to account for contribution of the aquifers to the heave as observed in the previous version of the Eclipse model.

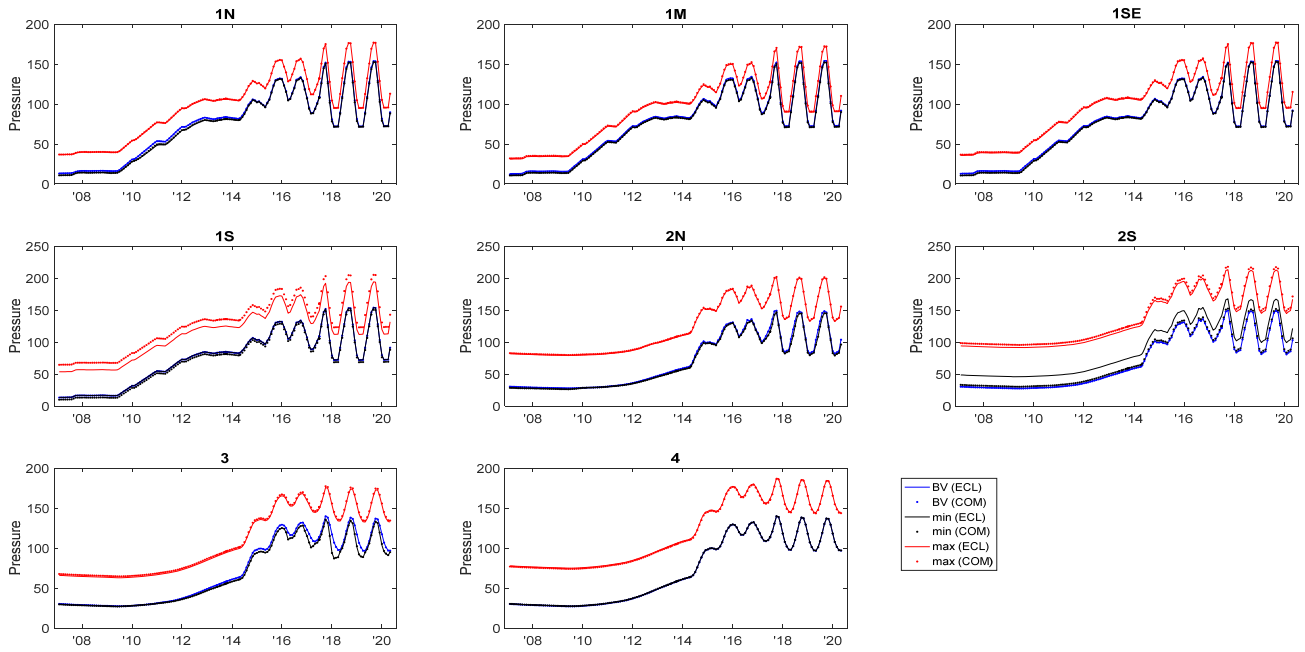

Figure 28: Comparison of minimum and maximum point pressure for each Reservoir block and the (GWC depth corrected) bulk volume average pressure between COMSOL and Eclipse

Initialization, Calibration and Constitutive Model

The virgin stress distribution is the result of tectonic, creep, depositional and erosional processes over geological time scales. Modelling of these processes to obtain the initial stress is not feasible because of the lack of data. Instead, the geology is taken as given and the initial stresses are calibrated on the available data. The stress calibration procedure is guided by theoretical relationships with 3 degrees of freedom that are strictly only valid for a 1D compaction model, i.e. a pancake reservoir that extends to infinity in the horizontal direction. The outcome of the stress is monitored so that the parameters could then be adjusted to achieve the required targets. The poro-elastic coefficient determines the stress change for given fluid pressure drop:

$$A_p = \alpha_B \frac{1-2\nu}{1-\nu} \tag{1}$$

The compaction coefficient c_m ($[1/Pa]$) gives the vertical reservoir strain for given fluid pressure drop:

$$c_m = \frac{\alpha_B}{E}\frac{(1-2\nu)(1+\nu)}{1-\nu} = \frac{A_p}{2G} \tag{2}$$

Where G ($[Pa]$) is the shear modulus. The theoretical relationship for the Biot coefficient α_B reads

$$\alpha_B = \left(1 - c_g K\right) \tag{3}$$

Where c_g (1/Pa) is the grain compressibility and K ([Pa]) the bulk modulus.

Stress initialization

Stresses are initialized in a three-step approach:

1. Vertical stress initialization. Load step with viscoelastic shear stress reduction to get a vertical stress distribution that increase uniformly with depth while Von Mises stresses are minimized.
    a. Shear stresses are reduced to 0.025% in Salt and 0.1% elsewhere.
2. Horizontal initialization step with viscoelastic salt creep to minimize deviatoric stresses in the Salt.
    a. Initial horizontal stress is obtained by multiplying vertical stress resulting from step 1 with horizontal over vertical stress multipliers that vary per domain.
    b. Shear stress in salt are reduced by 90% to simulate Salt creep and obtain Isotropic stresses.
    c. Shear stresses are reduced by 50% in Anhydrite/Carbonate layer below the salt and by 10% elsewhere to prevent high shear stress ratio's resulting from the salt creep initialization just below the salt.
3. Elastic equilibrium step to guarantee equilibrium conditions.

Calibration targets for the initialization/depletion stresses are:

- Matching depletion stress path corresponding to the injection test performed in 2007 in well BGM-8 (see Stress data in previous chapter).
- Isotropic stresses in the salt layer resulting from Salt creep over geological time scales.
- Maximum horizontal over vertical stress ratio of 0.9 in all layers except for the salt,
    - In line with lost circulation incidents in well BGM-17.
- A minimum horizontal stress over vertical stress ratio between 0.68-0.69, except in the Anhydrite/Carbonate layer which has a stress ratio of 0.9. This higher value is required to accommodate for the stress concentrations resulting from the salt initialization.

The shear and normal fault stresses on the midfield, east and west fault are mainly controlled by the behaviour of the minimum horizontal stress and vertical stress, which mostly coincide with the x and z direction of the grid. This makes the model fairly insensitive to the choice of the maximum horizontal stress which mostly coincides with the grid y-direction. The minimum horizontal stress in the non-reservoir layers was calibrated on the critical fault behaviour.

Stiffer reservoir response and Kelvin-Voigt time delay

The measured subsidence shows a much stiffer response during refill and the storage cycles than during depletion. This is a commonly observed elastoplastic response with permanent deformation occurring during the first loading. The behaviour could be modelled with an elastoplastic constitutive model, but this

introduces unknowns to calibrate for which no data is available. To avoid this, the stiffer response was modelled with an inelastic response, using different elastic compaction moduli during refill compared with initial depletion. The different stages are combined using superposition of the increments. Such an approach violates energy conservation, because the elastic deformation is not explicitly incorporated. However, it is a valid approach for the loading conditions of the reservoir since the average pressure after depletion is raised to a higher level. Compared with elastoplastic models this is isotropic plasticity, which is the simplest approximation, using a constant stiffness below the maximum load level.
The time delay observed in the GPS measurements cannot be explained by the aquifer response present in the Eclipse model. This time delay indicates a viscoelastic response rather than an elastic response. The viscoelastic response is approximated with the Kelvin-Voigt (KV) model. The KV model describes a damper-spring system in parallel, where the response of the spring is delayed by a damper (see Figure 8). Over time the influence of the damper diminishes and the response of the spring remains. The characteristic time scale for the damper is called the relaxation time. The relaxation time used will be a weighted averaged of the relaxation time observed in the 4 GPS stations. Because the characteristic time scale of the depletion phase is much longer than the delay time observed in the GPS measurement, the Kelvin-Voigt effect is not modelled during the depletion phase.

Stress path recovery to match seismicity

For the depletion phase the stress path is given by the stress measurements in well BGM-8 listed above. For the refill and storage cycles the actual stress is unknown by the lack of data.
However, it appears that the absence of large magnitude seismicity during refill and storage requires that the stress path in the middle of the reservoir fully recovers during the refill phase. This is the best case scenario. It was observed that for partial stress recovery, large scale seismicity can be expected at the midfield fault. This contradicts seismic observation which shows that the seismicity at the midfield fault has even come to a halt. The stress path is controlled by the poroelastic coefficient. Because the actual 3D response differs from the theoretical relationships, the poroelastic coefficient is used as a calibration parameter.

Parameter Calibration Matrix

Depletion and refill/storage were calibrated simultaneously. For both phases three degrees of freedom control the Geomechanical response.

In summary, for the depletion phase the compaction modulus follows from the subsidence (c_m=5x10^{-11}1/Pa) and the poroelastic coefficient follows from the stress data in well BGM-8 (A_p=0.79) . This leaves one degree of freedom for the depletion phase for which the Poison ratio is set. Because of the high poroelastic coefficient the choice for the Poison ratio already is limited to the range [0, 0.175]. The choice will be further limited by the requirements for the refill and storage calibration. Once these parameters are set the Young's Modulus, Biot coefficient and grain compaction modulus follow from the theoretical relationships for the biot coefficient, poroelastic coefficient and compaction modulus; Table 2 list the calibration matrix.

For the refill and storage phase the stiffer compaction modulus follows from the Geodetic Survey and GPS measurements (c_m=2x10^{-11}1/Pa). The grain compaction modulus is expected to remain unaltered over the lifetime of the reservoir, which is determined by the depletion phase. The poroelastic coefficient during refill and storage is set such that stress fully recovers. It appears that this considerably narrows the range for the Poison ratio during depletion.

Finally the time delay observed in the surface movement by the GPS measurements is simulated with the viscoelastic Kelvin-Voigt model. The relaxation in the model is matched to the observed GPS data.

Table 2: Parameter calibration matrix: the grain compaction modulus c_g, the Poisson ratio ν, the Young's modulus E, the Biot coefficient α_B, the Poroelastic coefficient A_p and the compaction modulus c_m, τ is the relaxation time for Kelvin-Voigt viscoelasticity

	A_p	c_m	ν	c_g	E	α_B	τ
	(-)	(1/Pa)	(-)	(1/Pa)	(GPa)	(-)	(days)
Depletion 1971-2007	0.79	5x10^{-11}	Chosen	Follows	Follows	Follows	N/A
Refill + Storage 2007ff	Refill seismicity	2x10^{-11}	Follows	Same as for depletion	Follows	Follows	GPS data

Sensitivity: Impact of Salt Creep on stress

Halite is often a combination of rock salt and other, more creeping salts like Carnalite. So, the shear stress response is somewhere in between the measured values for these salts, shown in Figure 29. Due to creep, the shear stress in the Halite strata will be relieved and the horizontal stress will increase. The second effect is that shear stress which arises because of differential compaction will be relieved after some time due to halite flow.

A more complex response is expected in the Bergermeer reservoir since the midfield fault is bounded by Halite in the South, where the fault completely separates the reservoir layer. The Halite flow and resulting higher stress can then reduce the normal stress on the fault near the fault tip (Orlic *et al*, 2011). So, it is hard to predict the combined effect on fault stability.

In this study Salt flow was modelled with a simple viscoelastic Maxwell model that captures the elastic response and allows for relief of shear stress with a reduction in shear modulus over time. This model represents the response of a single spring and multiple spring-dashpots in parallel as shown in Figure 30. The initial response of the system is fully elastic (combined effect of all springs) while over time shear modulus of the entire system reduces to the spring without dashpot because of the vanishing contribution of each of the spring-dashpot combo's by relaxation of the dashpots. In Appendix II the Viscoelastic model is fitted to the creep law.

Salt flow cannot account for the character of the delay which shows a subdued elastic response upon a quick pressure rise, because its initial response is elastic. As such the impact of Salt creep was only modelled as sensitivity to the depletion phase.

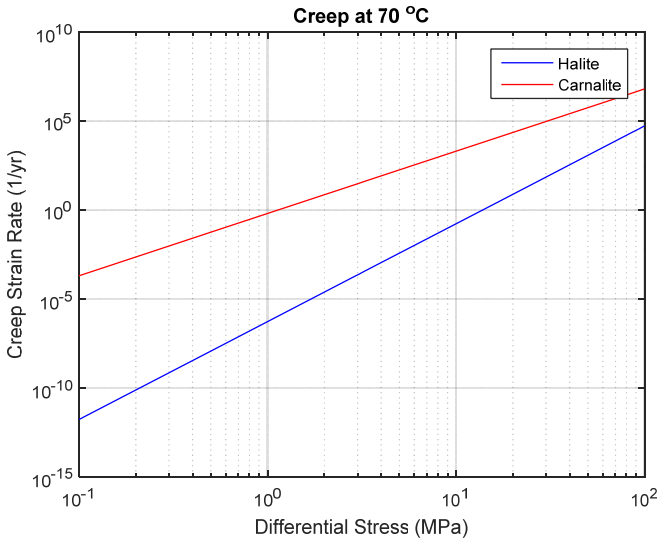

Figure 29: Creep rate per year for Halite and a creeping salt, Carnalite. The exact composition of Zechstein salt formations is poorly known, so it is best to taken an average of these values since even a thin layer of Carnalite (or Bischofite) can add significantly to overall creep strain.

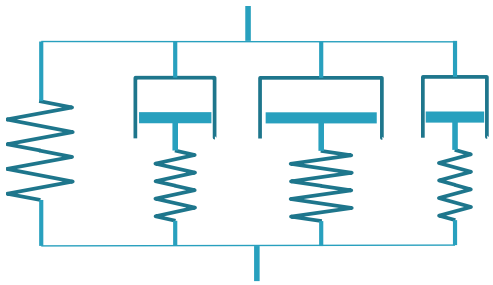

Figure 30: Generalized Maxwell Model models the relaxation of shear stress analogously to a spring and multiple spring-dashpots in parallel. Multiple branches are used to model strongly non-linear creep of salt.

Geomechanical Modelling Objectives and Seismic Management System

Seismic monitoring has a long history and was first successfully applied in deep, South African mines to warn for impending tunnel collapse. The technology was based on the observation, when lab rock samples were loaded to failure, that acoustic emissions in the sample started long before a fracture formed, see Figure 31. Acoustic emissions which were caused by micro-fracturing coalesced to a narrow zone that finally ruptured leading to collapse. The same mechanism was observed in mining tunnels where incipient failure caused an increased intensity of micro-seismicity that could be used to warn before a collapse (rock burst) happened.

This formed the basis for recent development of Traffic Light Systems (TLS) that are used to warn for large induced earthquakes. The same idea is used that before a large rupture occurs on a fault there will be small failures of single asperities, yielding micro-seismicity.

In principle, the TLS can stand on its own, but it is helpful to aid the monitoring with geomechanical modelling to understand any observed seismicity.

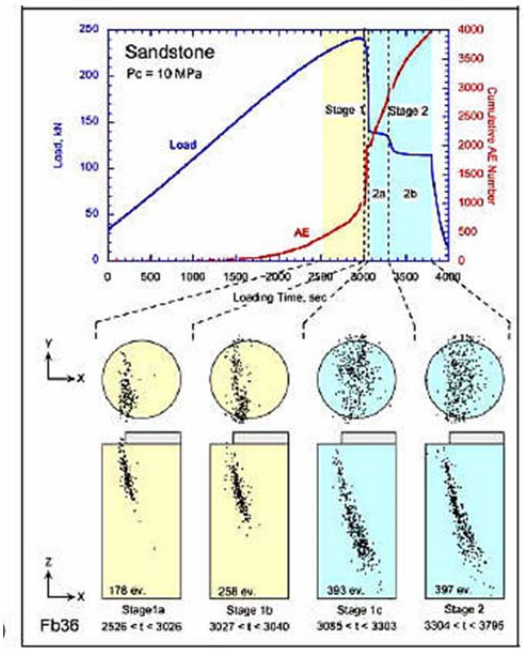

Figure 31: Observed acoustic emissions in a triaxial test on sandstone. When the sample reaches failure, the acoustic intensity increases on the incipient failure zone.

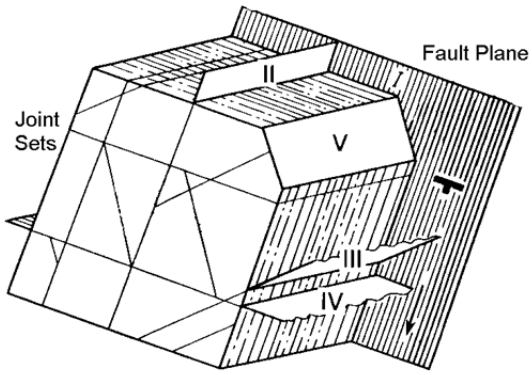

Figure 32: Schematic picture of fault zone that is commonly associated with sets of fractures adjacent to the core fault zone.

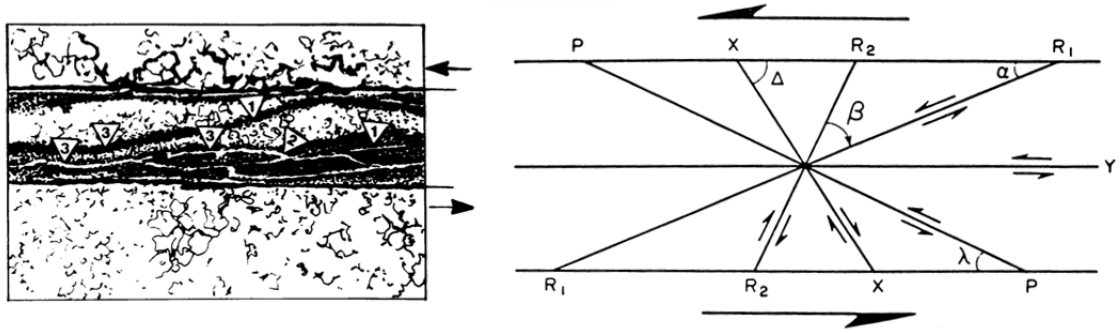

Figure 33: Microscopic image of fault zone with several secondary fracture types that form in a shear zone (Logan et al., 1992).

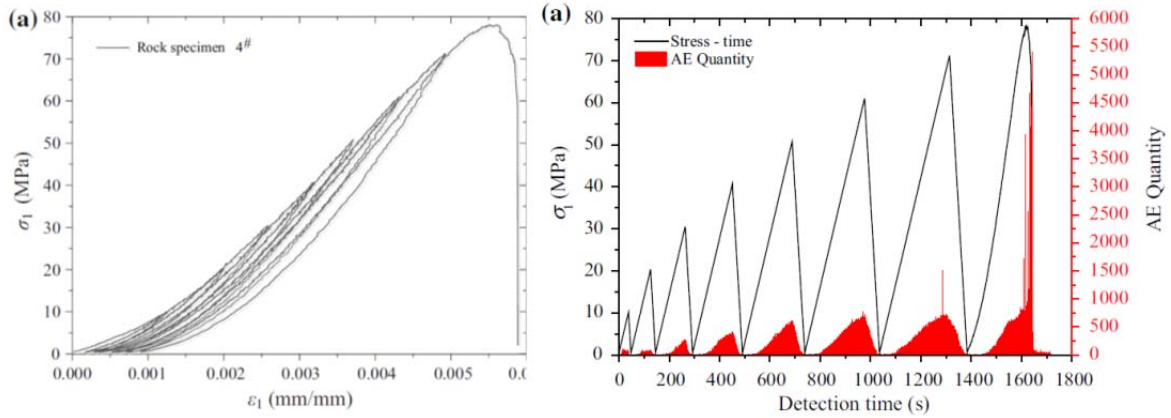

Figure 34: Cyclic loading of sandstone samples yields acoustic emission with Kaiser effect (Meng et al., 2016). Note that emissions still persist during unloading, but are sparse during initial re-loading.

That requires calibration of the model on observed seismicity which encounters two issues:

1. The biggest issue is the huge gap between the depletion earthquake magnitude and the magnitude of observed micro-seismicity during refill. While the depletion earthquakes were caused by slippage on an area of hundreds of metres in diameter, the micro-seismic magnitudes correspond to a few metres with the strongest event perhaps 30m. Given such small slippage area, it becomes necessary to consider the heterogeneity of the fault zone (Steacy *et al*., 1998; Rinaldo *et al*., 2016; Rutqvist *et al*., 2016). Fractures and faults are extremely heterogeneous as has been found in research on lab samples as well as field studies. A fault zone is commonly associated with extensive secondary fracture sets, as depicted in Figure 32 and Figure 33 (Logan *et al*., 1992). Straining such a complex fault zone may destabilize some of the fractures in the fault zone during loading and others during unloading. Since both geometry and stress will be heterogeneous, many asperities and small shear fractures may be critically stressed. This effect has been observed in lab tests of Acoustic Emissions (Meng et al., 2016), shown in Figure 34. The Kaiser effect is only valid for re-loading where few micro-seismic events occur, but during unloading there is still some micro-seismicity. Apart from stress reversal, also interactions between principal stresses (i.e stress path hysteresis) may give violations of the Kaiser effect that can explain unloading seismicity (Holcomb, 1993).
2. Apart from the gap in magnitude between the depletion earthquakes and the refill micro-seismicity there is another disparity between depletion and refill seismicity. During depletion, the fault was critically stressed after 1994, as evidenced by four earthquakes with magnitude above 3. Extrapolating this to smaller magnitude with the Gutenberg-Richter law, the number of earthquakes above magnitude 1.5 over this interval should be more than 100. After 1995, additional geophones were installed that should have observed a large number of weaker events, but none were detected. A completely different behaviour is seen in the micro-seismic data set where four hundred events were observed that followed the Gutenberg-Richter law. Assuming that slippage always starts in a non-

seismic manner, the behaviour during depletion may be explained by non-seismic slip when the slippage area remains small while slip becomes dynamic when a large area is slipping. However, such a mechanism appears to contradict the micro-seismicity observed during refill.

Most observed micro-seismicity in Bergermeer is likely caused by heterogeneity of a fault that is on average stable; as confirmed by the temporal character of the micro-seismicity. However, the largest event during refill had magnitude 0.9, which represents a slippage area that is 10% of reservoir height. Therefore, it is prudent to interpret at least the stronger micro-seismicity as a precursor of small earthquakes and the geomechanical model will be calibrated on the micro-seismicity to predict future seismicity.

Fault Stability Criterion: Predicting Seismicity

Since Dutch gas fields have no critically stressed faults either at reservoir level or in the deep subsurface (as evidenced by absence of regular natural earthquakes), the most plausible mechanism for induced earthquakes is transfer of compaction strain to faults by differential compaction (Roest *et al*, 1993; Bourne *et al.*, 2014). Since effective normal stress will increase due to depletion, the shear stress caused by differential compaction drives the fault into criticality. The criterion for fault slip in the geomechanical model is simplified to the Mohr-Coulomb criterion, which predicts slippage when the ratio of shear stress to effective normal stress exceeds the friction coefficient:

$$\frac{\tau}{\sigma_n - p} > \mu \tag{4}$$

The driving force in induced seismicity is reservoir pore pressure, since that causes changes in total stress and shear stress by reservoir volume change. However, the local pore pressure in the fault zone is also crucial since it may destabilize faults. This effect has been extensively observed in geothermal and waste water injection. More complicated is the effect of reservoir stress changes. In differential compaction, the shear stress is the dominant driver for seismicity, but the contribution from changes in the effective normal stress cannot be ignored. If the shear stress falls during refill, the effective normal stress may decrease more due to hysteresis or a pressure differential causing destabilization.

Still, this friction law is a simple model of the reality of fault slippage, since the contacts in a fault zone are far from uniform, but consist of many asperities that are in contact and carry much higher stress than the average stress. The above friction law is a simplification in the sense that two mechanisms determine friction: the normal stress determines contact area and shear stress determines failure of the contacts and slippage. In principle, these two processes may be elastic, but it is likely that in many rocks shearing is accompanied by some micro-fracturing or plasticity when asperities yield under shear.

Previous studies (TNO, 2008; Orlic, 2013) showed that slip on the faults has a significant effect on the final stress state. Assuming the stress effect from the earthquakes is frozen over a long period, a large area on the fault will remain close to the critical state.

There may also be a higher friction coefficient for onset of slip, which occurs in a non-seismic way but when the slip accelerates to the wave velocity the dynamic friction coefficient will be lower. In the pseudo-static model presented here, the friction coefficient will be used corresponding to the final stage of an earthquake. So, at the end of depletion the stress on the fault is just critical, but there will be no excess shear stress that could drive further slippage, in accordance with the observation that no big seismic events were induced. Any new seismicity will be possible if the shear stress is enhanced above the failure envelope.

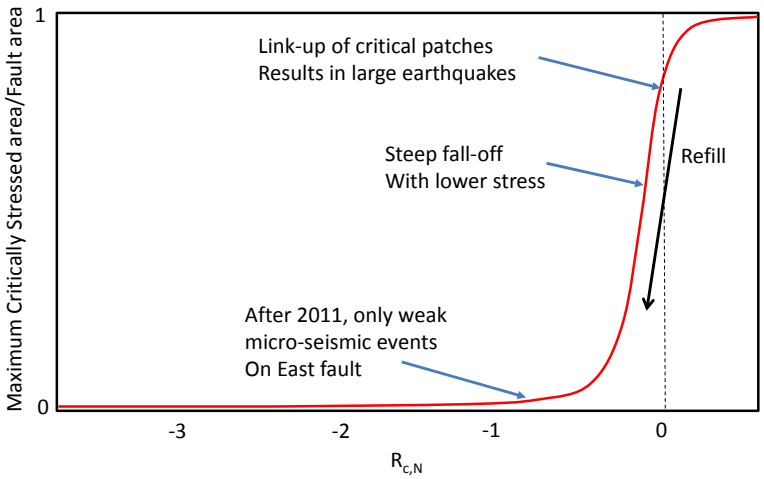

Figure 35: On a heterogeneous fault, the size of the largest critically stressed area falls off rapidly when the critical stress ratio is below the threshold friction coefficient for slippage. This corresponds with the observation that when the stress falls a bit below the critical value, only very small micro-seismic events area observed. (Conceptual behaviour)

There are two phenomena that must be considered for assessing seismic risk:

1. Large areas of the fault that may become critically stressed (with excess shear stress) so that earthquakes may be induced.
2. Micro-seismic activity, as observed on the faults that are caused by slippages that are very small and fall below the resolution of the model. This activity may be a telltale for large areas becoming critical, provided that the events are clustered. The micro-seismic activity in Bergermeer is not induced at a single location, so there are no large areas with excess critical stress. However, there is still a lot of activity at sub-critical stress, so we will derive a measure to assess how the activity depends on the stress level.

Large critically stressed areas can be covered within the framework of the model, by evaluating the critical stress ratio and determining the largest area with critical stress and excess shear stress.
So, two measures of seismic risk are proposed:

1. The peaks in critical stress ratio on the fault are measured with the maximum seismic magnitude that could be induced.
2. A measure will be derived for the Micro-seismic rate that is proportional to the rate of change of shear stress and that is a function of the average critical stress ratio computed over an area that was most critical after depletion. The average level of the critical stress ratio gives an indication of micro-seismic activity related to heterogeneities.

Of course, the two measures will overlap if the fault would become critical over most of its area. However, it is likely that during storage cycles, at an average pressure that is above the pressure for which the large depletion earthquakes occurred, there will be only micro-seismic activity as already observed during a number of storage cycles.

Ubiquitous seismic activity was observed over a large area of the fault. Although the depth location uncertainty is large, it shows at least that seismic events did not come only from the stress concentration near the juxtaposition point, but also came from parts of the fault that were subcritical. In order to relate the micro-seismic activity to the average stress computed by the model, we define a critical stress ratio over a large area (corresponding to the critical area after depletion). This normalized critical stress ratio, $R_{c,N}$, is a measure of the distance below the MC envelope over a representative area that might become critically stressed:

$$R = \frac{\tau}{\sigma_n - p} \Rightarrow \Delta R = R - \mu, \quad R_{c,N} = \frac{\int_A \Delta R dS}{A \Delta \mu} \tag{5}$$

Where μ is the calibrated friction coefficient, A is the area over which ΔR is integrated and $\Delta\mu$ is a characteristic range in friction coefficient that is used for scaling the normalized critical stress ratio. During refill, the normalized critical stress ratio becomes negative, while for small areas, slippage is still possible. Given the history of micro-seismicity, we can then relate the observed level of micro-seismicity to the forecast of the stress during future cycles. If the critical stress area over the area of interest remains below the level during the past storage cycles, it can be concluded that also the micro-seismicity will not exceed observed micro-seismic rate and magnitude.

Figure 35 shows the conceptual behaviour to account for micro-seismicity. At the end of depletion a large area that has slipped is located on the Mohr-Coulomb envelop or above, $R_{c,N}$>=0. If one would reduce the pressure, the value of $R_{c,N}$ would rapidly increase as would the risk of large scale seismicity. Similarly, during refill, the pressure increases and honouring the Kaiser effect, on average the fault does stabilize and $R_{c,N}$ will decrease. For an on average stable fault ($R_{c,N}$ <0), the likelihood of micro-seismicity has to drop as function of a decreasing stress ratio $R_{c,N}$, because stability only increases. Hence, if the average critical stress ratio $R_{c,N}$ in future operations stays below a (chosen) historical reference level, the likelihood of micro-seismicity will have to drop as well.

From a general expression for the total number of earthquakes over time (Harris, 1998; Dempsey and Suckale, 2017), the seismicity rate can be derived for a sub-critical fault based on the Mohr-Coulomb failure function:

$$F_{MC} = \tau - \mu\left(\sigma_n - p\right) \Rightarrow \Delta F_{MC} = \Delta\tau - \mu\left(\Delta\sigma_n - \Delta p\right) \tag{6}$$

For large slip areas this function determines failure ($F_{MC}\geq 0$), but when the average stress on the fault is sub-critical micro-seismicity is still observed and we propose that the failure of small fault patches or fault branches is related to shear strain of the fault zone. During refill, the micro-seismic clouds appear when the fault is shearing in the reverse direction compared with depletion. Therefore, the simplest explanation of the micro-seismicity is that reverse shear induces failure of small faults that have become critically stressed during depletion. The micro-seismic rate is then related to changes in shear stress:

$$\begin{aligned} &N = k\iint_{A_c} F_{MC} H\left(F_{MC}\right) dSdt \Rightarrow N_{MS} = k\iint_{A_c} \Delta\tau P\left(R_{c,N}\right) dSdt \\ &\dot{N}_{MS} \propto \int_{A_c} \Delta\dot{\tau} P\left(R_{c,N}\right) dS \end{aligned} \tag{7}$$

Where N is the total number of earthquakes induced on a fault that reaches the MC condition, given by the Heaviside step function, H, of the MC failure condition and N_{MS} is the total number of micro-seismic events, P is the probability of occurrence as function of average critical stress ratio and k is a matching parameter. The micro-seismic rate is determined over the largest contiguous critical area A_c. The usual condition for slippage given by the Heaviside step function of the failure function is replaced with a probability of the average critical stress ratio, in which the possibility for occurrence of micro-seismicity is extended to faults that are on average sub-critical.

For a Gaussian distribution of strength of the fault, the probability would fall off rapidly with average stress:

$$P = 0.5\left(1 - P_{res}\right)\left(1 + erf\left(aR_{c,N}\right)\right) + P_{res} \tag{8}$$

Where a is a match parameter and P_{res} is the residual probability at low stress. The probability approaches 1 for critical stress ratio equal to the friction coefficient, but falls off rapidly for sub-critical stress. For the Midfield fault the Gaussian density (described with the error function for the distribution) is used, while the East fault shows no discernible trend in seismicity with stress level, so only the residual probability is used.

Several possible explanations can be proposed for the seismicity that was observed on the East fault during refill and storage cycles. It turns out that pressure diffusion is unlikely and delayed stress response of the reservoir is possible, but has a rather short time scale. Another potential explanation could be time dependent friction caused by salt that has been smeared on the fault, from the thick Halite bed that is adjacent to the reservoir. However, salt should give an immediate elastic response (i.e a Maxwell effect rather than Kelvin-Voigt) so cannot explain the injection seismicity which should be caused by delayed response at the onset of shear strain.

The simplest explanation is that the above general expression for total number of earthquakes can be used to express seismicity rate in terms of shear stress rate. The seismic rate increases mostly during injection, provided that the slippage of small critical faults mostly occurs during unloading. This can be justified since

the large strain of the fault during depletion released all energy on small fractures that were critical for negative shear strain. So, the population of critical fractures that could be activated by negative shear stress is depleted. Fractures which are close to critical for positive shear strain will then slip during unloading, as observed in the lab tests of Figure 31.
This analysis is linked to the estimate of maximum magnitude in two ways: a large earthquake requires a large critically stressed area and the usual Gutenberg-Richter (GR) correlation that relates the rate of seismic activity with magnitude. It is doubtful that the standard GR relation applies to induced seismicity, since during depletion 4 large earthquakes were observed while there was a lack of smaller earthquakes which should have been observed according to the GR relation. On the other hand, the GR relation can be used to determine the probability of strong events from the micro-seismic activity. At least in some gas fields this provides a conservative estimate of the chance of large earthquakes. An increase in micro-seismic activity can then be interpreted as a warning signal for larger earthquakes.

Rate Effects

Depletion causes fault instability and the reverse conclusion could be drawn for re-fill of a previously depleted gas storage reservoir. Even if the fault slipped during depletion, the stress state will remain close to critical with high shear stress. Subsequently, the shear stress will become less when the reservoir rebounds and horizontal stress increases. However, this conclusion assumes perfect elastic response upon unloading which is often not expected for sedimentary rocks. Furthermore, an important difference between depletion and gas storage cycles is the difference in time scale. Therefore, it is relevant to also consider effects of loading rate on the stress in the reservoir and possible implications for seismicity.
Pressure diffusion has a characteristic time that will relate production or injection to compaction. Its effect on subsidence will be small, since it just involves a distribution of compacted volume, but it may have an impact on seismicity, since the pore pressure at the fault is relevant.
Compaction itself may depend on time, since deformation of rock is always accompanied with micro-fracturing which is time dependent (Dieterich, 1992). Furthermore, compaction is affected by surrounding rock layers, which may show a time dependent response such as the Zechstein salts.
Finally, seismic slip on faults may be time dependent as suggested by Dieterich (1992). Time dependent response of reservoir rocks is intimately related to time dependence of fault friction, since similar processes underlie compaction creep and time dependence of fault friction.
The first time-dependence that is observed in the reservoir response is the delay in uplift response upon re-pressurization. The time delay can be related to a viscous term in the response, which could be related to:

- Pressure diffusion, in particular the aquifer
- Halite flow
- Time dependent reservoir rock expansion

In the simulations, time dependence due to pressure diffusion and Halite flow and the implications for fault stability will be considered in detail. Pressure diffusion is embedded in the reservoir simulations, so this effect will emerge if relevant. However, the reservoir simulation model has high permeability throughout the reservoir, so any delay time is shorter than a week. So, the injection seismicity seen at the East fault and also the Midfield fault cannot be explained by pressure diffusion. Moreover, the immediate response in seismicity upon start of injection would need a high permeability conduit from injectors to the fault zone. In the context of the Bergermeer reservoir that is unlikely, since the fault zones are expected to be relatively tight. That may give a delay of pore pressure which could destabilize the fault during production, but not during injection. So, the simplest explanation of the injection seismicity is the shear rate applied to the fault at the start of injection.
Another reason creep processes play a role in seismicity is that finite slip is always an ingredient in fault slip mechanics (except for the smallest events that may involve one asperity), which implies that the set of asperities in contact is always changing. That introduces deformation history in the friction process, which motivated the introduction of not only rate, but also rate history in the description of friction. These so-called rate-state friction laws account for many observations of natural earthquakes, such as precursor events and aftershocks, although some observations remain hard to explain due to the lack of detailed measurements in fault zones and the likelihood that during slip the geometry of the fault asperities may change. So, it is always possible that events occur long after critical stress was reached, as may have happened with the strongest micro-seismic event in 2013.

Work Flow for Matching Subsidence and Seismic Activity

It was shown that an elastoplastic (or non-elastic) model with Kelvin-Voigt response to pressure change is needed that includes the stress change on the faults induced by the depletion earthquakes.
Apart from the friction coefficient (and possibly cohesion in the fault zone) there is also uncertainty about the pore pressure in the fault zone. Different scenarios have been used in previous studies for the pore pressure. As extreme cases, the pore pressure may still be virgin on the non-reservoir side and fully depleted at the reservoir side. That gives a big difference in critical stress ratio. In view of the large depletion in Bergermeer, the seismicity could be matched using average pressure in the fault zone with a reasonable friction coefficient. Therefore, the pore pressure will be part of the calibration procedure and the best match will be used.
The following observations will be addressed:

1. The observed depletion and injection surface subsidence and heave and heave delay.
2. Strong seismicity during depletion (magnitudes 3 in 1994 and 3.5 in 2001)
    a. The cumulative seismic moment should be matched in the depletion period.
3. Observed micro-seismicity on the Midfield fault during refill
    a. Refill seismicity is weak compared with depletion seismicity.
4. Extinction of activity on the Midfield fault above 100 bar reservoir pressure
5. Continuing activity on the East fault, concentrated at start-up of injection; decreasing activity over subsequent cycles

Table 3: Potential match parameters with their effect. The column Match indicates whether a parameter was included in the matching procedure (Y) or when it was deemed unnecessary or impractical to include it (N).

Parameter Group	Parameter	Match	Effect
Elastic Moduli	Modulus reservoir	Y	Depletion subsidence
	Unloading modulus	Y	Refill heave
	Poisson Ratio	Y	Subsidence and stress path
	Visco-elasticity: relaxation time	Y	heave delay
	Modulus non-reservoir	N	Onset of seismicity
Poro-elasticity	Biot coefficient	Y	Stress Path/Heave
Stress	Initial stress	N	Onset of seismicity
	Stress path	Y	Refill seismicity
Fault properties	Fault friction coefficient	Y	Onset of seismicity
	Pressure in fault zone: Average	Y	Onset of seismicity
Pore Pressure	Reservoir pressure distribution	N	timing of seismicity
	Aquifer pressure	N	heave delay
	non-reservoir pressure	N	effective stress on fault
salt creep	creep rate or visco-elastic relaxation	Sensitivity	seismicity, stress on fault

The potential matching parameters are listed in Table 3, with the effect of each parameter. Some parameters have been taken as given inputs, such as simulated reservoir pressure. Other parameters, such as initial stress state and properties of non-reservoir rock are also kept fixed, since there are alternative parameters that can be used for matching.

Therefore, calibration will involve the following steps:

1. Matching the measured stress state at virgin and depleted conditions
2. Matching the observed depletion and injection surface subsidence and heave.
    a. This will deliver the depletion stiffness as well as the refill stiffness of the reservoir.
    b. Also, time dependence of the response during refill can be obtained
3. Matching seismicity during depletion
    a. The cumulative seismic moment associated to the 4 depletion earthquakes in 1994 and 2001 is matched by calibrating the friction coefficient

4. Matching the observed micro-seismicity on the Midfield fault during refill
    a. Adjustment of the poroelastic response
5. Matching the extinction of activity above 100 bar reservoir pressure
    a. Accounting for continuous slip of the fault during refill and storage
6. Matching activity on the East fault, concentrated at start-up of injection

In principle, the observed surface subsidence also includes compaction of shallow, soft layers. However, the subsidence match focused on the cycles, so any long-term trends were disregarded. Since the GPS data agreed (within uncertainty) with the geodetic data, the long-term trend was of minor importance.

5 Calibration and stress Simulations during depletion

This section presents the result of the calibration and initialization procedures described in the previous section. First the resulting calibration parameters and the stress path are shown. Next the match of the subsidence during depletion and refill/storage is presented. After the initial stresses are shown the results for the elastic simulation are presented. The section ends with the description of the sensitivity in which the impact of salt creep on the depletion is investigated.

Resulting Calibration parameters

Table 4 lists the resulting calibration coefficients. For calibration of the depletion phase, the difference in stress state between virgin and depleted state in 2007 in well BGM-8 results in a poroelastic coefficient of 0.79. The observed surface heave during depletion determined the compaction coefficient ($5x10^{-11}$[1/Pa]). The Poison ratio was set as the remaining degree of freedom. Because of the high value of the poroelastic coefficient the range for the Poisson ratio was a priori limited to [0, 0.175].
For the refill and storage period, the compaction modulus follows from the Geodetic and GPS measurements ($2x10^{-11}$[1/Pa]). This is a reduction in the compaction behaviour by a factor 2.5 compared to the depletion. The grain compaction coefficient is considered to be constant over the lifetime of the reservoir and hence determined by the depletion phase. The absence of large magnitude seismicity during refill and storage required that the stress path in the middle of the reservoir during refill and storage does not show hysteresis w.r.t the depletion phase. The usage of an alternative stress path would result in seismicity of considerable magnitude during refill/storage which contradicts observation.
The refill stress path resulted in a poroelastic coefficient of 0.92, which limits the choice for the Poisson ratio during depletion to [0.15, 0.175]. This is because a high poroelastic coefficient in combination with compaction coefficient of $2x10^{-11}$ is only possible for grain compaction coefficients of $5.2x10^{-13}$ or smaller. For higher values the Poisson ratio would become negative. Within this narrow range, the Poisson ratio for the depletion coefficient was set to 0.175. The latter gives a depletion Young's modulus of 18GPa which corresponds to the value used in earlier studies.
Finally the relaxation time in the Kelvin-Voigt model was set to 69 days, which concerns a weighted average of the relaxation times observed in 4 GPS stations.
For completeness, Table 5 lists the corresponding bulk modulus that links the volumetric strain to a change in stress and the shear modulus that expresses the relation between shear stress and strain. The increased stiffness in both moduli is in line with the increase in young's modulus and the reduction of the Poisson ratio and of the same order as the increase in compaction modulus.

Table 4: Calibrated coefficients: the grain compaction modulus c_g, the Poisson ratio ν, the Young's modulus E, the biot coefficient, the Poroelastic coefficient A_p and the compaction modulus c_m, τ is the relaxation of the Kelvin-Voigt viscoelastiscity.

Phase	A_p	c_m	ν	c_g	E	α_B	τ
	(-)	(1/Pa)	(-)	(1/Pa)	(GPa)	(-)	(days)
Depletion 1971-2007	0.79	$5x10^{-11}$	0.175	10^{-13}	18	1	N/A
Refill and storage 2007ff	0.92	$2x10^{-11}$	0.07	10^{-13}	48	0.998	69

Table 5: Bulk (K) and shear modulus (G) for given Poisson ratio ν and Young's modulus E.

Phase	ν	E	K	G
	(-)	(GPa)	(GPa)	(GPa)
Depletion 1971-2007	0.175	18	9	8
Refill and storage 2007ff	0.07	48	19	23

Calibrated stress path

Figure 36 compares the resulting stress path in the middle of block 1M to the original elastic stress path. The fully elastic stress path is free of hysteresis which indicates limited pressure diffusion effects. For the inelastic simulation, during refill, the horizontal stress recovery is equal to the stress during depletion. For seismic risk, this is the best case since in some reservoirs stress has not recovered during pressure increase, which would give higher shear stress. However, if other effects, such as fault slip can explain observed micro-seismicity it is better to assume full stress recovery to keep the model as simple as possible.

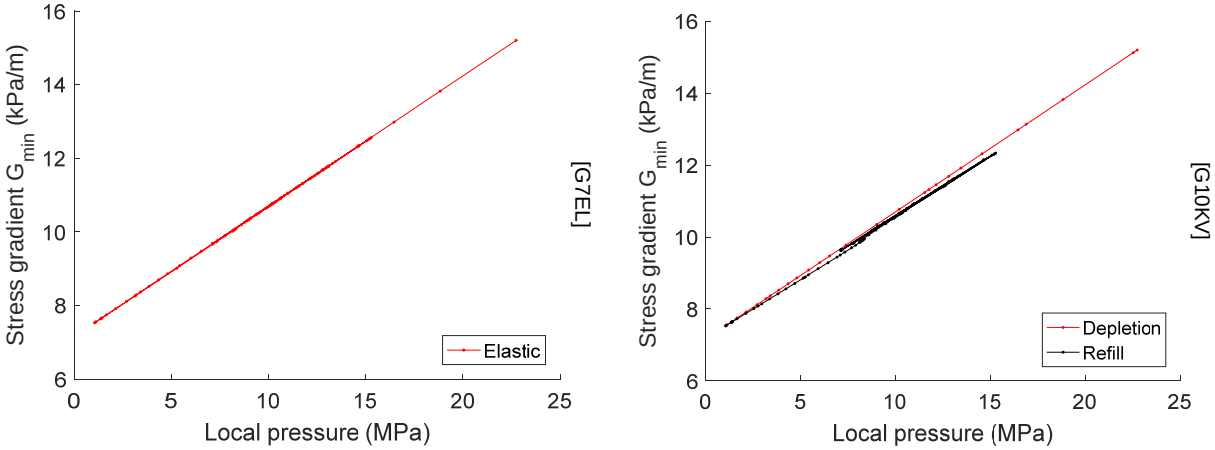

Figure 36: Stress path for (left) elastic simulation and (right) simulation including hysteresis in the middle of region 1M as shown in Figure 6. Simulations include depletion, refill and storage cycles

Match of the surface heave for depletion, refill and storage

The depletion is calibrated on the subsidence bowl and the stress reduction (see Table 4). Figure 37 shows that the subsidence bowl has a maximum depletion of 115mm, which matches the reported observed subsidence of 110-120mm. A Kelvin-Voigt fit of the simulated subsidence at each of the stations, shows a near instantaneous response of the Southern station TAQA-4 and TAQA-5 and a small delay in the Northern stations TAQA-2 and TAQA-5. This small delay can be attributed to a small delay in the pressure response of the Western blocks and Aquifers compared to the pressure in the Eastern block.

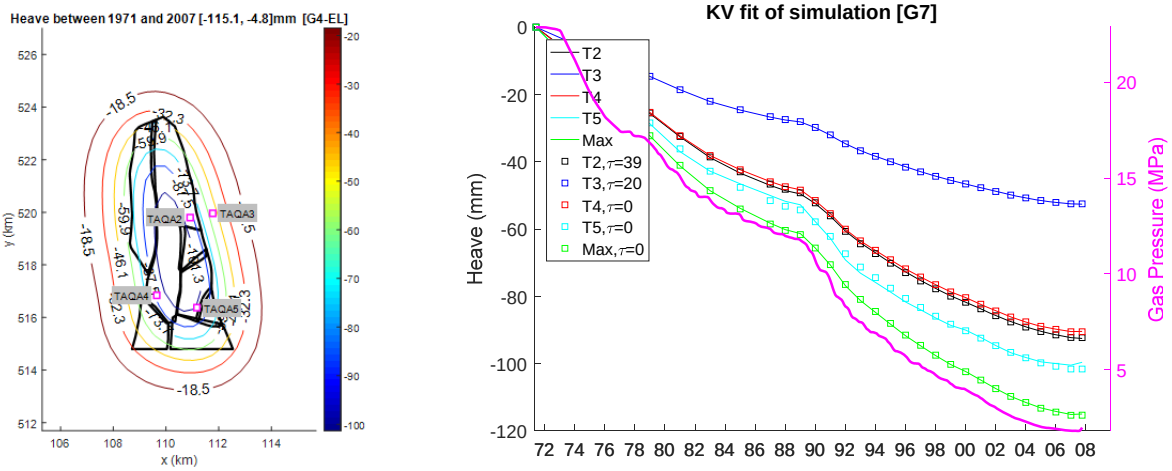

Figure 37: Subsidence during depletion. (Left) subsidence contours and (right) subsidence of the 4 GPS stations and the maximum subsidence vs the gas pressure. Squares indicate Kelvin-Voigt fit of the subsidence for each station. τ indicates the corresponding relaxation time

The stiffer response in the GPS and Geodetic data during refill and storage resulted in an increase of the compaction modulus by a factor 2.5. The time delay in the GPS surface heave, that is absent in the elastic response, was matched by adding Kelvin-Voigt viscoelasticity with a relaxation time of 69 days. This is

weighted average relaxation time of the 4 stations. Station 2 and 5 get double the weight of station 3 and 4, because of location and more reliable Geodetic data.
The simulated heave in each station shows a clear delayed response with respect to the pressure change (Figure 38). The simulation predicts a maximum surface heave of 11mm for an increase in Bulk Volume averaged pressure of 66 bar, between April 2014 and December 2016.
Comparison of the FEM simulation to the GPS response shows that the simulation predicts the same order of magnitude for the heave in the stations (Figure 39 and Table 6). The delay in the response heave is captured, but the FEM simulation overestimates the delay in the Southern station (TAQA-4 and TAQA-5) while it underestimates the delay in the Northern stations (TAQA-2, TAQA-3). The mismatch in the response of the individual stations might be explained by a shift in the heave dome. In view of the small number of observation stations and their position relative to the maximum heave no attempts were made to shift the heave dome.
Table 7 shows that the simulated heave in TAQA-2 and TAQA-5 is very close to the Geodetic measurement. The Geodetic measurement of station 4 is in contradiction with the GPS observations and the Geodetic measurements of station TAQA-2 and TAQA-5 and is therefore omitted.

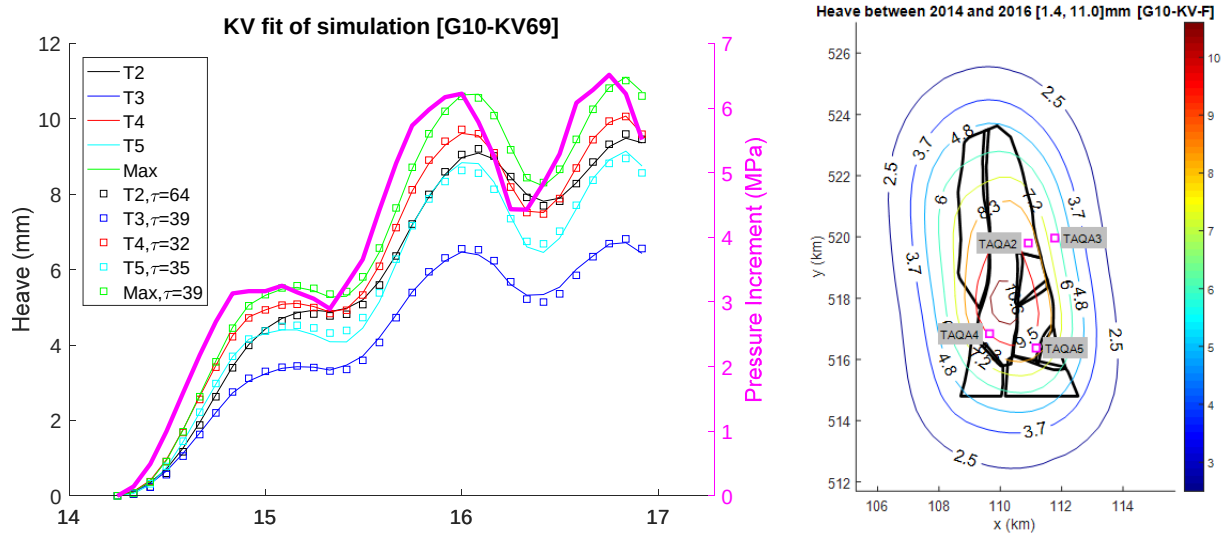

Figure 38: (left) Kelvin-Voigt fit (squares) of the response by inelastic FEM simulation (solid lines) vs the increment in bulk volume average pressure. The relaxation time for each of the stations is shown. (right) simulated heave increment by the non-elastic simulation over the period Apr/2014-Dec/2016

Table 6: Comparison of simulated heave to observed GPS in the period April/2014 to Dec/2016.

GPS	Weighting Factor	Observed Heave	Simulated Heave	Deviation Heave	Observed Relaxation Time	Simulated Relaxation Time	Deviation Relaxation Time
		(mm)	(mm)	(mm)	(days)	(days)	(days)
T2	2	10.5	9.5	-1.0	67	64	-3
T3	1	4.0	6.7	2.7	253	39	-213
T4	1	5.5	10.1	4.6	16	32	16
T5	2	7.3	9.1	1.8	8	35	26
Average		6.8	8.9	2.0	86	43	-43
Weighted average		7.5	9	1.5	69	45	-24

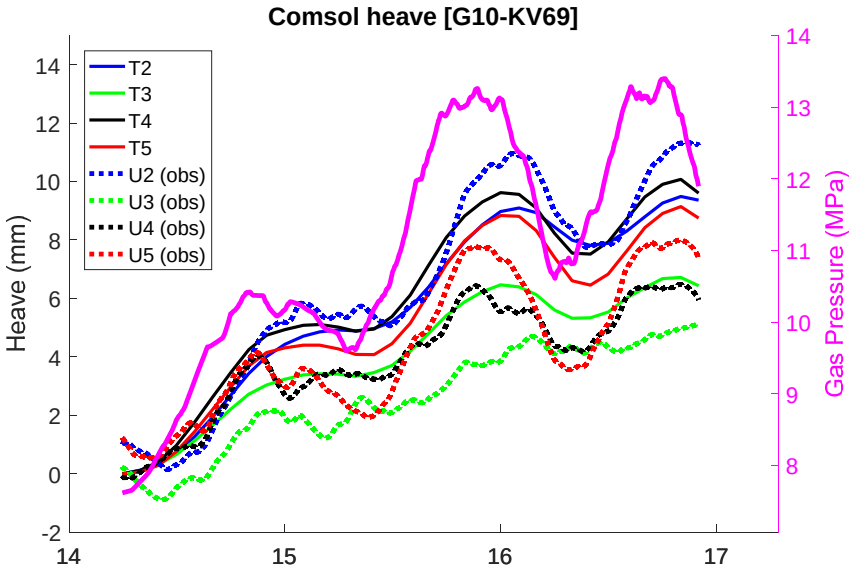

Figure 39: Comparison of the simulated heave (T2-T5) to the heave observed by the GPS signal (U2-U5). Right axis shows the gas pressure

Table 7: Comparison of simulated heave to Geodetic measurements in the period 2011-2016. (Geodetic measurement of station 4 is not considered realistic)

Geodetic	Observed Heave	Simulated Heave	Deviation
	(mm)	(mm)	(mm)
T2	15.2	14.2	-1.0
T3		10.1	
T4	4.2	15.1	10.9
T5	14.5	14.6	0.1
Max		17.2	

Calibrated Initial stress

Table 1 lists the average formation stresses, Figure 40-Figure 47 show the virgin conditions. The Virgin vertical stress distribution is close to a uniform increase with depth away from the faults (Figure 40), but shows reduced stresses and gradients close the West and East fault that result from heterogeneities in the stress initialization and formation densities. Heterogeneities in rock properties and stress initialization introduce stress rotations and stress discontinuity close to faults and domain transitions. Gradients are about 22-23kPa/m away from the Faults, while they vary in between 20-25kPa/m close to the Faults (Figure 40).
The minimum horizontal stress gradient is about 15-16kPa/m except in the Anhydrite/Carbonate formation (+/-21kPa/m) where it is at 90% of the vertical stress gradient and in the Salt layer (Figure 41) where it is close to the vertical stress gradient (+/-23kPa/m). This gives minimum horizontal over vertical stress ratio's in between 0.65-0.7 in the model (Figure 43), except for the salt layers that are calibrated to unity and in the Anhydrite/Carbonate that is calibrated at a ratio of 0.9.
Maximum horizontal over vertical stress ratio is calibrated at 0.9 except in the Salt where stresses are isotropic (Figure 43), resulting in maximum horizontal stress gradient of about 21kPa/m (Figure 42).

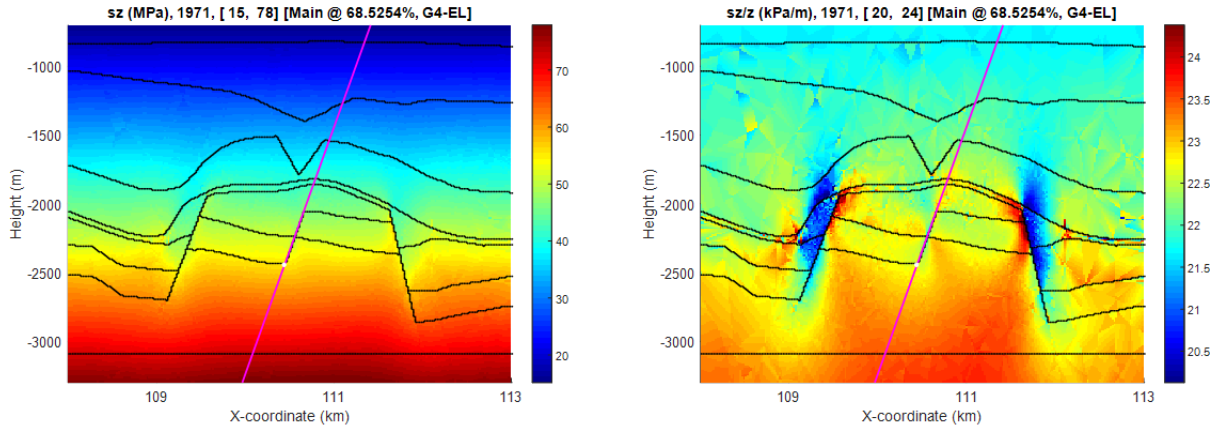

Figure 40: (Left) Initial vertical stress and (right) initial vertical stress gradient. Pink line is line parallel to the midfield fault.

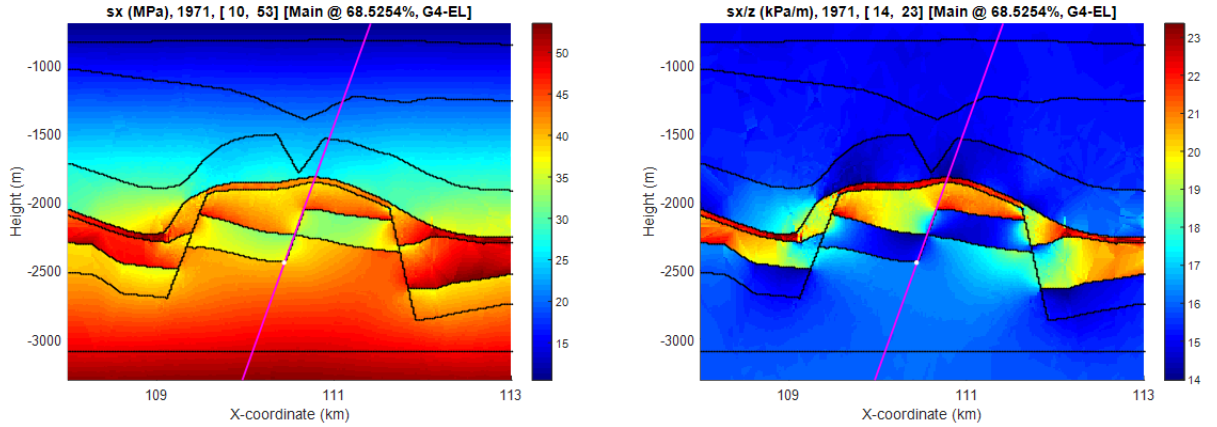

Figure 41: (Left) Initial minimum horizontal stress and (right) initial minimum horizontal stress gradient. Pink line is line parallel to the midfield fault.

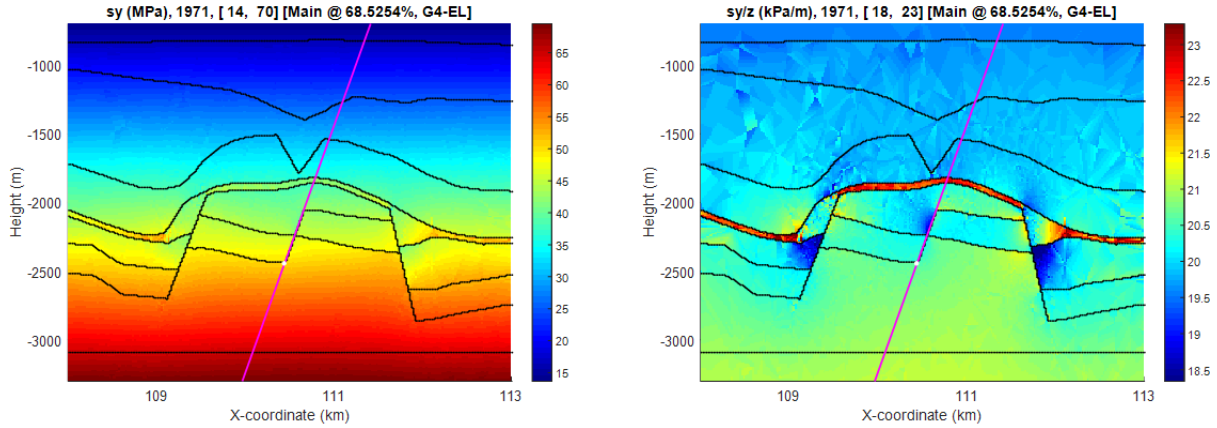

Figure 42: (left) Initial maximum horizontal stress and (right) initial maximum horizontal stress gradient

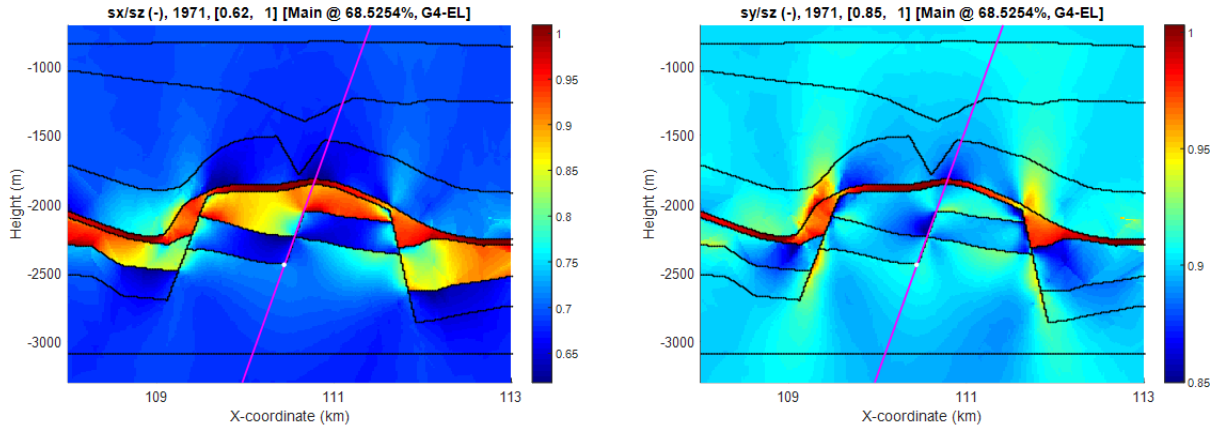

Figure 43: (Left) Initial minimum horizontal over vertical stress ratio (right) initial maximum horizontal over vertical stress gradient.

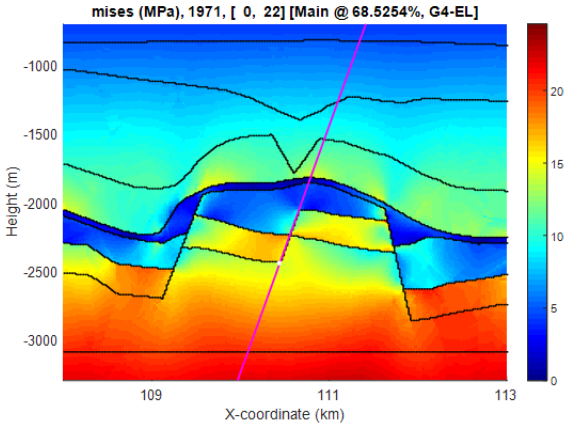

Figure 44: Initial Von-Mises stresses.

Von Mises stresses that quantify the magnitude of the deviatoric stress and indicate how far stresses deviate from isotropy are low in the Salt layer (Figure 44).
For the location indicated in Figure 45, Figure 46 and Figure 47 show pressure and stress profiles as function of the depth. Virgin pressure gradient is in between 10 and 11kPa/m. Average minimum stress gradient in between [-2140m, -2040m] in domain 1M is 15kPa/m at Virgin conditions and 7.6kPa/m in the depleted state 2007 (Figure 46).

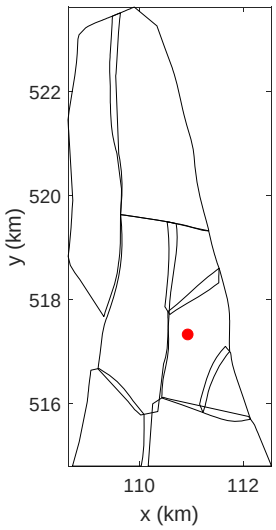

Figure 45: Location for the vertical log line used in Figure 46-Figure 47

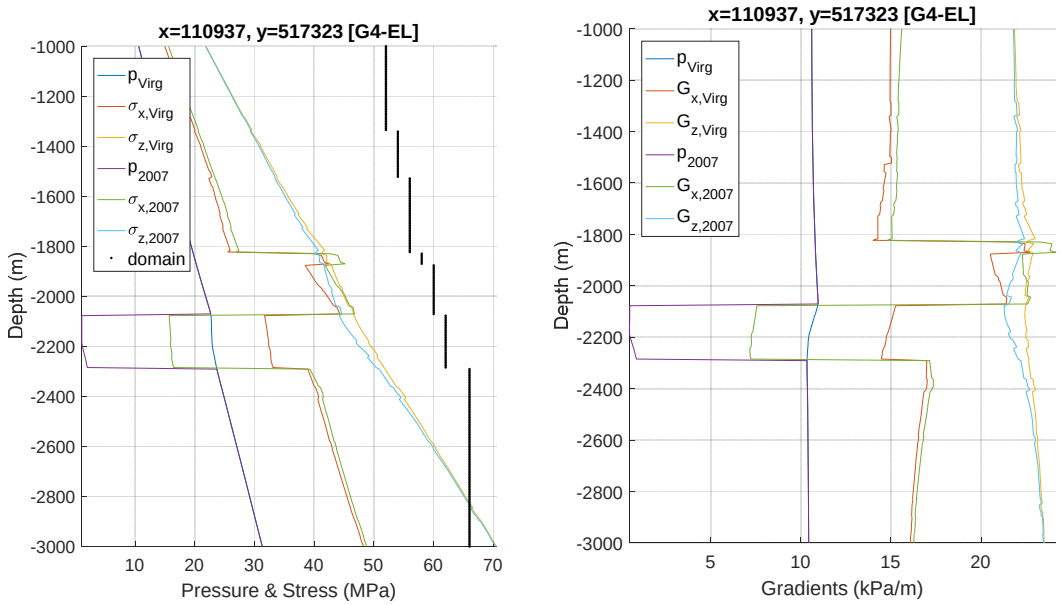

Figure 46: (Left) Pressure and stress and (right) pressure and stress gradient as function vs depth for the location shown in Figure 45.

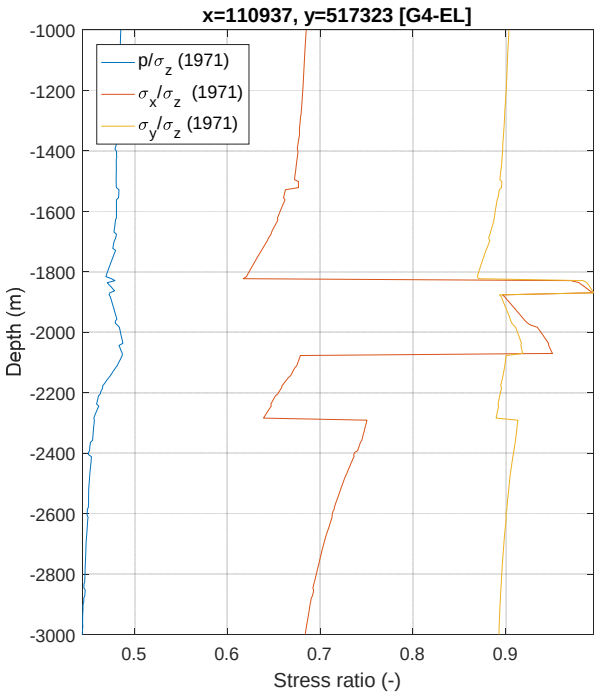

Figure 47: Pressure and stress ratio over the depth for the location shown in Figure 45.

Depletion phase Simulation

The pressure history is plotted in Figure 48 with discrete points at which the Eclipse simulation output was sampled. For an elastic model (and without salt creep) there is no time dependence, so the stress simulation consists of a succession of stationary steps with the pressure applied as external stress.
The elastic stress forms the basis of all further work and can tell whether some unexpected observations of micro-seismicity can just be explained with an elastic model. For instance, the refill seismicity occurred while the pressure difference on the Midfield fault was running quite high which might cause criticality of the fault.

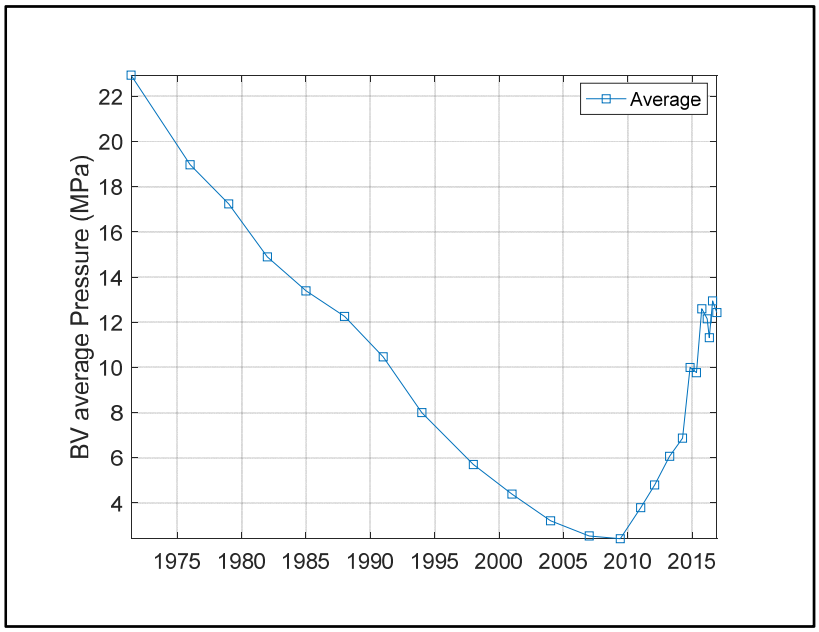

Figure 48: Average gas pressure evolution used for the elastic simulation.

Midfield Fault

Figure 49 shows the critical stress ratio (shear stress/effective normal stress) along the Midfield fault, on both sides of the fault plane. At the fault plane there is a discontinuity in stress since the pore pressure is discontinuous as are the rock properties. Although the FEM ensures equilibrium, there will be stress discontinuities due to material property contrast as well as numerical errors. So, the stress was computed on both sides of the fault plane at a small distance from the plane as well as the pressure which may have large differentials across the fault.
Figure 50 is the same plot, but in this case the pressure was averaged over the fault plane. In previous studies the average pressure was used, since it appeared to provide an explanation of seismicity that was consistent with standard values for the friction coefficient. It appeared that it is also easier to match the observed refill seismicity using average pressure, see the section in this chapter on the refill and storage cycles. So, in the remainder of the simulations, the average pressure will be used.
The pore pressure in the fault zone is unknown, so it is justified to treat this as a matching parameter. For the Midfield fault, it is justified to use average pressure where reservoir sands connect. However, at the East fault, the reservoir is bounded by non-reservoir layers. It is known from seismological research that damage zones at fault zones are about 1% of fault length, so the thickness should be about 10 m, and a core sliding zone of 10-20 cm. Even with permeability as low as 1 microD such a fault zone should be quickly depleted. That implies that taking average pressure is an upper limit of the actual pressure. It turned out the using minimum pressure for the East fault made only a minor difference since the critical area is partially below the reservoir so that pore pressure is determined by non-reservoir rock layers that do not deplete with the reservoir.

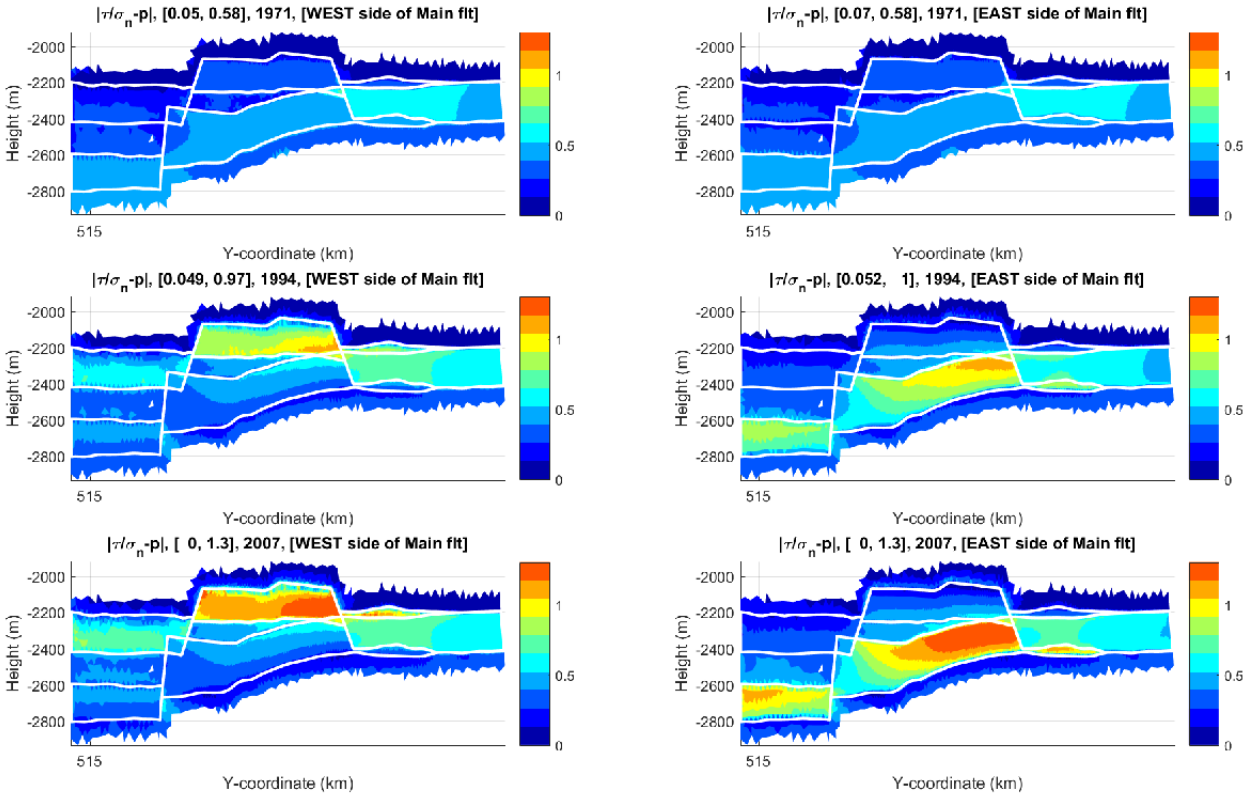

Figure 49: Critical stress ratio on both sides of the Midfield fault at different times. In the header of each plot, critical stress ratio, fault side, the year, minimum and maximum value, the fault name (Main is Midfield) and the simulation ID is shown.

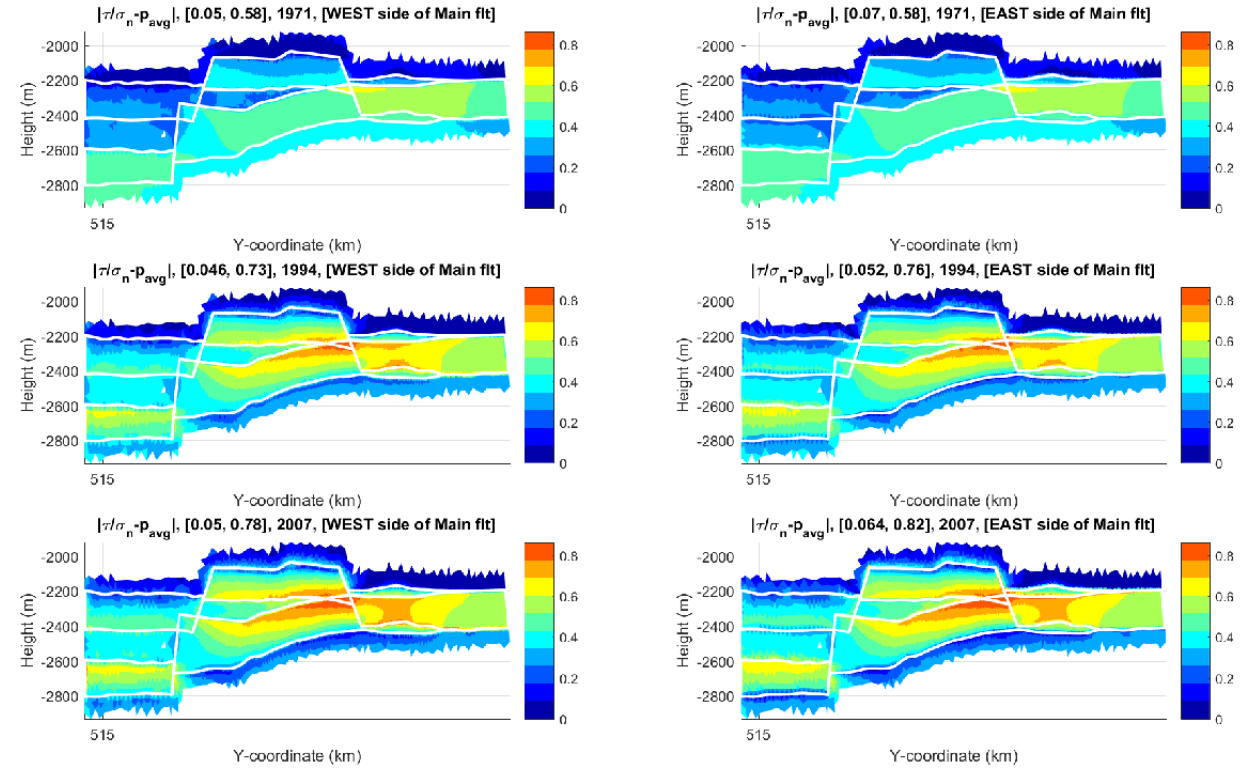

Figure 50: Critical stress ratio on both sides of the Midfield fault at different times, using averaged pore pressure in the fault. In the header of each plot, critical stress ratio, minimum and maximum value, the year, and the side of the fault (Main refers to midfield)

On the Midfield fault, there is clearly a large difference between the critical stress ratio for extreme pressure (either virgin or depleted) with the stress ratio for average pressure. Taking average pressure will yield a much lower estimate of critical stress ratio.
In Figure 50, we see a stress concentration near the scissor point where the sands get separated by the fault throw. This is due to superposition of the differential compaction effect from both reservoir blocks. However, the stress concentration only becomes visible when using the averaged fault zone pressure. The full picture of the stress concentration in a cross-section through the fault at the scissor point is shown in Figure 51 and in a cross-section through the fault where the main Fault intersects with Fault 1A-1B in Figure 52. The largest change in critical stress is seen at the non-reservoir side of the fault, because of the high pore pressure that gets close to the stress, so that effective stress becomes very small.

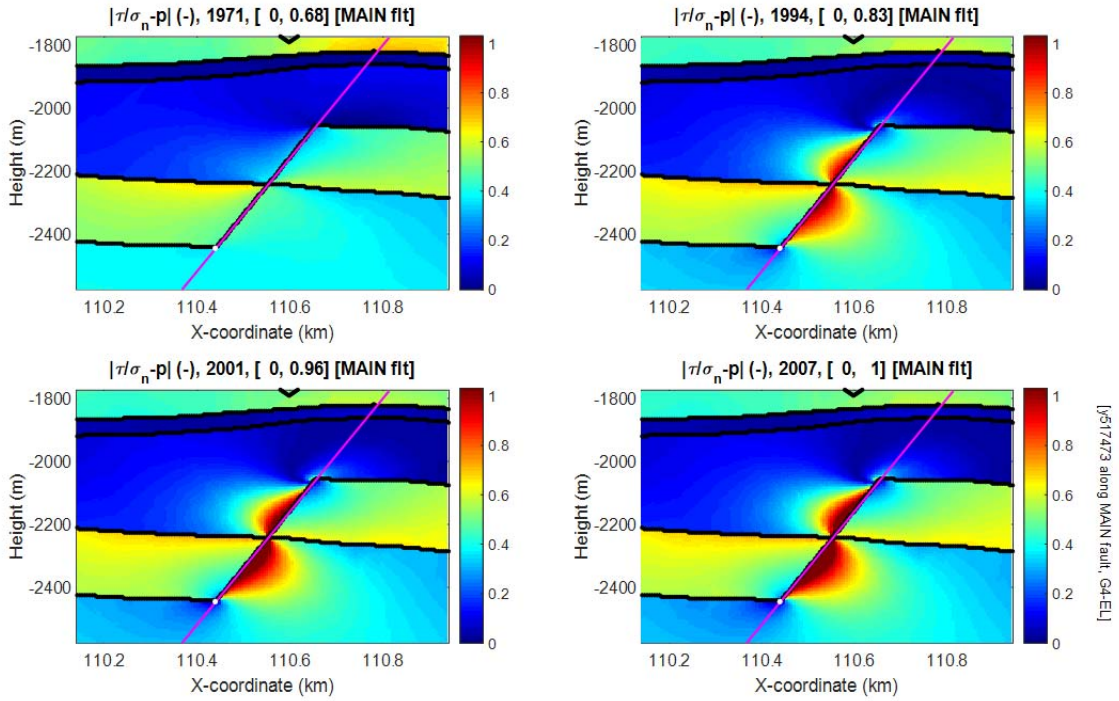

Figure 51: Critical stress ratio in a cross-section through the Midfield fault at different times, using local pressure. In the header of each plot, critical stress ratio, the year, minimum and maximum value and the fault name. Main refers to the midfield fault.

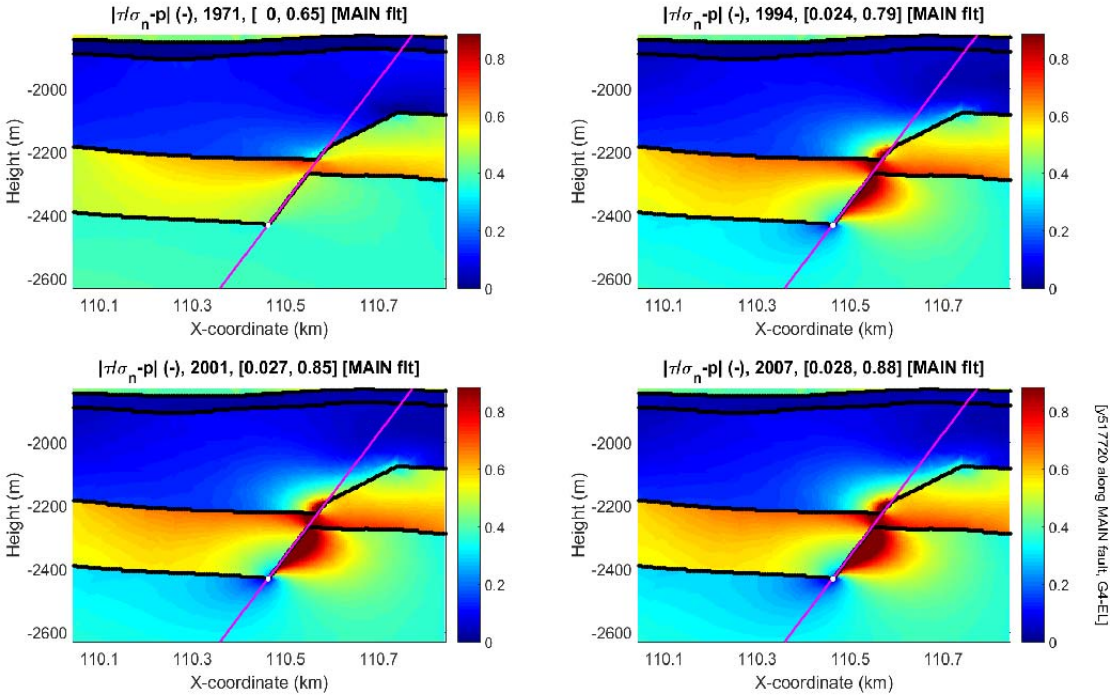

Figure 52: Critical stress ratio in a cross-section through the Midfield fault at different times, using local pressure. In the header of each plot, critical stress ratio, the year, minimum and maximum value and the fault name. Main refers to the midfield fault.

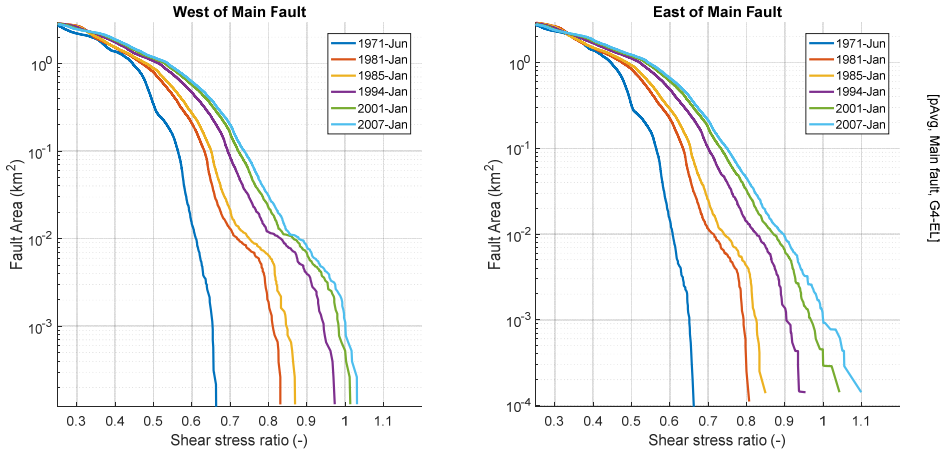

Figure 53: Cumulative fault area vs. critical stress ratio, using average pressure. On both sides of the fault the critical stress increases strongly with depletion. Main refers to the midfield fault.

The next step is to determine the area of the fault above a certain threshold friction coefficient. It is known from seismology that large earthquakes can only occur if a contiguous area of the fault zone becomes critically stressed. Moreover, detailed studies have shown that slip is confined to such a high stress area (Baisch, 2006, 2009, 2010). So, one of the objectives of stress analysis is to determine the maximum size of such stressed regions. Figure 53 shows plots of cumulative area vs. the stress ratio on that area. It shows that for a given threshold friction coefficient the shear area increases over time.

Shear area can be correlated with earthquake magnitude, as shown in Figure 3; such plots can be used to predict the friction coefficient vs. the gas pressure for a range of earthquake magnitudes. Since the total seismic moment associated with the depletion Earthquakes will significantly affect the state of the shear stress at the start of the refill, the next section will correct the stress during depletion for the seismic slip of all the depletion Earthquakes. The friction coefficient will be calibrated on the cumulative seismic moment.

Another way to look at the data is to plot the logarithm of the critical shear area vs. reservoir pressure for a given level of the threshold friction coefficient, see Figure 54. This is an indicator for the criticality. This plot shows that the potential increase in log critical area is quite small, which is qualitatively in agreement with observed earthquake magnitude in Bergermeer as well as other Dutch gas fields. In Bergermeer the later earthquakes had a magnitude of 3.5, so only just above the first earthquakes of magnitude 3.

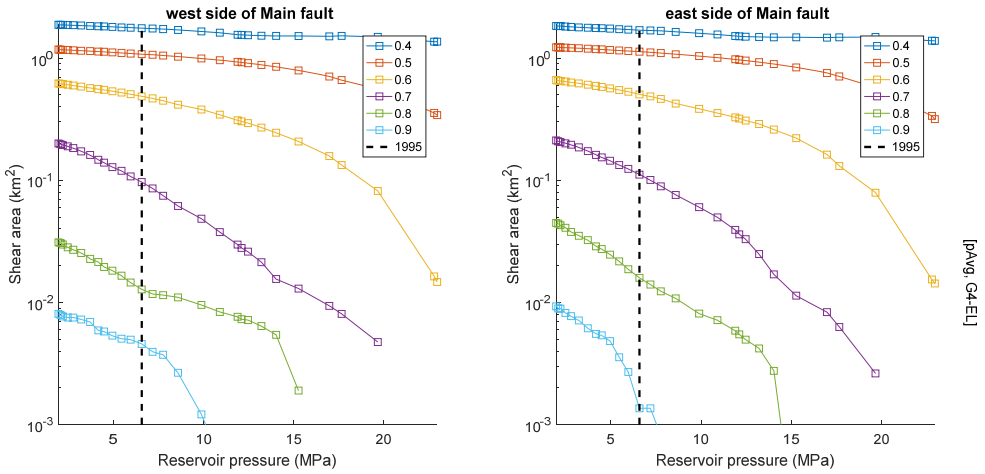

Figure 54: Shear area vs. reservoir pressure at the Midfield fault, for different levels of threshold friction coefficient. The pore pressure in the fault zone was averaged between both sides. Main refers to the midfield fault.

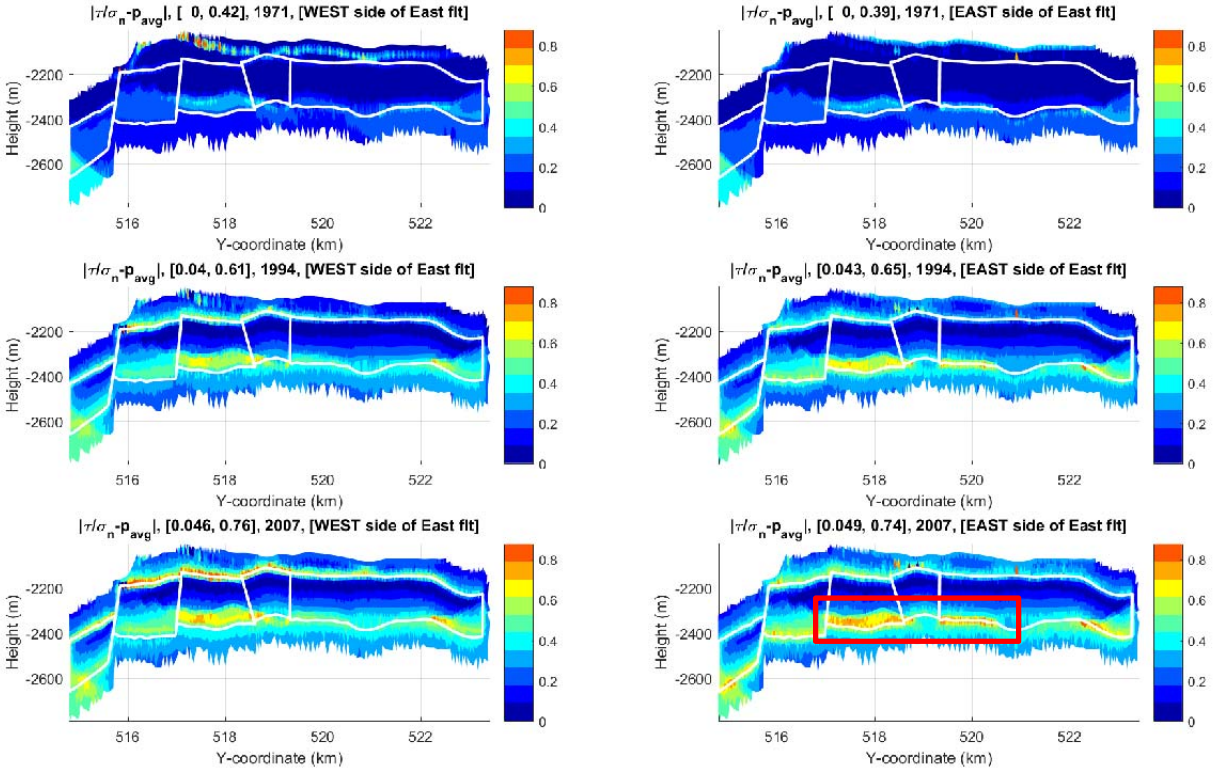

Figure 55: Critical stress ratio on both sides of the East fault at different times, using averaged pore pressure in the fault. The red rectangle indicates the window for the determination of shear area. It concerns a single connected area of elevated shear stress ratio. Since large events can only be induced on a contiguous area, we can exclude smaller unconnected stressed regions. In the header of each plot, critical stress ratio, minimum and maximum value, the year, and the side of the fault

East Fault

The critical stress ratio on the Eastern fault is plotted in Figure 55. The average pore pressure will also be used for this and other faults, even though the non-reservoir side is a seal. Another difference between the Midfield and Eastern fault is the presence of the Zechstein salt layer with high horizontal stress. The much higher stress in the salt has a dominant influence on the critical stress ratio which remains quite low. The computed stress at the East fault shows a noisier pattern, but we can see a band of higher stress ratio opposite the Anhydrite/Carbonate layers below the salt. There are also some high stress elements above the reservoir, but those are ignored since it appears to be an artefact from the salt layer. Figure 56 shows a cross-section through the East fault with the stress concentrations near the top and bottom of the reservoir.

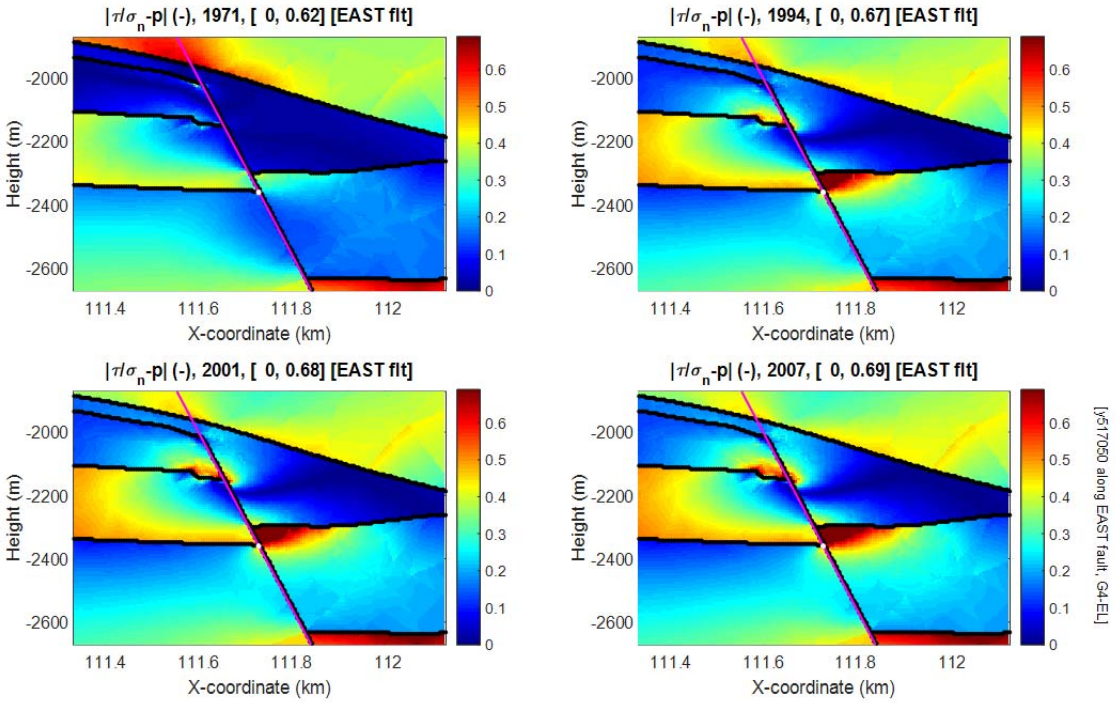

Figure 56: Critical stress ratio in a cross-section through the East fault at different times, using local pressure. In the header of each plot, critical stress ratio, the year, minimum and maximum value and the fault name.

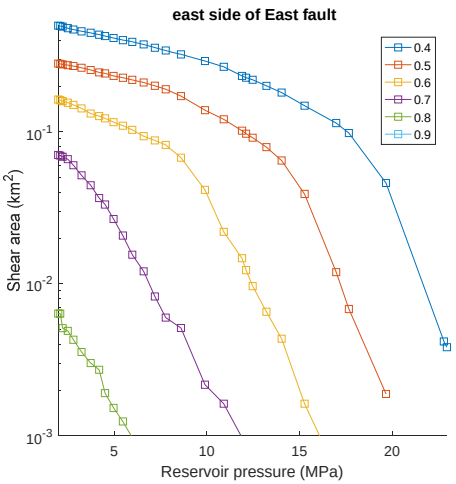

Figure 57: Critical area vs. reservoir pressure at the East fault, for different levels of threshold friction coefficient. The pore pressure in the fault zone was averaged between both sides.

Figure 57 shows the evolution of the shear area for a given threshold friction coefficient. The shear area increases with decreasing pressure and is larger for lower threshold friction coefficient. Compared to the midfield fault considerable smaller area get critically stressed for the same friction coefficient and pressure.
No detected seismicity was related to the East fault during depletion. As a worst-case scenario one can assume that the shear stress build up resulting from the compaction was never released. As an alternative one can assume that the east fault has slipped non-seismically or seismically but just below the detection limit (seismicity of magnitude 1.5). The (weak) seismic activity during refill suggests that in the past some activity occurred on this fault.
In the next section the friction coefficient will be calibrated to match the observed micro-seismicity and the absence of depletion seismicity. Both the scenario in which slip is allowed and the worst case scenario in which slip is absent will be considered.

West Fault

Figure 58 shows the shear stress ratio at the West fault at different times, which like the Midfield fault concerns a scissor fault. It shows that a large area of high shear ratio develops over time, where the Western Aquifer (block 4) at the west side and the Reservoir (block 2N) and Northern aquifer (block 3) shows an offset. Figure 59 shows the critical stress ratio at the scissor point which is like the scissor point for the midfield fault (Figure 51). Over time the critical stress ratio increases (Figure 60). Since the West Fault shows more critical behaviour than the Midfield fault while no seismicity has been detected, this implies that the West Fault is non-seismogenic, has strong cohesion, has a high friction coefficient and/or is permeable. Since no micro-seismicity activity was seen during at a later stage either, it is likely that the West fault was never seismically active.

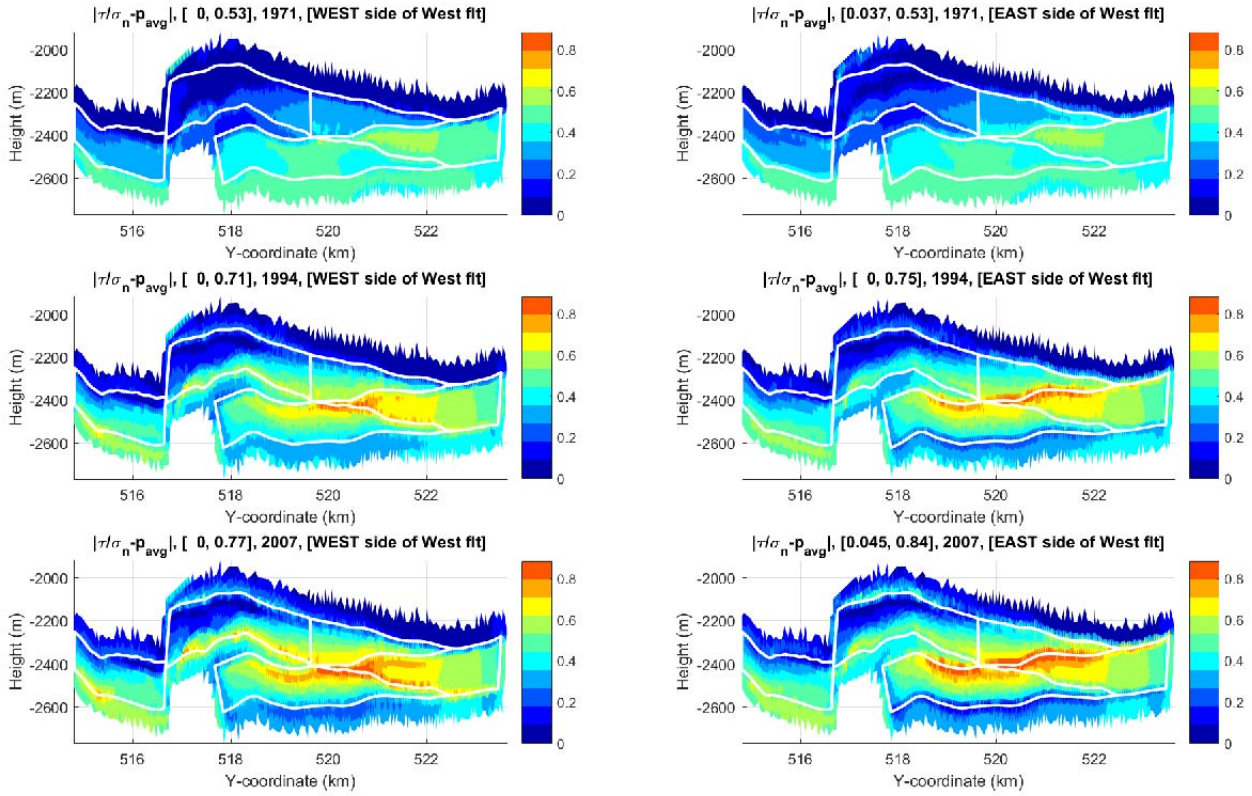

Figure 58: Critical stress ratio on both sides of the West fault at different times, using averaged pore pressure in the fault. In the header of each plot, critical stress ratio, minimum and maximum value, the year, and the side of the fault

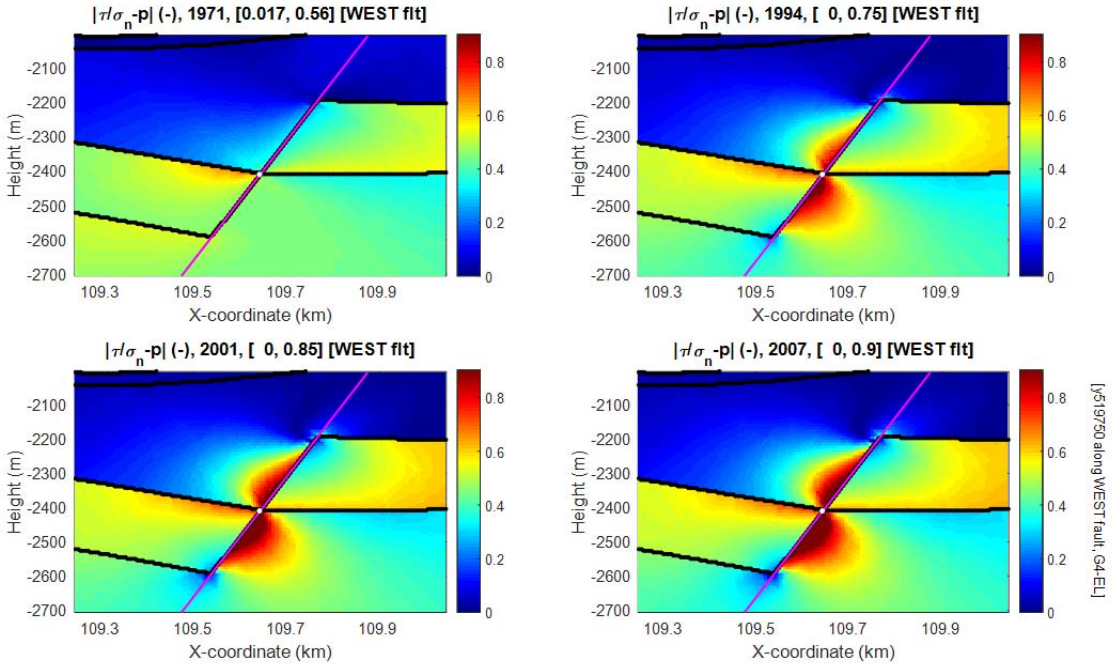

Figure 59: Critical stress ratio in a cross-section through the West fault at different times, using local pressure. The West fault is also a scissor fault; the cross-section is near the separation point of the reservoir and the aquifer on the west.

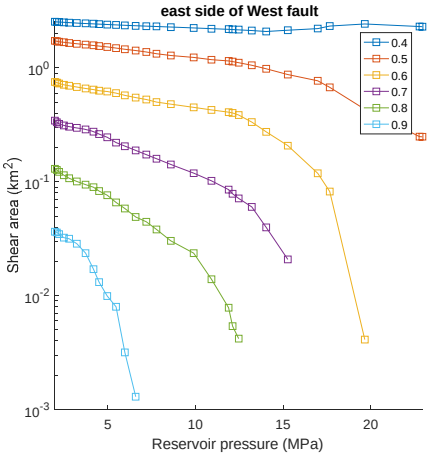

Figure 60: Critical shear area vs. reservoir pressure at the West fault, for different levels of threshold friction coefficient. The pore pressure in the fault zone was averaged between both sides.

Fault 1A-1B

This small fault is connected to the Midfield fault and shows many micro-seismic events during refill. So, it is of interest to investigate the stress on this fault. Figure 61 shows the critical stress ratio on the fault and Figure 62 shows the shear area as function of the gas pressure for low threshold friction coefficients in the range 0.2-0.6. On this fault the critical stress is quite low compared with the large faults that run north-south. So, it is understandable that the shear stress ratio will be much lower. Also, the fault offset is small which mitigates differential compaction. Therefore, it can be concluded that seismic activity is not expected and that the observed activity is likely a secondary effect from the shear strain on the Midfield fault.

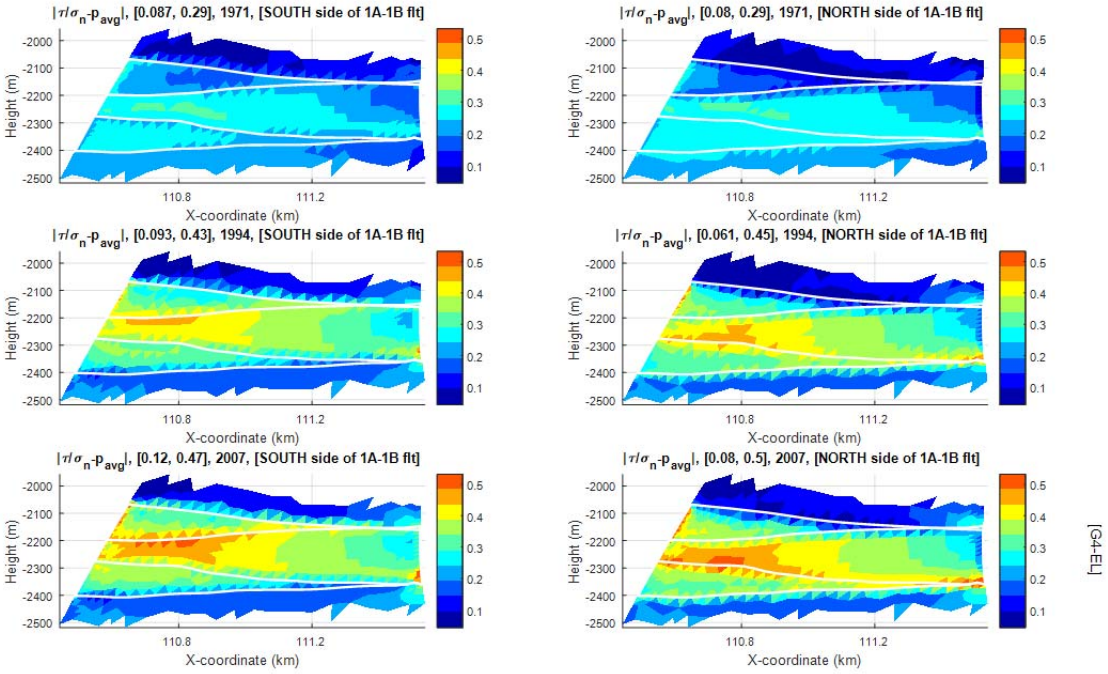

Figure 61: Critical stress ratio based on the average pressure at the 1A-1B fault for the elastic simulation. In the header of each plot, critical stress ratio, minimum and maximum value, the year, and the side of the fault

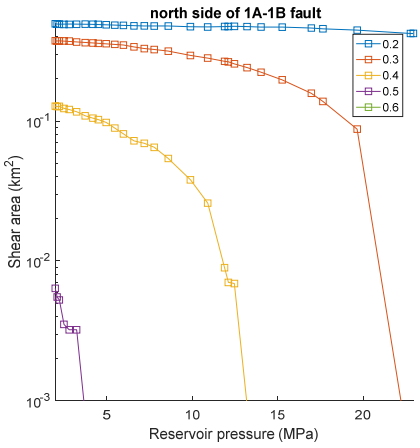

Figure 62: Critical shear area vs. reservoir pressure at the West fault, for different levels of threshold friction coefficient. The pore pressure in the fault zone was averaged between both sides

Effect of Salt Creep

Creep of the Salt layer can be added to the elastic model, to investigate its effect on the stress evolution, especially the time dependence. Salt creep was modelled with the Generalized Maxwell Model that simulates Viscoelastic shear reduction, in analogy to the relaxation of multiple spring-dashpot systems in parallel (see Figure 30, previous section).

It appears that salt creep does not significantly affect the criticality at the Midfield fault (Figure 63) or the West Fault.

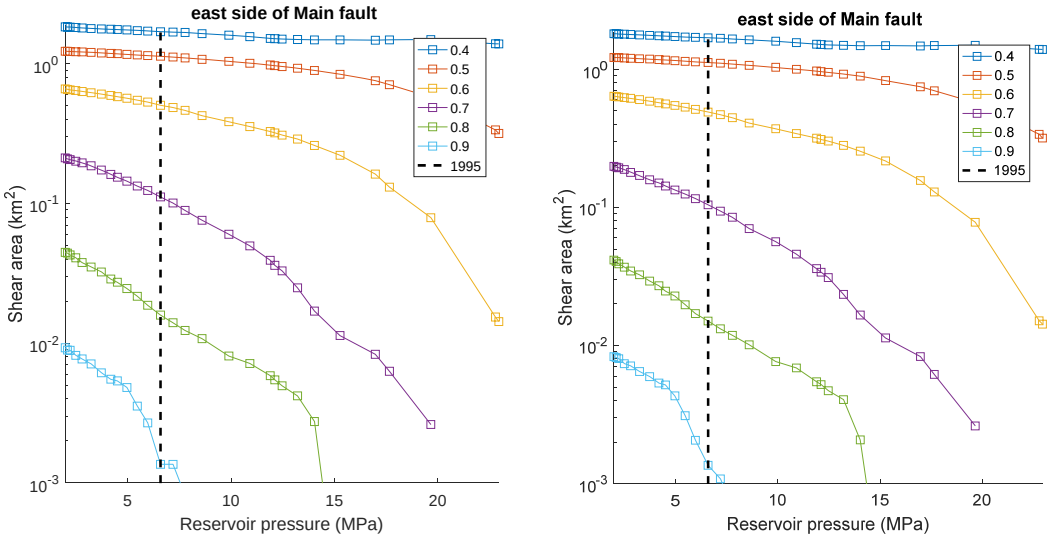

Figure 63: Simulated critical area at the midfield fault for the (left) elastic and (right) salt creep simulation for friction threshold friction coefficient in the range 0.4-0.9

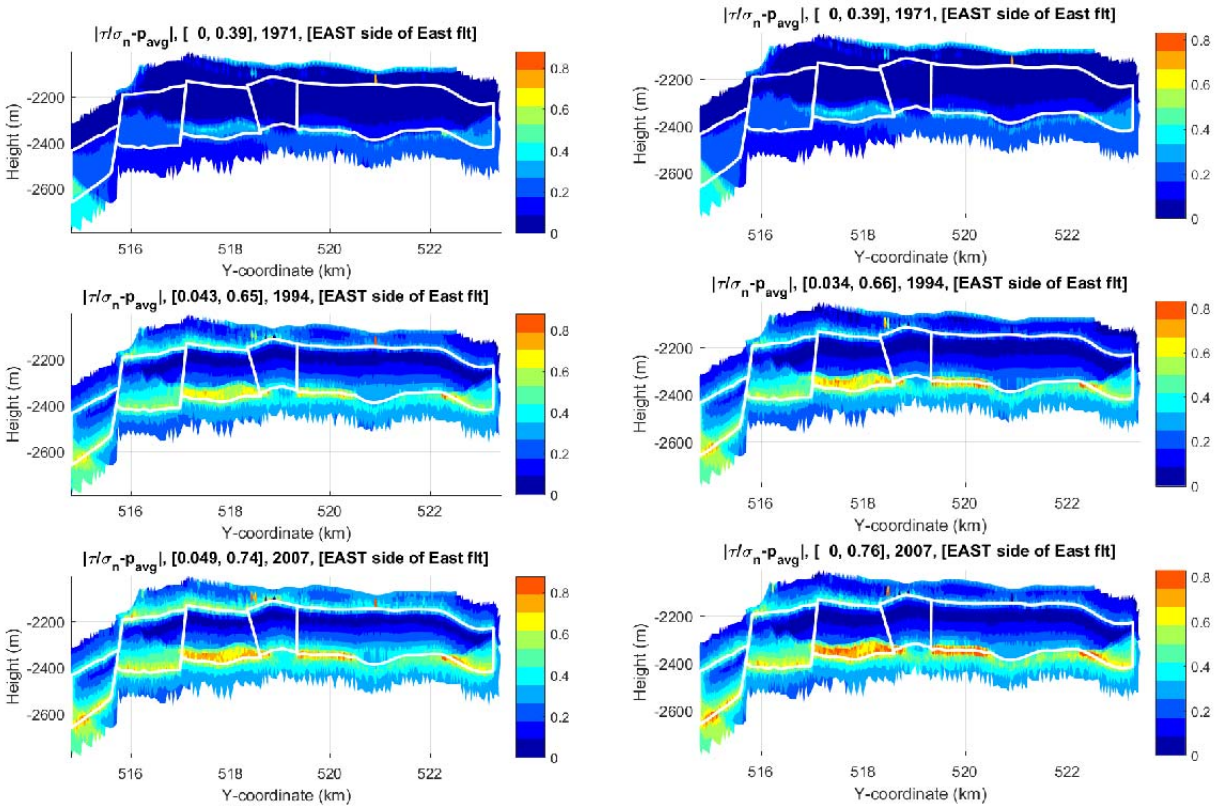

Figure 64: Critical stress ratio based on the average pressure at the East fault for (left) the elastic simulation and right the simulation including salt Creep

For the East fault, salt creep stabilizes the Fault at the reservoir salt interface (Figure 64, Figure 65), because shear stress is reduced and normal stresses increase. At the Reservoir and the Anhydrite/Carbonate interface the number of patches with high shear ratio increases, while the overall criticality stays level. This is reflected in the curves for the critical area (Figure 66), where the curves for low friction coefficients 0.4-0.6 (higher magnitude seismicity) hardly change and the curves for high friction coefficient (lower magnitude seismicity) become more critical. Moreover, since the initial response of salt to a change in pressure is elastic, salt creep cannot explain the increase in seismicity at the onset of injection. Because of this, salt creep will not be taken into account during refill and the storage.

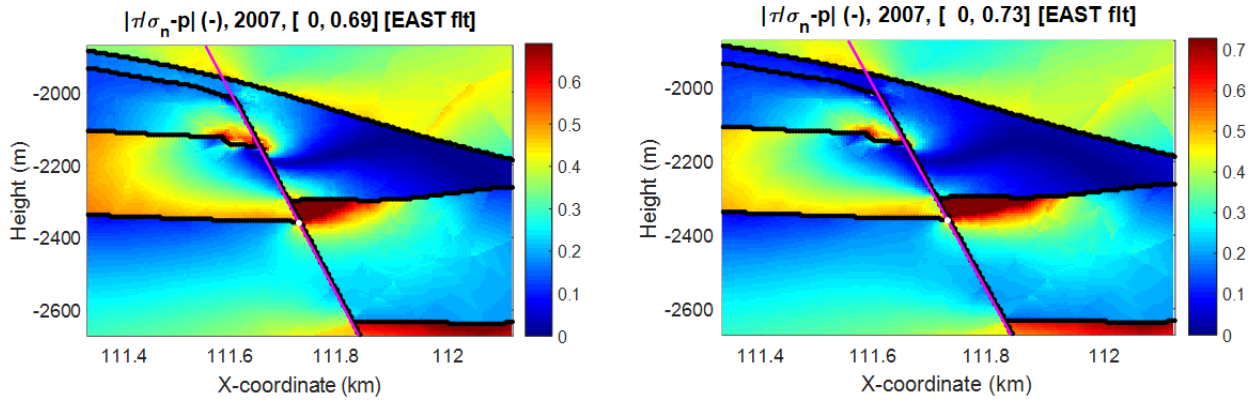

Figure 65: Critical stress ratio for the depleted reservoir (left) Elastic simulation and (right) Simulation including salt creep in a cross section through the east Fault close to intersection of blocks 1M and 1SE.

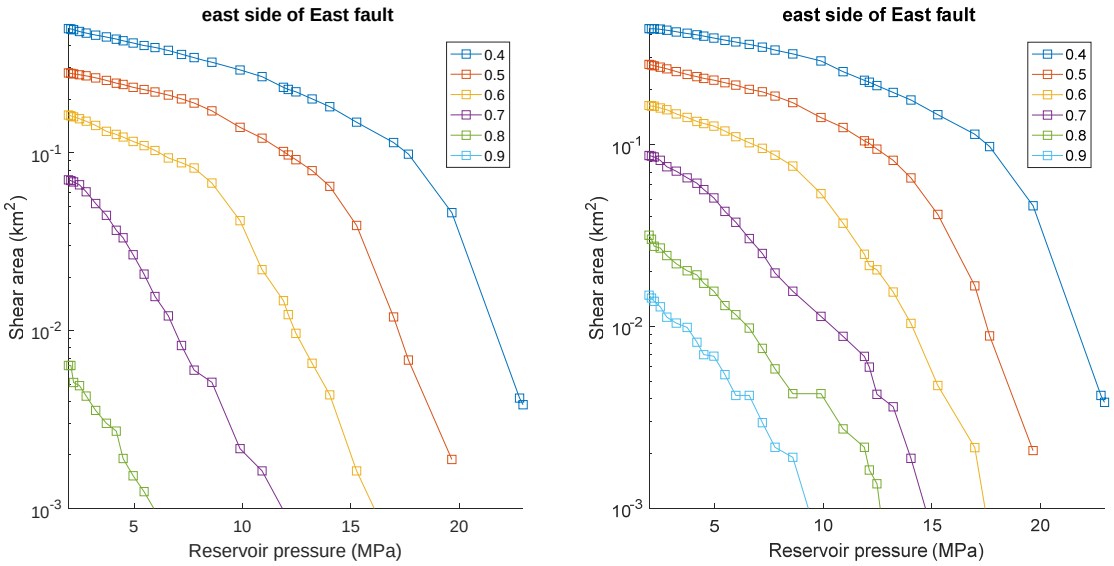

Figure 66: Simulated critical area for the East fault for the (left) elastic simulation and (right) the simulation including salt creep for friction coefficients in the range 0.4-0.9

6 Stress Simulations including slip correction

During depletion four earthquakes exceeding magnitude 3 occurred at the midfield fault (see Table 8). A magnitude 3 event involves a slip area of order $10^5 m^2$, which is a significant fraction of the total fault area that is in contact with the reservoir. The (seismic) slip associated to these four events should be explicitly accounted for, since it will significantly affect the state of the shear stress at the end of depletion and during refill.

This section shows how the shear stress in the centre of a slip area gets reduced by its excess shear, such that the fault stress path stays on the Mohr-Coulomb envelope. Since the correction of the excess shear averages to zero, the periphery of the slip area will see an increase in the shear stress magnitude because of redistribution of the excess shear from the centre. The following sections show how this depletion shear stress change at the periphery affects the critical stress during refill, storage and forecast.

Table 8: Seismic event during depletion, their magnitude (M_w), seismic moment (M_0) and the cumulative seismic moment (ΣM_0)

Date	M_w	M_0	ΣM_0
1994-08-06	3	4.00E+13	4.00E+13
1994-09-21	3.2	7.00E+13	1.10E+14
2001-09-09	3.5	1.90E+14	3.00E+14
2001-09-10	3.1	6.30E+13	3.63E+14

This section starts with the description of the results of a 2D slip model that is calibrated in the same way as the 3D stress model (see previous section). The difference between a 2D simulation including slip and a 2D simulation without slip are used to derive a slip correction for the 3D simulations and a correlation between slip size and shear stress magnitude. The justification is the fact that the shear stresses on the midfield and east fault in the 3D model are predominantly oriented in the dip direction.

With the slip correction in place the friction coefficient for the midfield in 3D model is calibrated on the cumulative seismic moment. The section ends with a study of the fault slip behaviour during refill, storage and forecast cycles for the midfield and east fault.

2D slip modelling results

A 2D steady state slip model was constructed (see Appendix III) at the most critical point at the midfield fault in the 3D model, i.e. the location where block 2N and block 1M make contact (see Figure 67). A steady state slip model was used and preferred over a stick-slip model, because the latter would introduce additional unknown quantities, like a time dependent friction coefficient or time dependent cohesion, for which no calibration data is available. The friction coefficient calibrated in this model is the dynamic friction coefficient that is a lower bound of the friction coefficient which is valid for dynamic slip. The model was calibrated in the same way as the 3D model such that the critical stress ratio of the 2D model is representative for the 3D case. In the 2D model slip is modelled as a continuous process, but such that the cumulative shear moment in 2001 equals the cumulative seismic moments of the depletion Earthquakes.

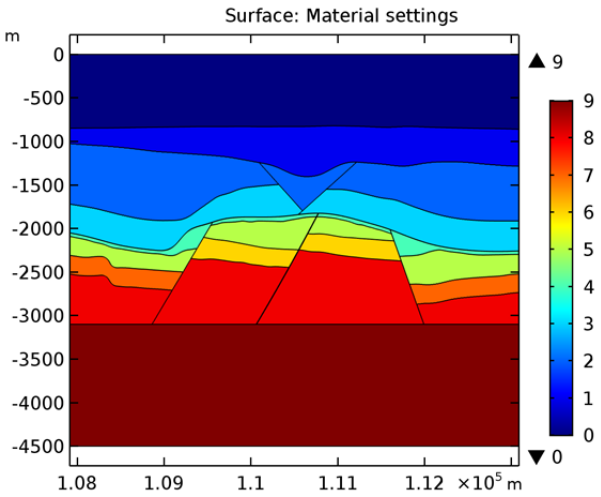

Figure 67: Geology of the 2D model. 2D model is a cross section at the most critical point at the midfield fault of the 3D model.

During depletion the shear stress at the fault increases at a faster rate than the effective normal stress. This causes the critical stress ratio to increase with decreasing pressure. Slip occurs when the Mohr-Coulomb Criterion is exceeded. By definition, slip means that the shear displacements of the two sides of a fault are different. When slip occurs, the shear stress at the centre of the slip area is reduced, such that the Critical Stress Ratio (CSR) does not exceed the MC failure envelop, while the stress at the edge of the slip area increases (Figure 68). The excess shear, being the difference between the shear stress for a simulation with slip and an elastic simulation, is zero when averaged over the height. As a consequence the area over which the fault becomes critical is larger when slip is included, as the comparison with an elastic simulation shows (Figure 68). During slippage, the normal fault stress does not show a significant change and remains the same as in the elastic simulation (Figure 68).

The change in shear stress by slip introduces stress path hysteresis for the points affected by slip (Figure 70), as shown for 8 points along the midfield fault (Figure 69). It also clearly shows how points at the periphery of the slip area (-2162m and -2358m) curves towards the MC failure envelop, because of the increase in shear stress over time. If one also accounts for the stiffer response during refill (Figure 70 right) the MC failure gets even exceeded, because coefficient hysteresis results in lower normal stresses at the rim of the depletion slip area.

To get a measure for the seismic moment in a 2D model, it is assumed that the shear area is proportional to the shear height squared. With this assumption and a friction coefficient of μ=0.65 determined by the 3D model, the cumulative seismic moment was matched in 2001. This gives a simulated cumulative seismic moment in 1995 that is in line with the observed cumulative seismic moment.

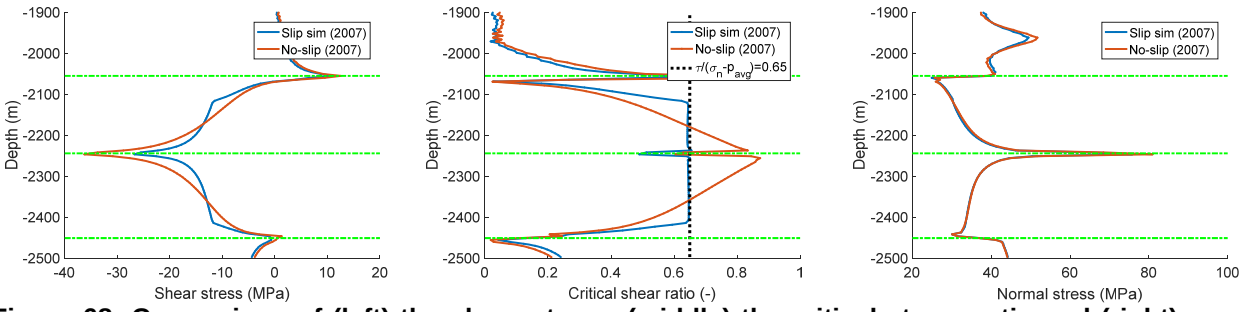

Figure 68: Comparison of (left) the shear stress, (middle) the critical stress ratio and (right) normal stress between a slip simulation with friction coefficient of 0.65 and elastic simulation without slip at the end of depletion 2007

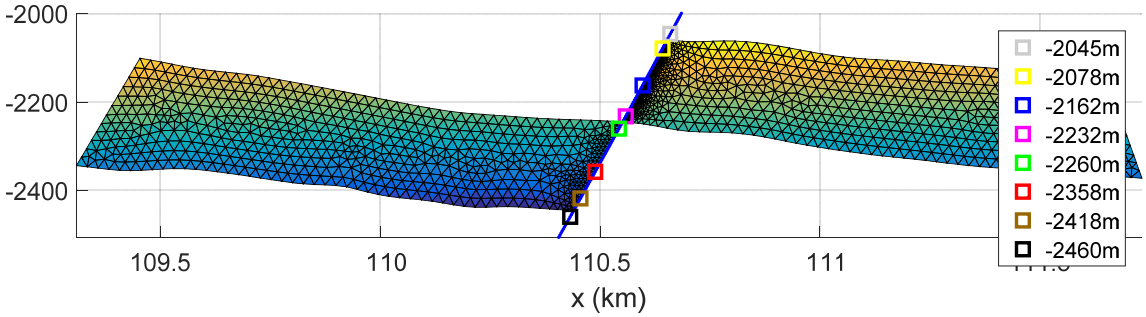

Figure 69: Selection of points along the midfield fault and the reservoir blocks adjacent to the midfield fault

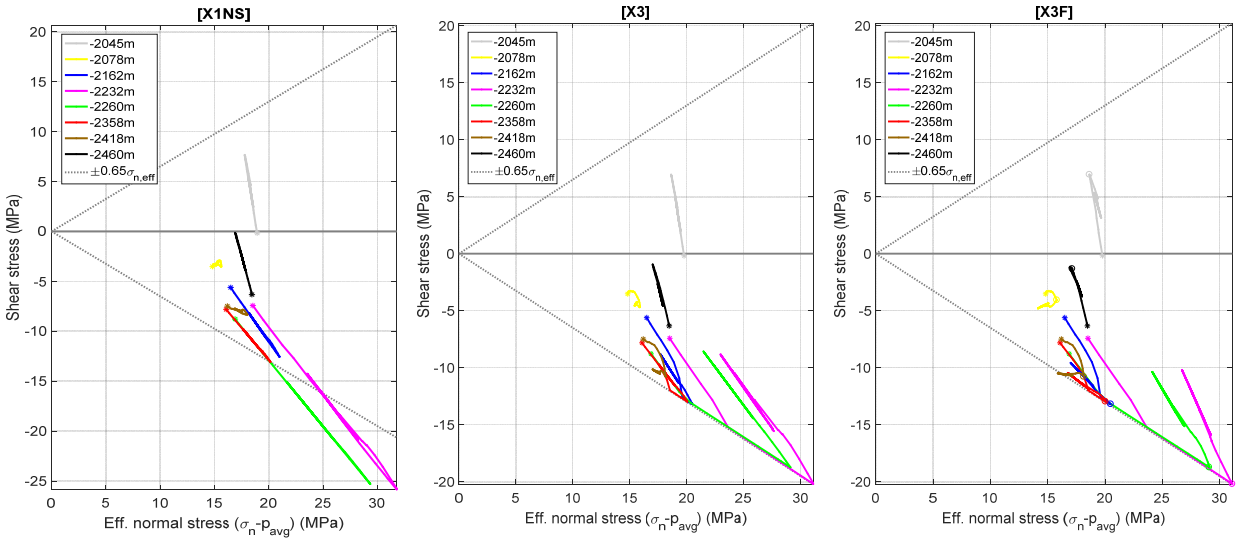

Figure 70: Mohr-Coulomb diagram for (left) full elastic simulation (middle) simulation including slip and (right) simulation that accounts for stiffer response during refill and includes slip during depletion. Simulation includes depletion, refill and storage. Location of the points is shown in Figure 116. Asterisks indicate the virgin situation. Friction coefficient used is 0.65

Conclusions for the 2D slip model

- Slip introduces stress path hysteresis at the fault.
- Slip does only affect the shear stress. The normal fault stress is not affected significantly.
- Depletion slip gives a shear stress change $\Delta\tau_{dep,slip}$ that affects the refill and storage. This $\Delta\tau_{dep,slip}$ reduces the magnitude of the shear stress in the centre of the slip area and increases the magnitude at the periphery of the slip area (compared to the elastic simulation).
- Calibrating the 2D model on the observed cumulative seismic moment in 2001, gives cumulative seismic moments in 1995 that are in line with the observed cumulative seismic moments.
- Simulations including slip give a larger critical area when compared to simulation without slip. This is caused by redistribution of excess shear stress resulting from slippage in which the shear stress is reduced in the centre of a slip area and elevated at the edges.
    - The average shear stress correction is zero.
- An elastic simulation including slip during depletion does not show criticality from refill onwards. However, criticality gets very close to the MC envelop at the periphery of the depletion slip area. The centre of the depletion slip area stabilizes.
- For a simulation that accounts for the increase in stiffness during refill and storage and has a flat stress path in the middle of the reservoir, refill and storage cycles show a slight increase in criticality at the periphery of the depletion slip area. This occurs at high fluid pressures and is

caused by the shear stress increment by depletion slip and a reduction in the normal stress by coefficient hysteresis.

Slip Modelling in 3D

The effect of a shear fracture is added to the stress computed with the three-dimensional model, as based on the 2D simulations and theoretical solutions for shear fractures (Westmann, 1965). Theory shows that only the shear stress changes on the fracture plane and not the normal stress, as can be expected from symmetry. The 2D simulations show that the effect of slip is not only a reduction in shear stress over the area that has critical stress ratio larger than the friction coefficient, but also an extension of the slip area beyond that area. The reason is that equilibrium requires that the shear stress is not only reduced in the critical area, but also enhanced outside the critical area so that the total change in shear stress due to the shear fracture is zero. Furthermore, it is known from theoretical solutions for shear fractures (Westmann, 1965; Kassir, Sih, 1966) that outside the slippage interval, the stress change is proportional to the well-known $1/\sqrt{r}$ dependence, where r is the distance from the fracture. For constant slip, the stress would be singular, but with slip falling to zero at the edges of the fracture, the singularity is relieved. So, a small amount is added to the distance from the fracture in order to avoid the singular behaviour. Using these observations, we can develop an estimate of the shear stress change in the 3D model due to slippage derived from the elastic simulation.
Figure 71 shows the interval (of length H) over which the shear stress (red line) exceeds the Mohr-Coulomb (MC) criterion (black line). That interval is extended with the condition that the integral of the shear stress correction is zero. The method was confirmed with the 2D simulation results. Figure 72 shows that the estimated shear stress is quite close to the simulated slip stress.

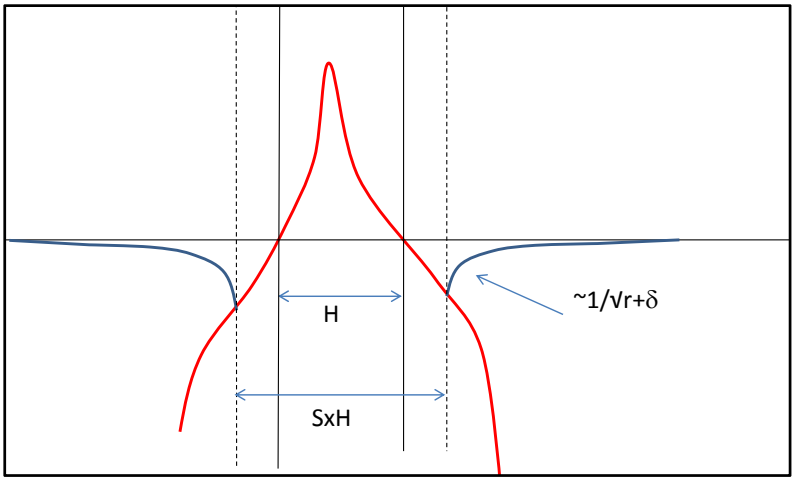

Figure 71: Slip stress is estimated from elastic shear stress exceeding MC criterion. The shear stress is extended using the MC condition and the equilibrium condition requiring the integral over the shear stress being zero. The extent of the sip area is a factor (S) times the height (H) of the zone with elastic stress above the MC envelope. Outside the slip region (SxH) the stress is estimated from the solution for a shear fracture and is proportional to $1/\sqrt{r}$ **.**

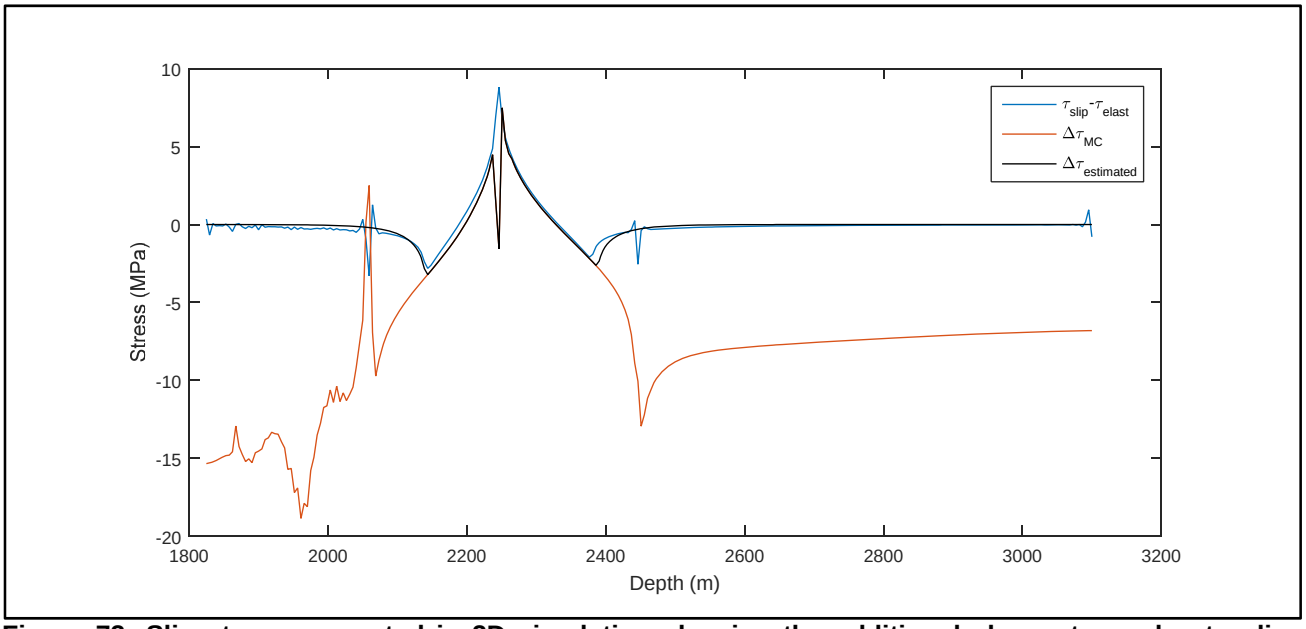

Figure 72: Slip stress computed in 2D simulation showing the additional shear stress due to slip from the simulation ($\tau_{slip} - \tau_{elast}$) as well as the estimated excess shear stress due to slip ($\Delta\tau_{estimated}$), derived from the elastic stress. The discontinuities occur at domain boundaries and are numerical artefacts.

Based on the shear stress correction we also estimate the slip, using the theoretical relations and the 2D simulations. The slip in the 2D simulation is plotted in Figure 73. The average slip is then correlated to the maximum shear stress correction, shown in Figure 74.

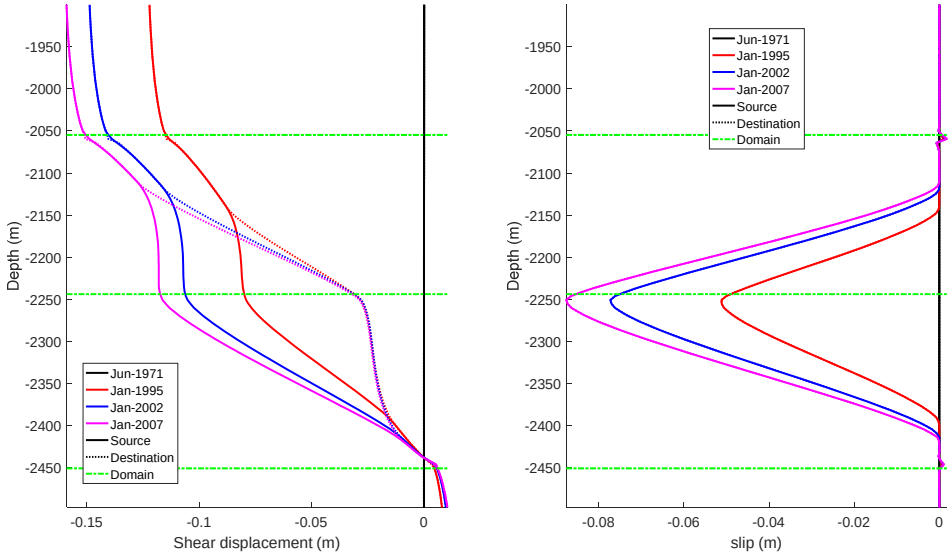

Figure 73: (Left) shear displacement for the source (west) and destination (east) side during depletion showing increased shear dislocation over time (right) Evolution of the fault slip during depletion. The green dashed line indicate the different domains.

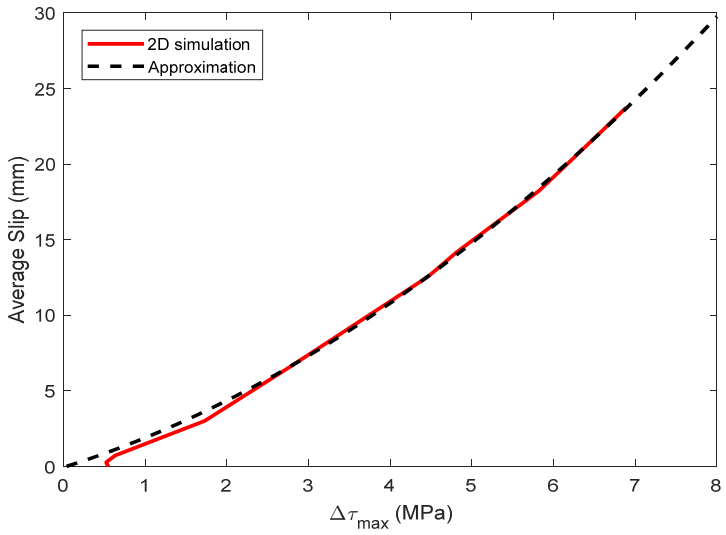

Figure 74: Correlation between average slip and maximum excess shear stress over the slip region in the 2D model. The dashed line is the approximation used for computing the slip in the 3D model.

In the 3D simulations there is both a dip-slip and strike-slip component and the correction is done separately for both components. It turned out that most of the slip was in the dip-slip direction, with only a small strike-slip component. Performing the procedure for the 3D simulations, the results of Figure 76 are derived from the elastic simulation in Figure 75. It is seen that the slip area is enlarged, especially above and below the most critical point; i.e. where the opposite blocks are just separated. That makes sense since the enlargement is proportional to the excess shear stress, which is largest near the most critical point.

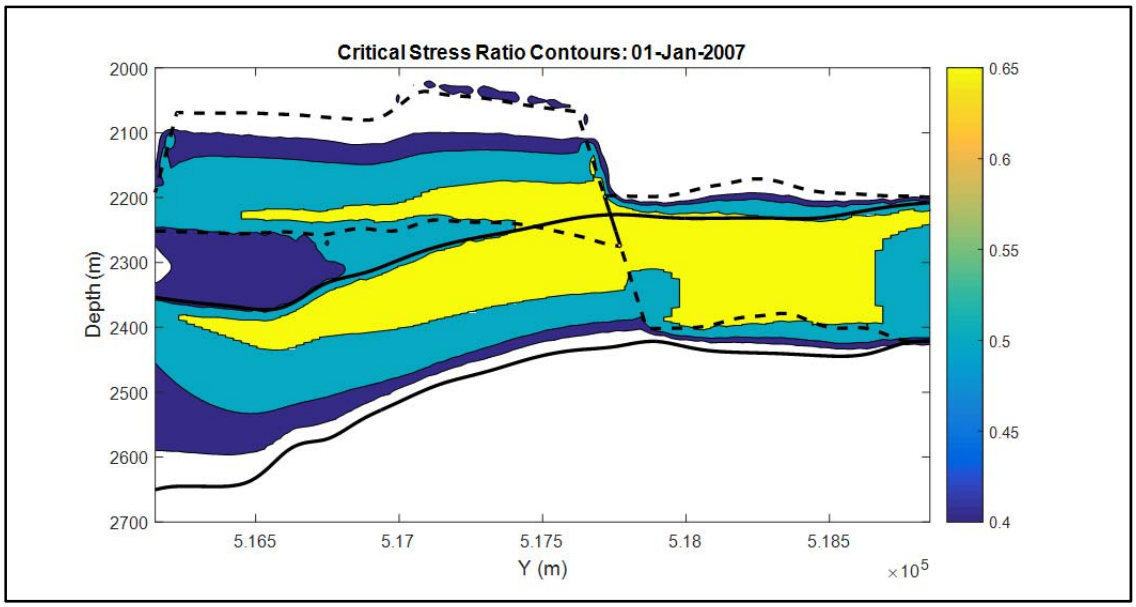

Figure 75: Elastic stress simulation gives a large area reaching a critical stress ratio of 0.65. Values of the critical stress ratio were capped at the critical value.

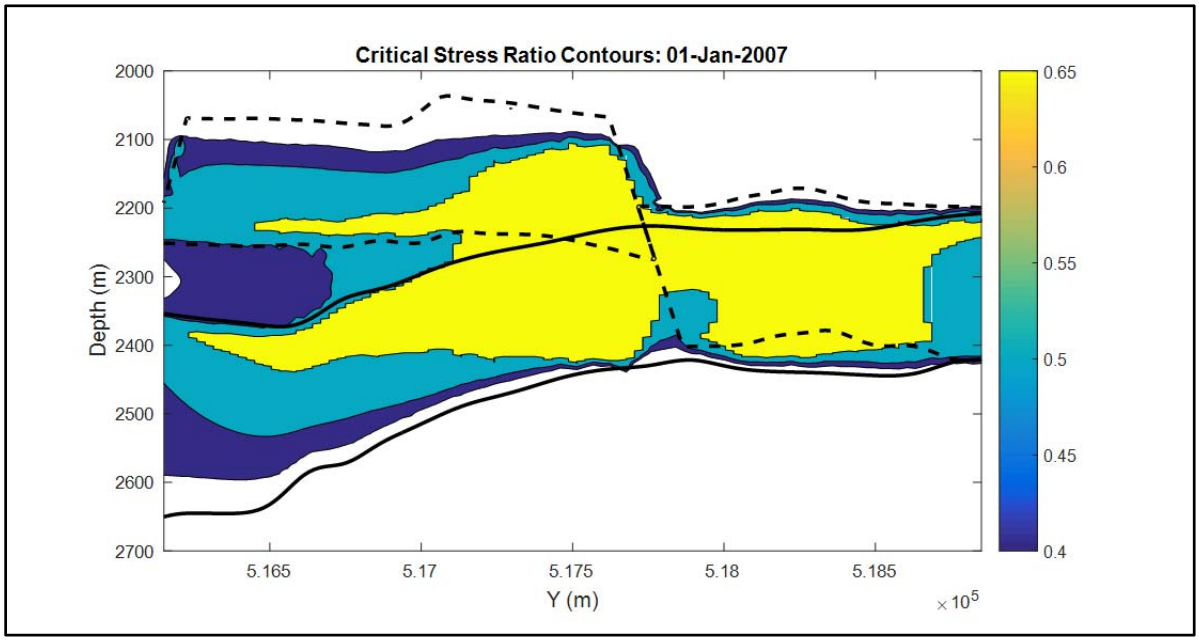

Figure 76: After slip application, the critical area has increased due to additional shear stress at the top and bottom of the stressed zone in Figure 75.

Slip and Maximum Magnitude during Depletion

The stress due to the shear dislocation can be correlated to the slip, so that an estimate is obtained of the maximum seismic moment and magnitude. Seismic moment in this section and the remainder of the document is computed via $GA_{slip}\overline{u}_{slip}$, with $\overline{u}_{slip}$ the average slip obtained from the excess shear stress and the correlation shown in Figure 74, A_{slip} the slip area and G the shear modulus.

This can be used to calibrate the model during depletion on the cumulative seismic moment that was observed in the four earthquakes. Figure 77 shows the computed and observed seismic moment for the Midfield fault using a friction coefficient of 0.65.

Using the computed slip yields a low estimate of the seismic moment, since the stress drop is small. However, it is consistent to calibrate the model on the computed slip and then use any slip that may occur in the refill phase to predict the seismic magnitude.

In previous work on Bergermeer fault slip (TNO, 2008, Orlic, 2013), the computed maximum slip varied strongly between 120 and 20 mm, in a 2D and 3D model, respectively. The current slip estimate falls in between these extremes, as listed in Table 9. For consistency, it is necessary to use the computed slip for magnitude estimates, because incorporating slip results in a large section of the fault that may be critically stressed but that doesn't necessarily result in large earthquakes. A large earthquake can only be induced if there is sufficient excess shear stress resulting in potential slip. It will be shown that during refill a large patch becomes critical, but with small excess stress so that the maximum seismic moment is still small.

Table 9: Size of slip area, average slip and moment magnitude in depletion and refill simulations.

Case	Slip Area (km2)	Average slip (mm)	Moment Magnitude
Depletion	0.6	20	3.5
Refill without slip correction	0.05	3	2.2
Refill with slip correction	0.05	0.2	1.5

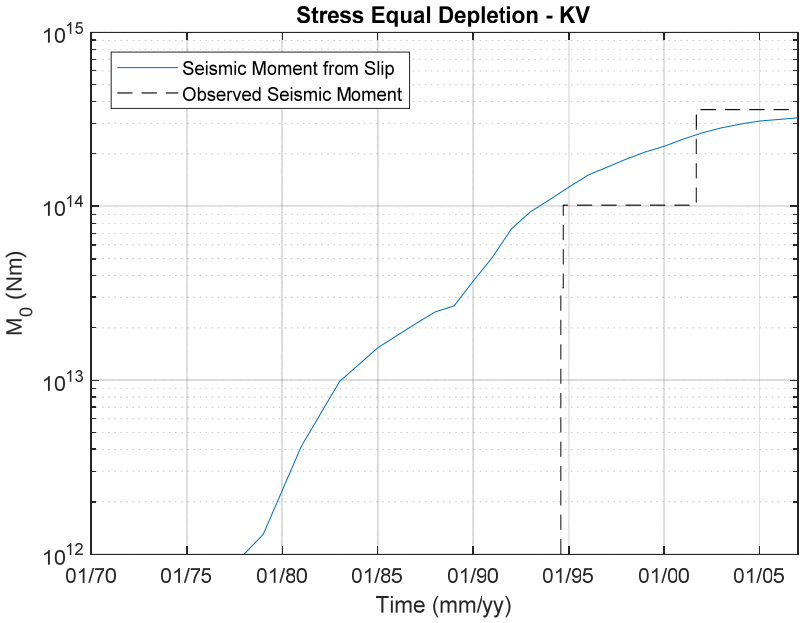

Figure 77: Seismic moment from slip on the largest critically stressed area of the Midfield fault.

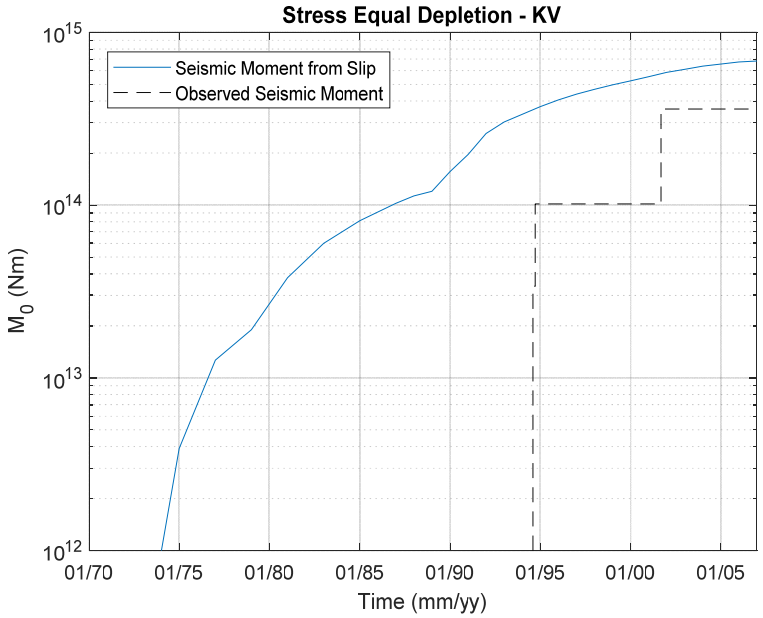

Figure 78: Seismic moment from slip on the largest critically stressed area of the Midfield fault, for a friction coefficient of 0.6.

It is possible that part of the slip was non-seismic or below the detection limit, so the critical area was also computed for a lower friction coefficient of 0.6, which can be considered a default value. Figure 78 shows that the seismic moment would be a bit larger for the lower friction coefficient. The effect of a lower friction coefficient on the match with observed seismicity and the forecast will be discussed in the next section.

For the East fault, it is unknown whether slip occurred during depletion, but it is likely since the fault becomes critical using a default friction coefficient (see Figure 79) and also because seismicity was observed on the East fault during refill. This is commonly observed for faults that have slipped during depletion. The West fault never showed any seismicity, while it is critically stressed during depletion, so it is likely that only non-seismic slip occurred. That might be the case also for the East fault, but it is better to take a conservative approach and assume depletion seismicity was just not noticed. That may have happened for a maximum magnitude of 1.5. Such events may have occurred given the cumulative seismic moment predicted

by the model. The seismic moment would be lower for a higher friction coefficient: a value of 0.67 would give a maximum magnitude of 1.5. However, a friction coefficient of 0.6, which is the default value, results in more shear stress redistribution, so is a conservative value for predicting refill and storage seismicity.

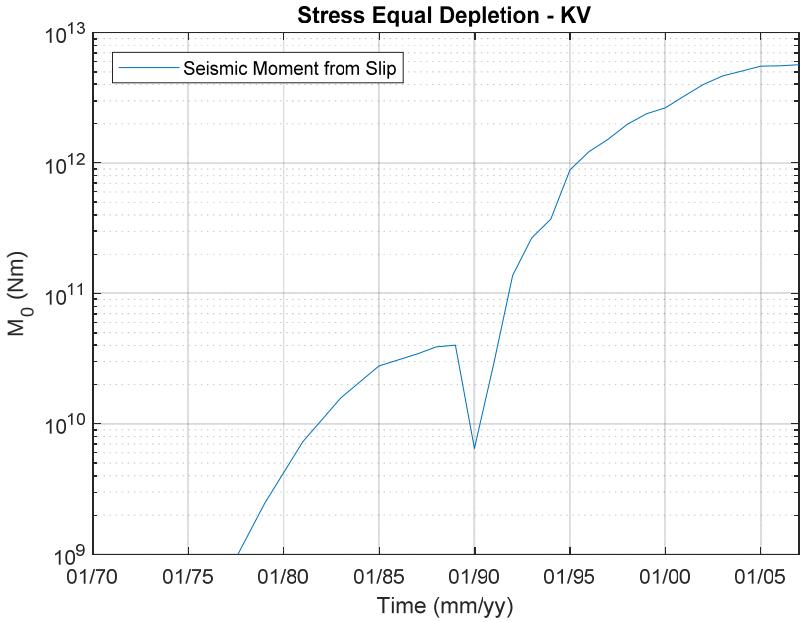

Figure 79: Seismic moment from slip on the largest critically stressed area of the East fault for a friction coefficient of 0.6. The dip is caused by disappearance of a critical area towards the north, while later the most critical area is at the Southern section of the fault.

Fault Slip for Storage cycles up to 133 bar

Midfield Fault

The base case scenario assumes that slippage will occur whenever the critical shear ratio exceeds the friction coefficient during refill or storage. The refill period until April 2014 is evaluated with intervals of about 2 Months, the storage and forecast with intervals of a month.

Assuming that the stress effect of the shear slippage due to earthquakes persists, the stress on the fault is significantly changed. At the start of refill a large area is still critical (Figure 76). Figure 80 shows that even at higher pressure in 2013 some areas remained critically stressed. Of course, this would not cause large earthquakes since that would require excess shear stress above the MC envelope. However, it can explain small micro-seismic events which represent only small slippages and energy release. The critically stressed regions are caused by the additional shear stress around the area that slipped in the depletion earthquakes.

Let's now look at the stress evolution at selected points on the fault. Points 1-3 are on the critically stressed regions caused by the additional shear stress, while points 4-6 are near the middle of the fault. Point 5 is near the juxtaposition point, where both fault blocks separate.

Figure 81 plots the time sequence for these points on a MC diagram. There is a distinct behaviour for points 1-3 compared with points 4-6. The latter points show immediate stabilization because the stress moves away from the failure envelope. The points near the regions that were critically stressed by additional shear stress remain for a while on the envelope. Points 1-2 even remain close to the envelope during the cycles. Finally, cumulative slip during storage cycling stabilizes these regions.

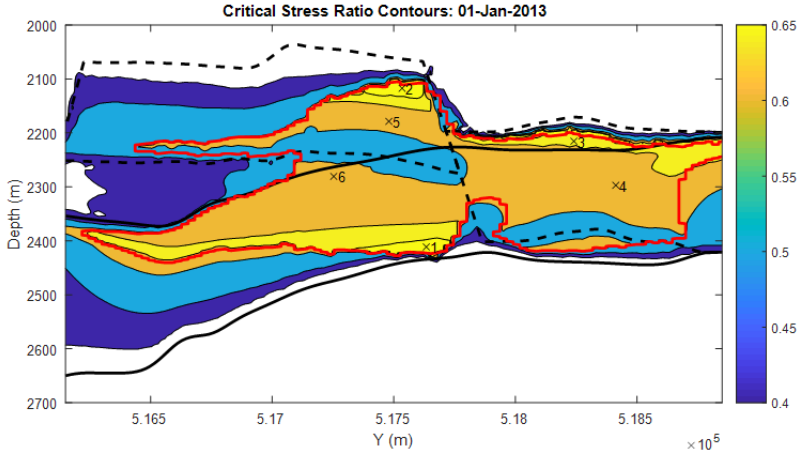

Figure 80: Contours of critical stress ratio on the Midfield fault, just before the time of the largest micro-seismic event. The only critically stressed patches occur at the boundaries of the maximum slippage area.

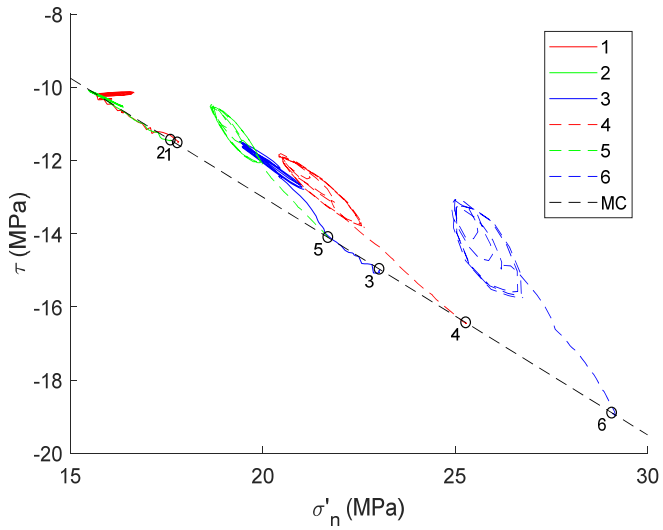

Figure 81: MC plot of selected points on the fault, shown in Figure 80.

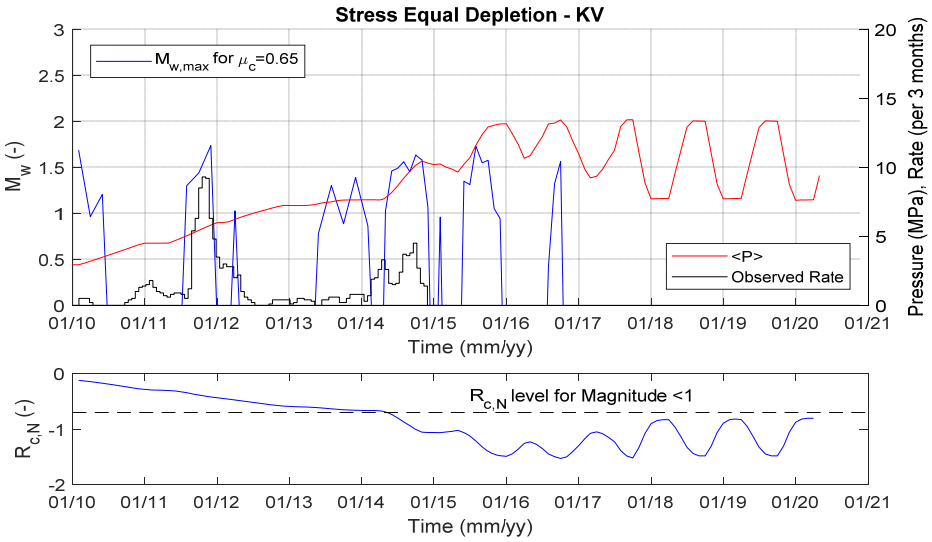

Figure 82: (Upper graph) Magnitude from slip for the Midfield fault with average gas pressure and observed micro-seismic rate for the 133 bar case. Rate is defined as events per 3 months times 0.1. (lower graph) average critical stress ratio.

Figure 82 shows both the maximum magnitude (upper graph) based on the peak in critical stress ratio as well as the averaged critical stress ratio (lower graph). The maximum magnitude during refill and storage cycles remains below magnitude 1.5, which corresponds to a small excess shear stress on the critically stressed area.

Micro-seismic activity ceased after 2014 which agrees qualitatively with the falling trend in maximum magnitude and the drop in average critical stress level. Apart from the history, also future cycles are shown over the full pressure range between 77 and 133 bar. Moreover, these forecast cycles use the maximum available injection and production rate. The maximum magnitude occurs during injection and at high pressure, while the average critical stress ratio is highest at low pressure, as would be expected. The reason for this counter intuitive behaviour of the peak stress is explained in Figure 83. The shear stress at the critical point (3) hardly fluctuates with the pressure cycles, since the high shear stress is caused by the additional shear stress from slip on the fault by the depletion earthquakes. The normal stress fluctuates with the reservoir pressure, giving a fluctuation in critical stress ratio at the critical point and even an excess over the MC envelope. The excess shear stress gradually disappears by continued slip and the critical point stabilizes, so that the maximum magnitude drops with subsequent cycles.

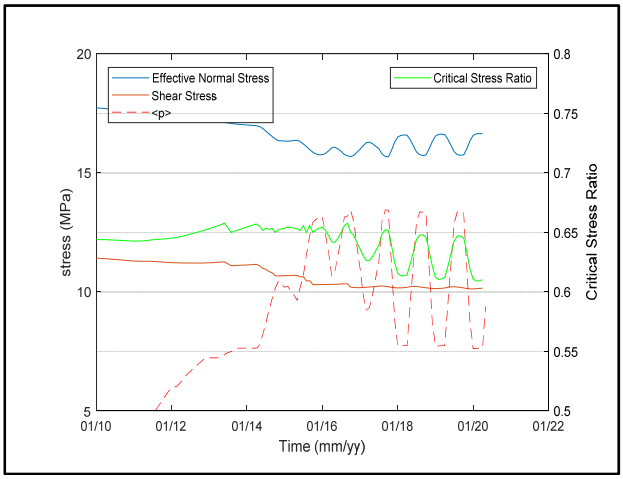

Figure 83: Normal stress, absolute value of shear stress and critical stress ratio for point 1 (see Figure 80) vs. time. For this point the critical stress ratio peaks at the high-pressure points, since the shear stress hardly changes, while the normal stress fluctuates with pressure. This is caused by the constant additional shear stress due to earthquake slip at this point.

Using the expression for the seismic rate in terms of the rate of change of shear stress and the probability function of critical patches (eq. 7), the observed rate can be matched as shown in Figure 84 The change in seismic rate is caused by a fault that stabilizes on average (reduction of $R_{c,N}$ giving a lower probability of seismicity) a shear rate that scales proportionally to the pressure rate. The match is only qualitative, but the response of seismicity rate to changes in shear stress is reflected in the predicted rate and the disappearance of seismicity can be matched with the assumption that the probability of critically stressed areas falls with the gradual stabilization of the fault. The model predicts that the seismicity would again increase during the cycles at full capacity. In these cycles, the shear rate will be much higher and also the critical stress ratio would be less negative since the pressure is lower than attained during the historical cycles. Still, the micro-seismic rate is predicted to remain low compared with previous activity. Moreover, the peak in the critical stress remains below the critical level for felt earthquakes. So, the model only predicts some weak micro-seismic events that pose negligible risk.

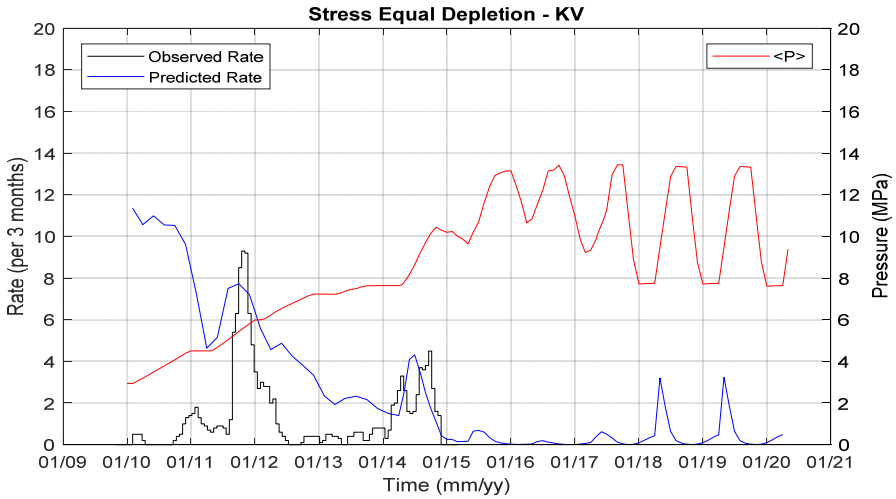

Figure 84: Micro-seismic rate and predicted rate for the 133 bar case. Rate is defined as events per 3 months times 0.1.

Sensitivity: Seismic risk when no slip correction is applied after depletion

The best match with the observed seismicity is obtained when we assume slippage on the fault during refill. However, the cumulative seismic moment that is observed is quite small since the micro-seismicity is weak. So, most slip must have been non-seismic. As a worst case we can also assume that the stress is not released and the critically stressed regions would have persisted after the earthquakes. So, at the date of the earthquakes in 1994 and 2001, the shear stress on the fault was corrected to the MC envelope, but no slip correction was applied afterwards. This yields the estimate of maximum magnitude shown in Figure 85.

This estimate of maximum magnitude far exceeds the magnitude of observed micro-seismicity. However, this might be a matter of chance or that stronger events are just impossible as happened during depletion. So, with these assumptions it may still be possible that a stronger event happens if for some reason the fault would become weaker or seismic slip is still induced. Even in that case the maximum magnitude of 2.2 is quite modest.

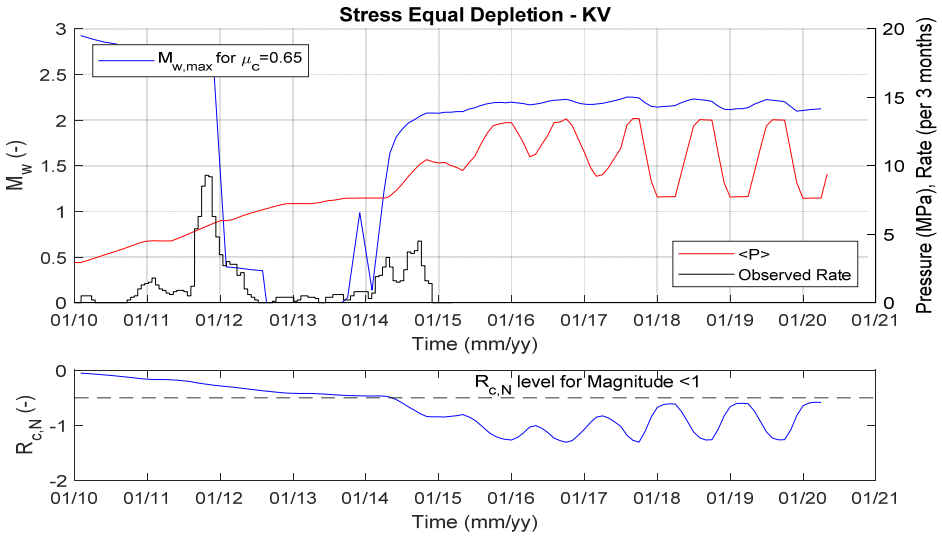

Figure 85: Magnitude from potential slip for the Midfield fault with average gas pressure and observed micro-seismic rate (upper graph) for the 133 bar case. In this case, no slip was applied during refill, so the critically stressed region persists. The maximum magnitude of 2.2 that is predicted for this worst case is still quite modest. Rate is defined as events per 3 months times 0.1. (lower graph) average critical stress ratio

Sensitivity: Impact of friction coefficient

Another sensitivity that can be considered is the calibration on friction coefficient in the depletion phase. The cumulative seismic moment could also be explained with a lower friction coefficient, assuming that part of the slip was seismic, while some non-seismic slip occurred. Using a friction coefficient of 0.6 will give a larger critical area and a stronger stress correction. This results in more criticality during refill, although the effect is insignificant if the fault is assumed to slip and remain on the MC envelope, see Figure 86.

When it is assumed that no slip occurs after depletion, the maximum magnitude is larger, as shown in Figure 87. Even in this case a maximum magnitude of 2.5 is modest compared with a level that is expected to cause damage. In view of the calibration, we see that the average critical stress ratio on the fault remains below the level for observed magnitude smaller than one. So, during the cycles no stronger micro-seismicity is expected than was experienced during refill of the reservoir.

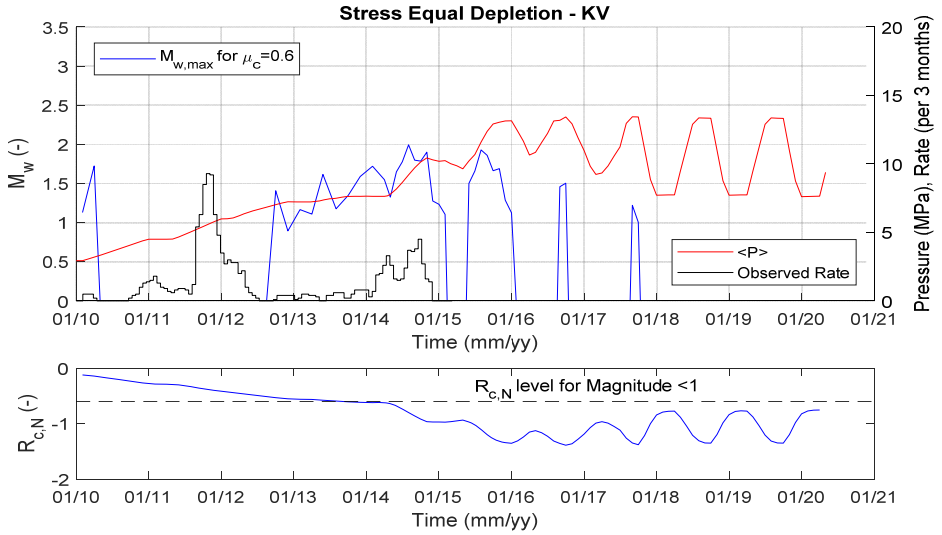

Figure 86: Magnitude from slip for the Midfield fault with average gas pressure and observed micro-seismic rate (upper graph) for the 133 bar case, using friction coefficient 0.6. During the refill period the stress on the fault was corrected for potential slip. Rate is defined as events per 3 months times 0.1. (lower graph) average critical stress ratio

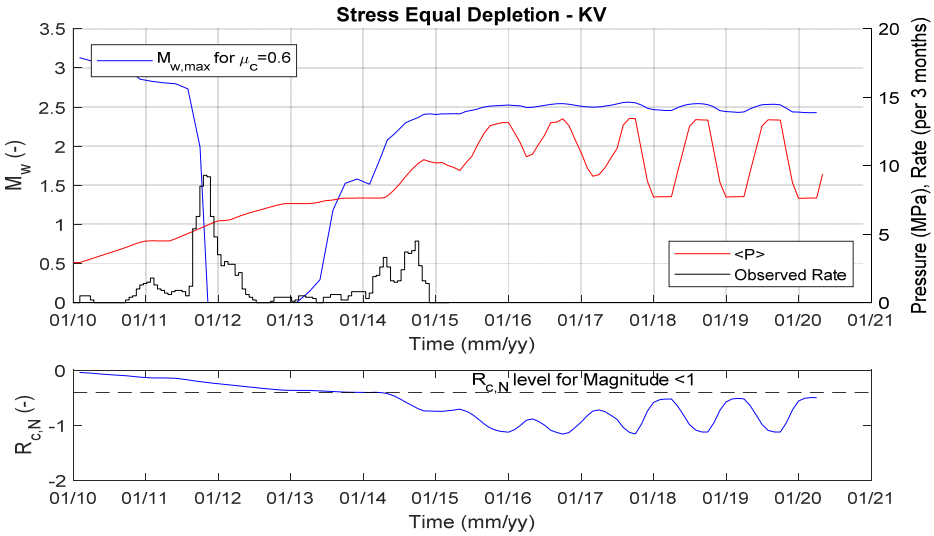

Figure 87: Magnitude from potential slip for the Midfield fault with average gas pressure and observed micro-seismic rate (upper graph) for the 133 bar case with friction coefficient 0.6. In this case, no slip was applied, so the critically stressed region persists. The maximum magnitude of 2.5 that is predicted for this case is not much higher compared with the prediction for the matched value of the friction coefficient. (lower graph) Average critical stress ratio

East Fault

As starting point for the refill phase at the East fault, it is assumed that during depletion several seismic events have occurred just below the detection limit of felt seismicity of magnitude M_w=1.5. For a default friction coefficient of 0.6, this gives a slip correction for which the cumulative seismic moment is equivalent to a single seismic event of magnitude M_w=2.5. The sensitivity below analyses the behaviour of the east fault in case no seismicity has occurred at all during depletion.

The East fault shows seismicity of low magnitude at the start of refill and the injection part of the storage cycles. However, the East fault stabilizes quickly during refill, so no seismicity is actually expected. The friction coefficient is unknown, but with a default friction coefficient of 0.6, the predicted magnitude could still be low enough to have been undetected. Figure 88 show the contours of critical stress ratio at the end of the refill period. The fault quickly stabilizes on the assumption that the critical regions have slipped, so that the critical stress ratio is capped at 0.6.

For a few points, indicated in Figure 88, the stress evolution is shown in Figure 89 and the MC plot of Figure 90. At the East fault the behaviour is quite normal, with the highest critical stress ratio at the low-pressure points. The MC plot also shows that the fault stabilizes and remains completely stable during the storage cycles.

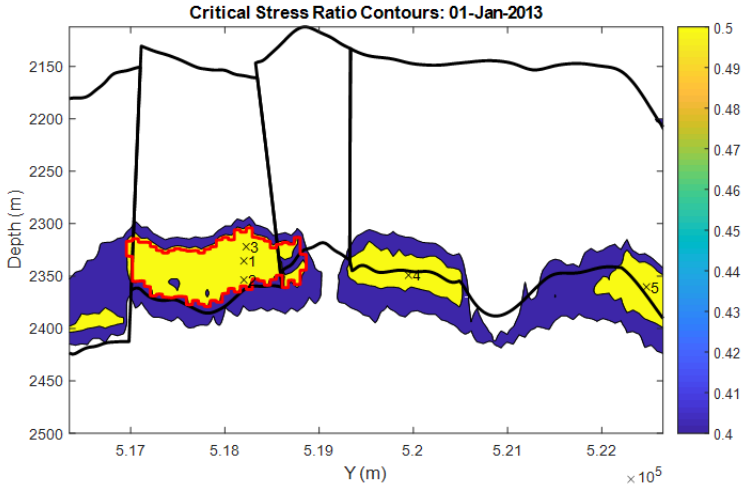

Figure 88: Contours of critical stress ratio on the East fault, after the first refill stage. The fault is stable for a friction coefficient of 0.6. The critical stress is determined for a much lower friction coefficient of 0.5 to capture any variations in micro-seismicity.

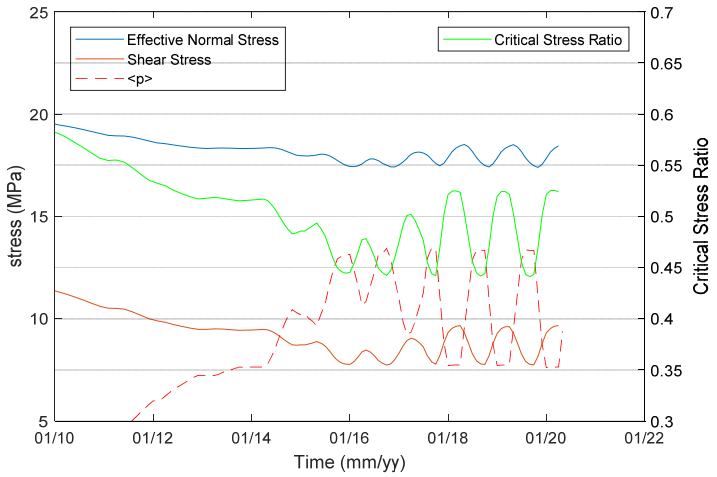

Figure 89: Normal stress, shear stress and critical stress ratio for point 1 (see Figure 88) vs. time. This point is stable and the critical stress ratio peaks at low pressure, as expected.

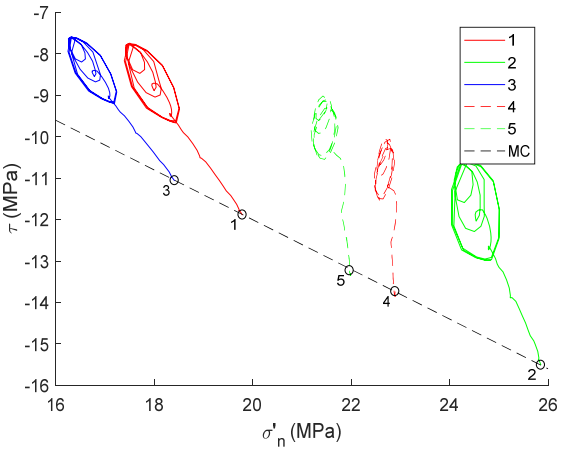

Figure 90: MC plot of selected points on the fault, shown in Figure 88.

Since the East fault is stable, it is relevant to look at an area defined by a lower friction coefficient of 0.5, to obtain a measure of average critical stress ratio. Figure 91 shows the maximum magnitude for a friction coefficient of 0.5 and the critical stress ratio for a model with friction coefficient 0.6, computed on the area defined by the lower friction coefficient of 0.5. It is seen that even for a much lower friction coefficient the maximum magnitude would be rather small. Also, the critical stress ratio remains always below the level for which the maximum observed magnitude was below -1. So, even during cycles with full pressure swing and high rate, only weak micro-seismicity is expected.

As argued before in the section on micro-seismic interpretation, the seismicity observed during refill and cycles is best explained by heterogeneities on a fault that has a large almost critically stressed area. The Midfield fault is much closer to critical than the East fault, but the micro-seismicity on the East fault is also much weaker and quite sparse with a few dozen events of magnitude below -1.

Taking the predicted micro-seismic rate proportional to shear stress rate (which scales proportionally to the pressure rate), the curve in Figure 92 is obtained. The match with observed seismicity rate is fair initially, but the observed rate falls of rapidly in 2016. So, it is unclear whether the rate would pick up again if the full capacity of the injection system were used, as assumed in the forecast cycles. Even if the seismicity rate would follow the shear stress rate and become higher during cycles with full injection capacity, the magnitude would be quite small. Assuming a response following the standard GR relation (with rate decreasing by 10 for a magnitude unit), a doubling of rate would result in an increase of the maximum observed magnitude with 0.3, for a given time period. This results in a maximum magnitude of -0.7.

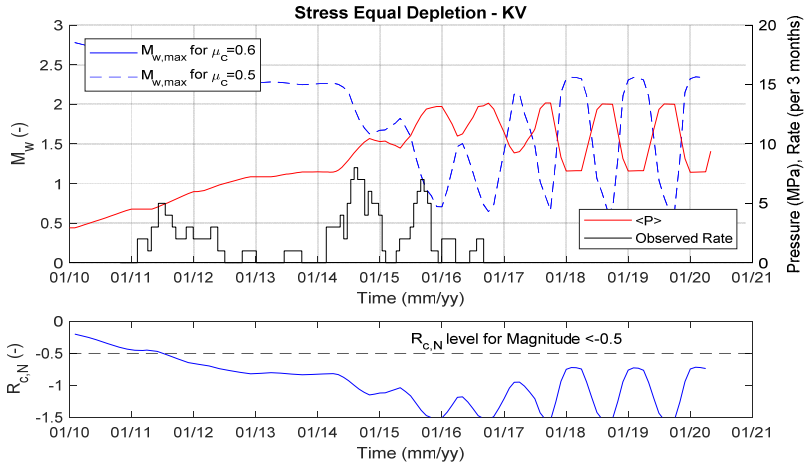

Figure 91: (upper graph) Magnitude from slip for the East fault with average gas pressure and observed micro-seismic rate for the 133 bar case. Rate is defined as events per 3 months. The line for μ_c=0.6 is absent because for μ_c=0.6 the model does not predict any seismicity after depletion. (lower graph) The average critical stress ratio on the most critical patch of the fault remains below the initial level at the start of monitoring.

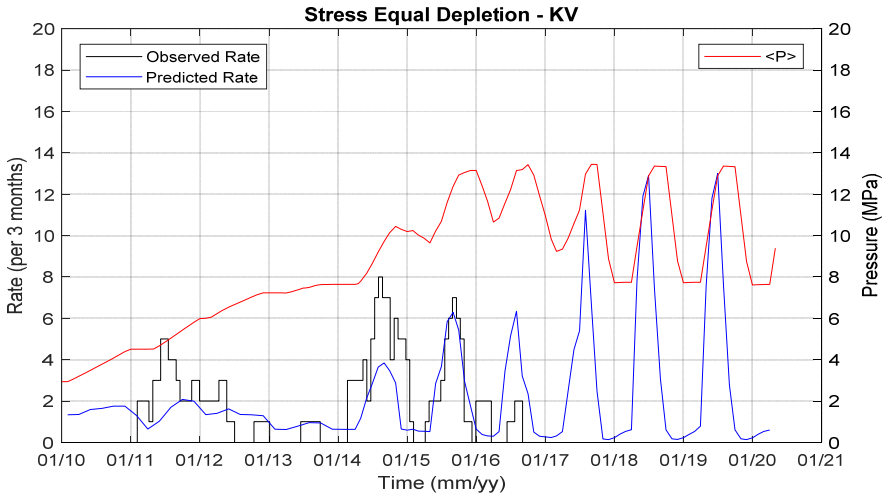

Figure 92: Micro-seismic rate and predicted rate that is derived from the shear stress rate on the fault for the 133 bar case. Rate is defined as events per 3 months.

Seismic risk for East Fault when no slip correction is applied

Since no earthquakes were detected at the East Fault during depletion it is also possible that the fault is locked (for instance by cohesion) and no slip has occurred. The micro-seismic activity would then be due to some slip on small fractures that have no cohesion. In that case the potential slip can be computed and the corresponding magnitude, as shown in Figure 93. Most likely the fault would remain locked, but could still induce earthquakes with magnitude 1.7 if for some reason it would still slip. This represents a felt earthquake, but is still below the expected damage limit for the Bergermeer reservoir.

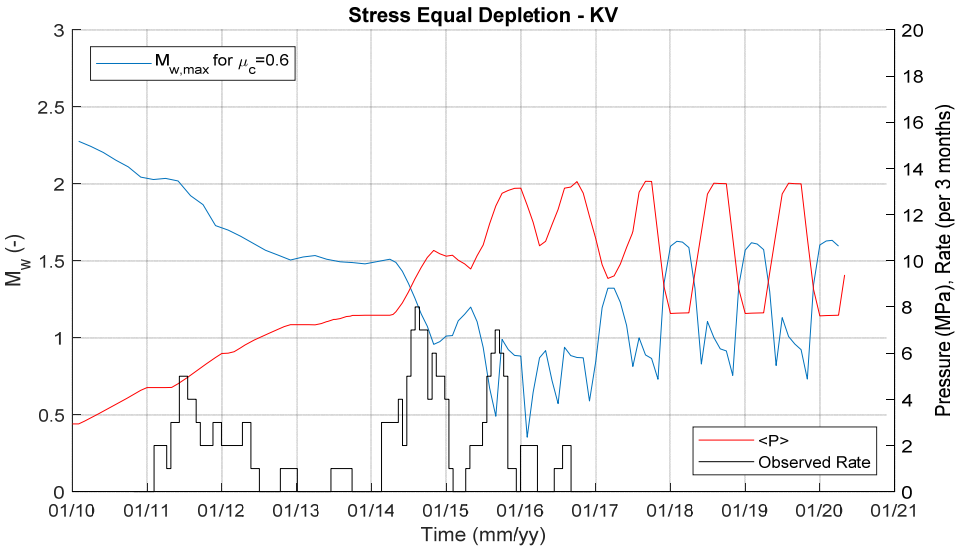

Figure 93: Magnitude from potential slip for the East fault with average gas pressure and observed micro-seismic rate (upper graph) for the 133 bar case. Rate is defined as events per 3 months. No correction was applied for slip during the depletion phase.

North-South shift in Seismic Activity

Micro-seismicity first occurred on the Northern part of the Midfield fault, which then subsided. Later, the Southern part became active. This is of course hard to explain, since the entire fault was close to critical stress. The stress ratio was computed for the most critically stressed patches in the north and south, shown in

Figure 94. The stress does indeed subside much faster for the Northern patch (see Figure 95), which can explain the rapid disappearance of the activity in the north. However, it is expected that the Southern patch would also show seismicity, since the critical stress ratio is high.
Perhaps, also in this case it is not the critical stress ratio, but the rate of change that determines seismic rate. The Northern patch shows a larger shear rate, while the Southern patch shows less change but the shear rate picks up later, see Figure 96. Perhaps, the Northern patch becomes quiet after a few years because the number of critically stressed fractures decreased by slippage.

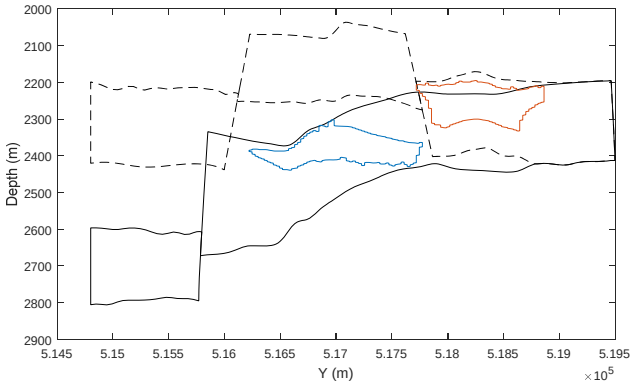

Figure 94: North and South critically stressed patches at the start of refill.

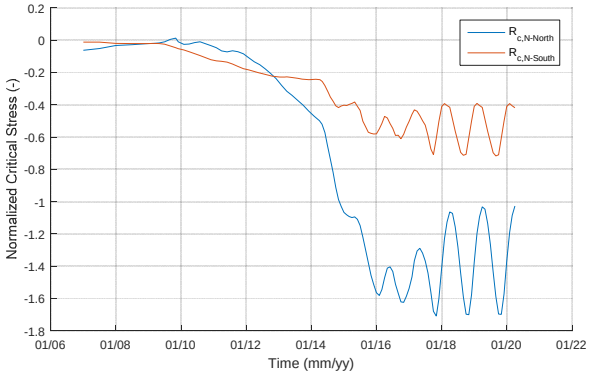

Figure 95: Critical stress ratio on Northern and Southern patches on the Midfield fault vs. time during refill of the reservoir. The stress ratio falls much faster for the Northern patch, which could explain the disappearance of seismicity on the Northern part of the fault. However, the stress evolution cannot explain that the seismicity on the Southern part of the fault only started later and then subsided.

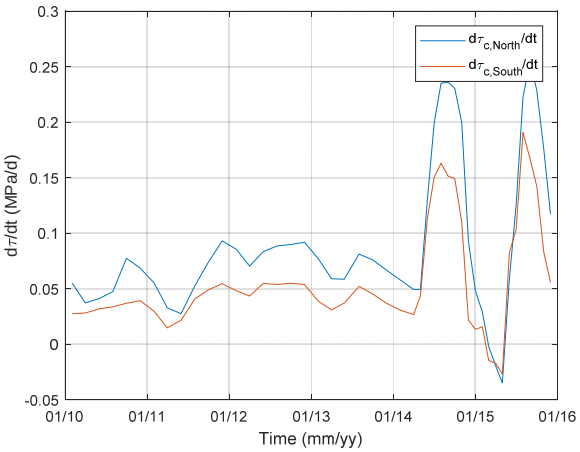

Figure 96: Rate of change of shear stress for the Northern and Southern patch on the Midfield fault vs. time.

Conclusions

- Calibration of the friction coefficient yields a best estimate of 0.65 for the Midfield fault. The model then predicts a cumulative seismic moment equivalent to the observed seismic moment. A smaller friction coefficient is also possible, but in that case the match with refill seismicity becomes poorer.
- Calibration of the friction coefficient for the East fault gives a friction coefficient of 0.6, which corresponds to multiple non-felt events with an equivalent cumulative magnitude of 2.5. This agrees with the observation that no felt earthquakes were observed at the East fault during depletion, which would have magnitude of about 1.5 for the Bergermeer reservoir. A few earthquakes of this magnitude could have happened during depletion without being detected as no micro-seismic monitoring was in place yet.
- Refill seismicity on the Midfield fault can be explained with the additional shear stress induced by slip from the depletion earthquakes.
    - Disappearance of seismicity on the Midfield fault can be matched by assuming continuous slip on the fault when it becomes critical. Much of this slip should be non-seismic since the micro-seismicity accounts only for a few percent of the seismic moment.
    - For the best match no seismicity is expected during future storage cycles.
    - Assuming a worst case that no slip has occurred on the Midfield fault during refill and storage cycles, the maximum possible magnitude for an earthquake during future storage cycles is 2.2.
- The East fault does not become critically stressed again during refill and storage cycles. The observed weak micro-seismicity is caused by critically stressed heterogeneities such as fractures and fault asperities that are only a few metres in diameter.
    - The micro-seismicity occurs mostly during injection periods. This can be explained since the Kaiser effect applies to re-loading, but weak micro-seismicity is still expected during unloading.
- If the East fault never slipped, there could still be excess stress on the fault, assuming a default friction coefficient of 0.6. If the fault would still slip, it could induce an earthquake with magnitude 1.7.

7 Subsidence and Heave for forecast cycles

Figure 97 shows the response in the heave for the forecast run with 77-133bar swing using the parameters that were calibrated on the refill and storage heave. Simulation predicts a maximum heave of 11.2mm starting from 2014 and a maximum swing of 8.2mm during the forecast cycles.
The Kelvin-Voigt fit of the simulation give a fairly good match. Moreover, the relaxation times belonging to the simulations including the forecast are close to the relaxation time for the storage cycles only. This is another indication that the pressure equilibrates fast within a block.

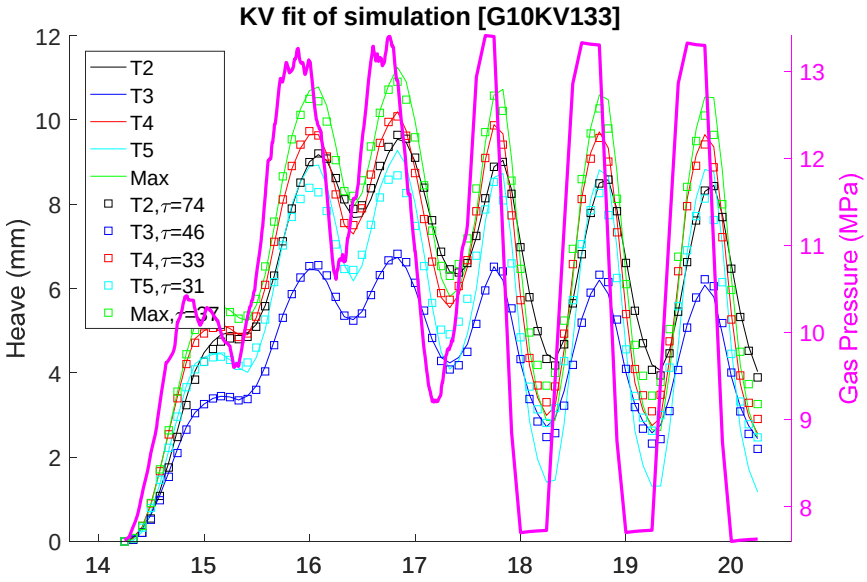

Figure 97: (Left axis) Response heave of the 4 observation stations and the maximum heave during the storage and 77-133bar forecast simulation (2014-2021). The squares are a Kelvin-Voigt fit of the FEM results for which the corresponding relaxation time are shown. (Right axis) gas pressure

8 Discussion and Conclusions

For Bergermeer gas storage, a new geomechanical model has been calibrated to all available measurements. This yielded a model that matches the observed seismicity. By proper calibration, the model establishes the link between observed and predicted seismicity. That is relevant for assessing the risk of future storage cycles.

In principle, faults that reach criticality can fail either in a creeping fashion or by releasing elastic energy generating seismic waves. Considering that most gas fields do not induce felt earthquakes, while the differential compaction effect should be strong enough to cause slippage on any faults, it is likely that on many faults the slip occurs non-seismically. For safety analysis, this means that slippage may go unnoticed, which is not much of a concern, except that under some conditions the fault might become seismic and still induce an earthquake. In the Bergermeer reservoir there are three main faults that were all critically stressed during initial depletion. However, only the Midfield fault induced felt earthquakes. It is commonly observed in gas storage reservoirs that faults which have induced earthquakes during depletion are also active during storage cycles. That would imply seismic activity on the East fault during depletion, but probably at such a low level that this activity was never felt or detected, implying a magnitude below 1.5. The West fault was critically stressed but showed no activity at all, indicating that it is non-seismogenic. It may have slipped in a creeping fashion, but could also have remained inactive because of high strength of the fault.

An important observation is the large gap between depletion seismic intensity and the much weaker micro-seismicity observed in the refill and storage phases. Weak micro-seismic events are commonly observed in underground formations when strain is applied, because rock formations deform with micro-fracturing (Nicholson, 1994). Moreover, rock formations are heterogeneous and small critically stressed faults are ubiquitous. Slippage areas of less than a few square metres generated these small micro-seismic events which are of no concern to seismic risk. Looking at the micro-seismic character it is possible to dismiss the micro-seismicity as just a secondary effect of the critical stress acquired during the original depletion. The micro-seismic analysis showed that no contiguous areas of the fault became critical, but just some scattered patches. Also, the small faults that are oblique to the midfield fault showed many events while these faults were not critically stressed. Perhaps they became stressed due to the depletion induced seismicity, but that would then also be a secondary response. Also, the events originated not only from the reservoir level, but were scattered all over the fault surface. This suggests that relief of shear strain by small dislocations in the fault zone could cause temporary critical stress and slippage on some fault patches. On the other hand, the larger micro-seismic events are observed at reservoir level, so that it appears justified to interpret them as a potential warning signal of fault instability. Interpreting the seismicity as a warning signal of fault instability by investigating systematic causes of the refill seismicity is therefore a prudent approach to the seismicity. So, in this study the micro-seismicity was interpreted as potential warning for larger seismic activity. However, the relative weakness of the micro-seismicity was also honoured by appropriate calibration of the model.

Seismic risk during refill, storage and forecast

Assuming that during depletion the Midfield fault has slipped to a stable configuration, given by a single friction coefficient, it is possible to compute the stress distribution. A crucial feature of slippage is that not only the peak in shear stress is reduced, but the shear stress is increased at the edges of the slip area. If the stress due to depletion slippage is frozen in, the additional shear stress causes criticality of the fault during refill of the reservoir. Since the critical area during refill is about 10% of the total slippage area during depletion, the surface area alone suggests potential for quite strong earthquakes. However, the excess shear stress above the failure condition in this area is rather small, so the magnitude of the potential earthquakes is also small. The best match with the observations is obtained when the fault is assumed to slip when it becomes critical. That can explain the disappearance of seismicity over time during successive storage cycles.

The stronger events during refill (up to magnitude 0.9) could be explained by heterogeneity of the fault and in that case it is unlikely that any large earthquakes could be induced during future storage cycles since those would require a large critically stressed area on the fault. On the other hand the stronger events may be caused by the stress concentration caused by the additional shear stress due to depletion slip. The strongest

micro-seismic event came from that location. Therefore, it is unlikely that the fault would still be locked since an event of magnitude 0.9 was triggered, while a larger event would also have been possible given the size of the critical area during refill.
Therefore, it is most likely that the fault has slipped non-seismically during refill with the micro-seismicity being invoked by heterogeneity and it is unlikely that larger events could be induced.
On the other hand, it was observed during depletion that the fault was critically stressed for a long time, without any seismic slip. So, as a worst case it was assumed that little slip occurred during refill, such that most of the shear energy is still stored, since the observed seismic moment in the micro-seismicity was only a few percent of the total moment. Even in that worst case, the fault could only induce a magnitude 2.2 earthquake. Although this would be a felt earthquake it is expected to fall below the damage limit for the Bergermeer area.

We calibrated the model to observed seismicity to forecast the expected fault behaviour during future storage cycles. For the Midfield fault, it is expected that little seismicity will be induced during future cycles, since the pressure cycles will cause some slippage of the fault that renders it more stable. The East fault is predicted to remain stable during the storage cycles, although micro-seismicity is still possible. Heterogeneities may slip and at higher injection rate the seismic rate may also increase, but the micro-seismicity will have a small magnitude.

Seismic risk based on Seismic Observations
For assessing risk, it remains most relevant to directly consider the information from the micro-seismic observations. That yields a reassuring conclusion since all lights are green concerning quantity as well as quality of micro-seismicity. Of most concern at the start of the project was seismic activity on the Midfield fault and this indicated only scattered patches where the fault slipped during refill. Since there is no indication of a large contiguous critical area, it is unlikely that large seismic events could be induced. Moreover, the activity on the Midfield fault has completely ceased after reaching 100 bar reservoir pressure. On the other hand, the reservoir pressure never dropped below 87 bar, so it cannot be excluded that the Midfield fault might be re-activated at lower pressure as the model would predict.
Currently, the only remaining activity is on the East fault. This has a transient character and is also diminishing over subsequent storage cycles. In view of these observations and the model interpretation, it is likely that further gas storage cycles will show only weak micro-seismic activity with magnitude below -0.7.

Conclusions

- Observed seismic activity is strongly clustered in space and time. Stress criticality on the Midfield fault has a transient signature as evidenced by seismic monitoring data. Fault patches that were seismically active during refill can become inactive after a certain amount of time has passed. This shows that there are no large areas of the fault that become critical, so only weak seismic events can be induced.
    - On the midfield fault, where most seismicity occurred a North-South migration of the seismicity was observed with time. This shift is probably related to a difference in shear stress recovery between Northern and Southern parts of the fault.
- The geomechanical response of the reservoir has been analyzed based on the relation between stress, surface displacement and seismicity:
    - Surface heave is smaller than predicted by elastic behaviour calibrated to depletion subsidence. The most plausible cause of the small heave and time delay of the surface displacement is rate and stress dependent stiffness in the reservoir.
    - Calibration of the friction coefficient yields a value of 0.65 for the midfield fault. The model then gives a cumulative seismic moment equivalent to the observed seismic moment. A smaller friction coefficient is also possible, but in that case the match with refill seismicity becomes poorer.
    - Calibration of the friction coefficient for the East fault gives a friction coefficient of 0.6, which corresponds to multiple non-felt events with an equivalent cumulative magnitude of 2.5. This agrees with the observation that no felt earthquakes were observed at the East fault during depletion, which would have magnitude of about 1.5 for the Bergermeer reservoir. A

few earthquakes of this magnitude could have happened during depletion without being detected as no micro-seismic monitoring was in place yet.
    - Most seismic activity since 2007 occurred during cushion gas injection. The activity was much weaker during the fast pressure increases during storage cycles and the activity on the Midfield fault has ceased. Therefore, the fault systems are stabilizing, which is explained by average stress recovery on the fault and continuous slippage.
    - Refill seismicity on the Midfield fault can be explained with the additional shear stress induced by slip from the depletion earthquakes.
        - Disappearance of seismicity on the Midfield fault can be matched by assuming continuous slip on the fault when it becomes critical. Much of this slip should be non-seismic since the micro-seismicity accounts only for a few percent of the potential slip.
        - The pressure differential between the two compartments had a minor effect on seismicity.
        - For the best match no seismicity is expected for the Midfield fault during future storage cycles.
- Seismic risk is deemed small for future gas storage cycles. This conclusion is supported both by observation and the calibrated model.
    - Assuming a worst case that no slip has occurred on the Midfield fault during refill and storage cycles, the maximum possible magnitude for an earthquake during future storage cycles is 2.2.
    - The East fault does not become critically stressed again during refill and storage cycles. The observed weak micro-seismicity is caused by critically stressed heterogeneities such as fractures and fault asperities that are only a few metres in diameter.
        - The micro-seismicity occurs mostly during injection periods. This can be explained since the Kaiser effect applies to re-loading, but weak micro-seismicity is still expected during unloading.
    - If the East fault never slipped, there could still be excess stress on the fault, assuming a default friction coefficient of 0.6. If the fault would still slip, it could induce a small earthquake with magnitude 1.7.

References

Bergermeer:

Baisch, S., and H.-P.Harjes, 2003. A model for fluid injection induced seismicity at the KTB. Geophys. Jour. Int., 152, 160-170.

Baisch, S., Carbon, D., Dannwolf, U., Delacou, B., Devaux, M., Dunand, F., Jung, R., Koller, M., Martin, C., Sartori, M., Secanell, R., and R. Vörös, 2009. Deep Heat Mining Basel - Seismic Risk Analysis. SERIANEX study prepared for the Departement für Wirtschaft, Soziales und Umwelt des Kantons Basel-Stadt, Amt für Umwelt und Energie, 553 pages.

Baisch, S., Vörös, R., Rothert, E., Stang, H., Jung, R., and R. Schellschmidt, (2010), "A numerical model for fluid injection induced seismicity at Soultz-sous-Forêts.", International Journal of Rock Mechanics and Mining Sciences 47, 405-413 DOI 10.1016/j.ijrmms.2009.10.001.

Baisch, S., Vörös, R., Weidler, R., and D., Wyborn, 2009. Investigation of Fault Mechanisms during Geothermal Reservoir Stimulation Experiments in the Cooper Basin (Australia). Bull. Seism. Soc. Amer., 99(1), 148-158.

Baisch, S., Weidler, R., Vörös, R., and R. Jung, 2006. A conceptual model for post-injection seismicity at Soultz-sous-Forêts. Geothermal Resources Council, Trans., 30, 601-606.

Baisch, S., Weidler, R., Vörös, R., Wyborn, D., and L. DeGraaf, 2006. Induced seismicity during the stimulation of a geothermal HFR reservoir in the Cooper Basin (Australia). Bull. Seism. Soc. Amer., 96(6), 2242-2256.

Baker RDS, (2011), "Dynamic Geomechanical Modelling of the Bergermeer Underground Gas Storage, Netherlands", Part 1 – Base Case Modelling, Part 2 – Scenario Modelling, version 2011 09 22.

Baker RDS, (2013), "Dynamic Geomechanical Modelling of the Bergermeer Underground Gas Storage, Netherlands. The Effect of Water Injector for Well Location BGM-03B", version 2013 11 11.

Bell, J.C. (1978), "Stresses from arbitrary loads on a circular crack", Int Journal of Fracture, Vol 15, No 1, February, 1979.

C. Haug, A. Henk, J. Nüchter, "Numerical modelling of production-induced stress changes and fault reactivation in Rotliegend gas fields of the North German Basin",79th EAGE Conference & Exhibition 2017 – Workshop Programme, Paris, France, 12-15 June 2017, Paper WS02 B06.

Dahm, T., Heimann, S., (2010), "Source parameter study of the 9/10 September 2001 earthquakes at Alkmaar".

Dempsey, David, Jenny Suckale, (2017), "Physics-based forecasting of induced seismicity at Groningen gas field, the Netherlands" , Geophys. Res. Lett., 44, doi:10.1002/2017GL073878.

Dowrick, David J. and David A. Rhoades, (2004), "Relations Between Earthquake Magnitude and Fault Rupture Dimensions: How Regionally Variable Are They?", Bulletin of the Seismological Society of America, Vol. 94, No. 3, pp. 776–788, June 2004.

Fenix Consulting Delft BV (Febr.2016)," Geomechanical Support for BGS+ Storage Plan Permit Application", Report for TAQA Energy BV.

Fokker, P.A., B.B.T. Wassing, F.J. van Leijen, R.F. Hanssen, (2013), "Data Assimilation of PS-InSAR Movement Measurements Applied to the Bergermeer Gas Field", International Workshop on Geomechanics and Energy – The Ground as Energy Source and Storage, Lausanne, Switzerland, 26-28 November 2013.

Hager, B.H. & Toksöz, M.N., 2009. Technical Review of the Bergermeer Seismicity Study, TNO Report 2008-U-R1071/B, Cambridge, MA, USA.

Hangx , S.J.T., C.J. Spiers, C.J. Peach, A. ten Hove and A.M.H. Pluymakers, "Mechanical behaviour and transport properties of anhydrite - implications for caprock integrity during long-term storage of CO2", Geophysical Research Abstracts, Vol. 14, EGU2012-9379-1, 2012.

Harris, R.A., (1998), "Introduction to special section: Stress triggers, stress shadows, and implications for seismic hazard", Journal of Geophys Research, V 103, B10, P24,347-24,358.

Holcomb, D.J., (1993), "Observations of the Kaiser Effect under multiaxial stress states: Implications for its use in determining in situ stress", 8 October 1993, DOI: 10.1029/93GL01270, Geophysical Review Letters.

Kaiser, J. (1950), "Untersuchung über das Auftreten von Geräuschen beim Zugversuch", Dr.-Ing. Dissertation, Fakultät für Maschinenwesen und Elektrotechnik der Technischen Universität München (TUM); 15.2.1950.

Kampman, N., Busch, A., Bertier, P., Snippe, J., Hangx, S.J.T., Pipich, V., Di, Z., Rother, G., Harrington, J.F., Evans, J.P., Maskell, A., Chapman, H.J., and Bickle, M.J., "Observational evidence confirms modelling of the long-term integrity of CO2-reservoir caprocks", Nature Communications 7, 12268 pp.

Kassir, M.K., G.C. Sih, (1966), "Three dimensional stress distribution around an elliptical crack under arbitrary loadings, Journal of Appl Mech, September 1966.

KNMI (2008), "Seismische analyse van de aardbevingen bij Alkmaar op 9 en 10 september en Bergen aan Zee op 10 oktober 2001", KNMI Technical report; TR-239.

KNMI, Bernard Dost, Femke Goutbeek, Torild van Eck and Dirk Kraaijpoel, (2010), "Monitoring induced seismicity in the North of the Netherlands: status report 2010"", De Bilt, 2012 | Scientific report; WR 2012-03.

Logan, J.M., C.A. Dengo, N.G. Higgs, Z.Z. Wang, (1992), "Fabrics of experimental fault zones: their development and relationship to mechanical behaviour", in Fault Mechanics and Transport properties of rock, ed. Evans, Wong), Academic Press.

Marel H. van der (2015), "Rapport voor Staatstoezicht op de Mijnen (SodM) GNSS Processing Groningen – Fase 1", Technische Universiteit Delft, Geoscience and Remote Sensing 30 April 2015 reference 1.

Meng, Q., M. Zhang, L. Han, H. Pu, T. Nie, (2016) "Effects of Acoustic Emission and Energy Evolution of Rock Specimens Under the Uniaxial Cyclic Loading and Unloading Compression", Rock Mech Rock Eng. (2016) 49:3873–3886.

Nicholson, C., R.L. Wesson, (1990), "Earthquake hazard associated with deep well injection- A report to the US Environmental Protection Agency", USGS 1951, Appendix A, p65.

Orlic, B. and Wassing, B.B.T., (2012), "Modelling stress development and fault slip in producing hydrocarbon reservoirs overlain by rock salt caprocks", 46th US Rock Mechanics / Geomechanics Symposium held in Chicago, IL, USA, 24-27 June 2012.

Orlic, B., Wassing, B.B.T. and Geel, C.R., (2013), "Field scale geomechanical modeling for prediction of fault stability during underground gas storage operations in a depleted gas field in the Netherlands", Proc. 47th US Rock Mechanics / Geomechanics Symposium held in San Francisco, CA, USA, 23-26, June 2013.

Panterra, (2010), "Bergen Concession Subsidence Study", Report No. G713-2, May 2010.

Pater, C.J. de and S. Baisch, 2011. Geomechanical Study of Bowland Shale Seismicity. Synthesis Report prepared for Cuadrilla Resources Ltd., 71 pages.

Q-con (2017), "Induced Seismicity in the Bergermeer Field: Quality Control and Re-Processing", Report to TAQA Energy BV.

Q-con (Jan.2016), "Induced Seismicity in the Bergermeer Field: Hypocenter Relocation and Interpretation", Report to TAQA Energy BV.

Q-con (Nov.2015), "Induced Seismicity in the Bergermeer Field: WP1 - Quality Control", Report to TAQA Energy BV.

Rinaldi, A.P., L. Urpi, D. Karvounis, (2016), "Effects of asperity distribution on fluid flow and induced seismicity during deep geothermal exploitation", European Geosciences Union General Assembly 2016, EGU, Division Energy, Resources & Environment, ERE, Energy Procedia 97 (2016) 470 – 477

Roest, J.P.A., Kuilman, W. (1994). Geomechanical analysis of small earthquakes at the Eleveld gas reservoir. In: 'Eurock '94; SPE/ISRM international conference, Delft, Netherlands', pp. 573–580.

Rutqvist, J. A.P. Rinaldi, F. Cappa, P.Jeanne,A. Mazzoldi, L. Urpi, Y. Guglielmi, V. Vilarrasa,(2016), "Fault activation and induced seismicity in geological carbon storage e Lessons learned from recent modeling studies"", Journal of Rock Mechanics and Geotechnical Engineering 8 (2016) pp789-804.

STAATSTOEZICHT OP DE MIJNEN, (2016), "METHODIEK VOOR RISICOANALYSE OMTRENT GEÏNDUCEERDE BEVINGEN DOOR GASWINNING TIJDELIJKE LEIDRAAD VOOR ADRESSERING MBB. 24.1.P, VERSIE 1.2", Den Haag

Steacey, S.J., J. McCloskey, (1998), "What controls an earthquake's size? Results from a hetereogeneous cellular automaton", Geophys. J. Int. 133, F11-F14.

Suckale, J. (2006), "Induced Seismicity In Hydrocarbon Fields", Advances In Geophysics, Vol. 51, CHAPTER 2., pp55-106, ISSN: 0065-2687, DOI: 10.1016/S0065-2687(09)05107-3

TAQA (2017), “Gasopslag Bergermeer Microseismische monitoring, Maandrapportage Februari 2017”.

TAQA Energy B.V., (2017), “Bodembewegingsanalyse, -modellering en – prognose Winningsvergunning Bergen II, Opslagvergunningen, Gasopslag Bergermeer en Alkmaar PGI”, ECM # 187610, Juli 2017.

TNO (2008), A.C. Muntendam-Bos, W.B.T. Wassink, C.K. Geel, M. Louh, K. van Thienen-Visser, “Bergermeer Seismicity Study , TNO report, 2008-UR-1071/B.

TNO (2009), A.G. Muntendam-Bos, B.B.T. Wassing, K. van Thienen-Visser, (2009), Effects of differential pressures across the central Bergermeer fault”, TNO-034-UT-2009-00171/B 16 January 2009.

TNO-060-UT-2011-01388/C, (2011), Wassing, B.B.T., Orlic, B., Leeuwenburgh, O., Geel, C.R., “3D Geomechanical Modelling of Fault Stability in the Bergermeer Field During Underground Gas Storage Operations”, 31 August 2011.

Westmann, R. A., (1965), “Asymmetric Mixed Boundary-Value Problems of the elastic half-space”, Journal of Appl Mech, June 1965.

Zehnger, A.T., (2012) “Linear Elastic stress analysis of 2D cracks”, Fracture Mechanics, Lecture Notes in Applied and Computational Mechanics, Springer.

Zöller, Gert and Matthias Holschneider, (2016), “The Maximum Possible and the Maximum Expected Earthquake Magnitude for Production-Induced Earthquakes at the Gas Field in Groningen, The Netherlands”, Bulletin of the Seismological Society of America, Vol. 106, No. 6, pp. 2917–2921, December 2016, doi: 10.1785/0120160220.

Groningen:

Bourne, S J & Oates, S., 2013. Probability of an earthquake greater than magnitude 4 due to gas production from the Groningen Field, Rijswijk, The Netherlands.

Bourne, S., Oates, S., and Bommer, J.J. A probabilistic seismic hazard assessment for the Groningen Field. Technical Report. Shell Global Solutions International. Rijswijk, The Netherlands (2013).

Bourne, S.J. & Oates, S., 2013. Induced strain and induced earthquakes within the Groningen Gas Field: Earthquake probability estimates associated with future gas production, Rijswijk, The Netherlands.

Bourne, S. J., S. J. Oates, J. van Elk, and D. Doornhof, (2014), “A seismological model for earthquakes induced by fluid extraction from a subsurface reservoir”, J. Geophys. Res. Solid Earth, 119, 8991–9015, doi:10.1002/2014JB011663.

Dost, B. and Kraaijpoel, D. (2012) The August 16, 2012 earthquake near Huizinge (Groningen). KNMI report, KNMI De Bilt, 2013.

Hettema, M.H.H., Schutjens, P.M.T.M., Verboom B.J.M., Gussinklo, H.J., (2000) Production-Induced Compaction of a Sandstone Reservoir: The Strong Influence of Stress Path. SPE Reservoir Eval. & Eng. 3 (4) PP. 342-347.

Muntendam-Bos, A. G., & Waal, J. A. de. (2013). Reassessment of the probability of higher magnitude earthquakes in the Groningen gas field: Including a position statement by KNMI.

Van den Bogert, P. Van Eijs, R., van der Wal, O (2013) Groningen Fault Stability Assessment

Visser, C. (edt.), Groningen Field Review 2012, Static Modelling and Hydrocarbon Volume Determination, Document number: EP201203204663.

Netherlands General:

BOA (1993) Eindrapport multidisciplinair onderzoek naar de relatie tussen Gaswinning en Aardbevingen in Noord-Nederland; Begeleidingscommissie Onderzoek Aardbevingen, 1993

De Crook, Th., H.W. Haak & B. Dost (1998). Seismich risico in Noord-Nederland.KNMI (Koninklijk Nederlands Meteorologisch Instituut), Techn. Rep., De Bilt, Netherlands.

Dost, B., Goutbeek, F., van Eck, T., Kraaijpoel, D. (2012) Monitoring induced seismicity in the North of the Netherlands: status report 2010. WR 2012-03.

Dost, B., T. van Eck & H. Haak (2004). Scaling of peak ground acceleration and peak ground velocity recorded in the Netherlands. Bolletino di Geofisica Teorica ed Applicata 45(3), 153-168.

Dost, Bernard et al., 2012. Monitoring induced seismicity in the North of the Netherlands: status report 2010,

Haak, H.W. and De Crook, T. Seismische analyse van aardbevingen in Noord-Nederland. KNMI report WR 94-1. KNMI, de Bilt (1994).

Houtgast, G. Aardbevingen in Nederland. KNMI report 179. KNMI, de Bilt (1992).

Kraaijpoel, D. & B. Dost (2013). Implications of salt-related propagation and mode conversion effects on the analysis of induced seismicity. Journal of Seismology 17(1), 95-107.

Kraaijpoel, D. et al., 2008. Location of induced earthquakes in the Netherlands gas fields. In ESC General Assembly 2008, September 7-12, 2008, Hersonissos.

NAM (2010) "Bodemdaling door Aardgaswinning –NAM-velden in Groningen, Friesland en het Noorden van Drenthe– Status Rapport 2010 en Prognose tot het jaar 2070" (EP201006302236)

NAM (2011a). Subsurface Technical Report Subsidence Modelling of Ameland Fields. UIE Report No: EP201105208617

NAM (2011b). Subsurface Technical Report Subsidence Modelling of Anjum and Waddenzee Fields. UIE Report No: EP201105208677

Roest, J.P.A., Kuilman, W. (1993). Geomechanische Analyse van de lichte aardschokken in het Eleveld reservoir, TU-Delft.

Van Eijs R., van Dalfsen, W. (2004) Borehole observations of maximum horizontal stress orientations in the Dutch upper crust. TNO-NITG – Information, December 2004.

Van Eijs, R.M.H.E., Mulders, F.M.M., Nepveu, M., Kenter, C.J., Scheffers, B.C. (2006) Correlation between hydrocarbon reservoir properties and induced seismicity in the Netherlands. Eng. Geology, 84, p99-111.

General:

Brudy, M., Kjørholt, H. (2001) Stress orientation on the Norwegian continental shelf derived from borehole failures observed in high-resolution borehole imaging logs. Tectonophysics 337, pp. 65-84.

Committee on Induced Seismicity Potential in Energy Technologies. Induced Seismicity Potential in Energy Technologies. The National Academies Press (2013).

Deichmann, N. (2006). Local magnitude, a moment revisited. Bulletin of the Seismological Society of America 96(4A), 1267-1277.

Geertsma, J. (1973) , Land Subsidence Above Compacting Oil and Gas Reservoirs, J. Petr. Tech., pp.734-744.

Geertsma, J. and van Opstal, G. (1973). A Numerical Technique for Predicting Subsidence Above Compacting Reservoirs, Based on the Nucleus of Strain Concept. Verh. Kon. Ned. Geol. Mijnbouwk. Gen., 28, pp. 63-78.

Glab, M. and Van Eijs. R (2001), Localisation of Sensitive Reservoir Settings for Induced Seismicity using FEM, Report TNO-NITG 00-320-A

Grasso, J.R. Mechanics of Seismic Instabilities Induced by the Recovery of Hydrocarbons. Pure and Applied Geophysics, Vol. 139, No. 3/4 (1992)

Hanks, T.C. & Kanamori, H., 1979. Moment magnitude scale. Journal of Geophysical Research, 84(B5), pp.2348–2350.

Hanssen, R. F. (2001), Radar Interferometry: Data Interpretation and Error Analysis, Kluwer Academic Publishers, Dordrecht.

Implementing Convection in a Reservoir Simulator: A Key Feature in Adequately Modelling the Exploitation of the Cantarell Complex, E. Manceau, E. Delamaide, J.C. Sabathier, S. Jullian, F. Kalaydjian, IFP; J.E. Ladron De Guevara, J.L. Sanchez Bujanos, F.D. Rodriguez, Pemex, 2001 71303-PA SPE Journal Paper

Kanamori, H. (1994), Mechanics of Earthquakes. Annual Rev. Earth Planet Sci., 22, p207-237.

Ketelaar, V. (2009), Satellite radar interferometry – subsidence monitoring techniques, Springer, Dordrecht, ISBN 978-1-402-09427-9

Klose, C.D., 2012. Mechanical and statistical evidence of the causality of human-made mass shifts on the Earth's upper crust and the occurrence of earthquakes. Journal of Seismology, 17, pp.109–135.

Leonard, M. (2010). Earthquake Fault Scaling: Self-Consistent Relating of Rupture Length, Width, Average Displacement, and Moment Release. Bulletin of the Seismological Society of America, 100(5A), 1971–1988. doi:10.1785/0120090189

Main, I., Irving, D., Musson, R. and Reading, A. Constraints on the frequency-magnitude relation and maximum magnitudes in the UK from observed seismicity and glacio-isostatic recovery rates. Geophysical Journal International (1999), Vol. 137, pp. 535-550.

McGarr, A., 1976. Seismic Moments and Volume Changes. Journal of Geophysical Research, 81(8), pp.1487–1494.

Mulders, F.M.M. (2003), Modelling of stress development and fault slip in and around producing gas reservoirs, Ph.D. thesis, Delft University of Technology.

Scholz, Christopher H. Earthquakes and friction laws. Nature (1998) 391(1st January 1998): 37-42.

Segall, P. (1989). Earthquakes triggered by fluid extraction. Geology, Vol. 17, pp. 942-946.

Segall, Paul, Grasso, J.-R. & Mossop, A., 1994. Poroelastic stressing and induced seismicity near the Lacq gas field, southwestern France. Journal of Geophysical Research, 99(B8), pp.15,423–15,438.

Suckale, Jenny. Moderate-to-large seismicity induced by hydrocarbon production. The Leading Edge March (2010): 310 – 319.

TNO 2012 R10198, (2012), L van Thienen-Visser, M. Nepveu, J. Hettelaar "Deterministische hazard analyse voor geïnduceerde seismiciteit in Nederland"

Salt Creep:

Breunese, J.N, van Eijs R.M.H.E., de Meer, Kroon I.C. (2003). Observation and prediction of the relation between salt creep and land subsidence in solution mining – The Barradeel case. Proc. SMRI Conf., Chester, UK.

Heard, H.C. (1972). Steady-state flow in polycrystalline halite at pressure of 2 kilobars. AGU Geophysical Monograph Series, 16: pp. 191-210.

Munson, D.E., and P.R. Dawson. (1979). Constitutive Model for the Low Temperature Creep of Salt (with Application to WIPP). SAND79-1853, Sandia National Laboratories.

Orlic, B. and Wassing, B.B.T. (2012), Modelling stress development and fault slip in producing hydrocarbon reservoirs overlain by rock salt caprocks, ARMA 12-145, 46th US Rock Mechanics / Geomechanics Symposium, Chicago, USA, 24-27 June 2012.

Spiers, C. J., J. L. Urai, G. S. Lister, J. N. Boland, and H. J.Zwart. (1986). The influence of fluid-rock interaction on the rheology of salt rock: Nuclear Science and Technology,EUR 10399 EN, 131 p.

Spiers, C.J. & Carter, N.L.(1998) Microphysics of rocksalt flow in nature. In: M. Aubertin & H.R.Hardy (eds.) The Mechanical Behaviour of Salt: Proceedings of the Fourth Conference Serieson Rock and Soil Mechanics, 22, TTP Trans Tech Publications, Clausthal-Zellerfeld, pp.115-128.

Weertman, J. (1955). Theory of steady-state creep based on dislocation climb. J. Appl. Phys. 26 (10), 1213–1217.

Rate dependence:

Dieterich, James H., (1992), "Earthquake nucleation on faults with rate- and state-dependent strength", Tectonophysics, 21 1 (1992) 1 15-134

Hartley, R.R. & Behringer, R.P., 2003. Logarithmic rate dependence of force networks in sheared granular materials. Nature, 421(6926), pp.928–31. Available at: http://www.ncbi.nlm.nih.gov/pubmed/12606996.

Pruiksma, J.P., J.N. Breunese, K. van Thienen-Visser (2013) A general framework for rate dependent compaction models for reservoir rock. TNO 2013 R11405

Kostrov, V.V., 1974. Seismic moment and energy of earthquakes, and seismic flow of rocks. Izv. Acad. Sci. USSR Phys. Solid Earth, Eng. Transl., 1, pp.23–40.

Lahaie, F. & Grasso, J.R., 1999. Loading rate impact on fracturing pattern: Lessons from hydrocarbon recovery, Lacq Gas Field, France. Journal of Geophysical Research, 104(B8), p.17941. Available at: http://doi.wiley.com/10.1029/1999JB900139.

Santarelli, F. J., Tronvoll, J. T., Svennekjaer, M., Skele, H., Henriksen, R. and Bratli, R. K. 1998. Reservoir stress path: The depletion and rebound. SPE/ISRM Eurock '98, Trondheim, Norway, 8th-10th July 1998. 7pp.

Waal, J.A. de (1986). On the rate type compaction behaviour of sandstone reservoir rock. PhD thesis, Technische Hogeschool, Delft.

International:

Ahorner, L., Pelzing, R. (1985) The source characteristics of the Liège earthquake on November 8, 1983, from digital recordings in West Germany. In: P. Melchior (ed), Seismic activity in Western Europe. D. Reidel, Dordrecht, pp. 263-289.

Amorèse, D., Grasso, J.-R., Plotnikova, L.M., Nurtaev, B.S. and Bossu, R. Rupture Kinematics of the Three Gazli Major Earthquakes from Vertical and Horizontal Displacements Data. Bulletin of the Seismological Society of America (1995), Vol. 85, No. 2, pp. 552-559. Avouac, Jean-Philippe. Earthquakes: Human-induced shaking. Nature Geoscience (2012) 5: 763–764.

Annunziata, G., E. Priolo, (2015), "MICRO-SEISMIC MONITORING OF UNDERGROUND GAS STORAGES THE "COLLALTO" SEISMIC NETWORK", 12th Offshore Mediterranean Conference and Exhibition in Ravenna, Italy, March 25-27, 2015.

Bardainne, T., Dubos-Sallée, N., Sénéchal, G., Gaillot, P. and Perroud, H. Analysis of the induced seismicity of the Lacq gas field (Southwestern France) and model of deformation. Geophys. J. Int. (2008) 172, 1151–1162.

Bourne, S.J. et al., 2006. Monitoring deformation of a carbonate field in Oman: Evidence for large-scale fault reactivation from microseismic, InSAR & GPS. In 68th EAGE Conference and Exhibition, Vienna.

Bourne, S.J., Maron, K., Oates, S.J. and Mueller, G. Monitoring Reservoir Deformation on Land - Evidence for Fault Re-Activation from Microseismic, InSAR, and GPS Data. 68th EAGE Conference & Exhibition (2006).

Dahm, T., Krüger, F., Stammler, K., Klinge, K., Kind, R., Wylegalla, K. and Grasso, J.-R. The 2004 Mw 4.4 Rotenburg, Northern Germany, Earthquake and Its Possible Relationship with Gas Recovery. Bulletin of the Seismological Society of America (2007), Vol. 97, No. 3, pp. 691–704.

Davis, S. D., Nyffenegger, P. and Frohlich, C. The 9 April 1993 earthquake in south-central Texas: Was it induced by fluid withdrawal? Bulletin of the Seismological Society of America (1995), 85 1888-1895.

Davison, J.M., Ita, J., Hofman, R.A., Seli, P. and Ong, P., (2010), Ensuring Production in the Malaysian F6 Field Using Field Monitoring and Geomechanical Forecasting, SPE 132195, Int. Oil & Gas Conf. and Exhibition, 8-10 June 2010, Beijing, China.

Deflandre, J.-P., F. Huguet, (2002), "MICROSEISMIC MONITORING ON GAS STORAGE RESERVOIRS: A TEN-YEAR EXPERIENCE", Institut Français du Pétrole, France, WORLDWIDE GAS PRODUCTION MONITORING AND STORAGE, pp 455.

Frohlich. C. Induced or triggered earthquakes in Texas: assessment of current knowledge and suggestions for future research. University of Texas at Austin Technical Report G12AP20001 (2012).

Guha, S. K. Induced earthquakes. Kluwer (2000). Keahey, R.A. Fashing Field, Atascosa-Karnes Counties, Texas. In Natural Gases of North America, Volume One, AAPG Special Volumes (1968).

Gutenberg, B. & Richter, C., 1954. Seismicity of the Earth and Associated Phenomena 2nd edition., Princeton University Press, Princeton, New Jersey.

Khaksar, A., White, A., Rahman, K. and Burgdorff, K., Ollarves, R., (2012), "Geomechanical Evaluation for Short Term Gas Storage in Depleted Reservoirs", 46th US Rock Mechanics / Geomechanics Symposium held in Chicago, IL, USA, 24-27 June 2012.

Maury, V.M.R., Grassob, J.-R. & Wittlinger, G., 1992. Monitoring of subsidence and induced seismicity in the Lacq Gas Field (France): the consequences on gas production and field operation. Engineering Geology, 32(3), pp.123–135.

Ottemöller, L., Nielsen, H. H., Atakan, K., Braunmiller, J. and Havskov, J. The 7 May 2001 induced seismic event in the Ekofisk oil field, North Sea. Journal of Geophysical Research (2005), Vol. 110, B10301.

Simpson, D.W. and Leith, W., (1985), "The 1976 and 1984 Gazli, USSR, earthquakes – were they induced?", Bulletin of the Seismological Society of America (1985), Vol. 75, No. 5, pp. 1465-1468.

Zoback, M. & Zinke, J., 2002. Production-induced Normal Faulting in the Valhall and Ekofisk Oil Fields. Pure and Applied Geophysics, 159, pp.403–420.

Appendix I: GPS Subsidence Analysis

In this Appendix the filtering of the GPS data and the fitting with the Kelvin-Voigt Model is explained. Figure 98 shows the unfiltered heave data of the stations TAQA2 to TAQA5 relative to the signal in a reference GPS station and the Bulk Volume average Eclipse pressure between October 2013 and January 2017. For subsidence and surface heave one should take the pressure change in the aquifer into account as well. Hence, for subsidence the bulk volume average pressure is the relevant measure and not the gas pressure. Figure 99 shows the same data after applying a Butterworth bandpass filter that filters away the high frequency noise. As zero reference level the average subsidence between 17-Jan-2014 and 24-Aug-2014 is taken. Table 10 lists the averaged average surface heave per bar of the 4 stations and the ratio with respect to station TAQA2. Figure 100 shows the ratio of the heaves of the station relative to station TAQA2

The surface heave data shows:

- A delayed response with respect to pressure changes.
- The strongest heave in TAQA2 followed by TAQA4 and TAQA5 that are close. Station TAQA3 shows the smallest increment in heave per bar pressure increment but exhibits a climbing trend which is absent in the other stations.
- Oscillations on top of the cyclic pressure response.

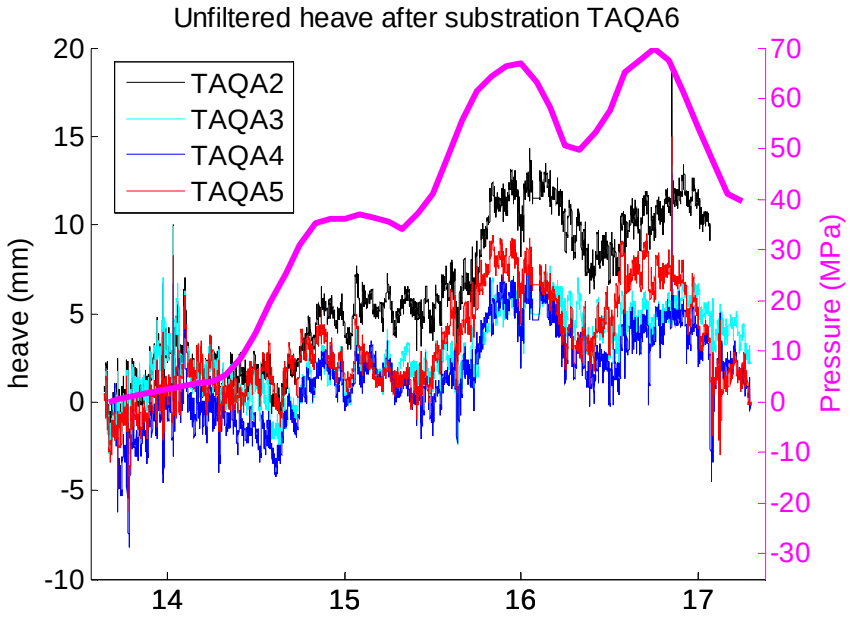

Figure 98: Unfiltered GPS data relative to reference station TAQA-6 on the axis and the Eclipse simulated bulk volume average reservoir pressure at the right axis

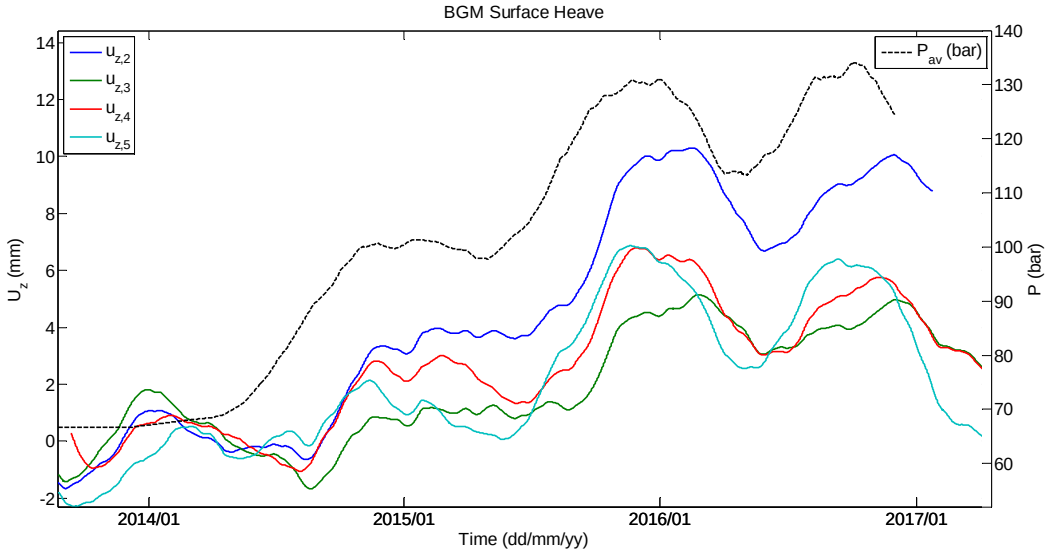

Figure 99: Bandwidth filtered GPS data relative to a reference station on the left axis and the Eclipse simulated bulk volume average reservoir pressure at the right axis. Data was filtered using a Butterworth bandpass filter that filters out the high frequency noise

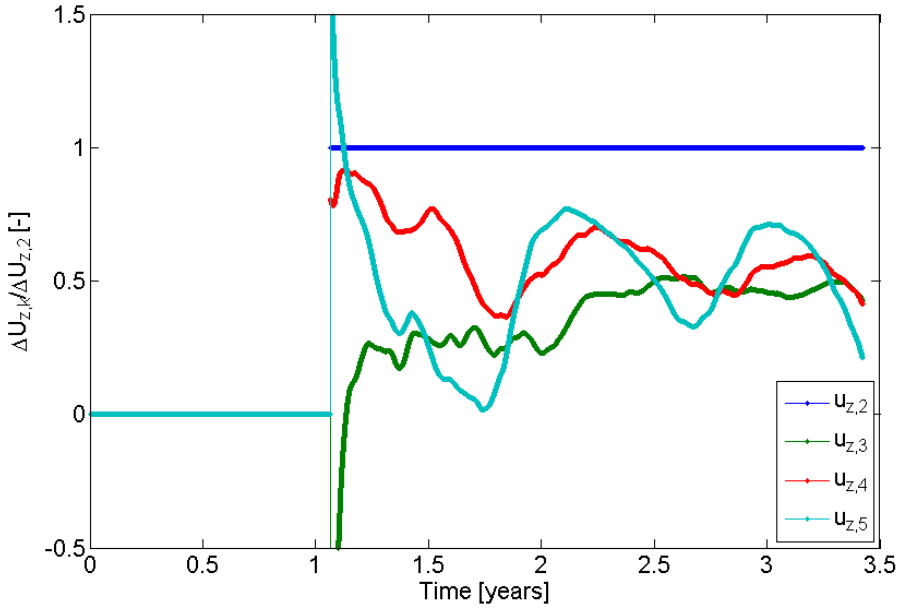

Figure 100: Surface heave ratio of each station w.r.t. TAQA2

Table 10: Time average magnitude of surface heave in 4 GPS stations and ratio w.r.t TAQA2

(Data)		TAQA2	TAQA3	TAQA4	TAQA5
DUZ/Dpavg	(mm/bar)	0.125	0.050	0.073	0.068
Ratio w.r.t TAQA2	(-)	1.00	0.40	0.59	0.54

Viscoelastic response – Kelvin Voigt model

The data of each station shows a clear time delay with respect to change in the pressure. This indicates a viscoelastic response rather than an elastic response. Here the observed GPS heave is fitted by convolving the pressure response in time with the viscoelastic Elastic time delay. The viscoelastic response is modelled by the Kelvin-Voigt model. In addition to the time delay the data shows oscillations on top of the periodicity

present in the pressure response. For each station the viscoelastic response to the pressure will be fitted together with the periodic signal.

Kelvin-Voigt model (KV)

The Kelvin-Voigt model describes a damped-spring system in parallel, where the spring response is delayed by a damper (see Figure 101). This model is commonly used to simulate the viscoelastic response in rock mechanics and simulates the evolution of the strain as function changes in the pressure. For small strain, the Kelvin Voigt model can be casted in the form:

$$\tilde{\eta}\frac{d\Delta u_{KV}}{dt} + \tilde{E}\Delta u_{KV} = \Delta p(t) \tag{9}$$

It expresses the evolution of the displacement increment as function of the pressure increment. Here $\tilde{E}$ ([Pa/m]) is the elastic coefficient and $\tilde{\eta}$([Pa*year/m]) the viscous coefficient, that are related to the Youngs modulus and viscosity, via

$$\tilde{E} = \frac{E}{\alpha_B L_z}, \qquad \tilde{\eta} = \frac{\eta}{\alpha_B L_z} \tag{10}$$

Where α_B is the Biot coefficient, L_z is the characteristic vertical length scale of the reservoir. The latter can be determined from the FEM model via:

$$L_z = \frac{\Delta U_z}{\Delta P} E = 0.6\frac{mm}{bar} 18GPa = 106m \tag{11}$$

Which is about half the reservoir height. The increment in pressure and displacement are defined relative to a reference time (t_0).

$$\begin{aligned} \Delta p(t) &\equiv p(t) - p(t_0) \\ \Delta u_{KV} &= u_{KV}(t) - u_{KV}(t_0) \end{aligned} \tag{12}$$

The time derivative in the KV model (9) models the viscous response of the damper. For large viscosities the damper dominates the response, while for small dampers the elastic response dominates.

For a zero initial displacement increment

$$\Delta u_{KV}(t_0) = 0, \tag{13}$$

the solution to (9) and (13) can be written as a convolution (or memory) integral

$$\Delta u_{KV}(t) = \frac{1}{\tilde{\eta}}\int_{t_0}^{t} \exp\left(-\frac{t-t'}{\tau}\right)\Delta p(t')dt' \tag{14}$$

where the relaxation time τ is defined as the ratio of the damper over spring strength:

$$\tau \equiv \frac{\tilde{\eta}}{\tilde{E}} = \frac{\eta}{E} \tag{15}$$

It quantifies the exponential convergence of the solution to its elastic response.

Behaviour for constant pressure drop (relaxation time and heave magnitude)

To make the behaviour of the KV model more insightful consider a constant pressure drop. For a constant pressure increment the integral (14) simplifies to:

$$\Delta u_{KV}(t) = \frac{1}{\tilde{E}}\left(1 - \exp\left(-\frac{t}{\tau}\right)\right)\Delta p \tag{16}$$

For long time ($t >> \tau$) the displacement increment converges to the elastic response:

$$\Delta u_{KV} = \frac{\Delta p}{\tilde{E}} \tag{17}$$

This shows that the magnitude of the displacement increment is eventually controlled by the elastic part and the time delay by the relaxation time τ. Fully elastic systems can be considered as a special case for which the relaxation time vanishes.

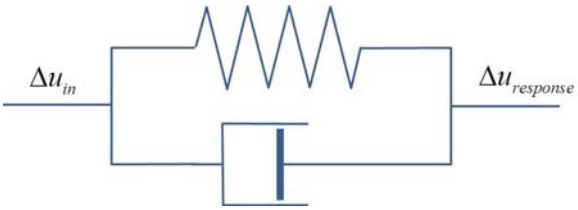

Figure 101: Kelvin-Voigt spring damper system

Fitting the surface heave of each stations / periodic filter

Besides the delay in the heave response with respect to the pressure signal, the response of each station shows a clear periodic (noise) signal that is not related to the reservoir pressure response. These (periodic) noise signals are commonly related to the location of the GPS satellites (semi-annual period of 175days), annual temperature evolution, precipitation and air pressure, but for Bergermeer such correlation was not found.

Although the origin of the periodic noise in the Bergermeer subsidence response is yet unclear, it has to be accounted for when fitting the data (see van de Marel, 2015). As such the total displacement of a station (Δu_k) consists of the Kelvin-Voigt response caused by the reservoir pressure change and a periodic response, where this study limited the periodic response to two frequencies.

$$\Delta u_k = \Delta u_{KV}(\tilde{E}_k, \tilde{\eta}_k) + \Delta u_0 + \sum_{i=1}^{2} A_{k,i} \sin\left(2\pi\left(t - t_{0,k,i}\right)/T_{k,i}\right) \tag{18}$$

Here $A_{k,i}$ is the amplitude, $T_{k,i}$ the period and $t_{0,k,i}$ the time shift of period *i* for station *k*. Consequently, the surface heave of each station is fitted separately by the following 9 parameters $\tilde{E}_k, \tilde{\eta}_k, \Delta u_0, A_{k,1}, t_{0,k,1}, T_{k,1}, A_{k,2}, t_{0,k,2}, T_{k,2}$. The optimization fit-function attempts to minimize the time-average deviation between the simulated and observed heave for GPS station k quantified as:

$$\in_k = \left(\int_{t_k}^{t_e} \left(\Delta u_k(t) - u_{obs,k}(t)\right)^2 dt\right)^{1/2} \tag{19}$$

Starting time in the fit is August 2014 and end time December 2016. The first part is not included as it may still show the relaxation to the pressure rise at earlier times. Table 11 lists the resulting fit parameter,

Table 12 the resulting physical parameters for a characteristic vertical reservoir length scale of 106m. The fit shows

- The Youngs Modulus scales inversely proportional to the surface heave (as they should).
- The viscosities are in the order of 10^{16} which is a typical value found in literature for Rock-Salt (see Spiers et al.). However, rock-salt creep seems unlikely to cause the relaxation as salt creep reacts elastically for short time (instantaneous response) and only gives a relaxation response for longer times, like in a spring-damper system in series. As the response of the overburden is expected to be elastic as well, the source of the damping is most likely the reservoir itself. A plausible explanation is a relaxation of the response due to creep.
- Relaxation times for the 4 stations are on average 0.25yr. However, relaxation times are much larger for the Northern stations. The relaxation of the Southern stations TAQA-4 and TAQA-5 is only a few days.
- The period of the first noise cycle is consistent for all 4 stations, but amplitude and phase shifts are inconsistent.
- The second noise period is quite comparable for stations TAQA-3 and TAQA-4 with a period of about 0.9 years but inconsistent over all.

Figure 102 shows a good fit between model (18) and the observed data for each of the 4 stations, with a standard deviation of about 0.5mm.

Table 11: Fit parameters for the individual stations

	$\tilde{E}$	$\tilde{\eta}$	Δu_0	T_1	A_1	t_1	T_2	A_2	t_2
Station	(Pa/m)	(Pa*year/m)	(mm)	(year)	(mm)	(year)	(year)	(mm)	(year)
TAQA2	5.84E+08	1.08E+08	-1.2	0.37	3.0	0.10	0.37	-3.2	0.12
TAQA3	1.04E+09	7.18E+08	-0.6	0.35	-0.4	0.21	0.86	-0.7	0.01
TAQA4	1.03E+09	4.45E+07	-0.8	0.39	-0.1	0.00	0.95	-1.1	0.73
TAQA5	9.33E+08	1.92E+07	-1.5	0.43	0.1	-0.98	0.29	-0.1	0.03

Table 12: Physical parameters (obtained for a characteristic length scale of 106m)

Station	tau	E – Youngs	Viscosity	E_ratio
	(days)	(GPa)	(Pa*s)	(-)
TAQA2	67	66.03	1.6E+16	100%
TAQA3	253	117.17	1.1E+17	56%
TAQA4	16	116.47	6.6E+15	57%
TAQA5	8	105.46	2.8E+15	63%

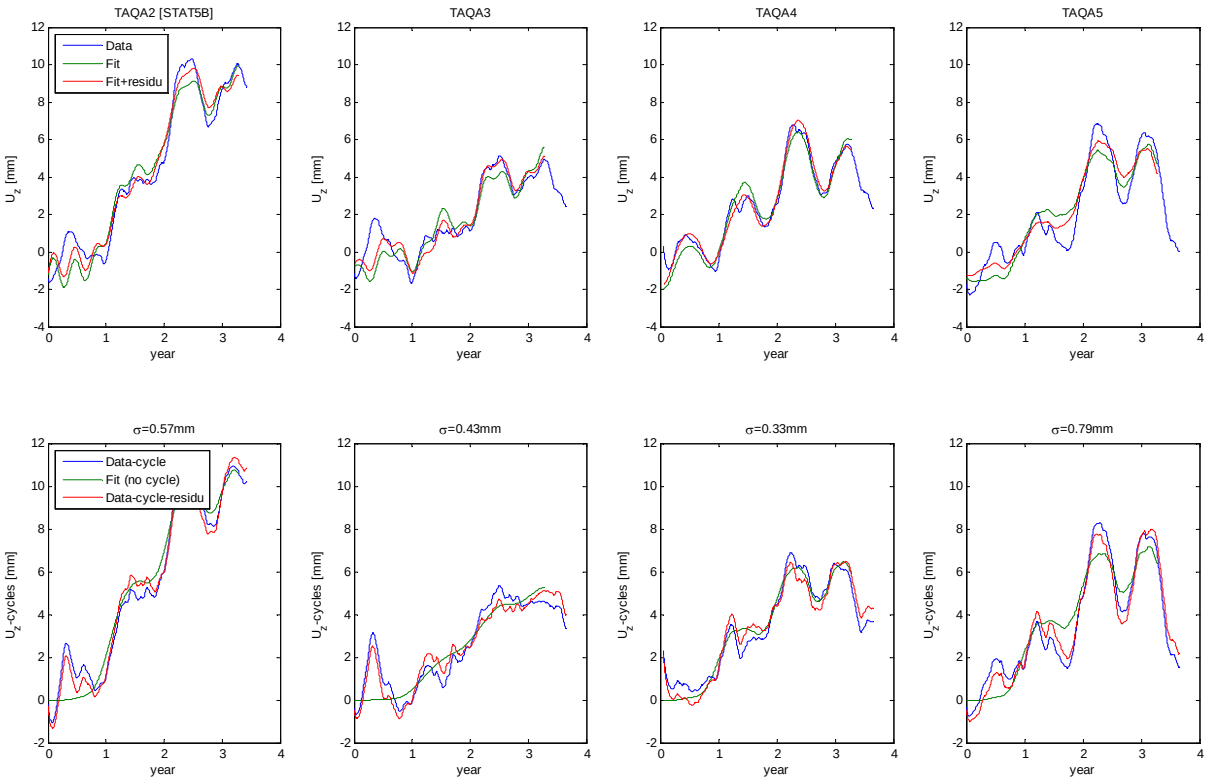

Figure 102: Model fit to observed pressure heave for stations Taqa 2-5. Top row fit of observed data. Bottom row: fit of filtered subsidence data.

Fitting the average residual of all stations

Figure 103 shows the deviation of the fits from the observed heave together with the average deviation, called the residual and defined as:

$$\in(t) \equiv \frac{1}{4}\sum_{k=1}^{4}\left(\Delta u_k(t) - \Delta u_{obs,k}(t)\right) \approx A_{residu}\sin\left(2\pi\left(t - t_{res,0}\right)/T_{res}\right) \qquad (20)$$

While the individual deviation is quite erratic the residual is still cyclic in nature with a period of 2 years. To improve the data fit the residual of all 4 stations is fitted as well. This was done because the Simplex

minimum search routine in the fitting procedure was not optimal, so that it was necessary to subtract also the period component of the residual. Figure 103 shows the resulting fit to the residual. Figure 102 (top row) compares the fit with and without residual to the observed surface heave, they are all in good agreement.

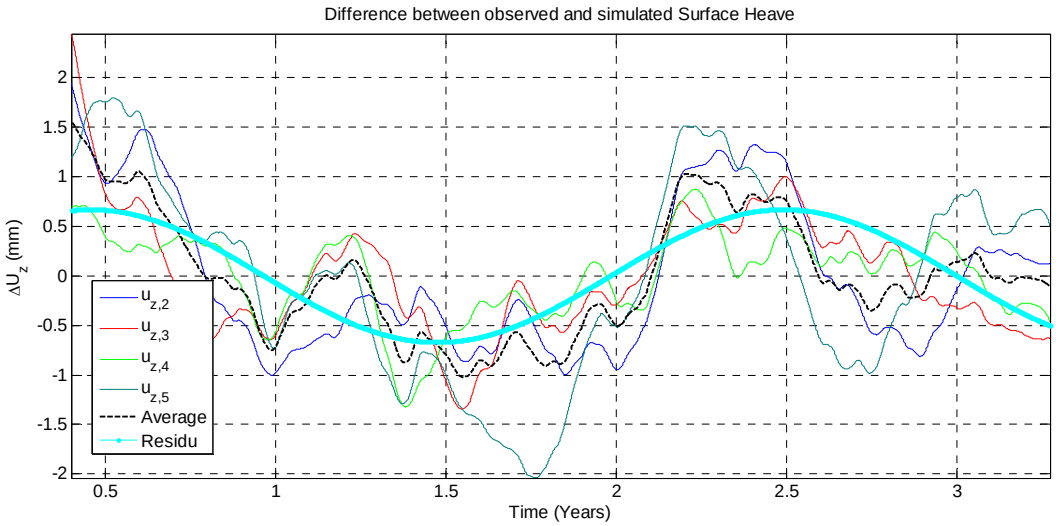

Figure 103: Fit of the residual heave

Filtered surface heave

The filtered observation data is the data that can be related to the (Kelvin-Voigt) pressure response only. It is the observed surface corrected for the cyclic response and for the residual noise:

$$\Delta u_{obs,KV,k} = \Delta u_{obs,k}(t) - \Delta u_0 - \sum_{i=1}^{2} A_{k,i} \sin\left(2\pi\left(t - t_{0,k,i}\right)/T_{k,i}\right) - A_{residu} \sin\left(2\pi\left(t - t_{res,0}\right)/T_{res}\right) \qquad (21)$$

Figure 102 (bottom row) shows the filtered surface heave of the four stations and the Kelvin-Voigt part of the fit. Corrected for the cyclic noise each station exhibits a similar trend. The Kelvin-Voigt part of the data fit ($\Delta u_{KV,k}$) is for all stations in good agreement.

Figure 104 shows the filtered observation of all station in combination with the Bulk Volume average reservoir pressure. These will be used for the comparison to the response of the FEM model

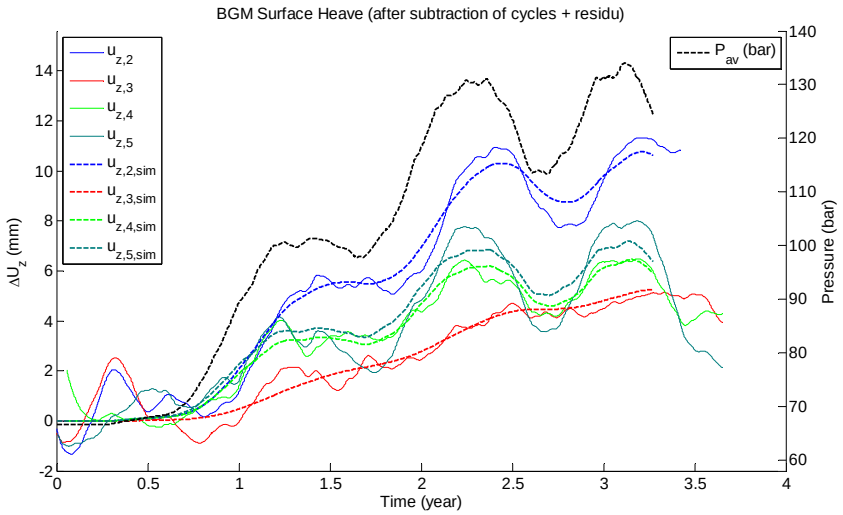

Figure 104: Filtered heave data (observation – cycle – residual) and Kelvin-Voigt fit at the left axis and the Eclipse simulated bulk volume average reservoir pressure at the right axis

Appendix II: Viscoelastic representation of Salt Creep

The salt flow was modelled with a simple viscoelastic Maxwell model that captures the elastic response and allows for relief of shear stress with a reduction in shear modulus over time. In the Maxwell model the deviatoric stress, $\sigma_{d,}$ is computed from strain history with a relaxation function Γ, that gives an initial elastic response and then relaxes shear stress with a lower shear modulus:

$$\sigma_d = 2\int_0^t \Gamma(t-t')\frac{\partial \varepsilon}{\partial t'}dt', \quad \Gamma(t-t') = G_{EL}\left[a_\infty + \sum_{i=1..N} a_i \exp(-t/\tau_i)\right], \quad a_\infty + \sum_{i=1..N} a_i = 1 \tag{22}$$

The Maxwell model represents the response of a single spring and multiple spring-dashpots in parallel as shown in Figure 30. In (22) G_{EL} is the elastic shear modulus, τ_i is the relaxation time of a dashpot, a_i is the fraction of the modulus accounted for by a spring connected to a dashpot and a_∞ the fraction of the modulus represented by the single spring. The initial response of the system is fully elastic with shear modulus G_{EL} while over time shear modulus of the entire system reduces to ($a_\infty G_{EL}$) because of the vanishing contribution of each of the spring-dashpot combo's.

A 2D tri-axial test is performed to match the Generalized Maxwell model to the creep law. In this study the salt creep is described by the Empirical creep

$$\partial_t \varepsilon \sim 10^{-7}\left(\sigma_{dev}/\sigma_{ref}\right)^5 \tag{23}$$

The stress dependency to the power 5 makes the creep behaviour very non-linear and its behaviour path specific. The viscoelastic response has to be calibrated to the Salt creep behaviour for a representative order of magnitude of the stress.

Figure 105 shows a 2D tri-axial cell in which the creep behaviour of a salt block of 20x10cm (h x w) is simulated. Initially the block is stressed isotropically to 50MPa, which corresponds to a depth of about 2000m at an average formation density of 2500kg/m3. At t=0 the Piston is lowered by 0.023mm and the rock is instantaneous deformed. The resulting strain is held constant in time. This introduces a stress differential $\sigma_z - \sigma_x$ of about 4MPA. Similar to a fluid salt cannot support shear stresses or stress differentials in the long and over time the stress will become isotropic. Figure 106 shows the fall off of the stress differential with time. For constant strain the Generalized Maxwell model simplifies to

$$\sigma_{dev} = 2\varepsilon_{vol} G_{EL}\left[a_0 + \sum_{i=1}^{N}\int_0^t a_i \exp\left(-\frac{t}{\tau_i}\right)dt\right] \tag{24}$$

The coefficient where fitted to the creep response over a time frame of 30 years. At least 3 Maxwell nodes (spring-dashpot) were required to get an accurate fit with the Creep law, as shown in Figure 106. The initial response is Elastic, which corresponds to the Elastic shear Modulus. The resulting coefficient that are used in are listed in Table 13

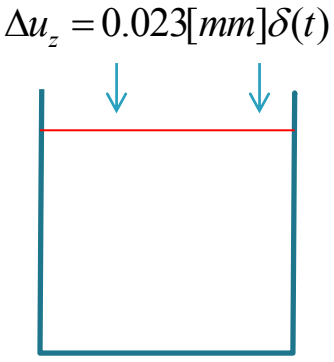

Figure 105: Tri-axial test. A block of Salt is initially isotropically stressed at 50MPa At t=0 the top piston is lowered by 0.023mm which introduces a stress differential. The strain is held constant while the salt creep starts to deform such that the stress differential vanishes over time.

Table 13: Fit coefficients of the Generalized Maxwell model with 3 nodes to the Empirical creep law for an initial stress differential of 4.2MPa

G_{EL}	a_{inf}	a_1	a_2	a_3	τ_1	τ_2	τ_3
GPa	(-)	(-)	(-)	(-)	(yr)	(yr)	(yr)
17.8	0.253	0.254	0.282	0.211	0.235	1.761	12.96

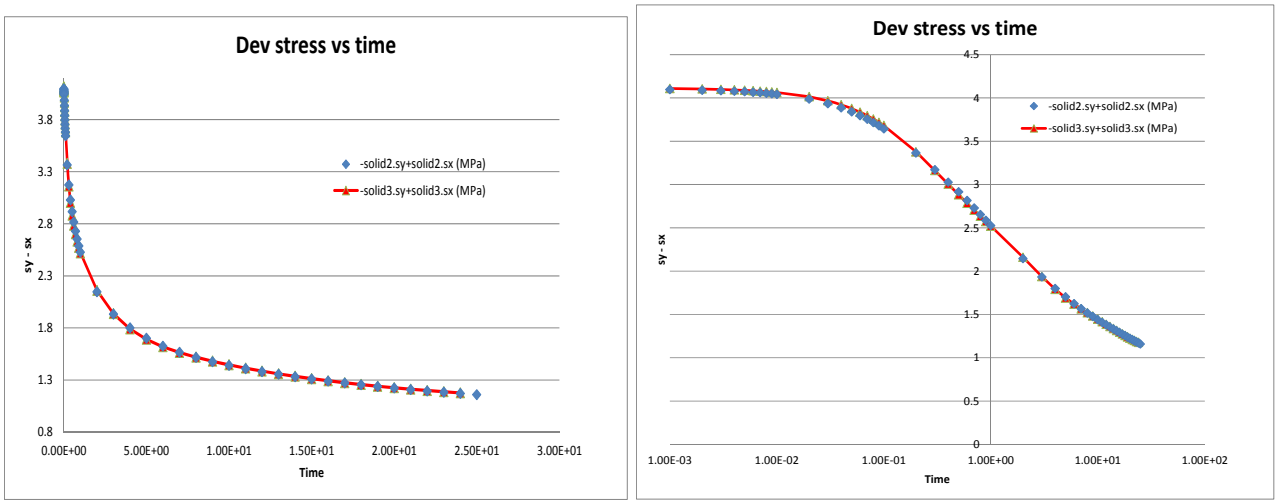

Figure 106: Comparison between salt creep (red line) and Generalized Maxwell model (blue triangles) of the evolution of the stress differential over time (left) linear scale (right) log-log scale.

Appendix III: 2D slip modelling

During depletion 4 Earthquakes exceeding magnitude 3 occurred (see Table 14). A magnitude 3 event involves a slip area of about $10^5 m^2$ (indicated as $O(10^5 m^2)$) which covers a significant fraction of the total fault area that is in contact with the reservoir. Because of this the (seismic) slip associated to these 4 events should be explicitly accounted for, since it will significantly affect the state of the shear stress at the end of depletion. The refill seismicity is of considerably smaller order and involves the slippage of much smaller area's ($O(<10^3 m^2)$). In the approach adopted here the slip is modelled as a continuous process, but such that the cumulative seismic moment in 2001 equals the cumulative seismic moments of the depletion Earthquakes. The difference between the 2D slip simulation and the 2D simulation without slip will be used to derive a slip correction for the 3D simulation. The justification is in the fact that the shear stress is predominantly oriented in the dip direction and that the along-strike shear component is much smaller.

Table 14: Seismic event during depletion, their magnitude (M_w), seismic moment (M_0) and the cumulative seismic moment (ΣM_0)

Date	M_w	M_0	ΣM_0
1994-08-06	3	4.00E+13	4.00E+13
1994-09-21	3.2	7.00E+13	1.10E+14
2001-09-09	3.5	1.90E+14	3.00E+14
2001-09-10	3.1	6.30E+13	3.63E+14

2D model construction

A 2D cross-section is selected at the most critical point in the 3D model, i.e. the scissor point where block 2N and block 1M make contact (see Figure 107). The model is calibrated in the same way as the 3D model (see section 4-5), i.e. the poroelastic coefficient follows from the stress measurements and the compaction coefficient from surface heave measurement while the Poisson ratio is chosen. For the refill the compaction coefficient follows again from the GPS measurements and Geodetic data. The degree of freedom that is left is used to bring the model behaviour in line with the observed refill seismicity. Figure 108 shows that the CSR for the 2D model without slip coincides with the corresponding cross-section of the 3D model, albeit with much more detail.

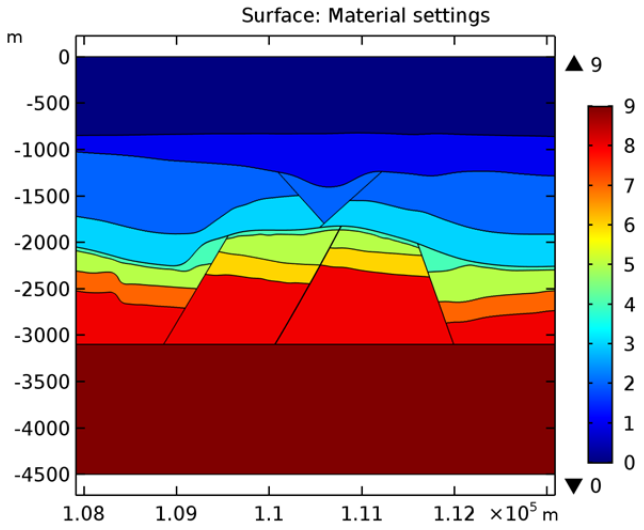

Figure 107: Geology of the 2D model. 2D model is a cross section at the most critical point at the midfield fault of the 3D model.

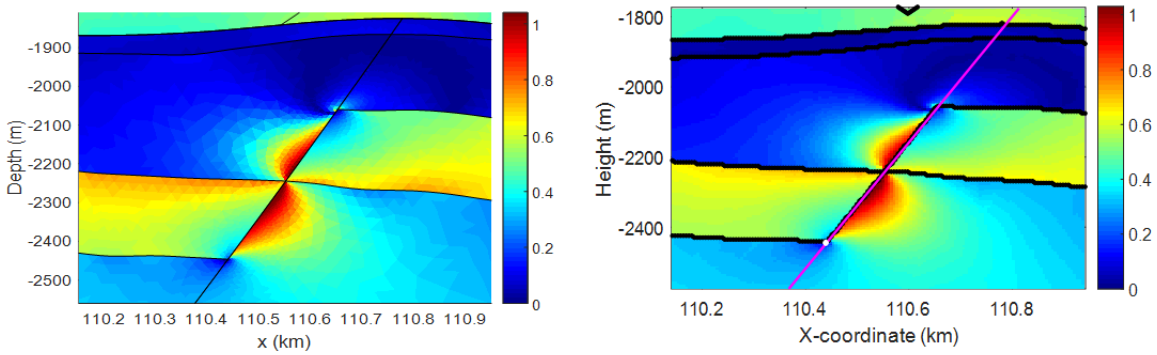

Figure 108: Critical Stress Ratio in 1994 at the most critical point (left) 2D model and (right) cross-section at 3D model.

Comsol slip modelling and depletion calibration

In COMSOL slip modelling requires the definition of a source and destination side (see Figure 109) where the source side will slide over the destination side in case the shear stress exceeds the Mohr-Coulomb failure criterion:

$$\tau > f\left(\sigma_n - p\right) \tag{25}$$

For the pressure the average of the pressure over both sides of the fault is taken. Slip means that the shear displacement of each side of the fault is different.

$$u_{slip} = u_{s,destination} - u_{s,source} \tag{26}$$

The destination side has to be discretized much finer than the source side (Figure 110). Slip modelling makes the model geometrically non-linear, which is expensive to solve even in 2D.

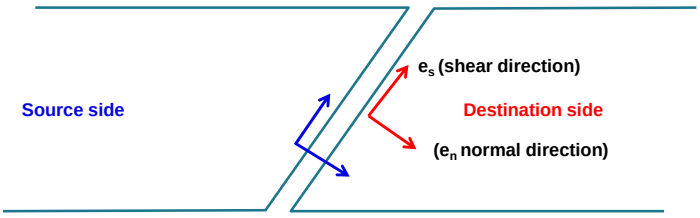

Figure 109: Source and destination sides of the fault.

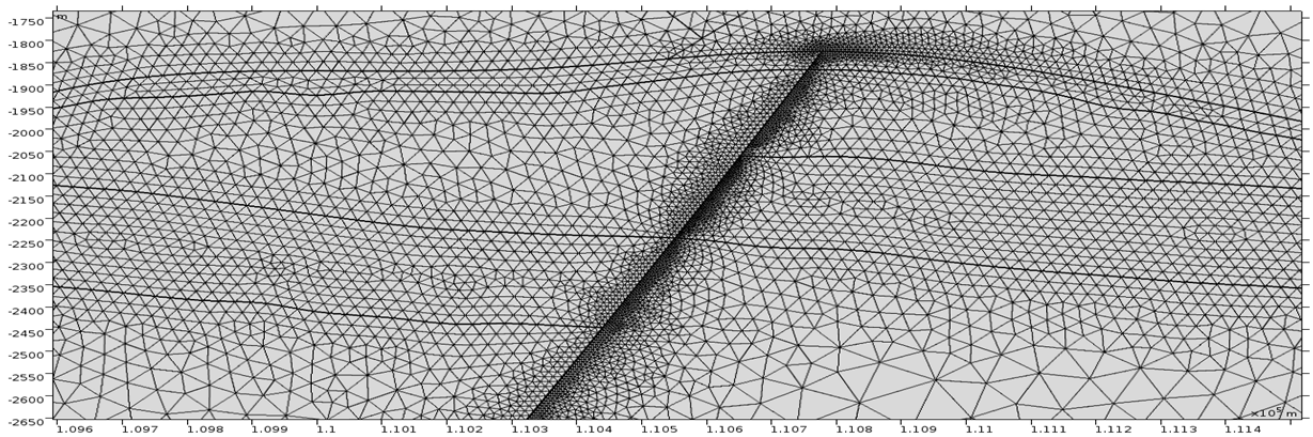

Figure 110: Discretization around the midfield fault. The destination side (east side) of the fault is discretized much finer than the source side (west side) of the fault.

Qualitative behaviour of the slip model

Differential compaction causes the fault shear stress to increase faster than the effective normal stress during reservoir depletion. When the failure criterion is reached, the fault starts to slip and the shear stress is reduced. Slippage means that the shear displacement of the source side differs from the shear displacement

of the destination side (Figure 111). The slip magnitude is the difference between the shear displacements at both sides. During depletion the slip area and the slip magnitude grow over time. Since no slip is computed during refill, the slip area remains constant during refill. During the slip simulation, the normal fault displacement is the same for the source and destination side throughout the simulation (Figure 112), such that the distance between the two sides of the faults remains unaltered and no gaps do appear.

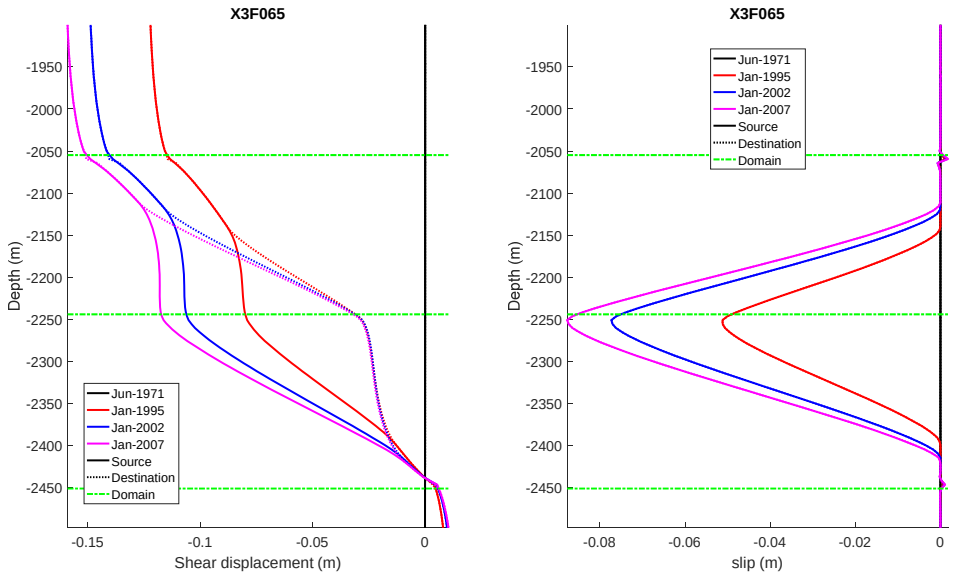

Figure 111: (Left) shear displacement for the source and destination side during depletion showing shear dislocation (right) Growth of the slip size during depletion.

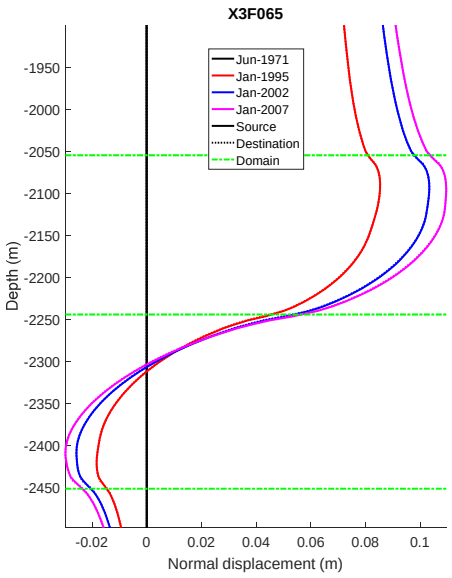

Figure 112: (left) Normal fault displacement during (left) depletion and (right) refill.

Calibration of depletion slip

For a 3D slip model the seismic moment can be directly computed from the seismic slip at the fault surface:

$$M_0 = \int_{A_{slip}} G\,|u_{slip}|\,dA, \qquad u_{slip} = u_{s,destination} - u_{s,source} \tag{27}$$

For the 2D simulation here, it is assumed that the missing dimension is proportional to the slip height, so that the slip area can be expressed as:

$$A \approx w h_{slip} h \tag{28}$$

Here w is a coefficient of proportionality used as fit parameter. Substitution gives the following approximate expression for the Seismic moment:

$$M_0 \approx w h_{slip} \int_{h_{slip}} G u_{slip} dh \tag{29}$$

From calibration of the cumulative seismic moment in the 3D model in 2001 a friction coefficient of f=0.65 results. To match the cumulative seismic moment in the 2D model, a coefficient of proportionality of $w = 7.8$ results. Figure 113 shows that the simulated seismic moment in 1995 also exceeds the required seismic moment after the first two Earthquakes in 1994. The slip height reaches 320m in 2001, which is approximately 80% of the possible height. This means that an area with width of about 2.5km has experienced slip. This is in line with the 3D model.

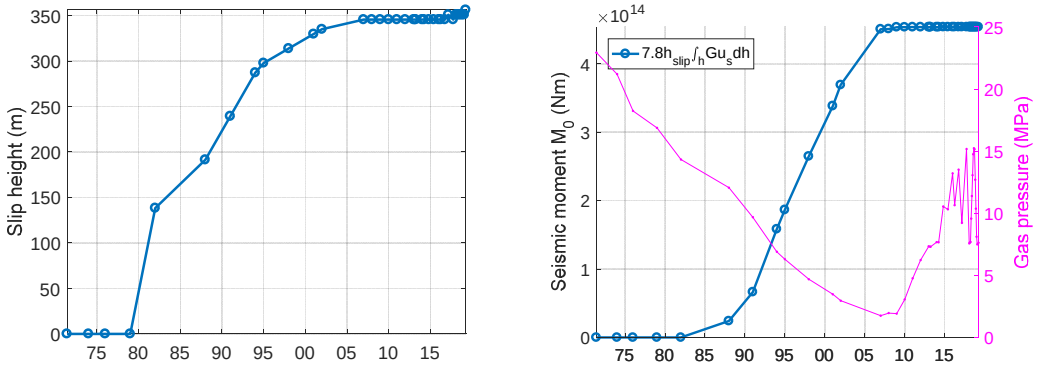

Figure 113: (Left) simulated slip height (Right) Cumulative Seismic Moment for the elastic model including slip with f=0.65.

Comparison of simulation with slip to elastic simulation

This section compares a simulation including slip during the depletion to an elastic simulation. In addition the impact of property hysteresis is studied to match the stiffer response during refill and storage. Table 15 shows the simulation matrix. Adding slip boils down to introducing a shear stress change ($\Delta\tau_{slip}$) as function of place and time which in the followed approach is constant after depletion. Coefficient hysteresis gives both a change in shear and normal stress at the fault.

Table 15: Simulation matrix and impact on shear and normal stress

Simulation	Description	Depletion Slip	Stiffer response after depletion	Impact on shear stress w.r.t Elastic	Impact on normal stress w.r.t Elastic
X1NS	Elastic	x	x	0	0
X3F065	Elastic + slip	v	x	$\Delta\tau_{slip}$	~0
X1NSF	Hysteresis	x	v	$\Delta\tau_{hyst}$	$\Delta\sigma_{n,hyst}$
X3F065F	Hysteresis + slip	v	v	$\Delta\tau_{hyst} + \Delta\tau_{slip}$	$\Delta\sigma_{n,hyst}$

Elastic simulation without slip [X1NS]

In the elastic simulation the Young's modulus, Biot coefficient and Poisson ratio are left unchanged over the entire simulation period and set equal to their calibrated values for the depletion phase (see Section 5). As a

consequence the stress path taken in the Middle of block 1M is free of hysteresis (Figure 114) but the compaction behaviour during refill/storage is not matched.
During depletion differential compaction causes the fault shear stress to increase at a faster rate than the effective normal stress. This results in an increase in the critical stress ratio as shown in Figure 115. Since there is little pressure hysteresis, this process is reversible and on pressurization the critical stress ratio decreases again. However, during depletion the critical stress ratio exceeds the threshold friction coefficient of μ=0.65 and during the refill and storage the most critical area does not drop below the friction coefficient.
For 8 selected points along the midfield fault (see Figure 116), this process is visualized in a Mohr-Coulomb plot and a plot of the CSR versus the average gas pressure. All 8 points show very little path hysteresis in the MC plot and in the CSR vs pressure plot for the most critical points. The hysteresis in the latter plot results from a slight amount of hysteresis between the average gas and average bulk volume pressure. The most critical points remain critical from refill onwards.

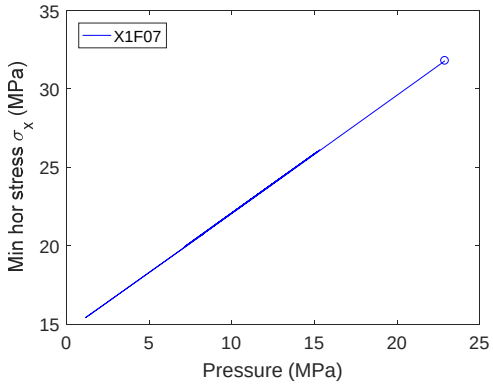

Figure 114: Stress path in the middle of block 1M for history and forecast for the elastic simulation.

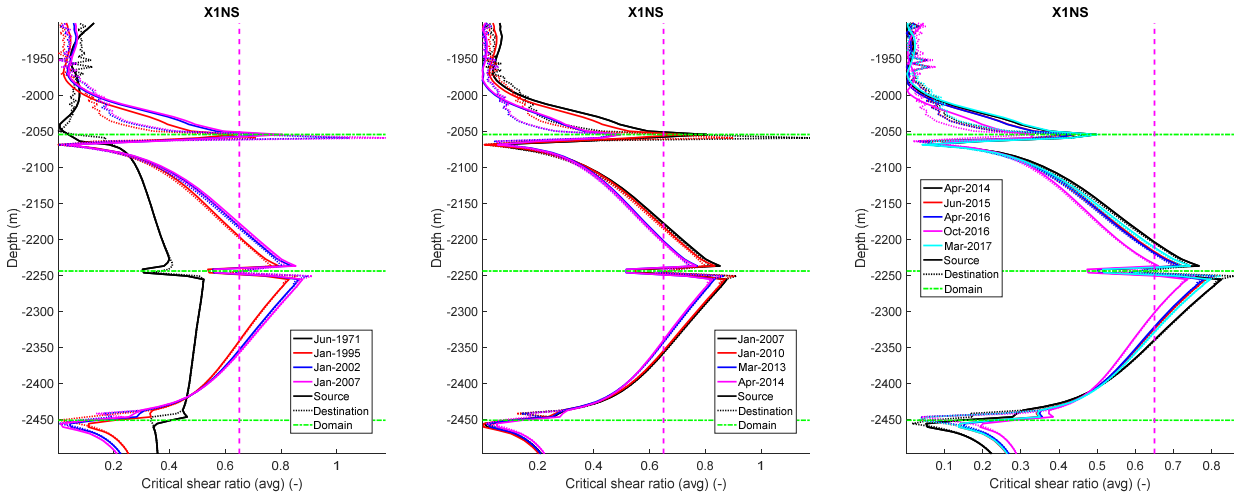

Figure 115: Critical Stress Ratio for the Elastic simulation without slip (left) depletion (middle) refill 2007-2014 and (right) historical storage 2014-2017.

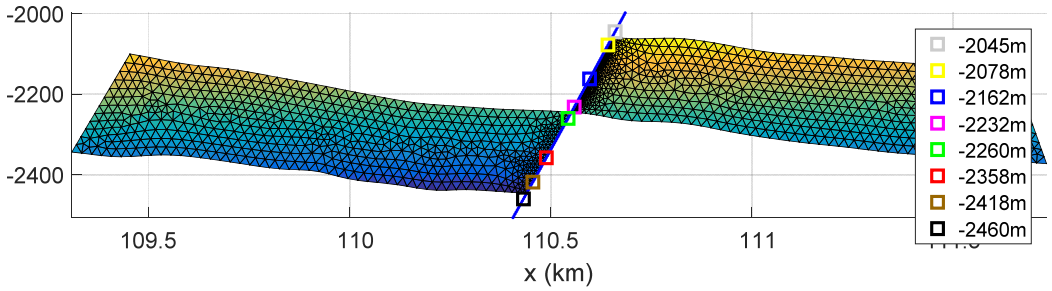

Figure 116: Selection of points along the midfield fault

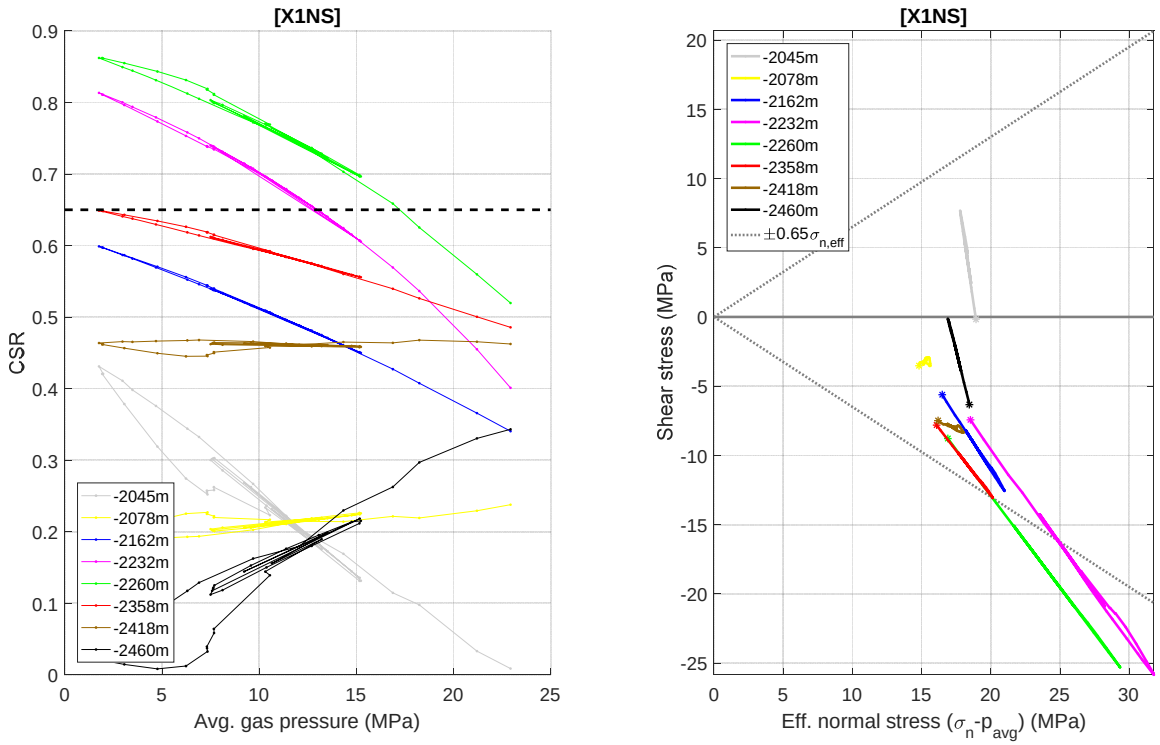

Figure 117: (left) Critical Stress ratio as function of average gas pressure (right) Mohr-Coulomb diagram for entire history and forecast for the elastic simulation without slip. The asterisk indicates virgin condition. Location of the points is shown in Figure 116.

Elastic simulation including slip during depletion [X3F065]

Now consider the impact of adding slip to the simulation during the depletion phase, while refill and storage are modelled without slip. Figure 118 and Figure 119 compare a simulation including slip to the simulation without slip at the end of depletion. Inclusion of slip hardly affects the normal stress at the fault (Figure 118), while the shear stress is considerably modified (Figure 119). When the shear stress exceeds the MC failure criterion, slip occurs and the shear stress is reduced in the critical area, such that the CSR stays on the MC envelop. The excess shear is redistributed such that the integral of the CSR over the height of the domain is zero (conservation of shear correction). Shear stress redistribution gives an increase of the shear stress at the periphery of the critical area which results in a critical area (i.e. the area where the CSR is equal or exceeds the friction coefficient) that is larger in slip simulation (Figure 119).

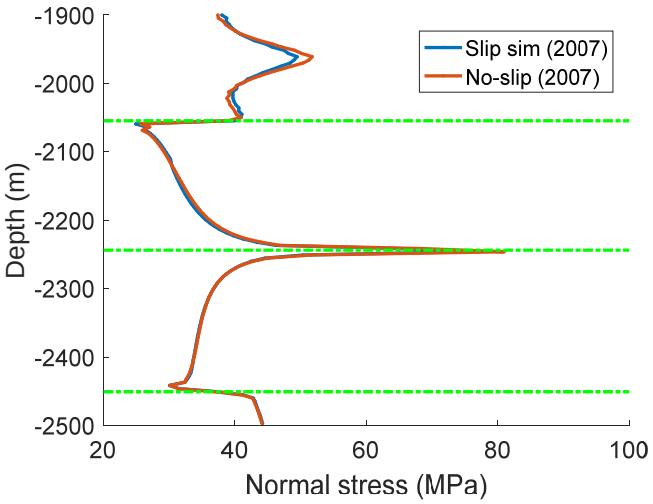

Figure 118: Comparison of the normal stress between Slip simulation and simulation without slip at end of depletion 2007. The slight mismatch above -2050m is outside the slip region and a numerical artefact in the slip model, present from the beginning.

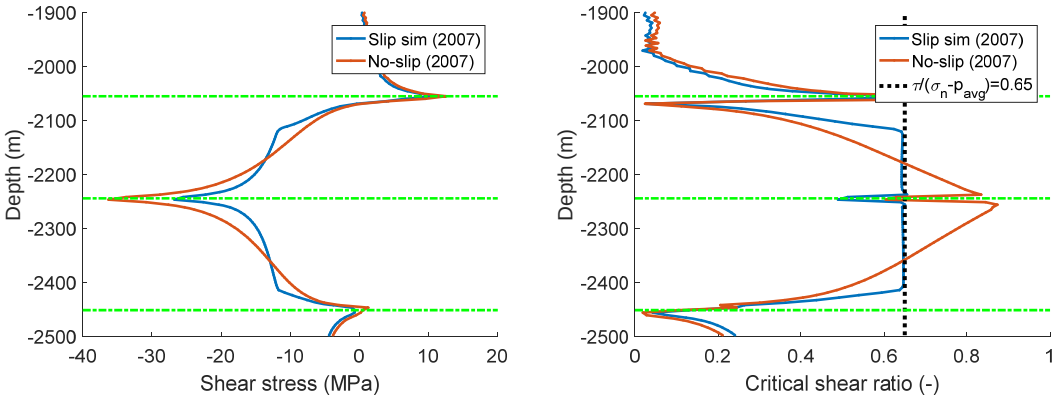

Figure 119: Comparison of (left) the shear stress and (right) the critical stress ration between the slip simulation and simulation without slip at end of depletion 2007.

Since only the shear stress is affected by slip, inclusion of slip will only give a location dependent shear stress change $\Delta\tau_{slip}(x,y,t)$ at the fault that evolves over time and that remains constant from the start of the refill. Figure 120 shows the increase of the shear stress and increase of the slip height, location where the CSR equals 0.65, during depletion. At the end of the depletion phase the fault has shown slippage over 75% of the height where the fault is in contact with the reservoir.

Snapshots of the Critical Stress Ratio show that during refill the section that became first critical during depletion becomes sub- critical while the periphery of the critical area shows a much slower recovery. This is caused by the shear stress increment ($\Delta\tau_{slip}$) at the periphery of the critical area resulting from the depletion slip. This counterbalances the reduction in shear stress during pressurization, such that the stress ratio $R_{crit} = \tau_{slip} / \sigma_{n,eff} = (\tau_{elastic} + \Delta\tau_{slip}) / (\sigma_n - p)$ may stay level or even start to increase because the effective normal stress still decreases or increasing pressure. During refill and storage cycles, points at the periphery of the area critical during depletion stay very close to the critical failure envelope.

For 8 selected points along the midfield fault (Figure 116), this behaviour is shown in more detail in the plot of the CSR as function of the average pressure and the evolution within the Mohr-Coulomb diagram (see Figure 122). The points that become critical during depletion (-2232m and -2260m) rapidly stabilize during refill while the points at the periphery of the critical area (at -2162, -2358m) stays very close to the failure envelope during refill and storage cycles. Comparing Figure 117 and Figure 122 clearly shows the growth of the shear stress for the points at the periphery of the slip area (blue and red line) as they curve towards the MC failure envelope.

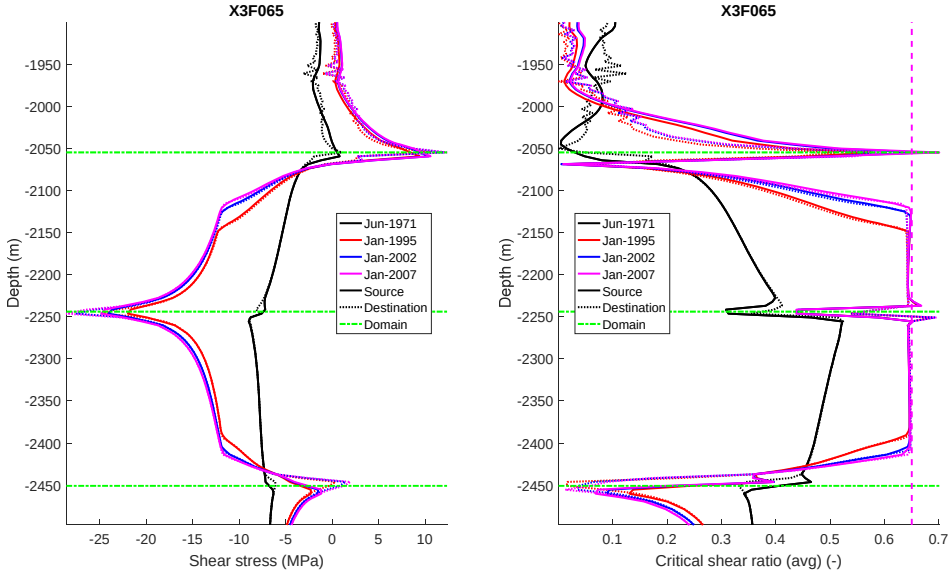

Figure 120: Evolution of the (left) shear stress and (right) crticial stress ratio during depletion for a friction coefficient of 0.65.

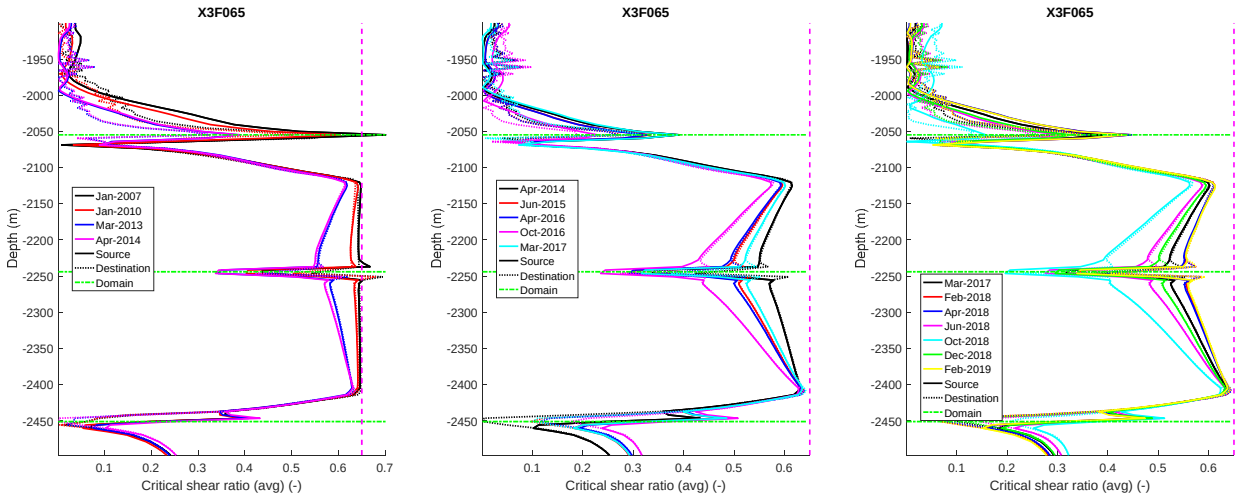

Figure 121: Evolution of the Critical Stress Ratio in time (left) refill (middle) storage and (right) forecast.

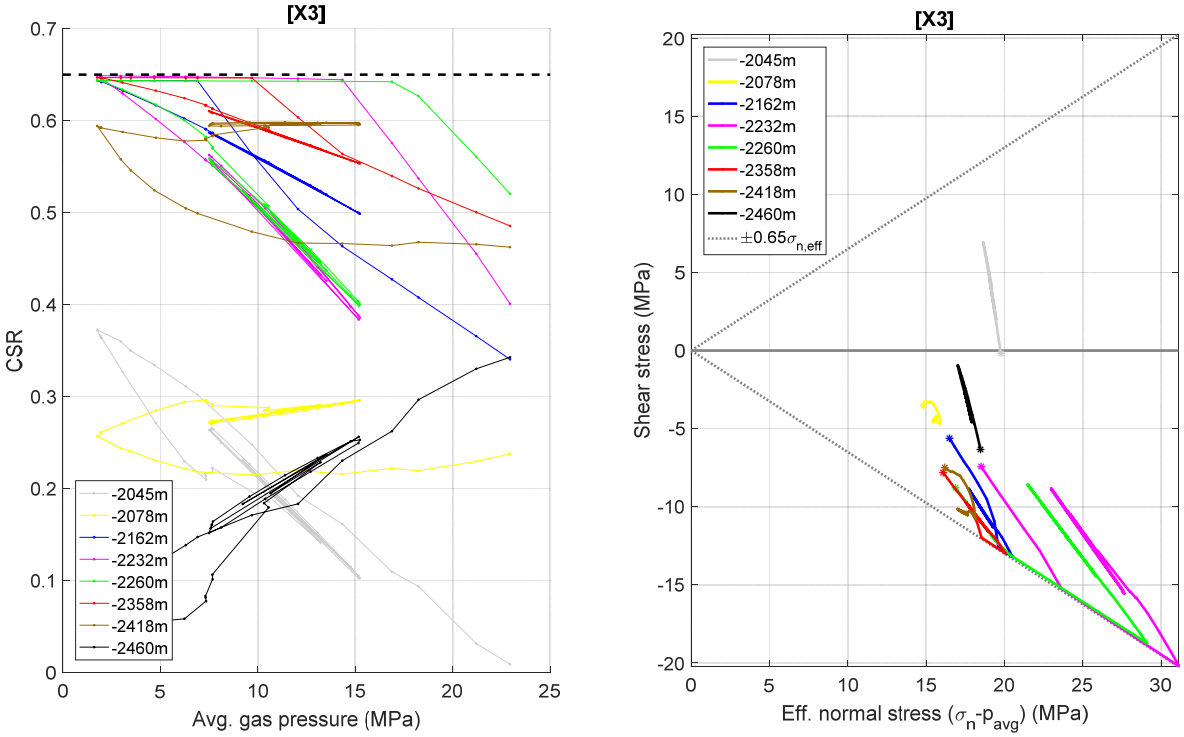

Figure 122: (left) Critical Stress ratio as function of average gas pressure (right) Mohr-Coulomb diagram for history and forecast. The asterisk indicates virgin condition. Location of the points is shown in Figure 116. Simulation including slip.

Refill with coefficient hysteresis after depletion without slip [X1NSF]

The observed response in surface heave during refill and storage indicates a much stiffer response during refill and storage, resulting in an effective (calibrated) compaction coefficient that is 2.5 times higher. The refill period from 2007-2014 showed seismicity up to magnitude 0.9 while during historical storage cycles micro-seismicity has been absent. To get as close to the seismicity as possible, the poroelastic coefficient is set such that the local stress path in the middle of the reservoir remains unchanged (Figure 123) while matching the increase in reservoir stiffness.

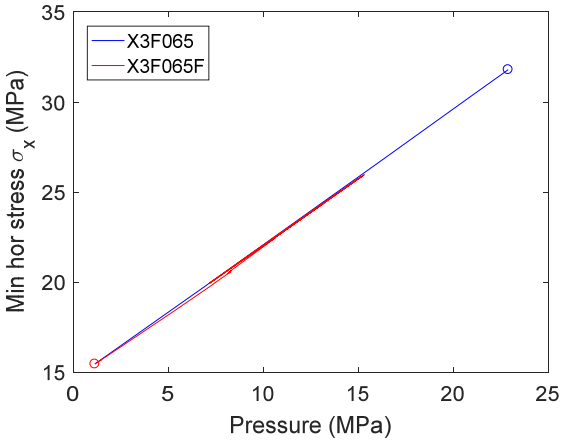

Figure 123: Stress path in the middle of block 1M in 2D slip model. Simulation including coefficient hysteresis.

Introducing hysteresis gives higher shear stresses over the entire height of the fault, when compared to the elastic simulation (Figure 124). This implies that a reduction in volumetric expansion dominates the increase in shear modulus. Normal stresses are elevated close to the centre where the east and west reservoir blocks make contact (-2350m<z<-2175m), while they are reduced at the rims (-2450m<z<-2350m or -2175m<z<-2050m). The combined effect of decreased normal stress and increased shear gives higher critical stress ratio at the rims (Figure 125), while at the centre the increase in shear is counterbalanced by an increase in normal stress.
This behaviour is also reflected in the Mohr-Coulomb diagram and the evolution of the Critical Stress Ratio, see Figure 126. Points in the middle of the reservoir move parallel along the MC envelop, while the lowest point in the reservoir (-2418m) even moves in the direction of the MC failure envelope for increasing pressure.

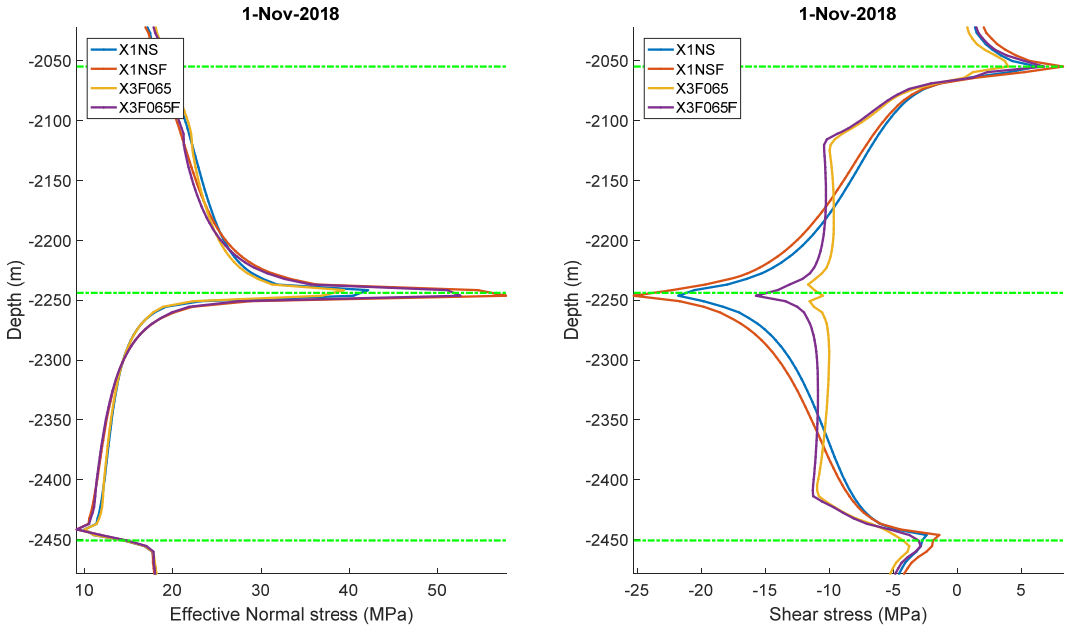

Figure 124: Comparison of (left) the normalr stress and (right) the shear stress in November 2018, between the elastic case (X1NS), case with hysteresis (X1NSF), elastic case with depletion slip (X3F065) and case with hysteresis and depletion slip (X3F065F).

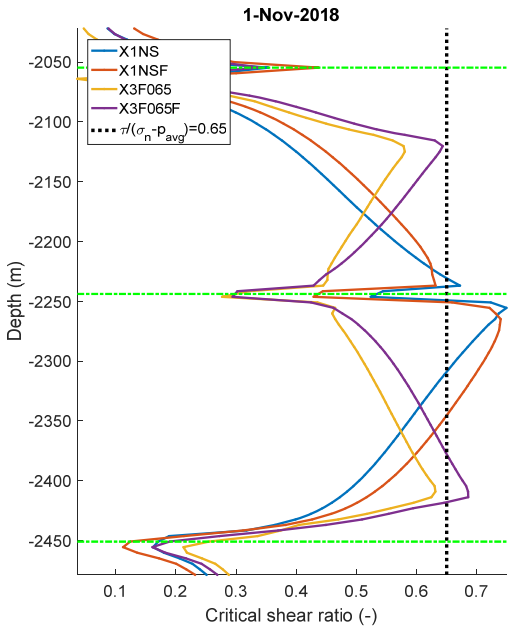

Figure 125: Comparison of critical stress ratio in November 2018, between the elastic case (X1NS), case with hysteresis (X1NSF), elastic case with depletion slip (X3F065) and case with hysteresis and depletion slip (X3F065F). Numerical artefacts dominate the behaviour close to the singularity at the contact point of the reservoir blocks.

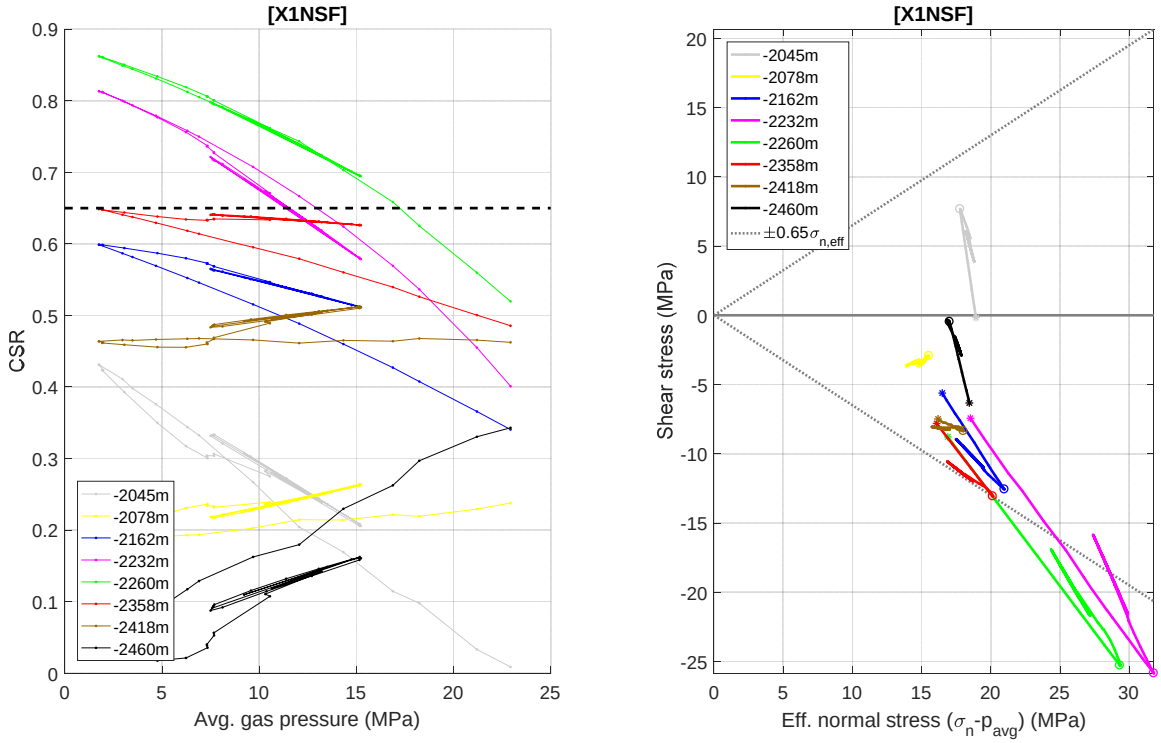

Figure 126: (left) Citical Stress ratio as function of average gas pressure (right) Mohr-Coulomb diagram for history and forecast. The asterisk indicates virgin condition the circle the start of the refill. Location of the points is shown in Figure 116. Simulation including coefficient hysteresis but without slip.

Refill with coefficient hysteresis after simulation with depletion slip [X3F065F]

Similar to the elastic case adding depletion slip effectively only results in a shear stress change $\Delta\tau_{slip}$ that is constant throughout the refill and storage period. At the centre, which is critical during depletion, the reduction in shear stress by the slip dominates over the shear increase resulting from the hysteresis (Figure 124) while the normal stress slightly increases because of the hysteresis. This causes the centre to stabilize during refill, storage and forecast (Figure 125, Figure 127). However, at the rims of the slip area the depletion slip gives an increase in shear stress while the coefficient hysteresis gives a decrease in normal stress (Figure 124). This causes the critical stress ratio to exceed the friction coefficient slightly at the end of the refill period and during the storage and forecast cycles (Figure 125, Figure 127). This happens again for increasing pressure as the slip shear stress correction ($\Delta\tau_{slip}$) dominates the numerator of the failure criterion while the effective normal stress decreases. Note however, that for refill and storage no slip is applied which would partially counterbalance the shear change resulting from depletion, but would again enhance the criticality at the centre. Overall the stress ratio stays close to the failure envelop.

This behaviour is also reflected in the CSR as function of the average gas pressure and the MC diagram (Figure 128). Points at the centre rapidly move away from the failure envelop because of the shear stress reduction by slip. For the same reason, the points at the rim that remained stable in the hysteretic simulation (-2418m) are now pushed over the failure envelop, because of the increase in shear resulting from the slip.

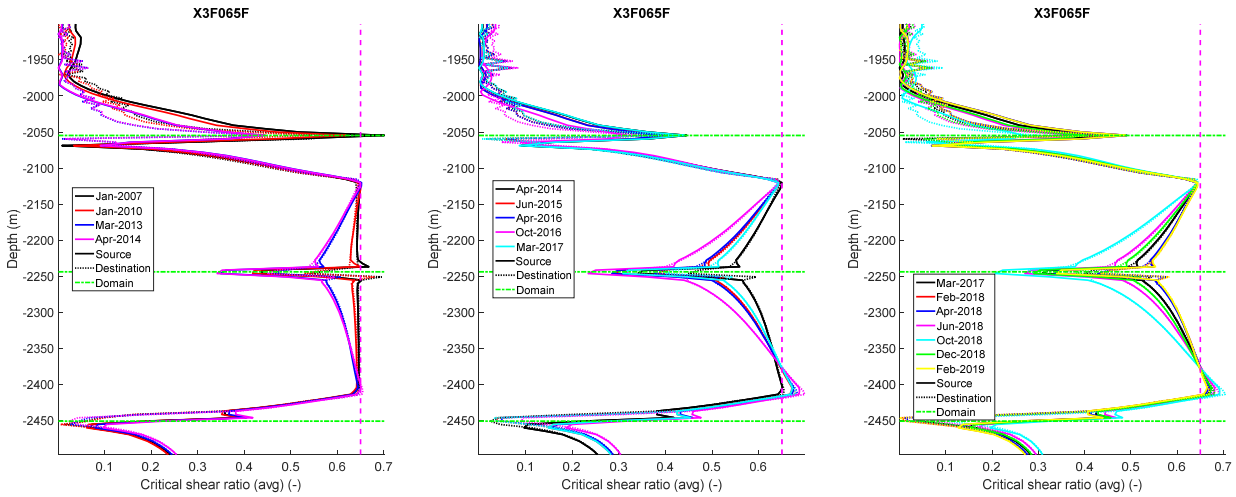

Figure 127: Snapshots of the Critical Stress Ratio along the midfield fault in time (left) refill (right) storage and forecast. Simulation including coefficient hysteresis.

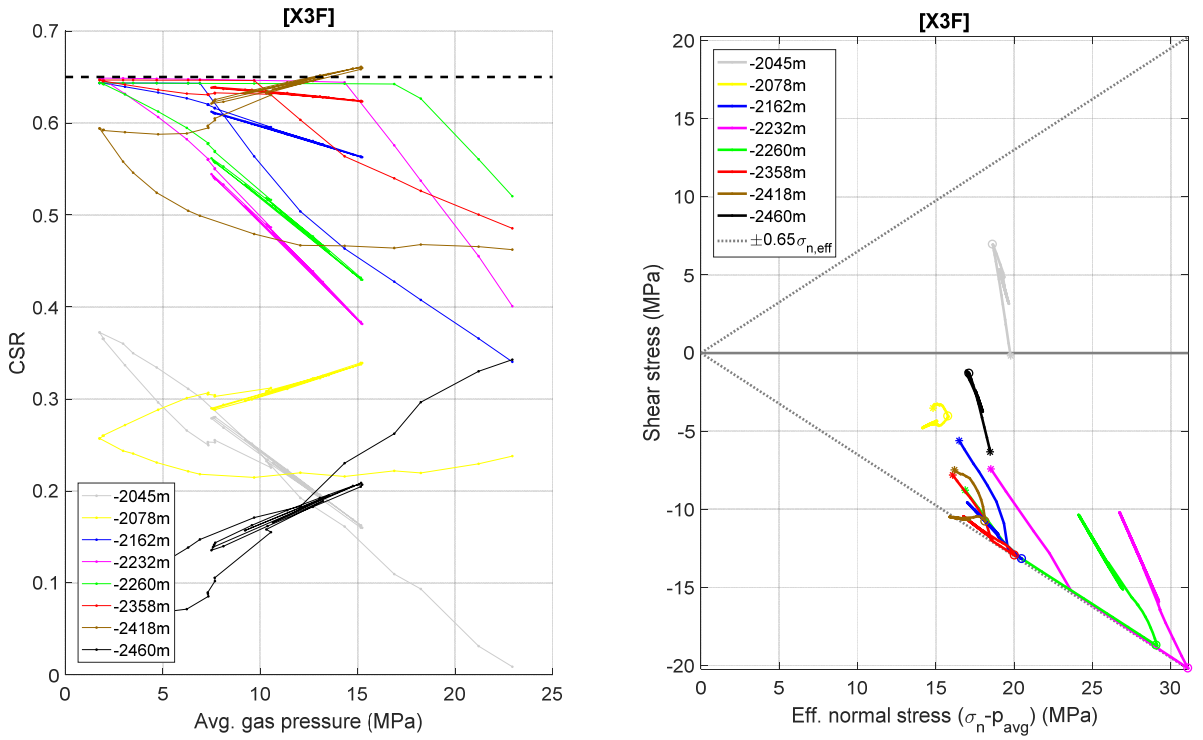

Figure 128: : (left) Citical Stress ratio as function of the average gas pressure (right) Mohr-Coulomb diagram for entire history and forecast for the simulation including coefficient hysteresis and slip. The asterisk indicates virgin condition the circle the start of the refill. Location of the points is shown in Figure 116.

Conclusions for the 2D slip model

- Slip introduces stress path hysteresis at the fault.
- Slip only affects the shear stress. The normal fault stress is not affected significantly.
- Depletion slip gives a shear stress change $\Delta\tau_{dep,slip}$ that affects the refill and storage. This $\Delta\tau_{dep,slip}$ reduces the magnitude of the shear stress in the centre of the slip area and increases the magnitude at the periphery of the slip area (in comparison to an elastic simulation).
- Calibrating the 2D model on the observed cumulative seismic moment in 2001, gives cumulative seismic moments in 1995 that are in line with the observed cumulative seismic moments.
- Simulations including slip give a larger critical area when compared to simulation without slip. This is caused by redistribution of excess shear stress resulting from slippage in which the shear stress is reduced in the centre of a slip area and elevated at the periphery.
    - The average shear stress correction is zero.
- An elastic simulation including slip during depletion does not show criticality from refill onwards. However, criticality gets very close to the MC envelop at the periphery of the depletion slip area. The centre of the depletion slip area stabilizes.
- For a simulation that accounts for the increase in stiffness during refill and storage and has a flat stress path in the middle of the reservoir, refill and storage cycles show a slight increase in criticality at the periphery of the depletion slip area. This occurs at high fluid pressures and is caused by the shear stress increment by depletion slip and a reduction in the normal stress by coefficient hysteresis.

Appendix IV: Water injection into the aquifer

It is estimated that gas production in the winter months may yield a water production of up to 800 m^3/d. So, over a period of 100 days a total volume of 80,000 m^3 should be handled. The water will be re-injected into the reservoir which should pose no problem since the water leg is about as permeable as the gas zone, so that the relatively small amount of water can be easily re-injected.
There are some potential hazards of this re-injection that need to be considered. Regarding the injection itself:

- Height growth of fractures
- Out of zone injection
- Leakage of water into overburden

Regarding seismic hazard it may be expected that:

- Increased pressure on faults:
    - Fracturing may induce high pressure for long fractures
- Cooling of reservoir and stress effect on faults

Considering hazards with the injection itself, the hazard is a function of the induced fracture length. If only a very small fracture can be induced the water will flow only into the aquifer in which the injection well is completed so that no undesired out of zone flow will happen.
If we consider the stress effect due to cooling the extensive modeling by TNO of the reservoir cooling due to gas injection can be used as reference. TNO found that the gas causes only minor cooling and an insignificant effect on the fault stress. Since only 80,000 ton of water will be injected while 3 million ton of gas is injected the effect of water cooling is negligible despite the higher heat capacity of the water.
A direct effect of high pore pressure is of course also depending on the fracture length and the overpressure needed to inject the water. Therefore, we will compute maximum fracture size that can be induced and the overpressure. If these are small, even in a worst case it can be concluded that safe operation will be guaranteed.
With respect to a previous water injection fracture simulation, the findings of the new data interpretation will be used. The most important changes are higher reservoir pressure with higher stress and the stiffer rock and smaller poro-elastic coefficient.
The stiffer rock and smaller poro-elastic coefficient have a large impact on expected fracture behaviour. In previous simulations it was found that water injection in this high permeability reservoir is unlikely to induce any significant fractures, but cooling of the reservoir will be more important. Moreover, stiffer rock will cause larger stress reduction by cooling since thermo-elastic stress is proportional to Young's modulus. In a worst-case simulation of the induced water injection fracture for a rate of 800 m^3/d over a period of 3 months, which corresponds with the maximum water production in the production period. For estimating the fracture size, we use a simple 2D model based on the work of Hagoort and Koning. There will be 3D effects when injecting into the water leg, which would yield a smaller fracture, because the pressure will be smaller.
Figure 129 shows that the pressure is only slightly above the reservoir pressure which was assumed (as a worst case) to stay at 150 bar (15 MPa). The induced fracture is shown in Figure 130 to reach about 22 m half length. Figure 131 shows that the most important stress change is due to cooling. The poro-elastic stress is proportional to the increase in injection pressure which is very small.

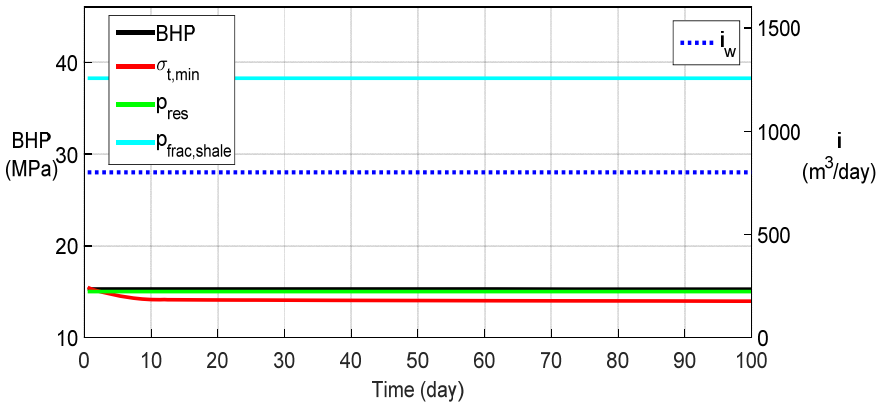

Figure 129: Simulated water injection pressure for the 150-bar pressure scenario. Also shown is the minimum stress, $\sigma_{t,min}$ the reservoir pressure p_{res} and the estimated shale stress. The right-hand scale is for the injection rate curve.

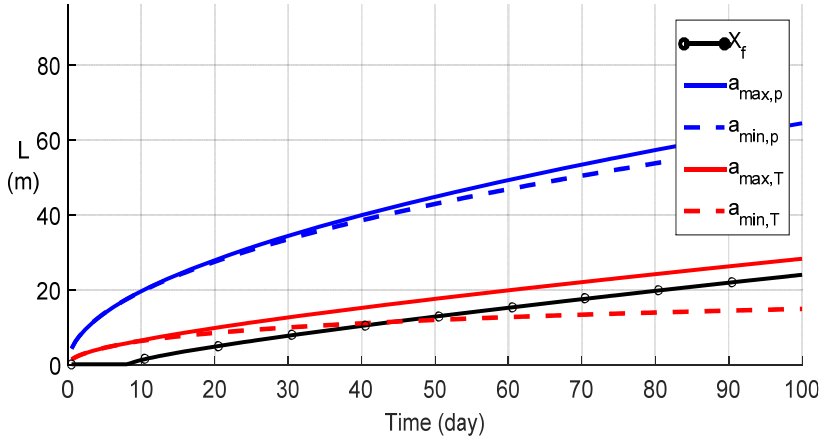

Figure 130: Simulated water injection fracture half length, X_f for the 150 bar pressure scenario. Also shown is the extent of the cooled front and flooded zone. The major and minor axes are a_{max} and a_{min} and suffix p designates flooded zone and suffix T designates cooled zone.

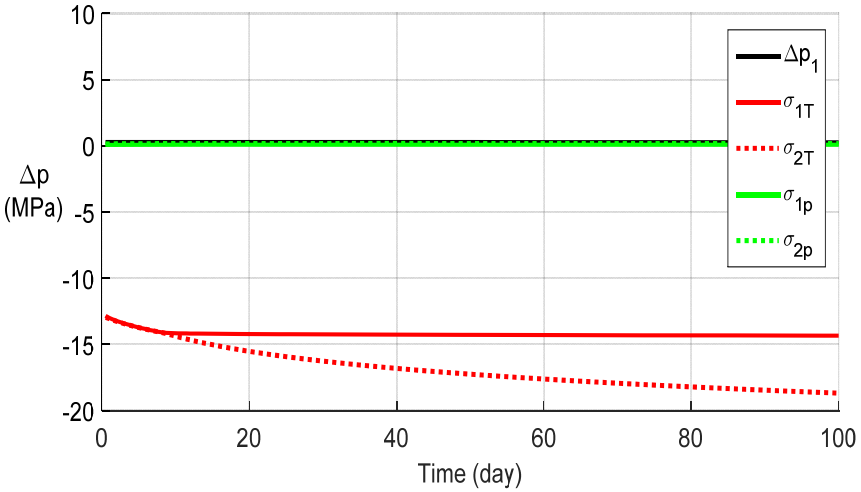

Figure 131: Simulated water injection pressure and stress changes for the 150-bar pressure scenario. The thermal stress is significant because of the assumed stiffer reservoir during re-fill. The minimum stress is σ_1 and maximum stress is σ_2. Suffix T denotes thermal stress change and suffix p is the poro-elastic stress.

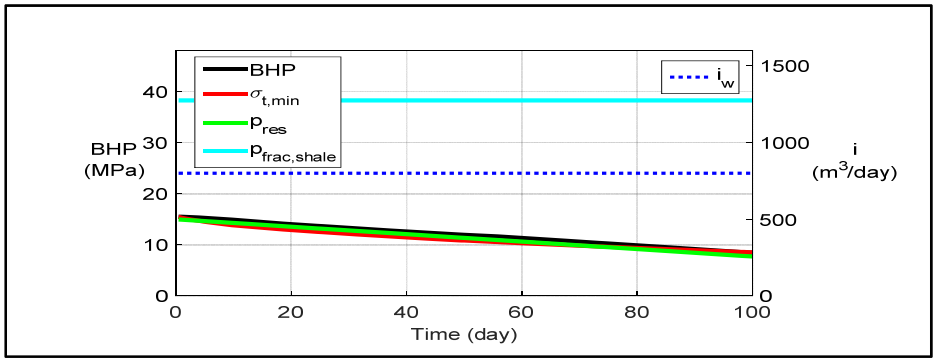

Figure 132: Simulated water injection pressure for the 150-bar pressure scenario, using falling reservoir pressure during the injection period.

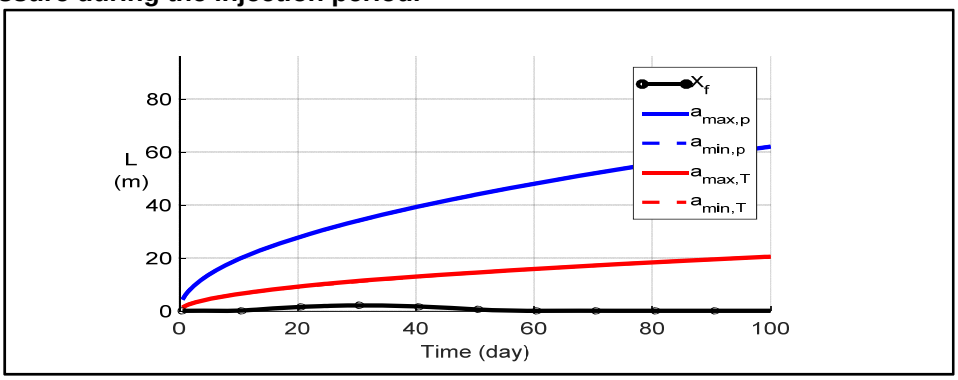

Figure 133: Simulated water injection fracture size for the 150-bar pressure scenario, using falling reservoir pressure during the injection period. Also shown is the extent of the cooled front and flooded zone.

If the reservoir pressure will follow the falling gas pressure to 77 bar (Figure 132), there will be hardly any fracture propagation as shown in Figure 133. The main reason for the absence of fracture propagation is the favourable stress but the small pressure needed to inject the water is also important.
The simulated fracture size is quite small compared with reservoir thickness so we used the plane strain approximation to the stress change. This means that vertical displacements are restricted by the surrounding rock, because the pressure penetration is small compared to reservoir height. Since the fracture is relatively short, no complications are expected with upward growth of the fracture. The distance of the injector to the faults is much larger than the fracture length, so growth of the fracture towards the faults is of no concern.
Baker (2013) has also considered the effect of water injection on the stress state at the fault. It was found that this effect was negligibly small compared with the differential compaction effect. TNO modelled the change in temperature due to gas injection which was of course much larger, due to larger injection volumes of gas.
In view of the small fracture (even in the worst-case assumption), the water injection could never raise the pressure near the faults. The injection zone has sufficient permeability and storage to allow equilibration of pressure. The small injection volumes will result only in small pressure disturbance near the injector. Yet, the historical water injection was so small that any effect could not be discerned, so field verification will need to await larger injection periods.

Appendix V: Geomechanical Model Construction

Fault planes and horizons were exported from a new Petrel model provided by TAQA, so that they could be imported into a CAD system to convert the discrete point sets to parametric surfaces by fitting splines to the discrete meshes. Surfaces were used of top North Sea (NS), top Vlieland Claystone (KN), top Upper Germanic Trias (UGT), top Lower Germanic Trias (LGT), top Zechstein Salt (ZET), Top platen Dolomite and Anhydrite (ZEB), Top Rotliegend (RO) and Top Carboniferous (BU), see Figure 17 .

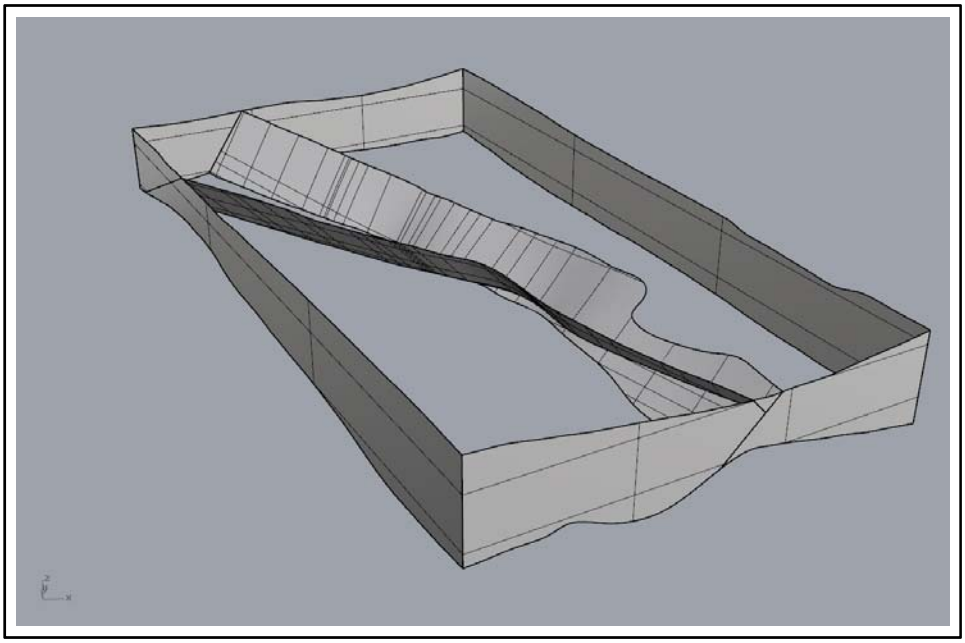

Figure 134: Model showing the two overburden faults, below the top Lower Germanic Triassic horizon. The Midfield fault in the overburden is the main fault; this fault coincides with the Midfield fault south of the reservoir but then turns away to the west. So, the fault system has two scissor faults: in the reservoir with an up and down thrown block and in the overburden with a shear in the east-west direction. Since the faults could be terminated on the top Zechstein surface, the two fault systems could be decoupled.

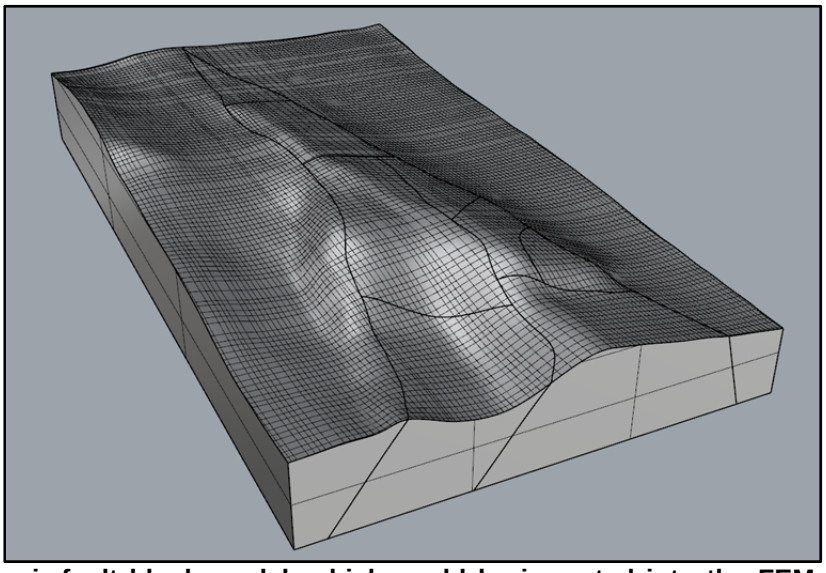

Figure 135: Reservoir fault block model, which could be imported into the FEM system as solids. Then these solid blocks could be cut by the horizons which were split up by fault block to accurately model the fault offsets.

The most efficient way to build the model was to first define the fault blocks using top and bottom surfaces and the fault planes, shown in Figure 18 and Figure 134. The fault blocks are shown in Figure 135. Then later each fault block is split up in units defined by intermediate horizons. The latter is best done in the FEM system. Making the fault blocks is relatively easy, but splitting up the horizons by fault block involves a lot of work. There are automatic procedures for removing so-called fault drag, by retracting the surfaces and then extrapolating them onto the faults, but this often requires user input.
The final challenge is combining the various domains to a union, which is obtained by recognizing the surfaces and contact edges of all domains. That is a complicated task that often requires user intervention since automatic procedures fail for the complex geometries of the adjacent domains at a fault. If the layers have a large offset at a fault, it is straightforward to define the new surfaces at the fault. However, when the offset is quite small those sliver surfaces need to be removed to avoid spurious fine gridding.
Potential complexity in the Bergermeer field is caused by the reservoir and overburden faults. The Midfield fault runs South-North and the reservoir is offset at this scissor fault which ends in the reservoir. In the overburden, the fault is continuous south of the Bergermeer field, but towards the north separates by tearing with an east-west offset. The reservoir and overburden parts of the fault could be decoupled by separating them on the Zechstein layer. There is also a smaller fault in the overburden that ends partially on the Midfield fault, see Figure 134. These overburden faults were added to the previous models to investigate potential seismicity in the overburden due to compaction and expansion of the reservoir. It turns out that this is not happening, but we kept these faults in the model for completeness.
The entire inner block model after cutting the fault blocks with the horizons is shown in Figure 19. This model is comparable in size to the previous Baker model and this is sufficient to model the fault stress, which is the primary objective. However, it is also important for a calibrated model to match the observed subsidence. Since the subsidence bowl gets very large it is necessary to extend the model. This can be done simply by embedding the inner block in a layer cake block, as shown in Figure 20. Subsidence is hardly influenced by detailed underground structure, although lamination (and contrasts in modulus) has some impact on subsidence. The Baker model showed boundary effects in the subsidence bowl, but this is much less in the extended model.